THE MINISTRY OF SCIENCE AND HIGHER EDUCATION OF THE RUSSIAN FEDERATION

ST. PETERSBURG STATE POLYTECHNICAL UNIVERSITY

JOURNAL

Physics and Mathematics

VOLUME 18, No.4.1, 2025

Peter the Great St. Petersburg
Polytechnic University
2025

ST. PETERSBURG STATE POLYTECHNICAL UNIVERSITY JOURNAL. PHYSICS AND MATHEMATICS

The journal is included in the List of leading peer-reviewed scientific journals and other editions to publish major findings of theses for the research degrees of Doctor of Sciences and Candidate of Sciences.

The publications are presented in the VINITI RAS Abstract Journal and Ulrich's Periodical Directory International Database.

The journal is published since 2008 as part of the periodical edition 'Nauchno-tekhnicheskie vedomosti SPb-GPU'.

The journal is registered with the Federal Service for Supervision in the Sphere of Telecom, Information Technologies and Mass Communications (ROSKOMNADZOR). Certificate ПИ № ФС77-52144 issued December 11, 2012.

The journal is in the **Web of Science** (Emerging Sources Citation Index), **Scopus,** the **Russian Science Citation Index** (RSCI) and the **Directory of Open Access Journals** (DOAJ) databases.

Address: 195251 Politekhnicheskaya St. 29, St. Petersburg, Russia.

Phone: 8 (812) 552-62-16.

http://ntv.spbstu.ru/physics

МИНИСТЕРСТВО НАУКИ И ВЫСШЕГО ОБРАЗОВАНИЯ РОССИЙСКОЙ ФЕДЕРАЦИИ

НАУЧНО-ТЕХНИЧЕСКИЕ ВЕДОМОСТИ

САНКТ-ПЕТЕРБУРГСКОГО ГОСУДАРСТВЕННОГО ПОЛИТЕХНИЧЕСКОГО УНИВЕРСИТЕТА

Физико-математические науки

ТОМ 18, №4.1

2025

Санкт-Петербургский политехнический
университет Петра Великого
2025

НАУЧНО-ТЕХНИЧЕСКИЕ ВЕДОМОСТИ САНКТ-ПЕТЕРБУРГСКОГО ГОСУДАРСТВЕННОГО ПОЛИТЕХНИЧЕСКОГО УНИВЕРСИТЕТА. ФИЗИКО-МАТЕМАТИЧЕСКИЕ НАУКИ

Журнал с 2002 г. входит в Перечень ведущих рецензируемых научных журналов и изданий, в которых должны быть опубликованы основные результаты диссертаций на соискание ученых степеней доктора и кандидата наук.

Сведения о публикациях представлены в Реферативном журнале ВИНИТИ РАН, в международной справочной системе «Ulrich's Periodical Directory».

С 2008 года выпускается в составе сериального периодического издания «Научно-технические ведомости СПбГПУ».

Журнал зарегистрирован Федеральной службой по надзору в сфере информационных технологий и массовых коммуникаций (Роскомнадзор). Свидетельство о регистрации ПИ № ФС77-52144 от 11 декабря 2012 г.

Журнал индексируется в базах данных **Web of Science** (Emerging Sources Citation Index), **Scopus**, а также включен в базы данных **«Российский индекс научного цитирования»** (РИНЦ), размещенную на платформе Научной электронной библиотеки на сайте http://www.elibrary.ru, и **"Directory of Open Access Journals"** (DOAJ).

Адрес редакции и издательства:

Россия, 195251, Санкт-Петербург, ул. Политехническая, д. 29.

Тел. редакции 8 (812) 552-62-16.

http://ntv.spbstu.ru/physics

PREFACE

Seventh Asian School-Conference on Physics and Technology of Nanostructured Materials (ASCO-Nanomat 2025) has been held under the auspices of the Institute of Automation and Control Processes of Far Eastern Branch of Russian Academy of Sciences and Presidium of Far Eastern Branch of Russian Academy of Sciences, in Vladivostok on July, 11–15, 2025. ASCO-NANOMAT 2025 was intended as a forum for senior and young scientists and technologists from Asian and European universities, academic institutes and industrial enterprises where they could present their latest findings and develop new synergies in the field of Physics and Technology of Nanostructured Materials and related subjects.

Vladivostok is a Russian city in Far Eastern region, geographically close to Asian countries: China, Japan, Korea, India, Taiwan, Australia and others. Therefore, the first aim of this School-Conference is to stimulate multidisciplinary contacts and cooperation between scientists form Asia and Europe. Russia here acts as a bridge connecting two parts of the World. The second aim is to give to young scientists the opportunity to deliver their presentations on the international conference and encourage them by the award for the best oral or poster report.

The conference was held in on-site ("face-to-face") mode in two parallel sections using two conference halls of the Presidium of the Far Eastern Branch of the Russian Academy of Sciences in Vladivostok.. More than 130 participants took part, including 41 speakers from Vladivostok, including young scientists, graduate students, and undergraduates from various cities across the Russian Federation. Several foreign scientists from Japan participated online as plenary and invited speakers because of their inability to travel to Vladivostok. The school-conference was successful. Participants, including renowned professors, young scientists, and graduate students from five countries in Asia and Europe, including the Russian Federation, delivered 8 plenary, 18 invited, 54 oral talks, and 46 poster presentations. All conference objectives were achieved. The ASCO-Nanomat 2025 was a multidisciplinary school-conference, which has been held for the seventh time, and had eight scientific sections:

- Physics of nanostructures and interfaces, self-organization processes, two-dimensional materials
- IVth group material's alloys based on Si, Ge, Sn and Pb: formation, structure and properties
- Physics of semiconducting nanostructures and heterostructures, including silicide, germanide and chalcogenide heterostructures: experiment, calculations and technology
- Optical materials and photonic crystals
- Formation and properties of ferromagnetic and ferroelectric materials, spintronics
- Nanostructured coverages, nanocomposites, functional hybrid materials: formation, structure and properties
- Biomaterials and sensors on their base
- Photonic devices: solar cells, nanophotonics, biophotonics



Abstracts of all reports were published electronically by Dalnauka publishing house.

At the end of the conference, 10 young scientists (under 35 years old) were awarded for the best oral and poster presentations.

Following the conference, participants in Vladivostok visited the Voroshilov Battery and the Pospelov Fort on Russky Island, as well as the famous beach in Lazurnaya Bay (Shamora), 30 km from Vladivostok, where they enjoyed swimming in the warm waters of Ussuri Bay.

The Publishing Committee and International Program Committee have selected 21 unpublished articles, which have been recommended for publication in the "St. Petersburg Polytechnic University Journal - Physics and Mathematics" as selected Proceedings.

We, the International Program Committee, are very pleased to publish selected articles of "ASCO-NANOMAT 2025" for scientists, researchers and students with interest in the physics and technology of nanostructured materials.

We would like to take this opportunity to thank all authors, Plenary and Invited lectors, the Organizing Committee and International Program Committee members for their contributions to the conference.

Professor Nikolay G. Galkin,
Chairman of ASCO-Nanomat 2025,
Vladivostok, Institute of Automation
and Control Processes FEB RAS
(galkin@iacp.dvo.ru)

Contents

Condensed matter physics

Simulation of physical processe

Atom physics and physics of clusters and nanostructures

Physical optics

Physical materials technology

CONDENSED MATTER PHYSICS

Conference materials
UDC 539.23+537.32+536.21
DOI: https://doi.org/10.18721/JPM.184.101

Si-Fe composites with embedded α-$FeSi_2$ nanocrystals: formation and thermoelectric properties

K.N. Galkin, O.V. Kropachev, O.A. Goroshko,
E.Yu. Subbotin, D.L. Goroshko, N.G. Galkin ✉

Institute of Automation and Control Processes, FEB RAS, Vladivostok, Russia
✉ galkin@iacp.dvo.ru

Abstract. The technology of embedding metallic iron disilicide (α-$FeSi_2$) nanocrystals (NCs) with different numbers of NCs multilayers and different doping levels of silicon multilayers with holes (10^{19} cm^{-3} and 10^{13} cm^{-3}) was tested on SOI substrates, and composites with 4 and 8 layers of embedded α-$FeSi_2$ NCs were grown using it. The maximum power factor 0.1 to 0.25 mW/(m×K²) at T = 450 K was observed in the composite with the maximum hole concentration in the silicon interlayers, and a decrease in the hole concentration led to a decrease in the power factor to 0.01 mW/(m×K²) at T = 450 K due to a sharp decrease in the sheet resistance with a weak increase in the Seebeck coefficient.

Keywords: silicon, α-$FeSi_2$ nanocrystals, crystal structure, doping, Si interlayers, conductivity, thermoelectric properties, power factor

Funding: The work was carried out with the support of the state assignment of the IACP FEB RAS FWFW-2006-0008

Citation: Galkin K.N., Kropachev O.V., Goroshko O.A., Subbotin E.Yu., Goroshko D.L., Galkin N.G., Si-Fe composites with embedded α-$FeSi_2$ nanocrystals: formation and thermoelectric properties, St. Petersburg State Polytechnical University Journal. Physics and Mathematics. 18 (4.1) (2025) 9–14. DOI: https://doi.org/10.18721/JPM.184.101

Материалы конференции
УДК 539.23+537.32+536.21
DOI: https://doi.org/10.18721/JPM.184.101

Композиты Si-Fe со встроенными нанокристаллами α-$FeSi_2$: формирование и термоэлектрические свойства

К.Н. Галкин, О.В. Кропачев, О.А. Горошко,
Е.Ю. Субботин, Д.Л. Горошко, Н.Г. Галкин ✉

Институт автоматики и процессов управления ДВО РАН, г. Владивосток, Россия
✉ galkin@iacp.dvo.ru

Аннотация. На подложках КНИ апробирована технология встраивания нанокристаллов (НК) металлического дисилицида железа (α-$FeSi_2$) с разным количеством мультислоев НК и разным уровнем легирования кремниевых мультислоев дырками (10^{19} $см^{-3}$ и 10^{13} $см^{-3}$) и по данной технологии выращены композиты с 4 и 8 слоями встроенных в кремний НК α-$FeSi_2$. Максимальный фактор мощности от 0.1 до 0,25 мВт/(м×K²) при T = 450 K наблюдался в композите с максимальной концентрацией дырок в кремниевых прослойках, а уменьшение концентрации дырок приводило к уменьшению фактора мощности до 0,01 мВт/(м×K²) при T = 450 K за счет резкого уменьшения слоевого сопротивления при слабом росте коэффициента Зеебека.

Ключевые слова: кремний, нанокристаллы α-$FeSi_2$, кристаллическая структура, легирование, прослойки Si, проводимость, термоэлектрические свойства, коэффициент мощности

Финансирование: Работа выполнена при поддержке государственного задания ИАПУ ДВО РАН (Тема FWFW-2026-0008).

Ссылка при цитировании: Галкин К.Н., Кропачев О.В., Горошко О.А., Субботин Е.Ю., Горошко Д.Л., Галкин Н.Г. Композиты Si-Fe со встроенными нанокристаллами α-$FeSi_2$: формирование и термоэлектрические свойства // Научно-технические ведомости СПбГПУ. Физико-математические науки. 2025. Т. 18. № 4.1. С. 9–14. DOI: https://doi.org/10.18721/JPM.184.101

Introduction

One of the approaches to creating efficient thermoelectric materials is to embed metal nanocrystals (NCs) into a semiconductor, such as germanium, which provides high matrix conductivity and an increase in the Seebeck coefficient [1]. It does not require high crystalline quality of materials with embedded nanocrystals and assumes the possibility of their random distribution in the semiconductor matrix, including silicon. NCs of transition metal silicides can be embedded into silicon, since they include both semiconductors [2] and metals [3]. It was known that embedding multilayers with one or two types of embedded NCs ($CrSi_2$ and β-$FeSi_2$) grown on an *n*-type silicon substrate resulted in efficient hole injection from embedded NCs, a change in the sign of the Seebeck coefficient from negative to positive, and an increase in the power factor in the temperature range from 200 K to 400 K [4]. At the same time, the incorporation of NC metal silicides into a silicon matrix with *p*-type conductivity and orientation (100), as well as the effect of doping silicon interlayers during the growth of multilayers on their thermoelectric parameters, remained unexplored.

In this paper, we investigated the formation of multilayers with embedded NCs of metallic iron disilicide (α-$FeSi_2$) in silicon-on-insulator (SOI) substrates of *p*-type conductivity with different numbers of NC multilayers and different doping levels of silicon multilayers, determined the phonon structure of the NCs, the conductivity and thermoelectric properties of the grown heterostructures in the temperature range of 80–450 K.

Materials and Methods

Multilayer heterostructures with embedded NCs of metallic α-$FeSi_2$ were grown in a VARIAN ultrahigh vacuum setup with a base pressure of 2×10^{-10} Torr equipped with a molecular beam source of iron (Fe), sublimation sources of silicon (Si) with different hole concentrations (p^+ and p^-) and a quartz thickness sensor. SOI Si(100) *p*-type wafers with a resistivity of (1–10) Ω × cm were chosen as substrates and Si sources. After low-temperature cleaning of the silicon surface at a temperature of 900 °C for 10 minutes, a 50 nm thick silicon buffer layer was deposited at $T = 700$ °C. Then, multilayer samples with embedded NCs of α-$FeSi_2$ were formed. This process consisted of four steps: (1) deposition of 0.5 nm Fe at room temperature; (2) annealing at $T = 630$ °C for 2 min and flash at $T = 1000$ °C for 5 s; (4) growth of the silicon layer (12 nm at $T = 630$ °C and 24 nm at $T = 700$ °C). To form 4-layer and 8-layer structures with embedded α-$FeSi_2$ NCs, these four steps were repeated 3 or 7 times, followed by growth of the capping silicon layer in two steps: 12 nm at $T = 630$ °C and 84 nm at $T = 700$ °C. Individual multilayers were grown with doped silicon interlayers with different hole doping: 10^{19} cm^{-3} (p^+) and 10^{13} cm^{-3} (p^-). For comparison with samples with embedded multilayers of α-$FeSi_2$ NCs, test samples were grown with 4 and 8 fictitious stages of silicon growth without deposition of iron atoms, but with annealing and stops (NC growth emulation or dummy composite (CS)) with different silicon sources (p^+ and p^-). A total of 3 samples with embedded α-$FeSi_2$ NCs and 3 samples with dummy CS were grown.

The morphology of the grown samples was studied using a Solver P47 scanning probe microscope in the tapping mode. The phonon structure of the grown samples was studied using an NTEGRA SPECTRA-II system in the Raman spectroscopy mode. The transport and thermoelectric properties of the samples were studied on a Kriotel (Russia) laboratory setup in a nitrogen atmosphere at temperatures of 80–450 K after preliminary formation of six Al contacts on an ADVAVAC PVD-2EB2R11 vacuum setup (To = 450 °C for 20 minutes) to measure conductivity and thermo-emf.

Results and Discussion

After unloading the samples with embedded α-$FeSi_2$ NCs and the reference samples with growth emulation, their surface morphology was studied by AFM. Due to the embedding of nanocrystals with a tetragonal lattice into silicon, a process of three-dimensional overgrowth of Si atop α-$FeSi_2$ NCs was observed and punctures were formed on the surface of the capping silicon layer. However, the yield of α-$FeSi_2$ NCs onto the surface of the composite was not observed. The root-mean-square roughness was minimal for 4-layer heterostructures both with embedded NC and without them (Table). Increasing the number of multilayers led to its 2–3-fold growth, but the depth of the observed punctures did not exceed 40 nm, which is less than the thickness of the capping silicon layer.

Table

Types of composites (CS), type of doping of Si interlayers, d_{CS} is total thickness of composite, σ_{rms} is root mean square roughness

Sample	Type of composite	Si interlayer doping	D_{CS}, nm	s_{rms}, nm
A	Dummy CS_1	p^+	256	2.0
B	4L α-$FeSi_2$	p^+	258	2.3
C	Dummy CS_2	p^+	375	7.0
D	8L α-$FeSi_2$	p^+	371	4.6
E	Dummy CS_3	p^-	417	0.51
F	8L α-$FeSi_2$	p^-	429	7.92

The study of the phonon structure of working samples by the Raman scattering method showed that multilayers with the supposed NC α-$FeSi_2$ do not have phonon peaks. This proves the absence of the semiconductor phase β-$FeSi_2$ [4] in the NC samples and indirectly confirms the formation of the α-$FeSi_2$ phase, which does not have resolved Raman scattering phonons [5].

The grown multilayer samples with embedded NCs (Table) represent a composite with randomly distributed NCs [4], to which the two-layer thermoelectric model [6] cannot be applied to isolate the contribution of the modified layer. The electrical and thermoelectric properties were analyzed by comparing the temperature dependences of the sheet resistance and the Seebeck coefficient for the SOI substrate, the emulated substrate (Dummy CS), and samples with embedded NCs. The data on the sheet resistance (Fig. 1, *a*) and the Seebeck coefficient (Fig. 1, *b*) were obtained for the SOI substrate and sample B with 4 layers of α-$FeSi_2$ NCs and the Dummy CS_1 (sample *A*), grown with heavily doped silicon interlayers (p^+). According to the sheet resistance dependencies, it was found that it is maximum for a clean SOI substrate (40 kW/□ at 320 K. At the same time, for embedded NCs or the Dummy CS Si sample, the sheet resistance decreases by 3–6 times depending on the temperature, so the doping of the intermediate silicon layers is strongly felt in the sheet resistance. The positive Seebeck coefficient for sample *B* with embedded NCs α-$FeSi_2$ increases from 360 μV/K at T = 80 K, reaches a maximum of 760 μV/K at T = 330 K and then saturates to 450 K (Fig. 1, *b*), which indicates the main contribution of holes. Sample *A* (Dummy CS_1) demonstrates an almost linear dependence of the Seebeck coefficient on temperature, increasing from +100 to +550 μV/K. That is, the incorporation of α-$FeSi_2$ NCs into the silicon composite leads to a sharp increase in the thermal generation of holes in the system compared to sample *A* (Dummy CS_1). For the SOI substrate with *p*-type conductivity, the large maximum

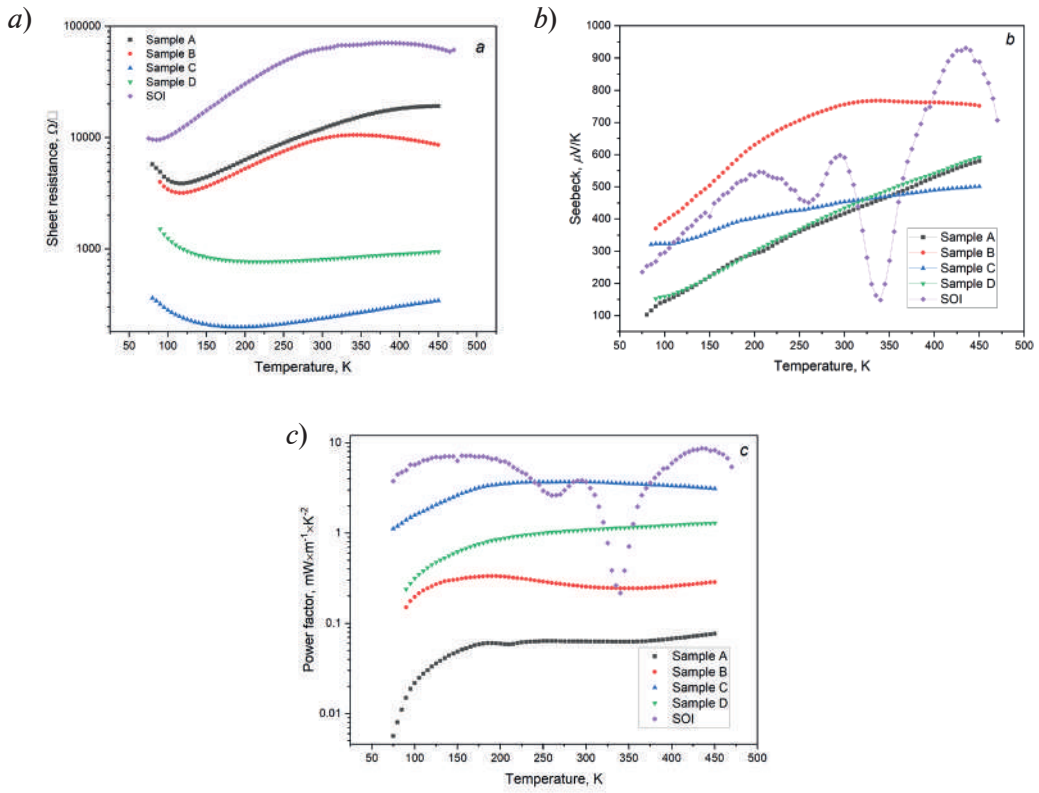

Fig. 1. Temperature dependences of the measured sheet resistance (*a*), Seebeck coefficient (*b*) and power factor (*c*) for the SOI-substrate, dummy CS_1 (samples *A*) and dummy CS_2 (sample *C*) and 4-layer an 8-layer composites in samples *B* and *D* with embedded α-$FeSi_2$ NCs respectively. The case of p^+ Si interlayer doping

(480 mV/K) for the Seebeck coefficient is observed at $T = 260$ K (Fig. 1, *b*), so the type of temperature dependences between substrate and grown samples are different. Calculations of the power factor showed (Fig. 1, *c*), that it remains minimal for sample *A* (Dummy CS_1), reaching 0.005 mW/(m×K^2) in the temperature range of 150–450 K. However, for sample *B*, the power factor reaches 0.02 mW/(m×K^2) at $T = 180$–450 K due to a higher sheet resistance and a lower Seebeck coefficient.

Doping of silicon layers to p^+ has a noticeable effect on the 8-layer sample *D* with embedded NCs (Table) and on the sample *C* (Dummy CS_2) (Table). In this case, for the latter sample, the sheet resistance with increasing temperature is lower than for the first by (6−10) times (Fig. 1, *a*). According to the Seebeck coefficient, sample *C* demonstrates a similar behavior as sample *A* (Fig. 1, *b*). For the multilayer sample with NC α-$FeSi_2$ (sample *D*), a smooth increase in the Seebeck coefficient is observed from 360 μV/K at $T = 80$ K to 750 μV/K at $T = 350$–450 K. Calculations of the power factor showed that it remains maximum for the Dummy CS_2 sample (*C*, Table), reaching 0.25 mV/(m×K^2) at $T = 250$ K and then reaching saturation (Fig. 1, *c*). For sample *D* with embedded NC α-$FeSi_2$, the power factor increases quasi-linearly with increasing temperature, reaching 0.1 mV/(m×K^2) at $T = 450$ K. That is, an increase in the number of embedded nanocrystal layers led to an increase (by 3–5 times) in surface resistance compared to sample *C* (Dummy CS_2) due to an increase in scattering on defects. The growth of the Seebeck coefficient in sample *D* is associated with the injection of holes into the composite layer. But this did not compensate for the decrease in the power factor for it compared to the Dummy CS_2 sample.

To determine the effect of decreasing the doping level of silicon interlayers on the thermoelectric parameters, a multilayer sample (8 layers) with a reduced hole concentration (p^-) was grown (Table, sample *F*). For sample *E* (Dummy CS_3), the sheet resistance (5 kΩ/□) at $T = 300$ K was significantly lower than for the SOI substrate (70 kΩ/□) at $T = 360$ K (Fig. 2, *a*). For sample *F*, the nature of the temperature dependence of the sheet resistance changed significantly, demonstrating

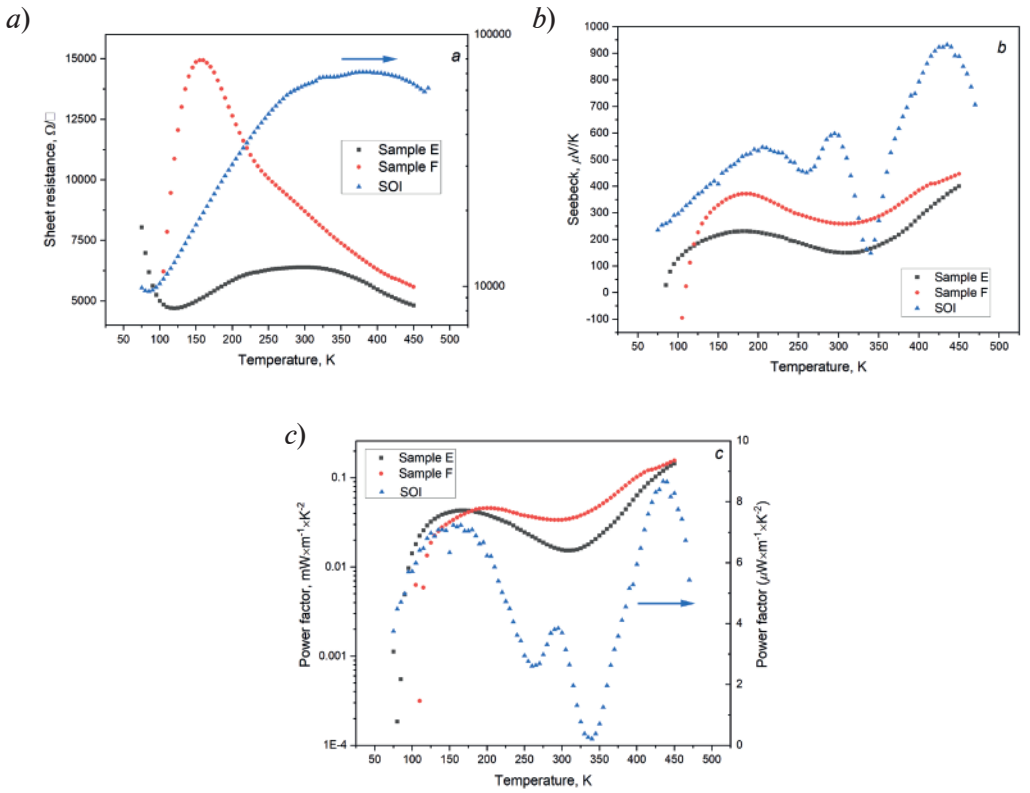

Fig. 2. Temperature dependences of the measured sheet resistance (*a*), Seebeck coefficient (*b*) and power factor (*c*) for the SOI-substrate, dummy CS_3 (sample *E*) and 8-layer composite in samples *F* with embedded α-$FeSi_2$ NCs. The case of p^- Si interlayer doping

a strong maximum (15 kΩ/□) at T = 160 K (Fig. 2, *a*). The difference in the behavior of the temperature dependences of the sheet resistance in samples *F* and *E* can be associated with a sharp increase in scattering on the built-in NCs compared to the multistep growth of silicon in the Dummy CS_3 sample. For the samples with embedded NC α-$FeSi_2$ (sample *F*) and sample *E* (Dummy CS_3), the Seebeck coefficient (Fig. 2, *b*) changes non-monotonically with temperature, but demonstrating a similar nature of the dependencies. Two maxima are observed for them, but the Seebeck coefficient is greater for sample *F*. The first maximum (370 μV/K for sample *F* and 220 μV/K for sample *E*) is observed at T = 160–180 K, and the second maximum (420 μV/K and 370 μV/K, respectively) at T = 450 K (Fig. 2, *b*). Calculation of the power factor from temperature for samples *E* and *F* and comparison with the SOI substrate showed that in the temperature range of 150–300 K, the most efficient thermoelectric is SOI substrate (0.1 mV/(m×K^2)). But with increasing temperature, the power factor for both samples (*E* and *F*) also increase, reaching a value of 0.01 mW/(m×K^2) at T = 450 K.

Conclusion

A comprehensive technology for embedding α-$FeSi_2$ NCs into SOI substrates has been developed using solid-phase epitaxy with different growth temperature modes (T = 630 °C and T = 1000 °C) for annealing 0.5 nm thick iron layers and molecular beam epitaxy (T = 630–700 °C) of Si interlayers. 4-layer and 8-layer samples with embedded α-$FeSi_2$ NCs and silicon interlayers (hole concentration: 10^{19} cm^{-3} and 10^{13} cm^{-3}), as well as multilayer samples with emulation of NC growth on SOI-(100) substrates have been grown. It was found that in the 8-layer heterostructure with the maximum hole concentration in the silicon interlayers, a sharp decrease in the sheet resistance is observed for the case of growth emulation compared to the incorporation of α-$FeSi_2$ NCs and some increase in the Seebeck coefficient at T = 80–35 K. This leads to an increase in the power factor to 0.25 mW/(m×K^2) for the sample with growth emulation and 0.1 mW/(m×K^2) for the sample with embedded α-$FeSi_2$ NCs at T = 200–450 K. A decrease in the hole concentration in silicon multilayers with embedded NC α-$FeSi_2$ leads

to both a decrease in the Seebeck coefficient and a decrease in the power factor (up to 0.01 mW/(m×K²) at $T = 450$ K due to a sharp increase in the sheet resistance during scattering at grain boundaries.

Acknowledgments

The study was carried out within the framework of the state assignment of the Institute of IACP FEB RAS (state budget topic FWFW-2026-0007).

REFERENCES

1. **Tanusilp S.,** Kurosaki K., Si-based materials for thermoelectric applications, Materials. 12 (2019) 1943.

2. **Murarka S.P.,** Silicide thin films and their applications in microelectronics, Intermetallics. 3 (3) (1995) 173–186.

3. Ed. by Borisenko V.E., Semiconducting Silicides (Berlin, Springer, 2000).

4. **Galkin N.G., Galkin K.N., Dotsenko S.A., Serhiienko I., Khovailo V.V., Gutakovskii A.K.,** Effect of embedding of $CrSi_2$ and β-$FeSi_2$ nanocrystals into *n*-type conductivity silicon on the transport and thermal generation of carriers, Applied Surface Science. 566 (2021) 150620.

5. **Pushkarev R.V., Fainer N.I., Katsui H., Kaichev V.V., Goto T.,** Structural features and surface composition of epitaxial α-$FeSi_2$ films obtained by CVD, Mater. Des. 137 (2018) 422–429.

6. **Bahk J.H., Favaloro T., Shakouri A.,** Thin film thermoelectric characterization techniques, Annual Review of Heat Transfer. 16 (2013) 51–99.

THE AUTHORS

GALKIN Konstantin N.
galkinkn@iacp.dvo.ru
ORCID: 0000-0001-5386-1013

SUBBOTIN Evgenii Yu.
jons712@mail.ru
ORCID: 0000-0001-9531-3867

KROPACHEV Oleg V.
chernobez@gmail.com
ORCID: 0000-0003-4300-0070

GOROSHKO Dmitrii L.
goroshko@iacp.dvo.ru
ORCID: 0000-0002-1250-3372

GOROSHKO Olga A.
olgagoroshko@iacp.dvo.ru
ORCID: 0009-0008-2152-140x

GALKIN Nikolay G.
galkin@iacp.dvo.ru
ORCID: 0000-0003-4127-2988

Received 12.09.2025. Approved after reviewing 20.11.2025. Accepted 08.12.2025.

Conference materials
UDC 535.215.6:538.971
DOI: https://doi.org/10.18721/JPM.184.102

The origin of the lateral photovoltaic effect in the $SiO_2/TeO_2/Bi_2Te_3/n$-Si(111) multilayer structure

T.A. Pisarenko [1] ✉, A.A. Yakovlev [1], V.V. Mararov [1],
V.V. Balashev [1, 2], K.V. Ignatovich [1], D.A. Tsukanov [1, 2]

[1] Institute of Automation and Control Processes FEB RAS, Vladivostok, Russia;
[2] Far Eastern Federal University, Vladivostok, Russia
✉ tata_dvo@iacp.dvo.ru

Abstract. The paper presents the study of the lateral photovoltaic effect in the $SiO_2/TeO_2/Bi_2Te_3/n$-Si(111) multilayer structure. The spectral dependences of photosensitivity identify the localization of the photogeneration process in the space charge region of the silicon substrate at the bismuth telluride layer thickness of 5 nm or more and in the Bi_2Te_3 layer at its thickness of less than 5 nm. It is established that lateral photosensitivity can serve as an indicator of the natural oxidation process of the protective transparent covering. We defined that the studied structure demonstrates promising results as photovoltaic cell when the Bi_2Te_3 layer thickness of 5 nm and illumination parameters of $\lambda = 730–830$ nm and $W = 0.8$ mW.

Keywords: lateral photovoltaic effect, topological insulator, silicon, multilayer structure, optoelectronics

Funding: The work was performed within the framework of the State Assignment "Physics of low-dimensional structures and semiconductor nanomaterials" (subject code FWFW-2021-0002).

Citation: Pisarenko T.A., Yakovlev A.A., Mararov V.V., Balashev V.V., Ignatovich K.V., Tsukanov D.A., The origin of the lateral photovoltaic effect in the $SiO_2/TeO_2/Bi_2Te_3/n$-Si(111) multilayer structure, St. Petersburg State Polytechnical University Journal. Physics and Mathematics. 18 (4.1) (2025) 15–20. DOI: https://doi.org/10.18721/JPM.184.102

Материалы конференции
УДК 535.215.6:538.971
DOI: https://doi.org/10.18721/JPM.184.102

Происхождение латерального фотовольтаического эффекта в многослойной структуре $SiO_2/TeO_2/Bi_2Te_3/n$-Si(111)

Т.А. Писаренко [1] ✉, А.А. Яковлев [1], В.В. Мараров [1],
В.В. Балашев [1, 2], К.В. Игнатович [1], Д.А. Цуканов [1, 2]

[1] Институт автоматики и процессов управления ДВО РАН, г. Владивосток, Россия;
[2] Дальневосточный федеральный университет, г. Владивосток, Россия
✉ tata_dvo@iacp.dvo.ru

Аннотация. В работе представлено исследование латерального фотовольтаического эффекта в многослойной структуре $SiO_2/TeO_2/Bi_2Te_3/n$-Si(111). Спектральные зависимости фоточувствительности идентифицируют локализацию процесса фотогенерации в области пространственного заряда кремниевой подложки при толщине слоя теллурида висмута 5 нм и более и в слое Bi_2Te_3 при его толщине менее 5 нм. Установлено, что латеральная фоточувствительность может служить индикатором

процесса естественного окисления защитного прозрачного покрытия. Мы определили, что исследуемая структура демонстрирует многообещающие результаты в качестве фотовольтаической ячейки при толщине слоя Bi_2Te_3 5 нм и параметрах освещения λ = 730–830 нм и W = 0,8 мВт.

Ключевые слова: латеральный фотовольтаический эффект, топологические изоляторы, кремний, многослойные структуры, оптоэлектроника

Финансирование: Работа выполнена в рамках Государственного задания «Физика низкоразмерных структур и полупроводниковых наноматериалов» (код темы FWFW-2021-0002).

Ссылка при цитировании: Писаренко Т.А., Яковлев А.А., Мараров В.В., Балашев В.В., Игнатович К.В., Цуканов Д.А. Происхождение латерального фотовольтаического эффекта в многослойной структуре $SiO_2/TeO_2/Bi_2Te_3/n$-Si(111) // Научно-технические ведомости СПбГПУ. Физико-математические науки. 2025. Т. 18. № 4.1. С. 15–20. DOI: https://doi.org/10.18721/JPM.184.102

Introduction

The development of optoelectronics opens up new possibilities, including current control using light [1–3]. One of the promising areas of optoelectronics development is the use of topological insulators (TI), which will increase the speed of response [2–5]. TIs are materials capable of conducting spin-polarized current along their surface, while remaining an insulator in the volume. For example, in Ref. [6], a study of the Bi_2Te_3 crystal surface showed that accelerated electrons are able to move along the surface of a TI practically without scattering – unlike movement in a conventional crystal – which means that they conduct current much faster, without heating losses [6].

The lateral photovoltaic effect (LPE), in which the surface potential difference of a certain system of materials varies linearly depending on the position of the incident laser beam, is one of the popular effects found in optoelectronics [7, 8]. As a rule, in silicon-based photovoltaic cells, lateral photovoltage is generated in the space charge region of silicon. However, since in the $SiO_2/TeO_2/Bi_2Te_3/n$-Si(111) structure both Si substrate and Bi_2Te_3 layer are absorbed in the visible spectrum, it is be interest to study the origin of LPE in this structure. Moreover, due to the spin splitting in Bi_2Te_3, when absorbing light, circular photovoltaic effect (CPE) is generated in it. Therefore, if the regions of LPE and CPE generation are separate, then photovoltaic cells based on the Bi_2Te_3/Si structure will expand the functionality of optoelectronic devices.

In this work, we studied the LPE in the $SiO_2/TeO_2/Bi_2Te_3/n$-Si structure by varying the thickness of the Bi_2Te_3 topological insulator layer under continuous and pulsed illumination, as well as the wavelength and power of laser radiation to identify the origin of the photogeneration process. Since the optical characteristics of the Bi_2Te_3/n-Si(111) structure depend on oxidation, in order to increase the reliability of the LPE characteristics we formed the compound protective transparent covering of SiO_2/TeO_2. The spectral dependences of the photosensitivity made it possible to determine the localization of the generation-recombination processes at different thicknesses of the topological insulator layer. According to the obtained results, the change in the localization of the photogeneration process in the Bi_2Te_3/n-Si(111) heterostructure is due to the kinetics of the energy structure with an increase of the thickness of the single-crystal Bi_2Te_3 film.

Materials and Methods

Thin-film growth using molecular beam epitaxy was conducted in a ultrahigh vacuum (UHV) chamber with a base pressure less than 5.0×10^{-10} Torr. We used *n*-type Si(111) wafers (40–70 Ω·cm) with dimensions 3×5×0.5 mm as substrates. Atomically clean Si(111)7×7 surface was prepared in situ by flashing to 1280 °C after the wafer was first outgassed at 600 °C for 6 h. Bismuth and tellur were evaporated from effusion cells with integrated shutters. The Bi_2Te_3 layers were grown

at a higher temperature of about 240 °C, at which the film grew in step-flow mode. To reduce the amount of Te vacancies, the Bi-to-Te flux ratio was chosen close to 1:14 with the growth rate of about 0.3 QL/min [4]. One quintuple layer (QL) has a thickness of 1 nm. A series of samples with Bi_2Te_3 layer thicknesses of 3, 5 and 10 nm were formed.

The Bi_2Te_3 films were covered by 2 nm of tellurium and then 1 nm of amorphous silicon to prevent oxidation of the functional Bi_2Te_3 layer, after cooling to the room temperature. The samples were exposed to air, the top silicon and tellurium layers were native oxidized. We got the formation of top optical transparent layers of paratellurid and silicon dioxise, so-called window layers [9]. As result the lateral photovoltaic effect was studied for the $SiO_2/TeO_2/Bi_2Te_3/n$-Si structure.

Lateral photovoltaic effect was investigated by using a Ti:sapphire laser (max power 0.6W) in continuous mode in wavelenght between 700–900 nm and He-Ne laser (ML101J25 with 633 nm). The wavelenght 385 nm was get on BBO (Beta Barium Borate) crystal by using a Ti:sapphire laser in femtosecond mode. Power radiation 0.25 mW for incident beam on asurface as well as a spot diameter after diaphragm 50 μm take place for both lasers. Lateral photovoltage (LPV) was measured with Keithley 2000 multimeter. The distance between the probes was 1 mm.The response time was investigated by a digital oscilloscope (Tektronix TDS 2012B) of 150 MHz.

Results and Discussion

It is known [4, 9–11] that in order to optimize the efficiency of multilayer thin-film photovoltaic cells, it is necessary to observe the criteria for selecting materials taking into account their energy parameters, loss mechanisms and recombination processes.

One of the loss mechanisms reducing the quantum efficiency of photovoltaic cells is reflection. This can be caused by light reflection at the interfaces and/or the outer surface. Another loss mechanism is the absorption of light near the surface. This problem is addressed by introducing the concept of a window/buffer/absorber heterojunction.

In addition, the generation of carriers is counteracted by the carriers' recombination [9, 10]. The recombination regions that affect the efficiency of a solar cell are the quasi-neutral recombination in the absorber layer, the recombination at space charge region, and recombination at the absorber/buffer interface. Recombination at the interface can be reduced by forming an epitaxial buffer layer [2, 3, 9].

In this work, photovoltaic cells are made on the basis of the Bi_2Te_3/n-Si(111) heterojunction covered with protective transparent layers of TeO_2 and SiO_2, which are usually called window layers. To increase efficiency, we used the same elements in subsequent layers [9]. The differences are in window materials and them properties. The absorption in transparent window layer is typically low due to the sufficiently high-energy band gap of the materials used for this layer. Unfortunately, the absorption by the Bi_2Te_3 buffer layer is a significant losses source in the studied structures. Here one has to choose between performance and losses.

In Fig. 1 we can see the lateral photovoltage dependence for photovoltaic cells with different thickness of Bi_2Te_3 buffer layer under continuous and pulse illumination. The dependence of the lateral photovoltage on the laser spot position is parameterized by the sensitivity (κ). In the top left insert of Fig. 1 the photoresponse dependences are presented in the LPV(t) graphical presentation format, since in this case the value of the photoresponse signal corresponds to the photosensitivity value. According to this parameter, the structure with a 5 nm-Bi_2Te_3 buffer layer is more promising for photosensitive detector.

Moreover, we defined the photoresponse performances of cover/Bi_2Te_3/n-Si(111) structures, top left insets in Fig. 1, although the photosensitivity of these structures were lower than those in metal-semiconductor or metal-oxide-semiconductor structures [5, 11], the response time of these structures were be faster.

The extreme dependence of photosensitivity on the Bi_2Te_3 layer thickness is typical for hybrid structures on silicon. However, note should be taken to the change in the sequence of the LPV(x) and $I(U)$ dependences with increasing Bi_2Te_3 buffer layer thickness. This fact indicates that in the Bi_2Te_3/n-Si(111) heterostructure, not only the change in the resistance of this system, but also the change in the energy structure of the Bi_2Te_3 buffer layer plays a role in the generation of lateral photovoltage. To understand this result, we conducted studies with varying laser illumination parameters such as wavelength and power.

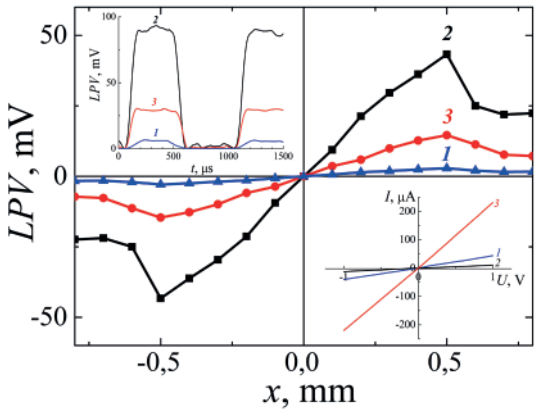

Fig. 1. Dependence of lateral photovoltage on the laser spot position in the $SiO_2/TeO_2/Bi_2Te_3/n$-Si(111) structure with the Bi_2Te_3 layer thickness: *1* – 3 nm, *2* – 5 nm, *3* – 10 nm. Inserts: *LPV*(*t*) photoresponse (top left); dark *I*-*V* characteristics (bottom right). Ti:sapphire laser (λ = 730 nm)

Figure 2 shows the spectral dependences of photosensitivity parameterized by the TI layer thickness, and the inset shows the dependences of the photovoltage near the contact on the laser illumination power.

As can be seen in Fig. 2, the dependence of the photosensitivity of heterostructures with a Bi_2Te_3 layer of thickness 5 QL or more correlates with the well-known absorption spectrum of silicon [12, 13], which clearly indicates the generation of nonequilibrium photocarriers in the near-surface silicon layer. Whereas with a Bi_2Te_3 layer thickness of 3 QL, the spectral dependence of the photosensitivity rather agrees with the absorption spectrum of thin bismuth telluride layers presented in the work, which have a hybridization gap in the ARPES (Angle-resolved photoemission spectroscopy) [14]. This transition is explained by the kinetics of the dispersion relations of bismuth telluride [14], according to which the electronic structure develops up to a film thickness of 5 QL, that is accompanied by an increase in conductivity [15]. It is known [16] that films at 5 QL have dispersion relations of the bulk structure of Bi_2Te_3. Whereas films with a thickness of 1-3 QL are characterized by the presence of surface states in the band gap [15, 16].

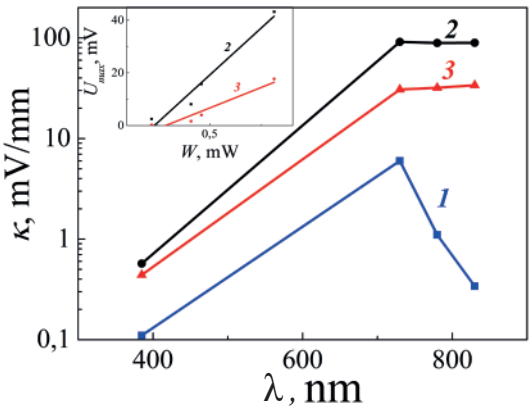

Fig. 2. Dependence of lateral photovoltage in the $SiO_2/TeO_2/Bi_2Te_3/n$-Si(111) structure on the laser illumination wavelength (Ti:sapphire laser). The insert shows the photosensitivity dependence on the laser illumination power incidenting on a surface. *1* – 3 nm Bi_2Te_3, *2* – 5 nm Bi_2Te_3, *3* – 10 nm Bi_2Te_3

Thus, in the $SiO_2/TeO_2/Bi_2Te_3/n$-Si(111) structure with a bismuth telluride thickness of 5 QL or more, the absorbing layer is the silicon space charge region, the bismuth telluride layer is the buffer layer, and the tellurium dioxide and silicon dioxide layers are protective transparent coatings, the so-called window layers. With the bismuth telluride thickness of 3 QL, the absorbing layer is the bismuth telluride layer, which significantly damages the photovoltaic properties.

The linear increase of lateral photovoltage with increasing laser power is due to the increase in the number of photogenerated carriers. At thicknesses of 5 QL and more, such a significant

increase in photovoltage is possible only when it is generated in the region of the space charge of silicon. In this case, the decrease in the slope of the $U_{max}(W)$ dependence for a thickness of 10 QL reflects both a decrease in resistance and an increase in absorption in the Bi_2Te_3 layer.

The most striking evidence of lateral photovoltage generation in silicon can be observed in the dependence of photosensitivity on the illumination wavelength. As can be seen in the inset in Fig. 2, the dependence inherits the nature of the absorption spectrum of silicon at both thicknesses of the buffer layer, which clearly indicates the generation of nonequilibrium photocarriers in the near-surface silicon layer. Thus, in the $SiO_2/TeO_2/Bi_2Te_3/n$-Si(111) structure, the absorbing layer is the silicon space charge region, the bismuth telluride layer is the buffer layer, and the tellurium dioxide and silicon dioxide layers are protective transparent coverings, the so-called window layers.

In addition, the kinetics of photovoltaic characteristics allows us to analyze the native oxidation processes of top protective layers. In order to increase the resistance and transparency of the window layer, it was proposed to form a combined transparent covering SiO_2/TeO_2. It is natural to assume that in this case, the amorphous silicon layer formed on the surface of the thinned tellurium layer is oxidized first. Due to the high electronegativity of tellurium, the oxidation process continues until the tellurium layer is completely oxidized, which follows from the current-voltage characteristics (CCV), bottom right insert Fig. 3. Such a covering improves the transport properties of the system, since its resistance increases by an order of magnitude, top left insert Fig. 3, but, unfortunately, requires a long formation time (120–150 days).

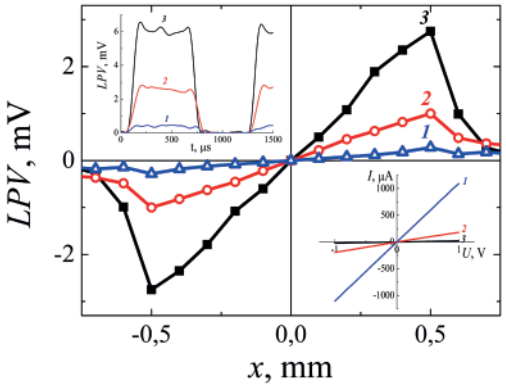

Fig. 3. Lateral photovoltage of the $SiO_2/TeO_2/Bi_2Te_3/Si$ structure during native oxidation: *1* – 10 days, *2* – 70 days, *3* – 150 days. Inserts: *LPV*(*t*) photoresponse (top left); dark *I-V* characteristics (bottom right). He-Ne laser (λ = 633 nm)

Since at the 5nm-Bi_2Te_3/n-Si(111) interface the absorber is the silicon substrate, and photogeneration occurs, where the energy parameters of the structures are identical, the reasons for the significant improvement of photovoltaic properties during oxidation of the $SiO_2/TeO_2/Bi_2Te_3/n$-Si(111) multilayer structure are an increase in the resistance and in the transparency of the covering layers, and a decrease of losses in a RC circuit, according to basic scheme of the LPE, proposed by us earlier [11].

Conclusion

This study revealed the role in a generation of lateral photovoltage of bismuth telluride layer and silicon space charge region, which absorb in the visible spectrum. It was shown that a bismuth telluride buffer layer no less than 5 nm thickness is optimal for position-sensitive detectors. It was found the $SiO_2/TeO_2/Bi_2Te_3/n$-Si(111) photovoltaic cells with a buffer layer made of a topological insulator and with protective transparent covering may have potential applications as high-speed optoelectronic devices.

REFERENCES

1. **Golub L.E.,** Spin transport in heterostructures, Physics-Uspekhi. 55 (8) (2012) 814.
2. **Hasegawa S.,** Surface and interface physics driven by quantum materials, Applied Physics Express. 17 (5) (2024) 050101.

3. **Chae J., Hong S.B., Kim D., Kim D.K., Kim J., Jeong K., Cho M.H.,** Enhancement of photoresponse in Bi_2Se_3/graphene heterostructures by effective electron-hole separation through internal band bending, Applied Surface Science. 554 (2021) 149623.

4. **Matetskiy A.V., Kibirev I.A., Hirahara T., Hasegawa S., Zotov A.V., Saranin A.A.,** Direct observation of a gap opening in topological interface states of MnSe/Bi_2Se_3 heterostructure, Applied Physics Letters. 107 (9) (2015) 091604.

5. **Hong S.B., Chae J., Kim D.K., Kim K., Jeong K., Kim J., Cho M.H.,** Enhanced photoinduced carrier generation efficiency through surface band bending in topological insulator Bi_2Se_3 thin films by the oxidized layer, ACS applied materials & interfaces. 12 (23) (2020) 26649–26658.

6. **Chen Y., Analytis J., Chu J.-H., Liu Z., Mo S.-K., Qi X.-L., Zhang H., Lu D., Dai X., Fang Z.,** Experimental realization of a three-dimensional topological insulator, Bi_2Te_3, Science. 325 (5937) (2009) 178–181.

7. **Yu C., Wang H.,** Large lateral photovoltaic effect in metal-(oxide-) semiconductor structures, Sensors. 10 (11) (2010) 10155–10180.

8. **Yang Y.,** Progress of lateral photovoltaic effect: theoretical models and materials, Journal of Physics: Conference Series. 2044 (1) (2021) 012151.

9. **Khoshsirat N., Yunus N.A.M.,** Copper-Indium-Gallium-Diselenide (CIGS) nanocrystalline bulk semiconductor as the absorber layer and its current technological trend and optimization, Nanoelectronics and materials development. (2016) 41.

10. **Wallmark J.T.,** A new semiconductor photocell using lateral photoeffect, In: Proceedings of the IRE. 45 (4) (1957) 474–483.

11. **Pisarenko T.A., Korobtsov V.V., Dimitriev A.A., Balashev V.V., Zheleznov V.V.,** Features of the Band Structure and the Mechanism of Lateral Photoconductivity in Hybrid Structures T/SiO_2/Si (T = Fe,Fe_3O_4, TiO_2), Physics of the Solid State. 64 (8) (2022) 1111–1120.

12. **Zhou Z.Q., Hu F., Zhou W. J., Chen H. Y., Ma L., Zhang C., Lu M.,** An investigation on a crystalline-silicon solar cell with black silicon layer at the rear, Nanoscale research letters. 12 (2017) 1–6.

13. **Wu C., Crouch C. H., Zhao L., Carey J.E., Younkin R., Levinson J.A., and Karger A.,** Near-unity below-band-gap absorption by microstructured silicon, Applied Physics Letters. 78 (13) (2001) 1850–1852.

14. **Gupta B.K., Sultana R., Singh S., Singh V., Awana G., Gupta A., Awana V.P.S.,** Unexplored photoluminescence from bulk and mechanically exfoliated few layers of Bi_2Te_3, Scientific Reports. 8 (1) (2018) 9205.

15. **Hatta S., Obayashi K., Okuyama H., ArugaT.,** Metallic conduction through van der Waals interfaces in ultrathin Bi_2Te_3 films, Scientific Reports. 11 (1) (2021) 5742.

16. **Li Y.Y., Wang G., Zhu X.G., Liu M.H., Ye C., Chen X., Xue Q.K.,** Intrinsic topological insulator Bi_2Te_3 thin films on Si and their thickness limit, Advanced Materials. 22 (36) (2010) 4002–4007.

THE AUTHORS

PISARENKO Tatiana A.
tata_dvo@iacp.dvo.ru
ORCID: 0000-0002-7977-7474

BALASHEV Vyacheslav V.
balashev@dvo.ru
ORCID: 0000-0003-1094-7444

YAKOVLEV Aleksey A.
yakovlev@iacp.dvo.ru
ORCID: 0000-0003-4821-3091

IGNATOVICH Konstantin V.
ignat@iacp.dvo.ru
ORCID: 0000-0002-3320-9236

MARAROV Vsevolod V.
vsevolod@iacp.dvo.ru
ORCID: 0000-0003-3761-3866

TSUKANOV Dmitry A.
tsukanov@iacp.dvo.ru
ORCID: 0000-0002-8900-3480

Received 12.09.2025. Approved after reviewing 27.10.2025. Accepted 29.10.2025.

Conference materials
UDC 539.216+537.226.4
DOI: https://doi.org/10.18721/JPM.184.103

Electrophysical properties of the Rochelle salt / asbestos nanocomposite material

T.G. Matveeva [1], M.S. Ivanova [2], V.G. Solovyev [2, 3] ✉

1 Pskov State University Branch in Velikiye Luki, Velikiye Luki, Russia;

2 Pskov State University, Pskov, Russia;

3 Military Telecommunication Academy named after the Soviet Union Marshal Budienny S.M., St. Petersburg, Russia

✉ solovyev_v55@mail.ru

Abstract. Electrical conductivity, dielectric permittivity and dielectric losses of a novel nanocomposite material obtained by the infiltration of an asbestos matrix with Rochelle salt were studied in the frequency range 100 Hz – 100 kHz. A low-temperature shift of the Curie point T_C of the "guest" substance's upper ferroelectric transition due to the influence of confined geometry was observed.

Keywords: Rochelle salt, Curie point, asbestos, matrix nanocomposites

Funding: We acknowledge Scientific and Educational Mathematical Center "Sofia Kovalevskaya Northwestern Center for Mathematical Research" for financial support of the present study (agreement No. 075-02-2025-1607, 27.02.2025).

Citation: Matveeva T.G., Ivanova M.S., Solovyev V.G., Electrophysical properties of the Rochelle salt / asbestos nanocomposite material, St. Petersburg State Polytechnical University Journal. Physics and Mathematics. 18 (4.1) (2025) 21–25. DOI: https://doi.org/10.18721/JPM.184.103

Материалы конференции
УДК 539.216+537.226.4
DOI: https://doi.org/10.18721/JPM.184.103

Электрофизические свойства нанокомпозиционного материала сегнетова соль / асбест

Т.Г. Матвеева [1], М.С. Иванова [2], В.Г. Соловьев [2, 3] ✉

[1] Филиал Псковского государственного университета в г. Великие Луки, г. Великие Луки, Россия;

[2] Псковский государственный университет, г. Псков, Россия;

[3] Военная академия связи им. С.М. Будённого, Санкт-Петербург, Россия

✉ solovyev_v55@mail.ru

Аннотация. В диапазоне частот 100 Гц – 100 кГц исследованы электропроводность, диэлектрическая проницаемость и диэлектрические потери нового нанокомпозиционного материала, полученного введением сегнетовой соли в матрицу асбеста. Обнаружен низкотемпературный сдвиг верхней точки Кюри T_C сегнетоэлектрического перехода вещества-«гостя», обусловленный ограниченной геометрией.

Ключевые слова: сегнетова соль, точка Кюри, асбест, матричные нанокомпозиты

Финансирование: Статья подготовлена в рамках реализации проекта «Научно-образовательный математический центр “Северо-Западный центр математических исследований имени Софьи Ковалевской”» (соглашение № 075-02-2025-1607 от 27 февраля 2025 г).

Ссылка при цитировании: Матвеева Т.Г., Иванова М.С., Соловьев В.Г., Электрофизические свойства нанокомпозиционного материала сегнетова соль / асбест // Научно-технические ведомости СПбГПУ. Физико-математические науки. 2025. Т. 18. № 4.1. С. 21–25. DOI: https://doi.org/10.18721/JPM.184.103

Introduction

The idea of using nanoporous “host” matrices (examples include opal, zeolite, and asbestos, etc.) for fabricating three-dimensional superlattices from nanoparticles of “guest” substances within the regular systems of calibrated voids and channels of these dielectric “host” matrices was proposed at the end of the twentieth century [1, 2].

One of the interesting applications of regular porous dielectric matrices is their use in the creation of quantum confined nanocomposite ferroelectric materials in order to study confined geometry effects. A theoretical explanation of the Curie point T_C shift towards lower temperatures [3] is based on Landau phenomenological theory. This low-temperature shift of the T_C value has been frequently observed in experiments with ferroelectric nanoparticles in porous matrices [4–8]. However, in some cases [9, 10] a T_C value shift towards higher temperatures is also possible in systems of ferroelectric nanoparticles in “host” porous matrices, compared with the temperature of the phase transition in a bulk “guest” substance.

The aim of this study was to determine experimentally the dielectric properties of the well-researched ferroelectric substance [11–18], i. e. Rochelle salt ($KNaC_4H_4O_6{\times}4H_2O$, hereinafter referred to as RS) embedded into a chrysotile-asbestos matrix near the upper ferroelectric Curie point (T_C = 297 K for the bulk RS material). Chrysotile-asbestos ($Mg_3Si_2O_5(OH)_4$, magnesium hydrosilicate) consists of fibers formed from twisted MgO and SiO_2 layers and contains parallel channels (tubes) with an internal diameter of ~ 5 nm (Fig. 1). This nanoporous “host” matrix was successfully used earlier for fabrication different nanocomposites [19, 20].

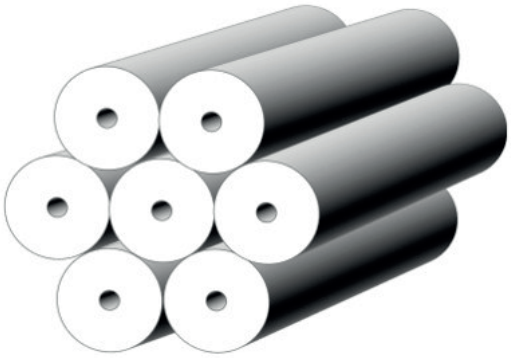

Fig. 1. Structure of asbestos porous dielectric matrix [20]

Materials and Methods

The Rochelle salt was embedded into asbestos matrix from a saturated aqueous solution at room temperature (mass concentration of the initial supersaturated solution was 1500 g/L at T = 303 K); the RS / asbestos nanocomposite sample was then washed with distilled water. Then the sample was dried at T = 300 K, and the procedure was repeated to increase the pore filling factor. After applying graphite contacts to the sample surfaces, it was clamped between

two copper electrodes (their sizes were 2mm×2mm) of the measuring cell. The thickness of the asbestos fiber bundle was about 1 mm. For control, similar measurements were also carried out on a bulk Rochelle salt, as well as on the asbestos "host" matrix. Temperature dependences of the nanocomposite electrophysical characteristics (dielectric permittivity, dielectric losses and electric conductivity) were studied using a high-precision RLC-meter MS5308 at frequencies of 100 Hz, 120 Hz, 1 kHz, 10 kHz and 100 kHz. The error bars did not exceed 5%. The temperature was measured on one of the electrodes using a two-channel thermometer GM1312 (instrument accuracy 0.1 K).

Results and Discussion

The temperature dependences of dielectric permittivity ε` for the initial asbestos matrix (curve *1*), for the bulk ferroelectric (curve *2*) and for the RS / asbestos nanocomposite (curve *3*) are presented in Fig. 2.

It is easy to see that due to the confined geometry there is a noticeable shift of T_C ($\Delta T \approx 3$ K) towards lower temperatures. This shift value is smaller than the low-temperature shift of T_C ($\Delta T \approx 5$ K) observed earlier [7] in the RS / zeolite nanocomposite since the diameters of the channels in asbestos (~ 5 nm) are larger than the diameters of the pores in NaA zeolite crystal (~ 1 nm). It should be also noted that the initial asbestos matrix has a much smaller ε` value (ε` ≈ 6 at 100 Hz) without any observable temperature dependence in the studied temperature range.

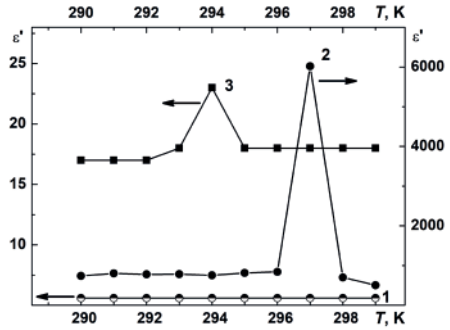

Fig. 2. Temperature dependences of the dielectric permittivity for the asbestos "host" matrix (curve *1*), for the bulk Rochelle salt "guest" substance (curve *2*), and for the RS / asbestos composite (curve *3*) at a frequency of $f = 100$ Hz

Arrhenius temperature dependence of the electrical conductivity for the RS / asbestos nanocomposite is presented in Fig. 3. One can see that the curve has a kink near the temperature $T_C \approx 294$ K of the ferroelectric-paraelectric phase transition in composite. The composite's electrical conductivity as well as the conductivity activation energy value $E = (0.56 \pm 0.02)$ eV in the paraelectric phase are higher than those for the initial asbestos matrix, where Arrhenius plot with very small activation energy (~ 0.04 eV) is monotonic without any features in the temperature region under study [21].

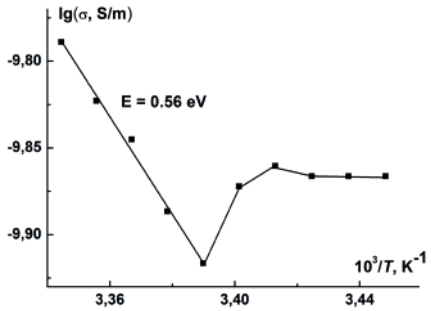

Fig. 3. Arrhenius temperature dependence of the electrical conductivity for the RS / asbestos nanocomposite at a frequency of $f = 100$ Hz

Figure 4 shows the frequency dependences of dielectric losses tgδ for the initial asbestos "host" matrix (curve *1*) as well as for the RS / asbestos nanocomposite (curve *2*). In both cases, it is possible to observe a power-law dependence of dielectric losses tgδ on frequency f ($\mathrm{tg}\delta \sim f^{-n}$), where the exponent is $n \approx 0.07$ for the initial asbestos "host" matrix and $n \approx 0.20$ for the RS / asbestos nanocomposite. Thus, both graphs display a smooth decrease of dielectric losses with frequency without any extremes in the studied frequency range from 100 Hz to 100 kHz which is typical for many dielectrics.

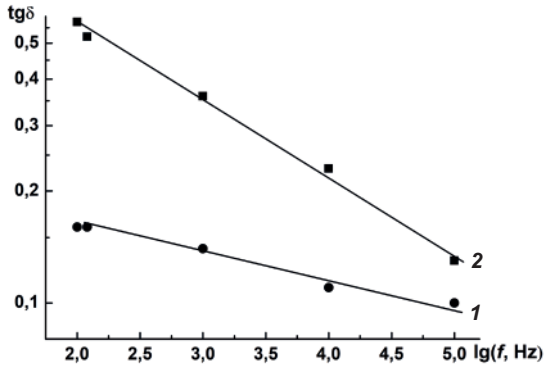

Fig. 4. Frequency dependences of dielectric losses for the asbestos "host" matrix (curve *1*) and for the RS / asbestos nanocomposite (curve *2*) at a temperature of $T = 295$ K

Conclusion

The novel nanocomposite ferroelectric / asbestos material obtained by the infiltration of a chrysotile-asbestos "host" matrix with a Rochelle salt "guest" substance demonstrates a shift of the Rochelle salt's upper ferroelectric transition Curie point T_C by ~ 3 K towards lower temperatures, compared with the temperature of the phase transition in a bulk ferroelectric. This shift value is smaller than the low-temperature shift of T_C observed earlier in the ferroelectric / zeolite nanocomposite since the diameters of the asbestos channels are larger than the diameters of the zeolite pores.

Acknowledgments

The authors are grateful to Yu. A. Kumzerov, A. A. Naberezhnov and A. I. Vanin for help and fruitful discussions.

REFERENCES

1. **Bogomolov V.N.,** Liquids in ultrathin channels (Filament and cluster crystals), Soviet Physics Uspekhi. 21 (1) (1978) 77–83.

2. **Stucky G.D., Mac Dougall J.E.,** Quantum confinement and host/guest chemistry: Probing a new dimension, Science. 247 (4943) (1990) 669–678.

3. **Zhong W.L., Wang Y.G., Zhang P.L., Qu B.D.,** Phenomenological study of the size effect on phase transitions in ferroelectric particles, Physical Review. B. 50 (2) (1994) 698–703.

4. **Pan'kova S.V., Poborchii V.V., Solov'ev V.G.,** The giant dielectric constant of opal containing sodium nitrate nanoparticles, Journal of Physics: Condensed Matter. 8 (12) (1996) L203–L206.

5. **Tien C., Charnaya E.V., Lee M.K., Baryshnikov S.V., Michel D., Böhlmann W.,** NMR studies of structure and ferroelectricity for Rochelle salt nanoparticles embedded in mesoporous sieves, Journal of Physics: Condensed Matter. 20 (21) (2008) 215205.

6. **Cizman A., Antropova T., Anfimova I., Drozdova I., Rysiakiewicz-Pasek E., Radojewska E.B., Poprawski R.,** Size-driven ferroelectric–paraelectric phase transition in TGS nanocomposites, Journal of Nanoparticle Research. 15 (8) (2013) 1807.

7. **Matveeva T.G., Ivanova M.S., Solovyev V.G., Vanin A.I.,** Electrophysical properties of the Rochelle salt dispersed in a porous dielectric matrix of type A zeolite, Physics of Complex System. 5 (4) (2024) 195–201.

8. **Milinskiy A.Yu., Baryshnikov S.V., Stukova E.V.,** Dielectric properties of a composite based on porous Teflon filled with ferroelectric $SC(NH_2)_2$, Izvestiya vuzov. Fizika. 68(3) (2025) 60–65.

9. **Rogazinskaya O.V., Milovidova S.D., Sidorkin A.S., Chernyshev V.V., Babicheva N.G.,** Properties of nanoporous aluminum oxide with triglycine sulfate and Rochelle salt inclusions, Physics of the Solid State. 51 (7) (2009) 1518–1520.

10. **Baryshnikov S.V., Charnaya E.V., Shatskaya Yu. A., Milinskiy A.Yu., Samoilovich M.I., Michel D., Tien C.,** Effect of confined geometry on linear and nonlinear dielectric properties of triglycine sulfate near the phase transition, Physics of the Solid State. 53 (6) (2011) 1212–1215.

11. **Valasek J.,** Piezoelectric and allied phenomena in Rochelle salt, Physical Review, XVII. (4) (1921) 475–481.

12. **Valasek J.,** Properties of Rochelle salt related to the piezoelectric effect, Physical Review, XX. (6) (1922) 639–664.

13. **Gurevich V.M.,** Elektroprovodnost' segnetoelektrikov [Electrical conductivity of ferroelectrics]. Moscow: The Committee on Standards, Measures, and Measuring Instruments of the Council of Ministers of the USSR Publ., 1969. (In Russian).

14. **Mitani S., Fukui S., Shibuya I., Shiozaki Y., Toyoda K., Pepinsky R.,** Crystal structure refinement of ferroelectric Rochelle salt, Ferroelectrics. 8 (1) (1974) 477–478.

15. **Solans X., Gonzalez-Silgo C., Ruiz-Pérez C.,** A structural study on the Rochelle salt, Journal of Solid State Chemistry. 131 (2) (1997) 350–357.

16. **Zhou G., Wu J., Wang A., Fenglei, He W.,** Investigation of ferroelectric phase transition of Rochelle salt, Ferroelectrics. 366 (1) (2008) 67–73.

17. **Malyshkina I.A., Gavrilova N.D.,** Low-frequency dielectric properties of the Rochelle salt and its deuterated analogue, Ferroelectrics. 268 (1) (2002) 41–46.

18. **Singaravadivelu S., Uthayakumar A., Balaji Bhargav P.,** Study of the relative growth rate, the anisotropy of electrical resistivity and anomalous photocurrent behavior of the unidirectional grown Rochelle salt crystals, Ferroelectrics. 550 (1) (2019) 112–126.

19. **Belotitskii V.I., Kumzerov Yu.A., Kalmykov A.E., Kirilenko D.A., Peschel U., Romanov S.G., Sorokin L.M., Sysoeva A.A., Zhuromskyy O.,** Optical properties of metal nanoparticles in chrysotile channels, Technical Physics Letters. 42 (6) (2016) 656–658.

20. **Vanin A.I., Kumzerov Yu.A., Solov'ev V.G., Khanin S.D., Gango S.E., Ivanova M.S., Prokhorenko M.M., Trifonov S.V., Cvetkov A.V., Yanikov M.V.,** Electrical and optical properties of nanocomposites fabricated by the introduction of iodine in porous dielectric matrices, Glass Physics and Chemistry. 47 (3) (2021) 229–234.

21. **Matveeva T.G., Ivanova M.S., Solovyev V.G.,** Electrophysical properties of the Rochelle salt / asbestos nanocomposite material, In: Proceedings of the Seventh Asian School-Conference on Physics and Technology of Nanostructured Materials, Vladivostok, 11 – 15 July 2025. Vladivostok: Dalnauka. (2025) 165–166.

THE AUTHORS

MATVEEVA Tamara G.
mtg88@yandex.ru
ORCID: 0009-0009-8382-1667

SOLOVYEV Vladimir G.
solovyev_v55@mail.ru
ORCID: 0000-0002-8452-6928

IVANOVA Marina S.
ivanovams@mail.ru
ORCID: 0000-0003-1602-4202

Received 12.09.2025. Approved after reviewing 02.10.2025. Accepted 02.10.2025.

Conference materials
UDC 538.9+539.1
DOI: https://doi.org/10.18721/JPM.184.104

Experimental and *ab initio* study of Si(111)(2/3)√3×(2/3)√3-Mg models

M.V. Ryzhkova [1] ✉, L.V. Bondarenko [1], D.A. Tsukanov [1, 2]

[1] Institute of Automation and Control Processes FEB RAS, Vladivostok, Russia;
[2] Far Eastern Federal University, Vladivostok, Russia
✉ lavric@iacp.dvo.ru

Abstract. In the present work, using VASP and AIRSS, we have modelled possible structures of Si(111)(2/3)√3×(2/3)√3-Mg. *Ab initio* density functional theory (DFT) calculations using pseudopotentials were employed to investigate structural models of the Si(111)(2/3)√3×(2/3)√3-Mg surface. A number of models were analyzed in a 2×2 surface cell. The study identifies the most energetically favorable structure in the 2×2 configuration as the "7-3_random" model, which contains 1.75 monolayers (ML) of Mg and 0.75 ML of Si. The results of ab initio calculations are well confirmed by experimental methods (STM and LEED observations).

Keywords: magnesium silicide, silicon surface, ultrathin films, density functional theory, ultra-high vacuum, surface structure, surface structure simulation, surface energy

Funding: The research was supported by the Government research assignment for IACP FEB RAS, project FWFW-2021-0002.

Citation: Ryzhkova M.V., Bondarenko L.V., Tsukanov D.A., Experimental and *ab initio* study of Si(111)(2/3)√3×(2/3)√3-Mg models, St. Petersburg State Polytechnical University Journal. Physics and Mathematics. 18 (4.1) (2025) 26–30. DOI: https://doi.org/10.18721/JPM.184.104

Материалы конференции
УДК 538.9+539.1
DOI: https://doi.org/10.18721/JPM.184.104

Экспериментальное исследование и *ab initio* расчеты моделей Si(111)(2/3)√3×(2/3)√3-Mg

М.В. Рыжкова [1] ✉, Л.В. Бондаренко [1], Д.А. Цуканов [1, 2]

[1] Институт автоматики и процессов управления ДВО РАН, г. Владивосток, Россия;
[2] Дальневосточный федеральный университет, г. Владивосток, Россия
✉ lavric@iacp.dvo.ru

Аннотация. В настоящей работе с использованием VASP и AIRSS проведено моделирование возможных структур Si(111)(2/3)√3×(2/3)√3-Mg. Для исследования структурных моделей поверхности Si(111)(2/3)√3×(2/3)√3-Mg были использованы расчеты *ab initio* методом теории функционала плотности (DFT) с использованием псевдопотенциалов. Ряд моделей был проанализирован в ячейке поверхности 2×2. В исследовании выявлена наиболее энергетически выгодная структура в конфигурации 2×2 – модель «7-3_random», содержащая 1,75 монослоя (МС) магния и 0,75 МС кремния. Результаты расчетов хорошо согласуются с экспериментом (наблюдения поверхности методами ДМЭ и СТМ).

Ключевые слова: силицид магния, поверхность кремния, сверхтонкие пленки, теория функционала плотности, сверхвысокий вакуум, структура поверхности, моделирование структуры поверхности, поверхностная энергия

Финансирование: Исследование выполнено при поддержке Государственного научного задания ИАПУ ДВО РАН, проект FWFW-2021-0002.

Ссылка при цитировании: Рыжкова М.В., Бондаренко Л.В., Цуканов Д.А. Экспериментальное исследование и *ab initio* расчеты моделей Si(111)2/3√3×2/3√3-Mg // Научно-технические ведомости СПбГПУ. Физико-математические науки. 2025. Т. 18. № 4.1. С. 26–30. DOI: https://doi.org/10.18721/JPM.184.104

Introduction

A considerable number of studies have focused on the investigation of magnesium silicide Mg_2Si on the Si(111) surface [1–4] due to its technological importance. However, atomic scale ultrathin films of Mg_2Si have not been explored theoretically and experimentally in detail, for example, a structural model of Si(111)(2/3)√3×(2/3)√3-Mg (thereafter (2/3)√3-Mg) surface structure has been proposed in [2], but comprehensive structure calculations was not performed. Here, in this study, we present the atomic model of the (2/3)√3-Mg reconstruction, in particular, atomic structure and composition were calculated used ab-initio calculations. The accuracy of the model was compared with experimental data. It should be noted that the periodicity of the structure obtained in diffraction experiments does not always reflect the real periodicity observed by the scanning tunneling microscopy. For example, in the case of the surface 3×1-Mg periodicity observed on the low-energy electron diffraction pattern, which reflects the arrangement of silicon atoms on the reconstructed surface, while scanning tunneling microscopy observations clearly show the 3×2 periodicity, which also takes into account the arrangement of silicon and magnesium atoms.

Materials and Methods

The Mg/Si(111) sample was prepared in the Omicron MULTIPROBE ultrahigh vacuum system (UHV) equipped with scanning tunneling microscopy (STM) and low-energy electron diffraction (LEED). The base pressure in UHV system was in the order of 1×10^{-10} Torr. The atomically clean Si(111)7×7 sample was first annealed in situ at 600 °C for several hours and finally was flashed to 1280 °C. Mg atoms were deposited from a Ta tube. The (2/3)√3-Mg surface phase was prepared by deposition of ~2 monolayers (ML) of Mg onto the Si(111)7×7 surface at 50–100 °C. Mg deposition rate was calibrated using well known Mg/Si(111) reconstructions: Si(111)3×2-Mg (1/6 ML of Mg) [5], Si(111)6×6-MgPb (1 ML of Mg) [6] and Si(111)4×4-MgPb (0.6 ML of Mg) surface phases [6].

The calculation was conducted using a plane-wave basis set and correlation functional projector-augmented wave pseudopotentials (PAW-PBE) with generalized gradient approximation (GGA) for the exchange-correlation energy. VASP ab initio program package was used for this study. Wave functions were performed using energy cutoff 250 eV. The geometry was optimized until the total energy was converged to 10^{-6} eV and the atomic forces reduced to 10^{-2} eV/Å. For Γ– point the 7×7×1 grid was used.

The (2/3)√3-Mg surface structure has been simulated using the slab with periodicity of Si(111)2×2. The slab consists of 6 Si layers and vacuum region with more than 20 Å to prevent interaction between surfaces in two adjacent cells. The dangling bonds of the bottom silicon layer have been saturated by hydrogen atoms. Two bottom layers and hydrogen atoms were fixed and the rest atoms in slab were allowed to move freely.

For structure search calculation the ab initio random structure search (AIRSS) was used. Energy convergence was 10^{-5} eV and 5×5×1 *k*-points grid was set for this case. Since the (2/3)√3 cell disrupts the periodicity of the silicon substrate, a 2×2 unit cell was used taking into account that 2×2 cell contains 3 subcells of (2/3)√3 cell.

The formation energy was calculated following this formula:

$$E_{form/1\times1} = \frac{E_{tot} - E_{slab} - n_{Si}\mu_{Si} - n_{Mg}\mu_{Mg}}{N},$$

where E_{tot} is total energy of calculated model, E_{slab} is energy of relaxed slab without silicon atoms in surface phase (usually 3 atoms), n_{Si} and n_{Mg} are numbers of Si and Mg atoms, respectively. μ_{Si} and μ_{Mg} are the chemical potentials for the Si and Mg, respectively, taken from bulk phases of these elements. N is a number of 1×1 cells in the given structure ($N = 4$ for 2×2, $N = 6$ for 3×2, $N = 3$ for 3×1 and $N = 49$ for 7×7 cell).

All calculations were performed using the resources of the Shared use center of Far-Eastern Computational Resource [7].

Results and Discussion

Figure 1, *a* shows the STM pattern obtained from the (2\3)√3-Mg surface at room temperature. It is evident that the surface has a 2×2 periodicity with one protrusion per cell (highlighted in white). Figure 1, *b* shows the Fourier transform of such a surface, with the 2×2 and (2\3)√3 spots observed in picture. Figure 1, *c* shows the LEED pattern of the same surface, with only the (2\3)√3 spots remaining. This resembles the situation with the 3×2-Mg surface phase, which also demonstrated different periodicities in the LEED and STM experimental pictures.

Initially, we considered the model of (2\3)√3-Mg surface presented in the article [2] and calculated its structure in the process of relaxation. It was shown that this model lost the periodicity of (2/3)√3 and leaving only the 2×2 periodicity. However, this model demonstrated a high formation energy (−0.153 eV/1×1) compared to other calculated models (Table).

We have modified this structure called as “model 9-3” (increased the Mg coverage to 2.25 ML: 9 atoms in a 2×2 cell, while the number of Si atoms remained the same (3 Si atoms or 0.75 ML of Si)). After calculations the formation energy for this structure decreased to −0.619 eV/1×1 (Table), while maintaining only the periodicity of (2/3)√3. It is worth noting that “model 9–3” best fits the parameters of the bulk magnesium silicide Mg_2Si structure: interatomic distances 4.48Å for Si-Si and Mg-Mg bonds.

Using AIRSS method, the most favorable structures were calculated for magnesium coverage of 1.75 ML (7 Mg and 3 Si atoms per 2×2 cell, called as “7–3_random” model), 2 ML (8 Mg and 3 Si atoms, “8−3” model) and 2.25 ML (9 Mg and 3 Si atoms, “9−3_random” model), as well as 2 ML (8 Mg and 2 Si atoms) and 2.25 ML (9 Mg and 1 Si atoms, “9–1” model).

Table

Parameters of models for (2/3)√3-Mg/Si(111) surface

Model	Energy, eV/1×1	Si-Si, Å	Mg-Mg, Å
(2/3)√3-Mg [2]	−0.153	4	4.9
9-3	−0.619	4.4	4.4
9−3_random	−0.703	3.5−4.5	3−3.7
8−3	−0.772	4.8−5.1	3.1−4.7
7−3_random	−0.822	4.3−4.6	3.9−4.5
8−2	−0.604	4.6	3.1−4.6
9−1	−0.467	–	3−3.3
Si(111)3×2-Mg	−0.53	–	–
3×1-Mg	−0.527	–	–
Si(111)7×7	−0.356	–	–
Mg_2Si [10]	–	4.48	4.48

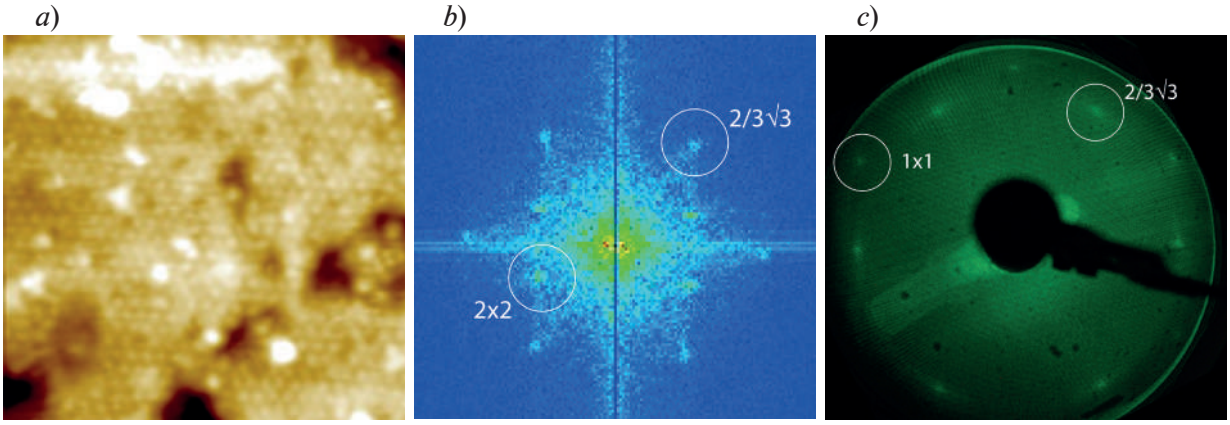

Fig. 1. STM picture (20×20 nm^2) obtained from the (2/3)√3-Mg/Si(111) (*a*), Fourier transform of STM pattern with the 2×2 and (2/3)√3 spots (one of the spots is marked with a white circle for each type) (*b*), LEED pattern from the (2/3)√3-Mg/Si(111) surface, beam energy E_p = 36 eV (*c*)

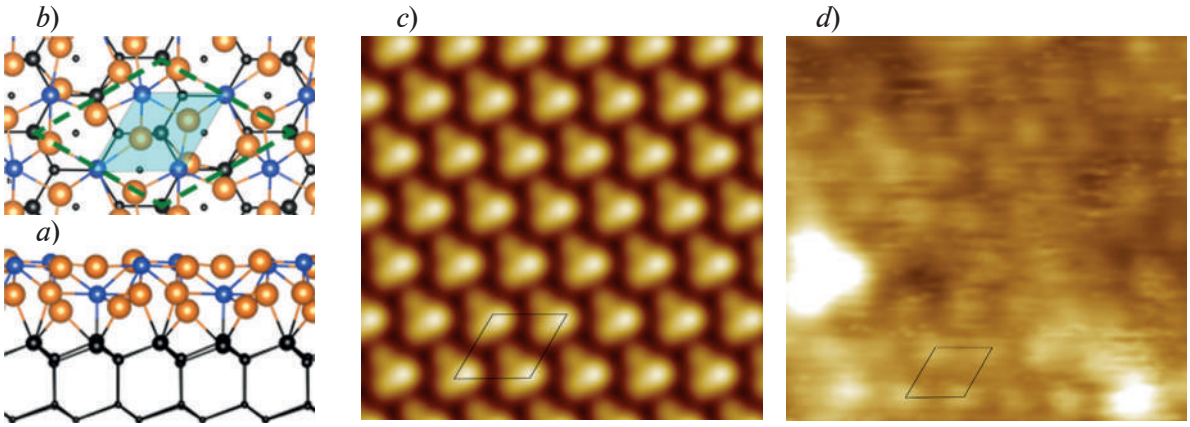

Fig. 2. Model "7-3_random" of (2/3)√3-Mg/Si(111) surface structure (Mg atoms seen as orange balls, Si atoms in Mg_2Si structure seen as blue, Si atoms in Si(111) structure seen as black, 2×2 cell is marked with a green rhombus and (2/3)√3 cell is marked with a light blue rhombus), top view and side view (*a*, *b*). Simulated STM picture of (2/3)√3-Mg/Si(111) surface (*c*). Experimental STM picture (6×6 nm^2) obtained from the (2/3)√3-Mg/Si(111) surface (2×2 cell is marked with a black rhombus) (*d*)

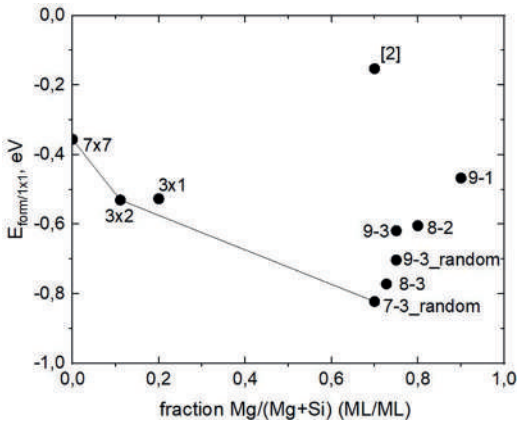

Fig.3. The formation energy versus fraction of magnesium

Thus, we found the model with the lowest formation energy (–0.822 eV/1×1) and structure consisting of 1.75 ML of Mg and 0.75 ML of Si atoms, model "7–3_random". In Fig 2, *a*, *b* its atomic structure is shown, top view and side view, moreover, in Fig. 2, *c* the simulated STM image shows an excellent match with surface structure observed experimentally by STM (Fig. 2, *d*).

Let us note that all calculated models have only a 2×2 periodicity; the (2/3)√3 periodicity is preserved only for silicon atoms with 3 Si atoms in structure. Considering models of magnesium silicide it is visible that 3 Si atoms in the slab surface prefer symmetric places T_4, H_3 and T_1, which ensures a (2/3)√3 periodicity.

Fig. 3 shows the results of calculations of the formation energy depending on the amount of Mg atoms placed in the Mg_2Si/Si(111) surface structure. This plot also contains reference points that relate to the calculations of the Si(111)3×2-Mg, Si(111)3×1-Mg and Si(111)7×7 surface reconstructions. The latter structures we have also calculated based on the models of alkaline earth adsorbates presented for 3×2 and 3×1 in the article [8] while surface structure of Si(111)7×7 was calculated related to standard DAS model [9]. It is seen that the most favorable structure for Mg_2Si/Si(111) ultrathin layer is "7−3_random" model that has 1.75 ML of Mg and 0.75 ML of Si with 2×2 periodicity that is confirmed by STM observation.

Conclusion

We have performed ab initio calculation and experimental study to investigate Si(111) (2/3)√3×(2/3)√3-Mg surface structure models. The most favorable structure with the lowest formation energy (−0.822 eV/1×1) is the "7−3_random" model that consist of 1.75 ML of Mg and 0.75 ML of Si atoms with 2×2 periodicity. The results of ab initio calculations are well confirmed by experimental methods used in this work (STM and LEED observations).

REFERENCES

1. **Lee D., Lee G., Kim S., Hwang Ch.,** Room-temperature growth of Mg on Si (111): stepwise versus continuous deposition, J.Phys.: Condens. Matter. 19 (2007) 266004.

2. **Galkin K.N., Kumarb M., Shivaprasad S.M., Galkin N.G.,** The model of the magnesium silicide phase (2/3√3×2/3√3)-R30°on Si(111), Physics Procedia. 11 (2011) 47–50.

3. **Fan T., Xie C., Wang Sh., Oganov A.R., Cheng L.,** First-principles study of thermoelectric properties of Mg_2Si−Mg_2Pb semiconductor materials, RSC Advances. 8 (2018) 17168.

4. **Min-Ju Y., Ping Z., Xiao-Long D.,** First-principle study of Mg adsorption on Si(111) surfaces, Chinese Physics B. 18 (2009) 1.

5. **Saranin A.A., Zotov A.V., Lifshits V.G., Katayama M., and Oura K.,** Family of the metal-induced Si(111)3×1 reconstructions with a top Si atom density of 4/3 monolayer, Surf. Sci. 426 (1999) 298.

6. **Tupchaya A.Yu., Bondarenko L.V., Yakovlev A.A., Vekovshinin Y.E., Mihalyuk A.N., Gruznev D.V., Denisov N.V., Matetskiy A.V., Aladyshkin A.Y., Zotov A.V., Saranin A.A.,** 2D system incorporating perforated Mg sheet sandwiched between Pb layer and Si(111), Appl. Surf. Sci. 589 (2022) 152951.

7. https://cc.dvo.ru

8. **Shuai Chai J., Li Zh., Xu L., Wang J.,** Structural stability and electronic properties of alkaline-earth metal induced Si(111)-(3×2) surfaces, Chem. Chem. Phys. 20 (2018) 25235.

9. **Takayanagi K., Tanishiro Y., Takahashi S., Takahashi M.,** Structure analysis of Si (111)-7×7 reconstructed surface by transmission electron diffraction, Surf. Sci. 164 (1985) 367.

10. **Jianfeng Y., Qingquan X., Shasha F., Huazhu T., Yunmei Y., Quan X.,** Two-dimensional Mg_2Si-111: A direct bandgap semiconductor with excellent optical response properties predicted by first-principles calculations, Phys.Lett.A. 475 (2023) 128849.

THE AUTHORS

RYZHKOVA Maria V.
lavric@iacp.dvo.ru
ORCID: 0000-0001-8990-7140

TSUKANOV Dmitry A.
tsukanov@iacp.dvo.ru
ORCID: 0000-0002-8900-3480

BONDARENKO Leonid V.
bondarenko@iacp.dvo.ru
ORCID: 0000-0002-2660-3622

Received 15.09.2025. Approved after reviewing 29.09.2025. Accepted 02.10.2025.

Conference materials
UDC 538.913
DOI: https://doi.org/10.18721/JPM.184.105

Ising model on Fibonacci lattices: ring topology of sphere, cut ring, and torus

A.S. Pochinok [1] ✉, A.V. Molochkov [1], M.N. Chernodub [2], A.K. Chepak [1]

[1] Far Eastern Federal University, Vladivostok, Russia;
[2] University of Tours, Tours, France
✉ pochinok.as@mail.ru

Abstract. We study the Ising model on two-dimensional surfaces discretized using the Fibonacci method with Delaunay triangulation, considering the ring, cut ring, and torus topologies. The phase diagrams reveal a universal critical temperature of $T_C \approx 3.33(3)J$ in the thermodynamic limit, which is consistent with the results for the Fibonacci sphere [1]. Despite the exclusion of topological defects (vertices with coordination numbers 5/7) in the ring and cut ring Fibonacci configurations, deviations from the critical temperature of the ideal flat triangular lattice are observed. The T_C values, similar to the spherical case, experience shifts. Notably, the torus, which possesses the minimal defect density (<1%), exhibits smooth convergence and negligible finite-size shifts in T_C. These results underscore the interplay between local connectivity and global topology in shaping critical phenomena.

Keywords: Ising model, topological defects, Fibonacci lattices, Monte Carlo simulation, phase diagrams

Funding: This study was funded by the grant from the Russian Science Foundation (RSF) No. FZNS-2024-0002.

Citation: Pochinok A.S., Molochkov A.V., Chernodub M.N., Chepak A.K., Ising model on Fibonacci lattices: ring topology of the sphere, cut ring and torus, St. Petersburg State Polytechnical University Journal. Physics and Mathematics. 18 (4.1) (2025) 31–36. DOI: https://doi.org/10.18721/JPM.184.105

Материалы конференции
УДК 538.913
DOI: https://doi.org/10.18721/JPM.184.105

Модель Изинга на решетках Фибоначчи: кольцевая топология сферы, кольцо с разрезом и тор

А.С. Починок [1] ✉, А.В. Молочков [1], М.Н. Чернодуб [2], А.К. Чепак [1]

[1] Дальневосточный федеральный университет, г. Владивосток, Россия;
[2] Университет Тура, г. Тур, Франция
✉ pochinok.as@mail.ru

Аннотация. Мы исследуем модель Изинга на двумерных поверхностях, дискретизированных методом Фибоначчи с триангуляцией Делоне, рассматривая топологии кольца, кольца с разрезом и тора. Фазовые диаграммы демонстрируют универсальную критическую температуру $T_C \approx 3{,}33(3)J$ в термодинамическом пределе, что согласуется с результатами для сферы Фибоначчи [1]. Несмотря на исключение топологических дефектов (вершин с координационными числами 5/7) в конфигурациях кольца и кольца с разрезом Фибоначчи наблюдаются отклонения от критической температуры идеальной плоской треугольной решетки. Значения T_C, аналогично случаю

сферы, испытывают сдвиги. Примечательно, что тор, обладающий минимальной плотностью дефектов (<1%), демонстрирует плавную сходимость и пренебрежимо малые сдвиги T_C. Эти результаты подчеркивают взаимосвязь между локальной связностью и глобальной топологией в формировании критических явлений.

Ключевые слова: модель Изинга, топологические дефекты, решетки Фибоначчи, Монте-Карло моделирование, фазовые диаграммы

Финансирование: Работа выполнена при поддержке гранта № FZNS-2024-0002 Министерства науки и высшего образования Российской Федерации.

Ссылка при цитировании: Починок А.С., Молочков А.В., Чернодуб М.Н., Чепак А.К. Модель Изинга на решетках Фибоначчи: кольцевая топология сферы, кольцо с разрезом и тор// Научно-технические ведомости СПбГПУ. Физико-математические науки. 2025. Т. 18. № 4.1. С. 31–36. DOI: https://doi.org/10.18721/JPM.184.105

Introduction

The two-dimensional Ising model is a fundamental system for studying phase transitions and critical phenomena [2]. Although its characteristics on standard flat lattices are thoroughly documented, the behavior on curved surfaces featuring non-trivial topology introduces novel theoretical questions and research avenues.

This research examines the ferromagnetic Ising model on curved surfaces, where the lattices are defined by a Fibonacci distribution and discretized using Delaunay triangulation [3]. This technique produces highly uniform tessellations consisting of nearly equal-area triangles [4], offering a robust approach for investigating the thermodynamic limit on curved geometries. A defining aspect of such lattices is the emergence of topological defects–specifically vertices with coordination numbers five and seven. Growth in the number of nodes within a Fibonacci sphere induces discrete transitions in the triangulation structure, marking sudden shifts in network connectivity. These structural changes significantly affect the system's statistical mechanics, giving rise to discontinuities reminiscent of first-order transitions as the sphere expands [1].

Fibonacci lattices have already been used in studies of the XY model [5] and have also proven effective in modeling magnetic resonance [6], among other applications. In turn, studying the ferromagnetic phase transition on curved surfaces will become an important aspect for modeling spherical nanoparticles and magnetic films.

Fibonacci lattices

Fibonacci lattices are characterized by an almost uniform and isotropic distribution of nodes. This allows for efficient discretization of curvilinear surfaces using triangles of approximately equal area. The structure is based on Fibonacci numbers. A Fibonacci number F is part of an infinite sequence in which each element, starting from the third ($i \geq 3$), is the sum of the two previous elements: $F_i = F_{i-1} + F_{i-2}$. The first few numbers in the sequence are: 0, 1, 1, 2, 3, 5, 8, 13, 21... In the limit of a large number of elements, the ratio of two consecutive numbers approaches the value of the golden ratio $g = (1+\sqrt{5})/2$.

The Fibonacci distribution on two-dimensional surfaces forms a structure consisting of two sets of spiral arcs [4, 7]. In these arcs, the distance between neighboring points is determined by Fibonacci numbers [8]. Some sets of spirals are twisted clockwise, while others are twisted counterclockwise. As the lattice radius (total number of nodes) increases, the number of dominant spirals grows. It can also be shown that the Fibonacci lattice is essentially the result of a sequential arrangement of elements along a single “generative spiral” [9]. The angular distance between elements of this generative spiral corresponds to g.

When discretizing Fibonacci surfaces using a set of triangles in our case, Delaunay triangulation – defects in connectivity properties are observed, as detailed for the sphere case in [1]. The number of neighboring vertices varies from 5 to 7, with points having 6 neighbors being predominant.

To examine the influence of lattice connectivity defects on the critical temperature of the Ising model, it is necessary to study the phase transition in a region where the number of 5- and 7-coordinated nodes tends to 0. Defective connectivity is primarily localized at the poles of the spherical lattice. Therefore, we use a ring topology of the Fibonacci sphere. This is achieved by excising the poles, i.e., the polar regions with a high concentration of coordination number defects. Such a structure forms an equatorial zone dominated by hexagonal order (6 neighbors), bringing it closer to a regular triangular lattice. The width of the equatorial region with 6 neighbors depends on the number of lattice sites N. The ring topology obtained by excising the poles of the triangulated sphere is shown in Fig. 1, *a*.

To most closely approximate the case of an ideal flat triangular lattice for result comparison, it is necessary to obtain a flat space with a Fibonacci distribution. In this work, we achieve such a configuration by removing nodes along one generatrix of the ring. Thus, we obtain a locally flat space (for all points except boundary ones) with a Fibonacci distribution with a hexagonal structure (Fig. 2, *b*).

A toroidal triangulated lattice is equivalent to an ideal flat triangular lattice with periodic boundary conditions, for which the known critical temperature of the Ising model is $T_C \approx 3.64$. Therefore, we investigate the phase transition on the Fibonacci torus (Fig 1, *c*). Similar to the sphere, the Fibonacci torus has points with 5 and 7 neighbors, but their number is significantly smaller (<1%) (Fig. 2). The Fibonacci torus was defined by equations (1, 2):

$$x = \left(R + r\cos\varphi\right)\cos\theta,\ y = \left(R + r\cos\varphi\right)\sin\theta,\ z = r\sin\varphi, \tag{1}$$

$$\varphi = \frac{2\pi k}{g}, \theta = \frac{2\pi k}{N}, \tag{2}$$

where k is the site index and N is the number of sites in the lattice.

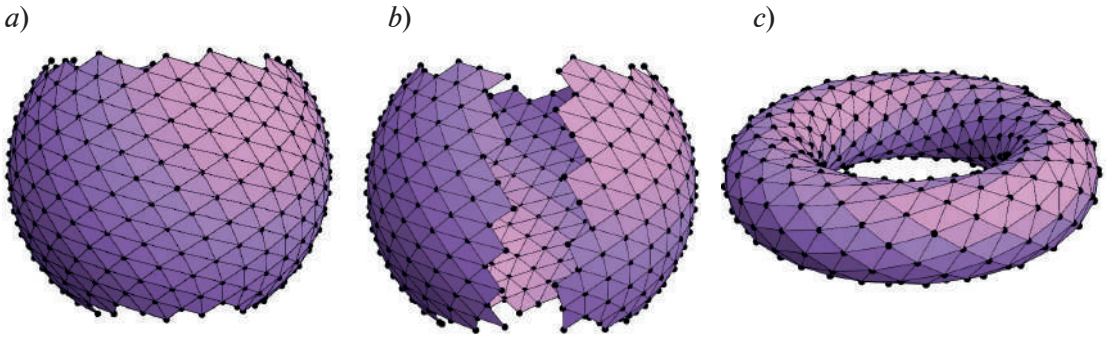

Fig. 1. Fibonacci lattices: ring (*a*); cut ring (*b*); torus (*c*)

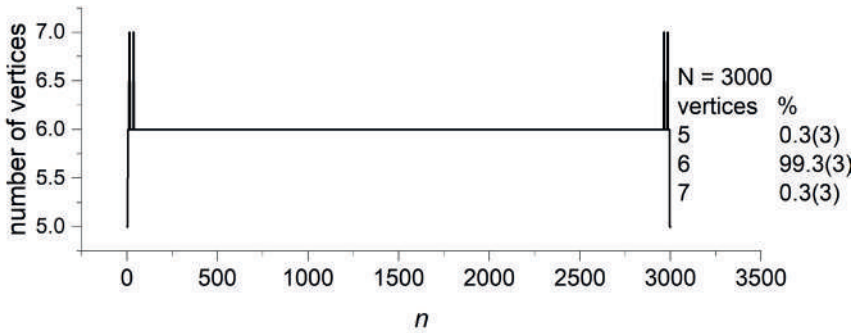

Fig. 2. Distribution of the number of neighboring vertices for a torus with 3000 and 47000 nodes

The Fibonacci torus exhibits interesting patterns related to its spiral structure. The Euler characteristic of the Fibonacci torus equals zero only for specific filling ranges. For example, in the filling range $2500 < N < 3000$, the lattices are topologically equivalent to a torus. For $N < 2500$, the Euler characteristic is not zero, indicating defects such as intersections of triangle bonds. Further statistical analysis revealed that the "true" torus occurs sequentially and was found for $N = \{7000 - 8000; 17000 - 23000; 46000 - ...\}$. Moreover, as the number of points increases, the width of the N range for "true" torus increases. This effect, similar to the sphere, may be associated with the formation of new spirals but requires more detailed study.

Ising model

The two-dimensional Ising model is one of the simplest statistical models, where the spin variable S_x represents the magnetic moment of an atom at site x. This variable can take values $S_x = +1$ or $S_x = -1$, corresponding to upward or downward orientation of the magnetic moment relative to the atomic crystalline plane. The Hamiltonian of the system is given by (3):

$$H = -J\sum_{\langle x,y\rangle} S_x S_y - h\sum_x S_x. \tag{3}$$

We consider dimensionless variables in units of the coupling $J = 1$. All calculations will be performed for systems in the absence of an external magnetic field $h = 0$.

A parameter critically sensitive to the phase transition is the magnetic susceptibility χ , which quantitatively characterizes fluctuations of the order parameter – spontaneous magnetization.

Within the formalism of the canonical ensemble and in the absence of an external magnetic field, the magnetic susceptibility is defined via fluctuations of the total magnetization M by the following relation:

$$\chi(T,N) = \frac{\left\langle M^2(T,N)\right\rangle - \left\langle M(T,N)\right\rangle^2}{T}, \tag{4}$$

where $M = \sum_x S_x$ is the total magnetic moment of the system.

Results and Discussion

The study of the Ising model phase transition on a ring lattice was conducted with fixed boundary conditions: spins at the ring boundaries were fixed in the +1 state. This spin fixation minimizes boundary fluctuations, simplifying the analysis of the contribution from internal nodes to the phase transition.

Numerical simulation was carried out using the Monte Carlo method, using the Metropolis algorithm.

The magnetic susceptibility of the Fibonacci ring (Fig. 3, *b* (right)) was calculated using formula (4). This effect arises because the size of the excised poles and the number of boundary points are related to the neighbor distribution. Critical temperatures for the three sequences, derived from Gaussian function approximation of the magnetic susceptibility peaks, are shown in Fig. 4. The magnetic susceptibility exhibits behavior similar to the sphere case [1], presenting analogous sequences. In the continuum limit, the critical temperature of the phase transition on the Fibonacci ring approaches that of the sphere, $T_C \approx 3.3$.

For a comparative analysis of the critical temperature behavior of the ferromagnetic phase transition between Fibonacci lattices and a flat triangular lattice, the magnetic susceptibility was calculated for the cut ring topology (Fig. 1, *b*). Such a lattice is considered to be locally flat if we consider the regions excluding the boundaries. The boundary conditions were similarly fixed.

The behavior of the magnetic susceptibility (Fig. 3, *a* (left)) is analogous to the ring case and presents itself as sequences. The plot of the critical temperature dependence on the inverse number of nodes is shown in (Fig. 4). For all sequences, the critical temperature differs insignificantly and, as in previous Fibonacci lattices, approaches $T_C \approx 3.3$ in the limit.

For further investigation of the Ising model phase transition on Fibonacci lattices, topologically correct torus with Euler characteristic equal to zero were selected, namely with $N = \{3000, 8000, 17000, 47000\}$. Using the same calculation methods, magnetic susceptibility was obtained for this set of lattices (Fig. 5).

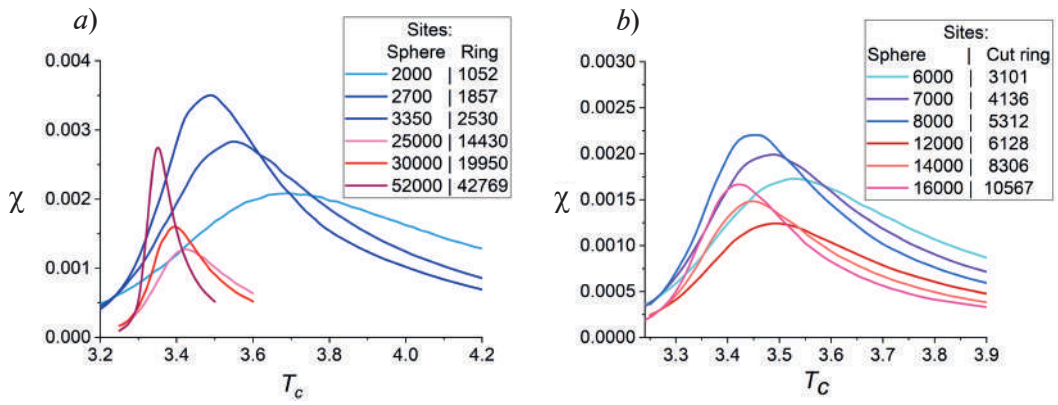

Fig. 3. Examples of two sequences of magnetic susceptibilities on Fibonacci ring (*a* – left) and Fibonacci cut ring (*b* – right) lattices. Data corresponding to two different sequences are highlighted with shades of similar colors

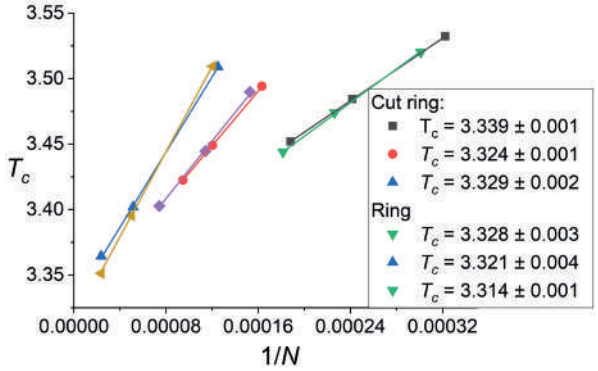

Fig. 4. Scaling of the pseudocritical temperature derived from the magnetic susceptibility approximation on the Fibonacci ring and cut ring as a function of the inverse number of sites, $1/N$

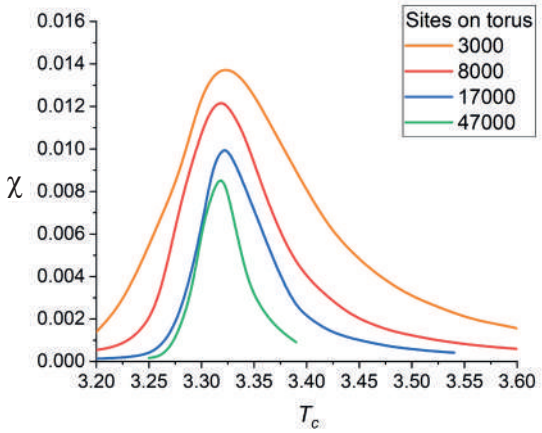

Fig. 5. Scaling of the pseudocritical temperature derived from the magnetic susceptibility approximation on the Fibonacci torus as a function of the inverse number of nodes, $1/N$

Unlike the sphere and its ring topologies, on Fibonacci torus the phase transition temperature is consistently $T_C \approx 3.2$. The value is constant due to the absence of abrupt changes in connectivity properties.

Since the torus corresponds to a flat triangular lattice with periodic boundary conditions, it was expected that the critical temperature would be close to $T_C \approx 3.64$ [10]. However, contrary to expectations, the critical point of the Ising model on the Fibonacci torus is close to the values on the sphere, ring, and Fibonacci cut ring.

Conclusion

In summary, it can be concluded that the Ising model on Delaunay-triangulated Fibonacci lattices demonstrates universal critical temperature behavior regardless of topology. The proximity of the $T_C \approx 3.33(3)J$ value to that of the flat triangular lattice emphasizes the role of quasi-isotropic node distribution and the predominance of hexagonal order. However, the slight deviation is due to the spiral structure of the Fibonacci distribution, which leads to a decrease in T_C compared to theoretical predictions for regular lattices.

REFERENCES

1. **Pochinok A.S., Molochkov A.V., Chernodub M.N.,** Fibonacci discretization of spherical surfaces and two-dimensional spin systems, arXiv preprint arXiv. 2301 (06849) (2023).

2. **Landau L.D., Lifshitz E.M.,** Statistical Physics, Volume 5, Elsevier. (2013).

3. **Delaunay B.,** Sur la sphère vide, Bulletin de l'Académie des Sciences de l'URSS. Classe des sciences mathématiques et naturelles. 6 (1934) 793–800.

4. **Swinbank R., Purser R.J.,** Fibonacci grids: A novel approach to global modelling, Quarterly Journal of the Royal Meteorological Society. 132 (619) (2006) 1769–1793.

5. **Song C.H., Gao Q.C., Hou X.Y., Wang X., Zhou Z., He Y., Guo H., Chien C.C.,** Magnetic properties of the Fibonacci spin chain, Physical Review Research. 4 (2) (2022) 023005.

6. **Saliba E.P., Barnes A.B.,** Magnetic resonance studies of Fibonacci-structured spin systems, The Journal of Chemical Physics. 151 (11) (2019) 114107.

7. **González Á.,** Fibonacci lattices for the evaluation and optimization of mapping functions, Mathematical Geosciences. 42 (1) (2010) 49–64.

8. **Hannay J.H., Nye J.F.,** Fibonacci numerical integration on a sphere, Journal of Physics A: Mathematical and General. 37 (48) (2004) 11591–11601.

9. **Bravais L., Bravais A.,** Essai sur la disposition générale des feuilles curvisériées, Annales des Sciences Naturelles, Botanique. 7 (1837) 42–110.

10. **Baxter R.J.,** Exactly Solved Models in Statistical Mechanics, Elsevier. (2016).

THE AUTHORS

POCHINOK Arina S.
pochinok.as@mail.ru
ORCID: 0000-0003-0430-168X

CHERNODUB Maxim N.
maxim.chernodub@su.se
ORCID: 0000-0003-2101-4914

MOLOCHKOV Alexander V.
molochkov.alexander@gmail.com
ORCID: 0000-0002-3578-703X

CHEPAK Alexander K.
chepak.ak@mail.ru

Received 16.09.2025. Approved after reviewing 01.12.2025. Accepted 04.12.2025.

Conference materials
UDC 537.622.4+539.213.1
DOI: https://doi.org/10.18721/JPM.184.106

Role of transition metals in modifying the exchange interaction and anisotropy of amorphous Fe-Si-B alloys

I.M. Sapovskii [1] ✉, T.R. Rakhmatullaev [1], K.E. Pinchuk [1],
G.S. Kraynova [1], I.A. Tkachenko [2], S.V. Komogortsev [3]

[1] Far Eastern Federal University, Vladivostok, Russia;
[2] Institute of Chemistry FEB RAS, Vladivostok, Russia;
[3] Kirensky Institute of Physics, Krasnoyarsk Science Center of the Siberian Branch of the RAS, Krasnoyarsk, Russia
✉ Sapovskii.im@dvfu.ru

Abstract: Comprehensive studies of the temperature-dependent properties of amorphous Fe-Co-Si-B-Mn alloys have been conducted using differential scanning calorimetry and induction vibromagnetometry. It is established that the investigated alloys exhibit a two-stage crystallization process; the presence of cobalt in the composition leads to a non-monotonic character of the thermomagnetic curves. The phase transition temperatures, including the Curie temperature, were determined. The spin-wave stiffness constant was calculated using a modified Bloch's law. The research results are important for understanding the effect of cobalt doping on the magnetic properties of iron-based amorphous alloys.

Keywords: amorphous alloys, exchange interaction, random magnetic anisotropy model

Funding: The work was carried out with the financial support of the state assignment of the Ministry of Science and Higher Education of the Russian Federation (project no. FZNS-2023-0012).

Citation: Sapovskii I.M., Rakhmatullaev T.R., Pinchuk K.E., Kraynova G.S., Tkachenko I.A., Komogortsev S.V., Role of transition metals in modifying the exchange interaction and anisotropy of amorphous Fe-Si-B alloys, St. Petersburg State Polytechnical University Journal. Physics and Mathematics. 18 (4.1) (2025) 37–43. DOI: https://doi.org/10.18721/JPM.184.106

Материалы конференции
УДК 537.622.4+539.213.1
DOI: https://doi.org/10.18721/JPM.184.106

Роль переходных металлов в модификации обменного взаимодействия и анизотропии аморфных сплавов Fe-Si-B

И.М. Саповский [1] ✉, Т.Р. Рахматуллаев [1], К.Е. Пинчук [1],
Г.С. Крайнова [1], И.А. Ткаченко [2], С.В. Комогорцев [3]

[1] Дальневосточный федеральный университет, г. Владивосток, Россия;
[2] Институт химии ДВО РАН, г. Владивосток, Россия;
[3] Институт физики им. Л.В. Киренского, ФИЦ «Красноярский научный центр Сибирского отделения РАН», г. Красноярск, Россия
✉ Sapovskii.im@dvfu.ru

Аннотация. Проведены комплексные исследования температурно-зависимых свойств аморфных сплавов Fe-Co-Si-B-Mn с использованием методов дифференциальной

сканирующей калориметрии и индукционной вибромагнитометрии. Установлено: исследованные сплавы имеют двухступенчатый процесс кристаллизации; присутствие кобальта в составе приводит к немонотонному характеру термомагнитных кривых. Определены температуры фазовых переходов, в том числе температура Кюри. Расчет спин-волновой константы жесткости проведен с использованием модифицированного закона Блоха. Результаты исследования важны для понимания влияния легирования кобальтом на магнитные свойства аморфных сплавов на основе железа.

Ключевые слова: аморфные сплавы, обменное взаимодействие, модель случайной магнитной анизотропии

Финансирование: Работа выполнена при финансовой поддержке государственного задания Министерства науки и высшего образования Российской Федерации (проект № FZNS-2023-0012).

Ссылка при цитировании: Саповский И.М., Рахматуллаев Т.Р., Пинчук К.Е., Крайнова Г.С., Ткаченко И.А., Комогорцев С.В. Роль переходных металлов в модификации обменного взаимодействия и анизотропии аморфных сплавов Fe-Si-B // Научно-технические ведомости СПбГПУ. Физико-математические науки. 2025. Т. 18. № 4.1. С. 37–43. DOI: https://doi.org/10.18721/JPM.184.106

Introduction

In recent decades, research on amorphous metal alloys has become one of the priorities of modern materials science due to their unique physical properties and a wide range of potential applications in various fields of technology [1–3]. Special attention is paid to studying the effect of alloying elements on the magnetic and structural characteristics of amorphous alloys, which opens up new prospects for creating functional materials with specified properties [4, 5].

The purpose of this work is a comprehensive study of the magnetic properties and thermal stability of a series of amorphous Fe-Co-Si-B-Mn alloys with variable cobalt content.

Materials and Methods

Ferromagnetic Fe-Co-Si-B-Mn alloys in the form of ~20 microns thick ribbons obtained by rapid quenching from a melt on a rotating copper disk in an argon atmosphere were studied [6–8]. The analysis of the structure of the samples at the atomic level was carried out using the X-ray diffractometer "KOLIBRI" of JSC "Burevestnik", Ka(Cu) = 1.54 Å, the X-ray profiles were obtained from the free side of the spinning tapes. Alloy compositions $Fe_{78}B_{13}Si_9$, $Fe_{62}Co_{18}B_{14}Si_6$, $Fe_{55}Co_{26}B_{14}Si_5$, $Co_{74}Fe_3Mn_3B_{15}Si_5$ determined roentgenofluorescence method (Shimadzu spectrometer EDX-7000, standard qualitative and quantitative analysis using a fixed element – boron). The analysis of the structural relaxation processes in the studied samples was carried out on a differential scanning calorimeter "DSC 404 F1 Pegasus". The measurements were carried out in the temperature range from 300 K to 973 K, and the heating rate was 10 K/s. The magnetic characteristics of the alloys were studied using an induction vibration magnetometer and a PPMS 9T Quantum Design installation.

Results and Discussion

X-ray diffraction analysis of Fe-Co-Si-B-Mn samples with varying degrees of cobalt and manganese doping confirmed their amorphous state, Fig. 1, *a*. The diffraction profiles of the studied samples are characterized by a wide diffuse maximum at an angle of $2\theta \approx 45^\circ$, corresponding to an amorphous matrix with a short-range order. With an increase in the cobalt content, a decrease in the radius of the first coordination sphere is observed, which indicates a decrease in structural disorder, Table 1.

When studying the thermal properties of amorphous Fe-Co-Si-B-Mn alloys by differential scanning calorimetry (DSC), a two-stage crystallization process was recorded for all

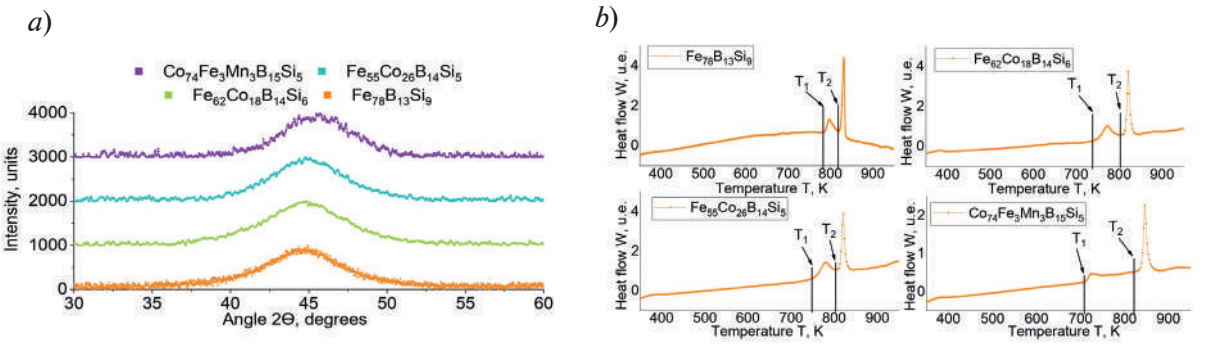

Fig. 1. X-ray diffraction profiles (*a*) and thermograms (*b*) of amorphous alloys $Fe_{78}B_{13}Si_9$, $Fe_{62}Co_{18}B_{14}Si_6$, $Fe_{55}Co_{26}B_{14}Si_5$, $Co_{74}Fe_3Mn_3B_{15}Si_5$

samples (Fig. 1, *b*). The first stage is characterized by the precipitation of α-(Fe, Co) nanocrystals Si [11], the second and final one is the crystallization of an amorphous matrix into metallides (FeB, Co_2B).

The complex nature of the structural relaxation of amorphous alloys $Fe_{78}B_{13}Si_9$, $Fe_{62}Co_{18}B_{14}Si_6$, $Fe_{55}Co_{26}B_{14}Si_5$, and $Co_{74}Fe_3Mn_3B_{15}Si_5$ was confirmed by an analysis of the temperature dependences of saturation magnetization in Fig. 2, *a*, and the Curie temperatures were determined. Alloy $Fe_{78}B_{13}Si_9$ is characterized by the classical behavior of magnetization with increasing temperature for amorphous alloys [9]. Which made it possible to directly determine the Curie temperature T_C, Table 1. Upon further heating, a paramagnetic plateau is observed before the crystallization of the alloy begins, and the nonmonotonic behavior of saturation magnetization makes it possible to determine the Curie temperature of the crystalline phases. Note: for amorphous alloys $Fe_{62}Co_{18}B_{14}Si_6$, $Fe_{55}Co_{26}B_{14}Si_5$, and $Co_{74}Fe_3Mn_3B_{15}Si_5$, the saturation magnetization does not decrease to zero with increasing temperature, so the temperature of the onset of crystallization of these alloys with the loss of magnetic phases is below the Curie temperature T_C for the amorphous state, Fig. 2, *a*.

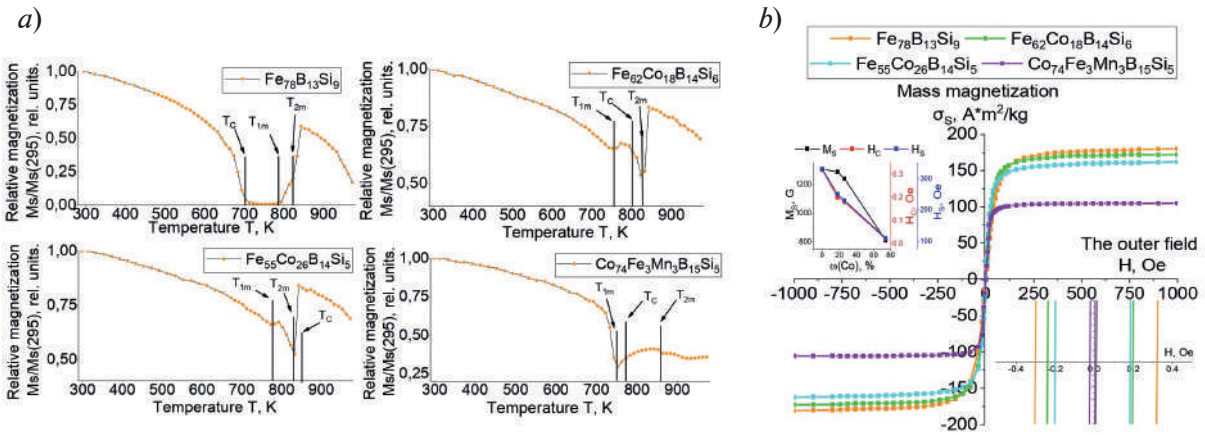

Fig. 2. Dependence of saturation magnetization on temperature (*a*) and hysteresis curves (*b*) for amorphous alloys $Fe_{78}B_{13}Si_9$, $Fe_{62}Co_{18}B_{14}Si_6$, $Fe_{55}Co_{26}B_{14}Si_5$, $Co_{74}Fe_3Mn_3B_{15}Si_5$

The determination of phase transition temperatures by the DSC method made it possible to correlate them with the characteristics obtained from thermomagnetic curves for $Fe_{78}B_{13}Si_9$, $Fe_{62}Co_{18}B_{14}Si_6$, $Fe_{55}Co_{26}B_{14}Si_5$, and $Co_{74}Fe_3Mn_3B_{15}Si_5$ alloys. Table 1. The difference is due to a complex, multi-stage crystallization mechanism in multicomponent systems, in which non-magnetic phases can also occur in Fe and Co transition metal alloys. Note that the addition of cobalt and an increase in its concentration in the alloy leads to an increase in the Curie temperature, which is associated, as mentioned below, with an increase in the exchange interaction constant. The decrease in T_C for $Co_{74}Fe_3Mn_3B_{15}Si_5$ (to 772 K) is primarily attributed to the significantly reduced iron content (3 at.%), which is the main ferromagnetic component in this

Table 1

Position 2θ, radius of the first coordination sphere R_1, phase transition temperatures T_1, T_2, released energy ΔH, obtained from DSC and vibromagnetometry methods T_{1m}, T_{2m}, T_C

Samples	2θ, deg.	R_1, Å	T_1, K	T_2, K	T_{1m}, K	T_{2m}, K	T_C, K
$Fe_{78}B_{13}Si_9$	44.66	2.49	782	819	787	824	701
$Fe_{62}Co_{18}B_{14}Si_6$	44.78	2.48	734	806	743	821	802
$Fe_{55}Co_{26}B_{14}Si_5$	44.96	2.47	744	804	774	832	861
$Co_{74}Fe_3Mn_3B_{15}Si_5$	45.54	2.44	702	828	748	855	772

system. The presence of Mn with its negative exchange interaction integral further contributes to this reduction, Table 1.

An analysis of the hysteresis curves showed that with an increase in the cobalt content in the amorphous alloys of the Fe-Si-B system, there is a consistent decrease in the saturation magnetization of the M_S and the coercive force, Fig. 2, *b*, Table 2. The alloy $Co_{74}Fe_3Mn_3B_{15}Si_5$ demonstrates the lowest H_C value, which makes it a promising candidate for use in devices operating in alternating magnetic fields [10]. However, its reduced M_S limits its use in highly inductive applications. The $Fe_{62}Co_{18}B_{14}Si_6$ alloy demonstrates the most balanced properties.

Studies of the saturation magnetization dependence on temperature in the range of 50 K–300 K, at a field strength of 1000 Oe (Fig. 3, *a*) revealed differences in the behavior of the samples. For the Fe-Si-B alloy, a standard increase in magnetization is observed with a decrease in temperature; alloys with cobalt showed an abnormal bending of the curves in the region of 150 K.

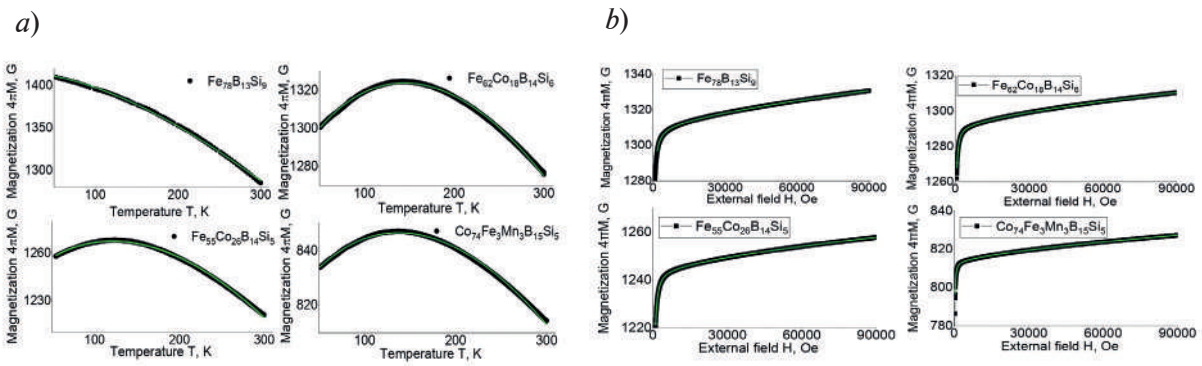

Fig. 3. Dependence of saturation magnetization on temperature in the range (50–300) K (*a*) and dependence of magnetization on the external magnetic field within the limits (*b*) for amorphous alloys $Fe_{78}B_{13}Si_9$, $Fe_{62}Co_{18}B_{14}Si_6$, $Fe_{55}Co_{26}B_{14}Si_5$, $Co_{74}Fe_3Mn_3B_{15}Si_5$. The green line shows the approximation curve

To analyze the low-temperature dependences, a modified Bloch function was used, taking into account the Holstein-Primakoff correction [11]:

$$\left(M_S(T) = M_S(0)\cdot\left(1 - B\cdot T^{(3/2)}\right) + C\cdot f_{HP}\cdot T\right), \tag{1}$$

where M_S is the saturation magnetization, B is the Bloch constant, and C is the approximation parameter, f_{HP} is the Holstein-Primakov function

Based on the Bloch constant obtained for amorphous alloys $Fe_{78}B_{13}Si_9$, $Fe_{62}Co_{18}B_{14}Si_6$, $Fe_{55}Co_{26}B_{14}Si_5$, $Co_{74}Fe_3Mn_3B_{15}Si_5$, Table 2, the spin-wave stiffness constant D [12] was calculated:

$$D = \frac{k_B}{4\pi}\left(\frac{2.612 g\mu_B\mu_0}{M_0 B}\right)^{\frac{2}{3}},\ A = \frac{D\cdot M_S}{2g\mu_B}, \tag{2}$$

where μ_B is the Bohr magneton, g is the Lande multiplier, and k_B is the Boltzmann constant. These characteristics B and D allowed us to obtain the values of the exchange interaction constant A for the studied alloys, Table 2.

With an increase in the cobalt concentration in the Fe-Si-B matrix, an increase in the spin-wave stiffness constant D is observed, Table 2 and the exchange interaction constant A. In the $Co_{74}Fe_3Mn_3B_{15}Si_5$ alloy, the negative sign of the Mn exchange interaction compensate the increase in the exchange interaction due to cobalt.

Table 2

Parameters of approximation by Bloch's law and exchange interaction constants of the studied amorphous alloys

Samples	$M_S(0)$, G	H_S, Oe	H_C, Oe	B, 10^{-5} K$^{-3/2}$	D, meV·Å^2	A, 10^{-7} erg/cm
$Fe_{78}B_{13}Si_9$	1416	330	0.32	2.48	84.9	4.77
$Fe_{62}Co_{18}B_{14}Si_6$	1257	250	0.2	6.01	80.5	4.46
$Fe_{55}Co_{26}B_{14}Si_5$	1233	230	0.18	4.30	102	5.44
$Co_{74}Fe_3Mn_3B_{15}Si_5$	812	110	0.02	5.69	112	3.90

The analysis of the parameters of random magnetic anisotropy for the amorphous alloys under study was performed based on the dependences of magnetization on the external field in the range from 0 to 90 kOe at room temperature, Fig. 3, *b*.

To analyze the obtained dependences, the classical law of approximation of magnetization to saturation was supplemented by the first term of the Holstein-Primakov function. The modified approximation equation has the following form:

$$M = M_S \cdot \left(1 - \frac{(\alpha \cdot H_a)^2}{H^{\frac{1}{2}}\left(H^{\frac{3}{2}} + H_L^{\frac{3}{2}}\right)}\right) + \chi H + A\sqrt{H}, \quad (3)$$

where H_a is the field of local anisotropy of magnetic correlations; H_L is the correlation field, α is the symmetry coefficient, χ is the high-field magnetic susceptibility, and $\sqrt{H}$ is the first term of the Holstein–Primakov function.

From the obtained approximation parameters, the values of the local anisotropy Klocal and the length of the magnetic correlations L_C are determined according to the following formulas [13], Table 3.

$$K_{local} = \frac{H_a \cdot M_S}{2},\ L_C = \sqrt{\frac{2A}{M_S \cdot H_L}}. \quad (4)$$

Table 3

Parameters of the approximation of the curves in Fig. 3, *b* using the law of approximation of magnetization to saturation, the constant of random local magnetic anisotropy K_{local}, the length of magnetic correlations L_C for the studied amorphous alloys

Samples	H_a, Oe	M_S, G	H_L, Oe	K_{local}, 10^6 erg/cm^3	L_C, nm
$Fe_{78}B_{13}Si_9$	3428	1304	1917	5.7	8.9
$Fe_{62}Co_{18}B_{14}Si_6$	2016	1286	779	3.3	14.1
$Fe_{55}Co_{26}B_{14}Si_5$	2831	1240	1037	4.5	12.4
$Co_{74}Fe_3Mn_3B_{15}Si_5$	1110	811	309	1.2	34.4

Conclusions

It is shown that magnetically soft amorphous alloys $Fe_{78}B_{13}Si_9$, $Fe_{62}Co_{18}B_{14}Si_6$, $Fe_{55}Co_{26}B_{14}Si_5$ and $Co_{74}Fe_3Mn_3B_{15}Si_5$ in the range of temperatures studied are characterized by a two-stage process of transition to an equilibrium state. The effect of cobalt content on thermal stability shows a non-monotonic behavior. While some compositions exhibit decreased crystallization temperatures, others demonstrate increased thermal stability, as evidenced by T_1 and T_2 values in Table 1. This behavior indicates a complex interplay of structural and compositional factors, which is associated with accelerated structural relaxation and reduced thermal stability of the amorphous phase; there is a decrease in saturation magnetization (~ 800 Gs), as well as a significant decrease in coercive force (0.02 Oe). The $Co_{74}Fe_3Mn_3B_{15}Si_5$ fast-quenched alloy has the minimum H_C, but the lowest M_S value, which limits its use in devices with high magnetic induction. The Curie temperature, T_C ~700 K., has been experimentally determined for the amorphous $Fe_{78}B_{13}Si_9$ alloy. The addition of Co to the basic matrix is accompanied by a decrease in the crystallization temperature and an increase in T_C for the amorphous state.

An analysis of the low-temperature dependence of the magnetization of the studied alloys revealed an abnormal bend in the temperature range of about 150 K. This feature may be due to the specifics of the structure of amorphous alloys, where the variability of interatomic distances is observed, which has a complex effect on the exchange interaction, affecting not only the quantitative characteristics, but also the sign of the exchange integral. The formation of regions with antiferromagnetic exchange interaction is a key factor determining the characteristic feature of low-temperature magnetic dependences in the form of an inflection of the magnetization curve. The calculations performed showed an increase in the spin-wave stiffness constant and an increase in the correlation length for the Co-enriched alloys studied.

REFERENCES

1. **Jiang H., Shang T., Xian H., Sun B., Zhang Q., Yu Q., Bai H., Gu L., Wang W.,** Structures and Functional Properties of Amorphous Alloys, Small Struct. 2 (2) (2021) 2000057.

2. **Silveyra J.M., Ferrara E., D.L. Huber T.C.,** Mon-son, Soft magnetic materials for a sustainable and electrified world, Science. 362 (6413) (2018) 0195.

3. **Fiorillo F., Bertotti G., Appino C., Pasquale M.,** Soft Magnetic Materials, Wiley Encyclopedia of Electrical and Electronics Engineering. (2016) 1–42.

4. **Li H., Liu T., Pingbo C., He A., Li Q., Luan J.,** Design of Fe-based nanocrystalline alloys with superior magnetization and manufacturability, Mater. Today. 42 (2023) 49–56.

5. **Yang Z.Z., Zhu L., Ye L.X., Gao X., Jiang S.S., Yang H., Wang Y.G.,** Nanoscale structural heterogeneity perspective on the improved magnetic properties during relaxation in a Fe-based metallic glass, J. Non. Cryst. Solids. 571 (2021) 121078.

6. **Kekalo I.B.,** Processes of Structural Relaxation and Physical Properties of Amorphous Alloys, NUST MISIS, Moscow. (2014).

7. **Glezer A.M., Shurygina N.A.,** Amorphous-Nanocrystalline Alloys, FIZMATLIT, Moscow. (2013).

8. **Skulkina N.A., Nekrasov E.S., Denisov N.D., Kuznetsov P.A., Mazeeva A.K.,** Inhomogeneity of magnetic characteristics of a cobalt-based amorphous alloy in the quenched state, Physics of Metals and Metallography. 122 (11) (2021) 1135–1141.

9. **Kotvitskii A.N., Krainova G.S., Frolov A.M., Ivanov V.A., Kuchma A.S.**, Effect of annealing on the magnetic characteristics of spun iron-based ribbons, Bulletin of the Russian Academy of Sciences: Physics. 79 (6) (2015) 795–799.

10. **Zhu H., Stoyanov S., Parsons P., Mclaughlin B., Xiao J.,** Advanced soft magnetic materials for high frequency and high power application, Conference Proceedings – IEEE Applied Power Electronics Conference and Exposition – APEC. (2011) 163–167.

11. **Neuweiler A., Hofmann B., Kronmüller H.,** Approach to magnetic saturation in nanocrystalline and amorphous $Fe_{73.5}Cu_1Nb_3Si_{13.5}B_9$, Journal of Magnetism and Magnetic Materials. 153 (1996) 28–34.

12. **Sapovsky I.M., Ilyin N.V., Krainova G.S., Rakhmatullaev T.R., Tkachenko I.A., Plotnikov V.S., Pinchuk K.E., Frolov A.M.,** Temperature Dependence of Magnetization and Exchange Interaction in Amorphous Fe-Ni-Si-B Alloys, Fizika metallov i metallovedenie. 125 (3) (2024) 253–260.

13. **Ilin N.V., Komogortsev S.V., Kraynova G.S., Davydenko A.V., Tkachenko I.A., Kozlov A.G., Tkachev V.V., Plotnikov V.S.,** Magnetic correlations peculiarities in amorphous Fe-Cu-Nb-Si-B alloy ribbons, J. Magn. Magn. Mater. 541 (2022) 168525.

THE AUTHORS

SAPOVSKII Igor M.
sapovskii.im@dvfu.ru
ORCID:0009-0003-9316-728X

KRAYNOVA Galina S.
kraynova.gs@dvfu.ru
ORCID: 0000-0001-9344-3983

RAKHMATULLAEV Temur R.
rakhmatullaev.tr@dvfu.ru
ORCID: 0009-0000-6927-1341

TKACHENKO Ivan A.
tkachenko@ich.dvo.ru
ORCID: 0000-0002-1770-1546

PINCHUK Kirill E.
pinchuk.ke@dvfu.ru
ORCID: 0009-0005-6764-6089

KOMOGORTSEV Sergey V.
komogor@iph.krasn.ru
ORCID: 0000-0002-2686-3643

Received 29.09.2025. Approved after reviewing 20.10.2025. Accepted 22.10.2025.

Conference materials
UDC 535.015; 535.37
DOI: https://doi.org/10.18721/JPM.184.107

Two bands in PL spectra of InGaN/GaN superlattice embedded in GaN nanowire

E.A. Subbotina [1], A.S. Subbotina [1], A.Yu. Serov [1], N.G. Filosofov [1],
V.O. Gridchin [2, 3], N.V. Sibirev [1] ✉, G.E. Cirlin [3, 2], I.V. Shtrom [1]

[1] St. Petersburg State University, St. Petersburg, Russia;
[2] Alferov University, St. Petersburg, Russia;
[3] Institute for Analytical Instrumentation RAS, St. Petersburg, Russia
✉ n.sibirev@mail.spbu.ru

Abstract. We present a study of the growth and optical properties of an embedded InGaN/GaN superlattice in nanowires. Nitride nanowires with embedded superlattice were grown by molecular beam epitaxy on a silicon substrate. The optical properties of the resulting nanostructures were studied using low-temperature photoluminescence. Photoluminescence spectrum of InGaN/GaN superlattice exhibits two distinct emission bands. These bands correspond to the radiation from the different parts of the InGaN insertions. The second band in the photoluminescence spectrum is associated with the penetration of In into the GaN barrier.

Keywords: photoluminescence, nanowires, indium gallium nitride, molecular beam epitaxy

Funding: The samples were grown under support of RSCF grant No. 23-79-00012.The optical measurements were supported by the research grant of St. Petersburg State University (ID 129360164).

Citation: Subbotina E.A., Subbotina A.S., Serov A.Yu., Filosofov N.G., Gridchin V.O., Sibirev N.V., Cirlin G.E., Shtrom I.V., Two bands in PL spectra of InGaN/GaN superlattice embedded in GaN nanowire, St. Petersburg State Polytechnical University Journal. Physics and Mathematics. 18 (4.1) (2025) 44–48. DOI: https://doi.org/10.18721/JPM.184.107

Материалы конференции
УДК 535.015; 535.37
DOI: https://doi.org/10.18721/JPM.184.107

Две полосы в спектре фотолюминесценции от сверхрешетки InGaN/GaN, заключенной в нитевидный нанокристал GaN

Е.А. Субботина [1], А.С. Субботина [1], А.Ю. Серов [1], Н.Г. Философов [1],
В.О. Гридчин [2, 3], Н.В. Сибирев [1] ✉, Г.Э. Цырлин [3, 2], И.В. Штром [1]

[1] Санкт-Петербургский государственный университет, Санкт-Петербург, Россия;
[2] Академический университет им. Ж.И. Алфёрова РАН, Санкт-Петербург, Россия;
[3] Институт аналитического приборостроения РАН, Санкт-Петербург, Россия
✉ n.sibirev@mail.spbu.ru

Аннотация. В данной работе мы представляем описание синтеза и оптических свойств сверхрешетки InGaN/GaN внедренной в нитевидный нанокристалл GaN. Синтез массива нитевидных нанокристаллов осуществлялся методом молекулярно-пучковой эпитаксии на кремниевой подложке. Оптические свойства наноструктур на основе

нитридных нитевидных нанокристалов были изучены методом низкотемпературной фотолюминесценции.Нитевидные нанокристаллы GaN с квантовыми дисками InGaN демонстрируют две отчетливые полосы излучения в спектре фотолюминесценции. Полосы соответствуют излучению от квантовых дисков InGaN. Возникновения второй полосы в спектре фотолюминесценции может быть связано с проникновением In в барьер в барьер GaN.

Ключевые слова: фотолюминесценция, нитевидные нанокристалы, нитрид галлия, молекулярно-пучковая эпитаксия

Финансирование: Оптические измерения были выполнены в рамках Гранта СПбГУ номер 129360164. Рост образцов при поддержке гранта Российского научного фонда номер 23-79-00012.

Ссылка при цитировании: Субботина Е.А., Субботина А.С., Серов А.Ю., Философов Н.Г., Гридчин В.О., Сибирев Н.В., Цырлин Г.Э., Штром И.В. Две полосы в спектре фотолюминесценции от сверхрешетки InGaN/GaN, заключенной в нитевидный нанокристал GaN // Научно-технические ведомости СПбГПУ. Физико-математические науки. 2025. Т. 18. № 4.1. С. 44–48. DOI: https://doi.org/10.18721/JPM.184.107

Introduction

Recently, the study of the optical properties of nitride nanowires (NWs) has attracted the interest of researchers. The unique properties of these direct-gap semiconductors allow for the wavelength to be changed from the near-UV range to the near-IR range by changing the chemical composition [1]. While the geometry of NWs allows them to grow directly on silicon. The opportunity to create diodes based on GaN NWs with InGaN insertions has already been demonstrated [2]. Even more single-photon emission at room temperature from InGaN quantum dots in NWs was shown [3]. InGaN ternary compounds with a high In content (In > 30%) have a tendency toward phase decomposition due to the notable difference in bond lengths between In–N and Ga–N, so-called “miscibility gap” [4, 5]. This feature complicates the growth of InGaN thin films with high In content. Moreover, the growth of high-quality InGaN/GaN epilayers with high In content is also complicated due to the high dislocation density, resulting from the notable lattice mismatch between InN and GaN. We investigate InGaN/GaN heterostructures through the NW growth to overcome these limitations. Due to a very efficient relaxation of elastic stress on strain-free sidewalls, NW heterostructures can be grown in lattice-mismatched systems without structural defects or with a largely reduced dislocation density compared to epi-layers [6].

Materials and Methods

Growth experiments were carried out on one-side polished *n*-type Si substrates in a Riber Compact 12 MBE system. The surface orientation of the substrate was (111) with a 4° miscut toward the [110] direction. The MBE chamber is equipped with Addon RF-N 600 plasma source and Knudsen cells of Ga and In. Prior to loading into the growth chamber, the substrate was etched in a 47.5% hydrofluoric acid solution for 40 seconds, followed by a 60 second washing in deionized water. After that, the substrate was transferred into the MBE chamber and thermally cleaned at 855 °C for 20 min. Then, the substrate temperature was cooled down to 620 °C. The substrate temperature was obtained using an Optris CT Laser 3MH1 pyrometer calibrated on the 7×7 to 1×1 surface reconstruction of the Si(111) substrate. Next, the nitrogen plasma was ignited at a source power of 350 W with a nitrogen flow of $4.4 \cdot 10^{-6}$ Torr, and the substrate was nitridated for 20 min to form thin SixNy layer. At the next stage, two monolayers of Al were deposited onto the formed SixNy layer for 6 seconds in the absence of nitrogen plasma. Next, the substrate temperature was increased to 805 °C, the nitrogen plasma was ignited at the same parameters, and the Ga source was opened to grow GaN NWs. This procedure allowed one to achieve N-polar GaN NWs. The beam equivalent pressure (BEP) of Ga corresponded to $1.5 \cdot 10^{-7}$ Torr.

After a 18h of growth, the Ga source was closed, and the substrate temperature was decreased to 600 °C. The In and Ga sources were opened with BEPs equal to $1 \cdot 10^{-7}$ Torr each other to form InGaN insertions. After the formation of each 3–4 nm InGaN insertion, a 9–10 nm GaN barrier was grown at the same substrate temperature. This process was repeated 15 times to obtain a stack of InGaN quantum wells (QW) in GaN NWs. A scheme and SEM image of the obtained nanostructure is shown in Figure 1.

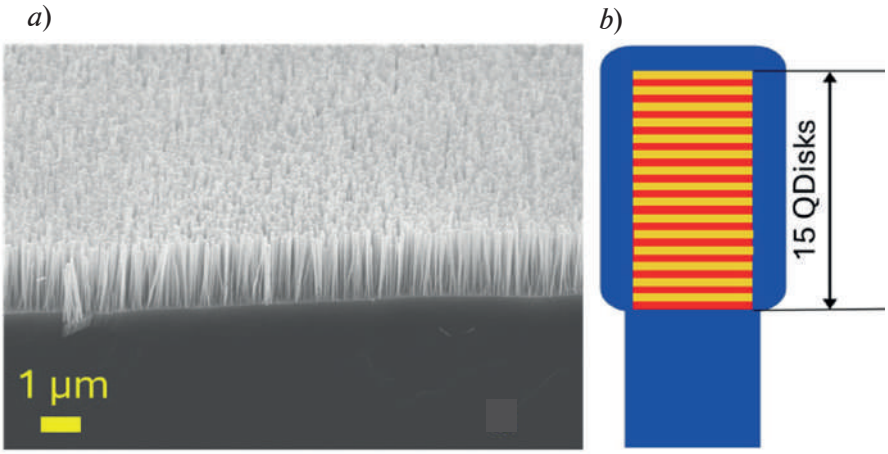

Fig.1. SEM image of GaN NWs with InGaN superlattice(*a*) and a scheme of the NW with the superlattice structure (*b*)

To study the opportunity of increasing indium content in active region during the growth, a second growth was carried out with the BEPs of In and Ga set to 1.2×10^{-7} Torr and 0.8×10^{-7} Torr, respectively.

Results and discussion

The optical properties of the synthesized samples were studied using an MDR-204-2 monochromator. The samples were placed in a closed-cycle helium cryostat. The photoluminescence (PL) was excited by a He-Cd laser (excitation wavelength $\lambda = 325$ nm, radiation power $W = 50$ kW·cm^{-2}) at $T = 5$K.

The PL spectra of InGaN/GaN superlattices embedded in GaN NWs demonstrate two PL bands in both samples, see Fig. 2. The PL band maxima were for 2.8 eV; 3.2 eV Sample 1 and for 2.1 eV; 2.6 eV Sample 2, respectively. The PL maxima were successfully shifted from the blue to the orange spectral region by increasing the In BEP and decreasing the Ga BEP. The In/Ga ratio was 1/1 for Sample 1 and 1.2/0.8 for Sample 2.

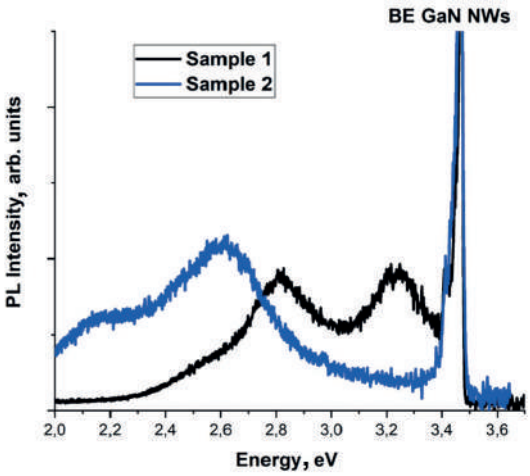

Fig. 2. PL spectra of GaN nanowires with fifteen InGaN quantum disks

Previously, the properties of InGaN/GaN superlattices embedded in GaN NWs were investigated in paper [7], where two PL bands with the spacing between maxima about 0.5 eV were also observed on the spectrum. The authors of that paper assumed that the observed PL bands are related to the formation of two emission levels from the superlattice regions with different indium concentrations and thicknesses. The In-rich region has greater thickness and less indium content near the sidewalls [7]. Our additional studies confirm that, in our case, the situation is similar. The existence of two bands could be explained in terms of spontaneous radial segregation.

Conclusion

GaN NWs with fifteen InGaN quantum disks were grown on a Si(111) substrate using MBE with different In/Ga flux ratios. The opportunity to overcome "miscibility gap" in InGaN NWs is shown. InGaN NWs without structural defects and with high indium content are demonstrated. The PL spectra of InGaN superlattices exhibit two distinct emission bands. The existence of two bands can be explained by spontaneous radial segregation. The PL band maxima were successfully shifted from the blue to the orange spectral region by increasing the In BEP and decreasing the Ga BEP. Which allows us to effectively change the wavelength of radiation from the InGaN QWs embedded in GaN NWs. The increase in the In content does not lead to the formation of additional nonradiative recombination centers.

Acknowledgments

The samples were grown under support of RSCF grant No. 23-79-00012.The optical measurements were supported by the research grant of St. Petersburg State University (ID 129360164).

REFERENCES

1. **Gridchin V.O., et al.,** Multi-colour light emission from InGaN nanowires monolithically grown on Si substrate by MBE, Nanotechnology. (32) (2021) 335604.

2. **Pratim K. Saha, et al.,** Room temperature single-photon emission from InGaN quantum dot ordered arrays in GaN nanoneedles, Appl. Phys. Lett. (121) (2022) 211101.

3. **Bondarenko D.N., Gridchin V.O., Kotlyar K.P., Reznik R.R., Kirilenko D.A., Baranov A.I., Dragunova A.S., Kryzhanovskaya N.V., Maksimova A.A., Cirlin G.E.,** Physical properties of GaN nanowires with core-shell InGaN/GaN insertions grown by PA-MBE on Si substrate, St. Petersburg State Polytechnical University Journal. Physics and Mathematics. 16 (1.2) (2023) 179–184.

4. **Ho, I., Stringfellow G.,** Solid Phase Immiscibility in GaInN. Appl. Phys. Lett. 69 (18) (1996) 2701–2703.

5. **Karpov S.Y.,** Suppression of Phase Separation in InGaN Due to Elastic Strain. MRS Internet J. Nitride Semicond. Res. 3 (1) (1998) 16.

6. **Dubrovskii V.G., et al.,** Instantaneous growth of single monolayers as the origin of spontaneous core–shell $In_xGa_{1-x}N$ nanowires with bright red photoluminescence, Nanoscale Horiz. The Royal Society of Chemistry. (2024).

7. **Kehagias Th., et al.,** Nanostructure and strain in InGaN/GaN superlattices grown in GaN nanowires, Nanotechnology. 24 (2013) 435702.

THE AUTHORS

SUBBOTINA Elizaveta A.
st121055@student.spbu.ru

SUBBOTINA Aleksandra S.
aleksandrasubbotina.01@mail.ru

SEROV Alexey Yu.
serovpobox@gmail.com
ORCID: 0000-0003-1122-9014

FILOSOFOV Nikolai G.
n.filosofov@spbu.ru
ORCID: 0000-0001-6004-3553

GRIDCHIN Vladislav O.
gridchinvo@gmail.com
ORCID: 0000-0002-6522-3673

CIRLIN George E.
cirlin@beam.ioffe.ru
ORCID: 0000-0003-0476-3630

SIBIREV Nickolay V.
n.sibirev@mail.spbu.ru
ORCID: 0000-0002-7566-2522

SHTROM Igor V.
igorstrohm@mail.ru

Received 10.01.2025. Approved after reviewing 09.12.2025. Accepted 09.12.2025.

Conference materials
UDC 537.622
DOI: https://doi.org/10.18721/JPM.184.108

Curvature-induced localization of magnetic domains in thin multilayer magnetic films on the surface of porous alumina

K.A. Rogachev [1] ✉, A.Yu. Samardak [1], M.A. Bazrov [1],
A.F. Shishelov [1], M.I. Sobirov [1], A.V. Ognev [1, 2], A.S. Samardak [1, 2]

[1] Far Eastern Federal University, Vladivostok, Russia;
[2] Sakhalin State University, Yuzhno-Sakhalinsk, Russia
✉ kirpers26@gmail.com

Abstract. The curvature of the ferromagnetic nanostructure is among its most important properties because of the great influence on its magnetic behavior, induced by strong shape magnetic anisotropy. In this work, we discuss the preparation and investigation of the magnetic properties of Pt/$[Co/Pt]_{x9}$/Pt thin films on the surface of convex (nanodomes) and concave (nanopits) nanorelief, in the form of anodized aluminum oxide and aluminum matrices with an etched anodized oxide layer, respectively. For all samples, the presence of perpendicular magnetic anisotropy was observed, which was also observed in the reference samples on the smooth surface of SiO_2. We show that an increase of the anodizing voltage leads to an increase in the interpore distance and curvature of the surface, which has a great influence on the coercive force and residual magnetization. In addition, we present the study of magnetic configuration of the obtained films, which showed the presence of the localization of magnetic domains on nanodomes and possible presence of skyrmions.

Keywords: porous oxide matrices, anodizing, thin films, skyrmions

Funding: This work was supported by the Russian Ministry of Science and Higher Education (State Task No. FZNS-2023-0012).

Citation: Rogachev K.A., Samardak A.Yu., Bazrov M.A., Shishelov A.F., Sobirov M.I., Ognev A.V., Samardak A.S., Curvature-induced localization of magnetic domains in thin multilayer magnetic films on the surface of porous alumina, St. Petersburg State Polytechnical University Journal. Physics and Mathematics. 18 (4.1) (2025) 49–54. DOI: https://doi.org/10.18721/JPM.184.108

Материалы конференции
УДК 537.622
DOI: https://doi.org/10.18721/JPM.184.108

Наведенная пространственной кривизной локализация магнитных доменов в тонких многослойных магнитных пленках на поверхности пористого оксида алюминия

К.А. Рогачев [1] ✉, А.Ю. Самардак [1], М.А. Базров [1],
А.Ф. Шишелов [1], М.И. Собиров [1], А.В. Огнев [1, 2], А.С. Самардак [1, 2]

[1] Дальневосточный федеральный университет, г. Владивосток, Россия;
[2] Сахалинский государственный университет, г. Южно-Сахалинск, Россия
✉ kirpers26@gmail.com

Аннотация. Кривизна ферромагнитной наноструктуры является одним из ее важнейших свойств из-за большого влияния на ее магнитное поведение, вызванного

сильной магнитной анизотропией формы. В этой работе мы обсуждаем получение и исследование магнитных свойств тонких пленок Pt/[Co/Pt]$_{x9}$/Pt на поверхности выпуклого (нанокупола) и вогнутого (наноямки) нанорельефа, в виде анодированного оксида алюминия и алюминиевых матриц с протравленным анодированным оксидным слоем, соответственно. Для всех образцов наблюдалось наличие перпендикулярной магнитной анизотропии, которая также наблюдалась в контрольных образцах на гладкой поверхности SiO_2. Мы показываем, что увеличение напряжения анодирования приводит к увеличению межпорового расстояния и кривизны поверхности, что оказывает большое влияние на коэрцитивную силу и остаточную намагниченность. Кроме того, мы представляем исследование магнитной конфигурации полученных пленок, которое показало наличие локализации магнитных доменов на нанокуполах и возможное присутствие скирмионов.

Ключевые слова: пористые оксидные матрицы, анодирование, тонкие пленки, скирмионы

Финансирование: Работа выполнена при поддержке Министерства науки и высшего образования Российской Федерации (Государственное Задание № FZNS-2023-0012).

Ссылка при цитировании: Рогачев К.А., Самардак А.Ю., Базров М.А., Шишелов А.Ф., Собиров М.И., Огнев А.В., Самардак А.С., Наведенная пространственной кривизной локализация магнитных доменов в тонких многослойных магнитных пленках на поверхности пористого оксида алюминия // Научно-технические ведомости СПбГПУ. Физико-математические науки. 2025. Т. 18. № 4.1. С. 49–54. DOI: https://doi.org/10.18721/JPM.184.108

Introduction

In recent years, skyrmions have been center of interest in the fields of nanomagnetism and spintronics of science due to the unique properties of these topological quasiparticles, such as high stability, small sizes and the ability to move under the influence of low current densities [1]. Such properties open the prospect of their effective use as a unit of information transfer and storage in novel spintronics devices [2]. However, there are a number of difficulties that currently prevent their widespread use, with the stabilization of skyrmions at room temperature and in the absence of an external magnetic field [1] being among them. An approach to solving this problem is to use curved geometries nanostructures, which can create conditions for the formation and stabilization of skyrmions [3, 4].

Thin magnetic films with curved geometry, which are created by depositing magnetic materials on substrates with curved nanoscale relief, are an interesting object for research, as their geometry can cause magnetic phenomena that are not characteristic of flat films [3–5]. A recent experimental study has shown that a curved surface of asymmetric Pt/Co/Ta can significantly increase the stability and localization of skyrmions in nanodomes [6].

In this work, we investigate further the influence of curvature of the substrate and study the localization of magnetic domains in thin films with symmetric Pt/Co/Pt interfaces not only on a convex curved surface but also on a concave one to analyze the influence of mirrored substrate relief and different anodization voltages on magnetic properties of the magnetic films.

Materials and Methods

To modulate the surface, anodic alumina oxide (AAO) and aluminum with an AAO were used, which were obtained by electrochemical anodization of aluminum in a solution of 5% orthophosphoric acid H_3PO_4. To achieve a more even surface, the aluminum substrates were pre-annealed in a vacuum at a temperature of 500 °C for 30 minutes, then electrochemical polishing of aluminum was carried out in a solution of 1:4 $HClO_4$ + C_2H_5OH for 1.5 minutes at an initial temperature of 2 °C (cryostat KRYO-VIST-04) and a current density of 500 mA/cm^2 (laboratory power supply Agilent 6030A). After obtaining a smooth mirror-like surface, aluminum was anodized

in a 5% solution of H_3PO_4 at a temperature of 2 °C with a constant voltage of 90, 120 and 150 V for 6, 4 and 2 hours, respectively. For each used voltage, two types of substrates were achieved – first type was obtained by etching of AAO to obtain nanopits in the aluminum and second type synthesized by etching of aluminum to obtain nanodomes on AAO. Then, using magnetron sputtering (Omicron), Pt(4 nm)/[Co(0.7 nm)/Pt(2 nm)]$_{x9}$/Pt(2 nm) films were deposited on the surface of nanodomes and nanopits. In addition, reference samples were synthesized by deposition of films on the flat surface of the silicon oxide substrate. The surface morphology was studied by scanning electron microscopy (SEM, ThermalScientific SCIOS 2) and atomic force microscopy (AFM, NT-MDT NTEGRA Aura). The magnetic properties of the samples were determined by vibrational magnetometry (VSM, LakeShore VSM 7410). Magnetic force microscopy (MFM, NT-MDT NTEGRA Aura) was used to visualize the magnetic configuration.

Results and Discussion

The morphology of domes on AAO templates and its imprint in aluminum as pits was investigated by SEM (Fig. 1, *a*) and AFM (Fig. 1, *b*) prior to deposition of magnetic films. For ease, the following sample notation was introduced: nanodomes – D, nanopits – P, the numbers indicate the anodizing voltage divided by 10. The letter L at the end of the sample name indicates that a magnetic film is deposited on the sample surface. As in the analysis of the dependence of the geometric dimensions of nanodomes and nanopits on the anodizing voltage shown (Fig. 1, *c*), with an increase in voltage, the diameter of the structures on the surface increases proportionally from 250 ± 25 nm at 90 V to 400 ± 19 nm at 150 V for nanodomes and from 270 ± 12 nm at 90 V to 390 ± 29 nm at 150 V for nanopits, which is typical for AAO. Moreover, with increasing voltage, the height of the obtained structures also increases from 53 ± 6 nm at 90 V to 61 ± 9 nm at 120 V and to 90 ± 11 nm at 150 V for nanopits and 40 ± 6 nm at 90 V to 52 ± 9 nm at 120 V for nanodomes. The decrease in the height of the nanodomes with increasing voltage from 120 to 150 V and the overall lower height of the nanodomes compared to the nanopits may be associated with the impossibility of accurately studying the relief using AFM due to the large curvature of the surface at the boundary of two nanodomes.

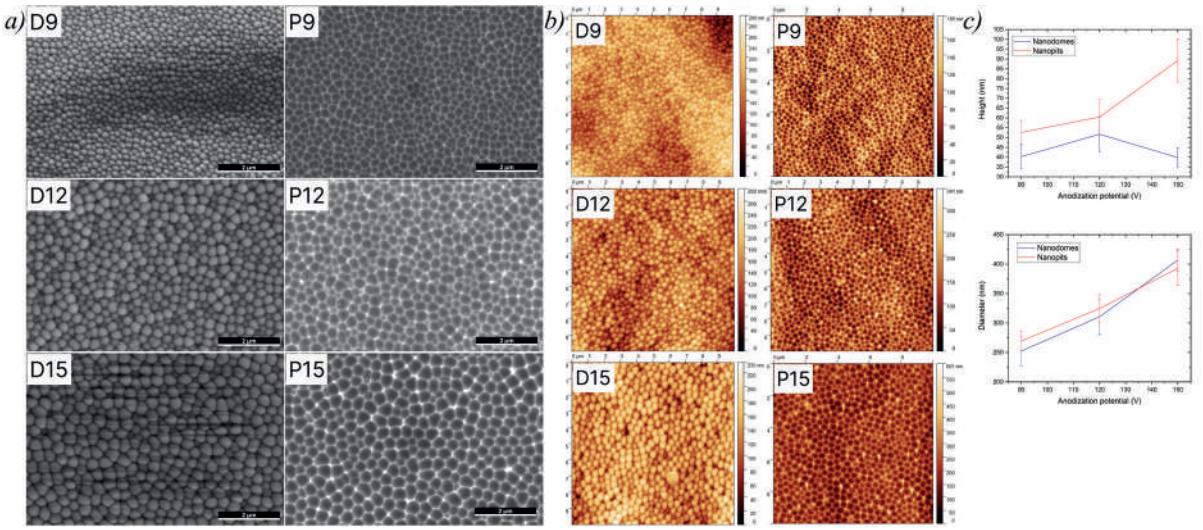

Fig. 1 SEM (*a*) and AFM (*b*) images of the surface of substrates with nanodomes (D) and nanopits (P) obtained at different anodizing voltages. Dependence of the geometric dimensions of the obtained nanoscale surface curvatures on the anodization voltage obtained from AFM (*c*)

After studying the geometric parameters of the nanorelief, thin Pt(4 nm)/[Co(0.7 nm)/Pt(2 nm)]$_{x9}$/Pt(2 nm) films were sputtered on the prepared substrates. The study of the magnetic properties of the films by VSM is presented in Fig. 2. To achieve hysteresis loops, samples were magnetized in the out of plane direction of the external magnetic field H in a range of ±1 kOe.

All samples were able to maintain out of plane anisotropy despite the different curvatures of the underlayer (Fig. 2, *a*, *b*), yet all of the films obtained on the surface of the modulated nanorelief

were characterized by a lower residual magnetization M_R/M_S in comparison to the reference sample, which may be induced by additional points of nucleation induced by inhomogeneities of their substate surfaces. The coercive force H_C of the films in nanopits decreases drastically from 244 Oe at an anodizing voltage of 90 V to 230 Oe at 120 V and 167 Oe at 150 V, while residual magnetization follows the same trend with a decrease from 0.893 at 90 V to 0.832 at 120 V and 0.745 at 150 V. The change in the magnetic behavior of the films on nanodomes with the change of anodization voltage is different in comparison to that of the films on nanopits, with oscillating M_R/M_S and H_C values. At 90 V, M_R/M_S and HC are 0.69 and 160 Oe, respectively, at 120 V, M_R/M_S and HC increase to 0.92 and 202 Oe, respectively. With an increase of anodization voltage up to 150 V, the decrease of these values is observed, marking values of M_R/M_S and H_C as 0.65 and 132 Oe. Since the dependences of M_R/M_S and H_C coincide more with the dependence of the height on the anodization potential (Fig. 1, *c*), we can conclude that the height of nanodomes and nanopits influences their magnetic behavior much more than the diameter of the pores.

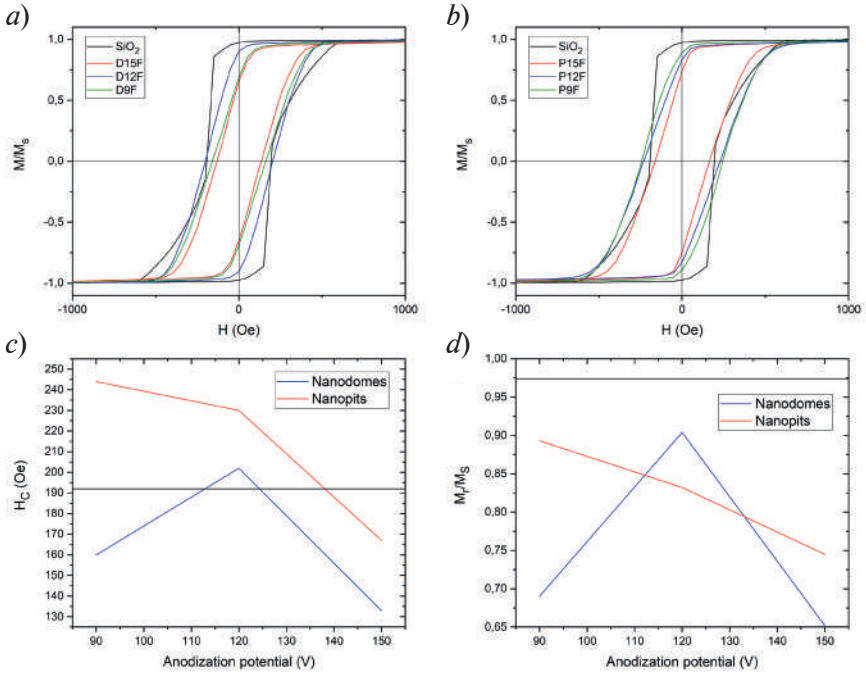

Fig. 2. Magnetic characteristics of the obtained multilayer films: (*a*) hysteresis of films on nanodomes and (*b*) nanopits in an out of plane configuration of **H**, dependence of (*c*) residual magnetization and (*d*) coercive force on anodization voltage (straight gray lines in graphs (*c*) and (*d*) indicate residual magnetization and coercive force of the reference film on the surface of oxidized silicon)

The study of the domain structure of the samples by MFM (Fig. 3) showed that the magnetic configuration of the reference film on the surface of oxidized silicon has a labyrinth domain structure, which is typical for such films [7]. A similar structure is also observed in the film obtained on the surface with a modulated nanorelief. In all samples, round "bubble" domains were observed, which are signs of possible presence of skyrmions [6, 8, 9]. However, for films obtained on the surface of nanodomes, a higher localization of individual domains on the nanodomes is observed. The magnetic configuration of sample D12F exhibits a predominantly labyrinthine structure with a small number of localized bubble domains. The magnetic configuration of sample D15F demonstrates an increase in the number of bubble domains arising from the breakdown of the labyrinthine domain structure. Sample D9F exhibits the highest number of individual localized domains, weakly or not at all connected to their neighbors. The decrease in coercive force H_C and residual magnetization M_R/M_S for the D9F and D15F samples compared to the D12F sample could be connected to higher localization of the magnetic domains and the partitioning of the labyrinthine domain structure into bubble domains. In contrast, the magnetic configuration of films obtained on the surface of nanopits is mostly characterized not by localized bubble domains, but by a labyrinthine structure, as in the control sample.

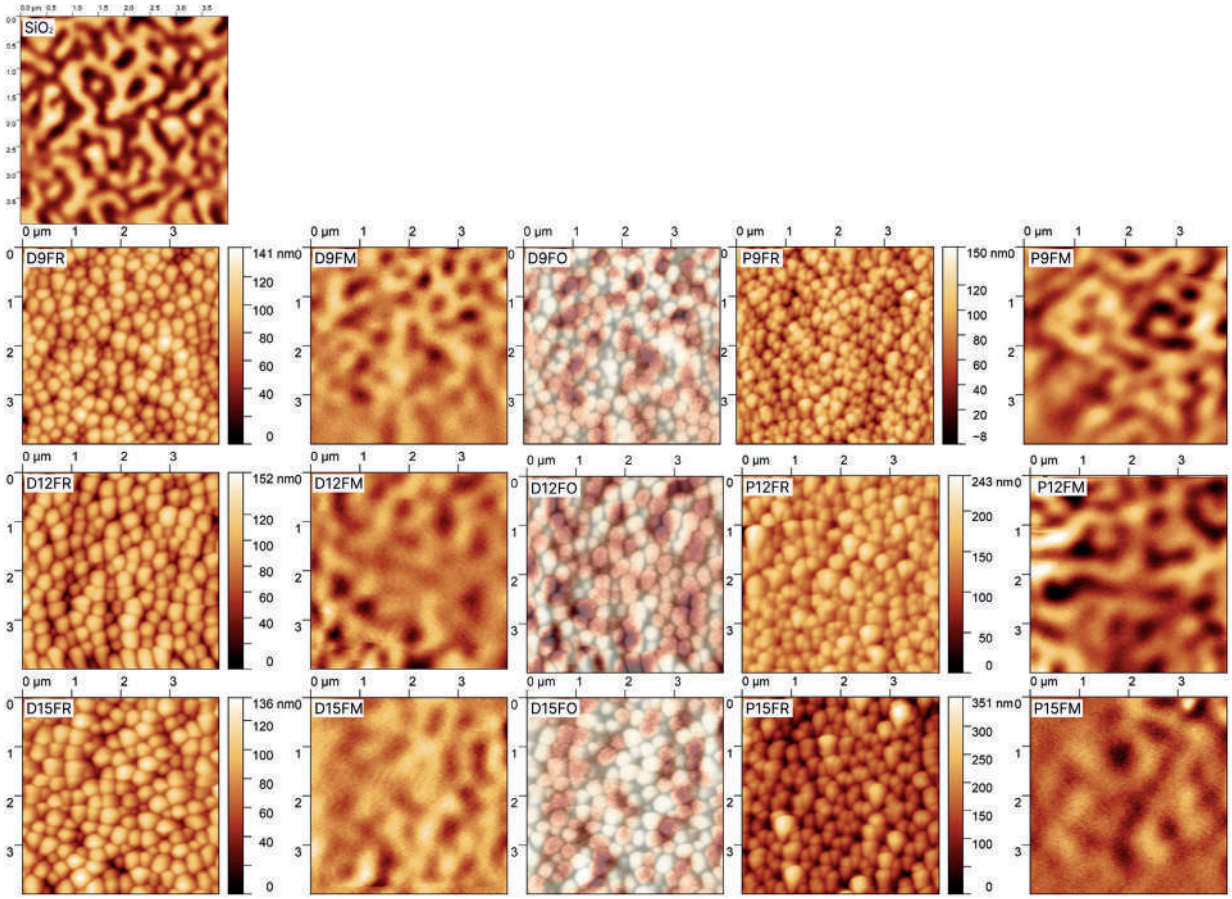

Fig.3 MFM image of the film scattering fields on the surface of SiO_2, surface relief (postfix "R") and MFM image of the scattering fields (postfix "M") of the obtained films (postfix "O" means the imposition of the MSM image on the surface relief)

Conclusion

As a result of the carried out work, multilayer Pt(4 nm)/[Co(0.7 nm)/Pt(2 nm)]$_{x9}$/Pt(2 nm) films were obtained by magnetron sputtering on the surface of AAO substate with non-trivial morphology. Despite the curvature of the underlayer, samples achieved on nanodomes and nanopits tend to maintain the perpendicular magnetic anisotropy, similar to a reference sample obtained on flat silicon oxide. It was shown that magnetic properties of the films depend heavily on the anodization voltage during the preparation of AAO templates, with an increase in the voltage leading to an increase in the curvature of the surface and a decrease of the coercive force H_C and residual magnetization M_R/M_S. In addition, the presence of bubble domains and observed localization of magnetic domains on nanodomes were shown as a result of studying the domain structure of the films. As was discovered, the localization of the magnetic domains heavily depends on the curvature of the underlayer as well, and nanodomes and nanopits are characterized by different domain structures, despite being mirror reflections of each other.

REFERENCES

1. **Fert A., Reyren N. and Cros V.,** Magnetic skyrmions: advances in physics and potential applications, Nature Reviews Materials 2 (2017) 17031.

2. **He M., Xu N., Gao Y., Hu C., Cai J., Zhang Y.,** Mixed-Type Skyrmions in Symmetric Pt/Co/Pt Multilayers at Room Temperature, Materials. 15 (2022) 8272.

3. **Streubel R., Fischer P., Kronast F., Kravchuk V.P., Sheka D.D., Gaididei Y., Schmidt O.G., Makarov D.,** Magnetism in curved geometries, Journal of Physics D: Applied Physics 49. (2016) 363001.

4. **Carvalho-Santos V.L., Corona R.M., Altbir D., Castillo-Sepúlveda S.,** Shifts in the skyrmion stabilization due to curvature effects in dome- and antidome-shaped surfaces, Physical Review B. 102 (2020) 024444.

5. **Kravchuk V.P., RoЯler U.K., Volkov O.M., Sheka D.D., Van den Brink J., Makarov D., Fuchs H., Fangohr H., Gaididei Y.,** Topologically stable magnetization states on a spherical shell: Curvature-stabilized skyrmions, Physical Review B. 94 (2016) 144402.

6. **Tejo F., Toneto D., Oyarzъn S., Hermosilla J., Danna C.S., Palma J.L., da Silva R.B., Dorneles L.S., Denardin J.C.,** Stabilization of Magnetic Skyrmions on Arrays of Self-Assembled Hexagonal Nanodomes for Magnetic Recording Applications, ACS Applied Materials & Interfaces. 12 (2020) 53454–53461.

7. **Ermolaeva O.L., Gusev N.S., Skorohodov E.V., Petrov Yu.V., Sapozhnikov M.V., Mironov V.L.,** Magnetic Force Microscopy of Nanostructured Co/Pt Multilayer Films with Perpendicular Magnetization, Materials. 10 (2017) 1034.

8. **Jiang W., Upadhyaya P., Zhang W., Yu G., Jungfleisch M.B., Fradin F.Y., Pearson J.E., Tserkovnyak Ya., Wang R.L., Heinonen O., Te Velthuis S.G.E., Hoffmann A.,** Blowing magnetic skyrmion bubbles Science. 349 (2015) 283–286.

9. **Yang Q., Cheng Y., Li Y., Zhou Z., Liang J., Zhao X., Hu Z., Peng R., Yang H., Liu M.,** Voltage Control of Skyrmion Bubbles for Topological Flexible Spintronic Devices, Advanced Electronic Materials. 6 (2020) 2000246.

THE AUTHORS

ROGACHEV Kirill A.
rogachev.ka@dvfu.ru
ORCID: 0000-0002-8193-3851

SOBIROV Mukhammad I.
sobirov.mi@dvfu.ru
ORCID: 0000-0002-8954-8413

SAMARDAK Aleksey Yu.
samardak.aiu@dvfu.ru
ORCID: 0000-0002-0795-374X

OGNEV Aleksey V.
ognev.av@dvfu.ru
ORCID: 0000-0002-1619-3666

BAZROV Michail A.
bazrov.ma@dvfu.ru
ORCID: 0009-0002-4092-135X

SAMARDAK Aleksandr S.
samardak.as@dvfu.ru
ORCID: 0000-0001-5917-4361

SHISHELOV Aleksandr F.
shishelov.af@dvfu.ru
ORCID: 0000-0002-9703-4623

Received 20.09.2025. Approved after reviewing 10.10.2025. Accepted 13.10.2025.

Conference materials
UDC 539.216.2
DOI: https://doi.org/10.18721/JPM.184.109

Interfacial ferromagnetism in sputtered Pt/Gd/Pt system at room temperature

A.A. Turpak [1] ✉, A.S. Pashenko [1], A.V. Prikhodchenko [1], E.V. Tarasov [1],
N.N. Chernousov [1], M.A. Kuznetsova [1], A.V. Davydenko [1]

1 Far Eastern Federal University, Vladivostok, Russia
✉ turpak.aa@dvfu.ru

Abstract. The magnetic properties of ultrathin Pt/Gd/Pt films prepared by magnetron sputtering were investigated. The Gd layer thickness varied from 1 to 15 nm. At room temperature, the samples exhibited a weak saturation magnetization, predominantly of interfacial origin. The measured interfacial magnetic moment was 14.5 $\mu ergG^{-1}cm^{-2}$. The contribution of bulk Gd layers to the saturation magnetization was found to be negligible. The shape of the hysteresis loops did not depend on the Gd layer thickness. Crystallization into a face-centered cubic structure was observed only for the 15 nm Gd layer. The results of this study emphasize the importance of interfacial ferromagnetism in the Pt/Gd/Pt system.

Keywords: gadolinium, superparamagnetism, multilayer films, magnetization, magnetic susceptibility, magnetic ordering temperature, size-dependent magnetic properties

Funding: Highly efficient switching of magnetisation via spin orbital angular momentum in magnetic nanoheterostructures for field-free SOT-MRAM memory and in-memory computing devices, No. 25-42-00083; The work was supported by the Ministry of Science and Higher Education of the Russian Federation (State Task No. FZNS-2023-0012).

Citation: Turpak A.A., Pashenko A.S., Prikhodchenko A.V., Tarasov E.V., Chernousov N.N., Kuznetsova M.A., Davydenko A.V., Interfacial ferromagnetism in sputtered Pt/Gd/Pt system at room temperature, St. Petersburg State Polytechnical University Journal. Physics and Mathematics. 18 (4.1) (2025) 55–61. DOI: https://doi.org/10.18721/JPM.184.109

Материалы конференции
УДК 539.216.2
DOI: https://doi.org/10.18721/JPM.184.109

Межфазный ферромагнетизм в напыленной системе Pt/Gd/Pt при комнатной температуре

А.А. Турпак [1] ✉, А.С. Пашенко [1], А.В. Приходченко [1], Е.В. Тарасов [1],
Н.Н. Черноусов [1], М.А. Кузнецова [1], А.В. Давыденко [1]

[1] Дальневосточный федеральный университет, г. Владивосток, Россия
✉ turpak.aa@dvfu.ru

Аннотация. Исследованы магнитные свойства ультратонких пленок Pt/Gd/Pt, полученных методом магнетронного распыления. Толщина слоя Gd варьировалась от 1 до 15 нм. При комнатной температуре в образцах зафиксирован слабый магнитный момент насыщения, имеющий преимущественно интерфейсную природу. Измеренный интерфейсный магнитный момент составил 14,5 $мкЭргГс^{-1}см^{-2}$. Вклад в магнитный момент насыщения от объемных слоев Gd оказался пренебрежимо мал. Форма петель гистерезиса образцов не зависела от толщины слоя Gd. Кристаллизация в

гранецентрированную кубическую структуру наблюдается лишь при толщине Gd, равной 15 нм. Результаты проведенного исследования подчеркивают важность интерфейсного ферромагнетизма в системе Pt/Gd/Pt.

Ключевые слова: гадолиний, суперпарамагнетизм, многослойные пленки, намагниченность, магнитная восприимчивость, температура магнитного упорядочения, размерно-зависимые магнитные свойства

Финансирование: Высокоэффективное переключение намагниченности через спин орбитальный вращательный момент в магнитных наногетероструктурах для бесполевой SOT-MRAM памяти и устройств типа «вычисление в памяти», № 25-42-00083; Работа выполнена при поддержке Министерства науки и высшего образования Российской Федерации (Государственное задание №FZNS-2023-0012).

Ссылка при цитировании: Турпак А.А., Пашенко А.С., Приходченко А.В., Тарасов Е.В., Черноусов Н.Н., Кузнецова М.А., Давыденко А.В. Межфазный ферромагнетизм в напыленной системе Pt/Gd/Pt при комнатной температуре // Научно-технические ведомости СПбГПУ. Физико-математические науки. 2025. Т. 18. № 4.1. С. 55–61. DOI: https://doi.org/10.18721/JPM.184.109

Introduction

Gadolinium is a ferromagnetic material with a Curie temperature of 293.4 K in the bulk state [1]. In bulk samples and thick Gd films, a hexagonal close-packed (hcp) structure is formed. However, in ultrathin films, a face-centered cubic (fcc) phase is observed [2]. In films with a thickness of about 10 nm and an fcc structure, a Curie temperature above 300 K was recorded, and the saturation magnetization at 50 K reached approximately 100 $\mathrm{ergG^{-1}cm^{-3}}$.

Due to its unique magnetic properties, Gd is widely used in the creation of ferrimagnetic systems. For example, $\mathrm{Co}_x\mathrm{Gd}_{1-x}$ alloys exhibit ferrimagnetism [3]. The magnetic parameters of ferrimagnetic alloys, including the compensation temperature and saturation magnetization, can be precisely tuned by varying the alloy composition. In Pt/Co/Gd heterostructures, it has been established that the magnetic moments of ultrathin Gd layers deposited on Co are antiparallel to those of Co [4]. However, some studies, based on density functional theory calculations, have shown that in Pt/Co/Gd structures, only the magnetization of the two interfacial monolayers of Gd is oriented antiparallel to the magnetization in the Co layers, whereas the magnetization in the bulk Gd layers is aligned parallel to that in the Co layers [5].

In multilayer Pt/Co/Gd systems, the breaking of inversion symmetry along the film normal leads to the emergence of perpendicular magnetic anisotropy, spin–orbit torque [6], and the Dzyaloshinskii–Moriya interaction [7]. The presence of these effects in magnetic media is important for the development of information storage devices based on such media, for example, skyrmion-based memory [8]. To stabilize labyrinth and skyrmion magnetic configurations, superlattices of the form $[\mathrm{Pt/Co/Gd}]_n$ are employed [9]. It is believed that at room temperature the spontaneous magnetization in the Gd layers is caused by antiferromagnetic coupling with the magnetization of the Co layer, occurring at the Co/Gd interface.

In this work, the possibility of ferromagnetism arising solely from the Pt/Gd and Gd/Pt interfaces is investigated in a symmetric trilayer Pt/Gd/Pt system fabricated by magnetron sputtering. The aim of the study is to determine the crystal structure and magnetic properties of the Pt/Gd/Pt system while varying the thickness of the Gd layer.

Materials and Methods

The samples were fabricated by magnetron sputtering onto naturally oxidized silicon substrates $\mathrm{Si/SiO_2}$. Deposition was carried out in an Omicron vacuum chamber equipped with a substrate holder rotating at 40 revolutions per minute and four magnetron targets, ensuring uniform deposition of different materials without breaking the vacuum environment.

The thickness of the deposited layers was monitored using a quartz crystal thickness monitor with an accuracy of 0.1 nm. The sample structure was Pt (3 nm)/Gd (1–15 nm)/Pt (3 nm). For brevity, a sample with a Gd layer thickness of X nm will hereafter be denoted as Gd(X).

Deposition was carried out in an argon atmosphere at a base pressure of $P_0 = 1\times10^{-8}$ Torr and a working pressure of 1×10^{-3} to 5×10^{-3} Torr at a temperature of 300 K.

Magnetic properties and anisotropy were investigated using vibrating sample magnetometry (VSM) at room and low temperatures. The work presents magnetic hysteresis loops obtained with a SQUID magnetometer. The sample structure was studied by X-ray diffraction (XRD).

Results and Discussion

Analysis of the XRD spectra shown in Figure 1 indicates that a polycrystalline fcc Gd structure with (222) texture forms only in the Gd(15) sample, whereas thinner Gd films remain amorphous.

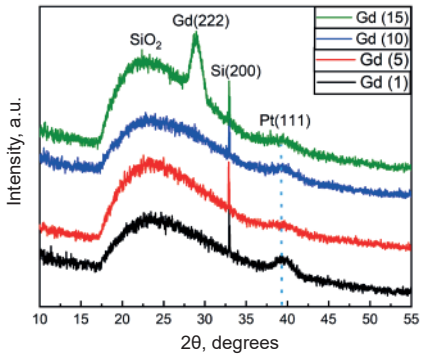

Fig. 1. XRD spectra of Pt/Gd/Pt samples with varying Gd layer thickness; formation of the fcc structure is observed only at a Gd thickness of 15 nm

The normalized magnetic hysteresis loops of the samples, measured at room temperature in magnetic fields oriented parallel (IP) and perpendicular (OOP) to the sample plane, are shown in Fig. 2, *a* and 2, *b*, respectively. The presented hysteresis loops were obtained after subtracting the linear signal from the nonmagnetic layers of the samples and the sample holder from the experimental loops.

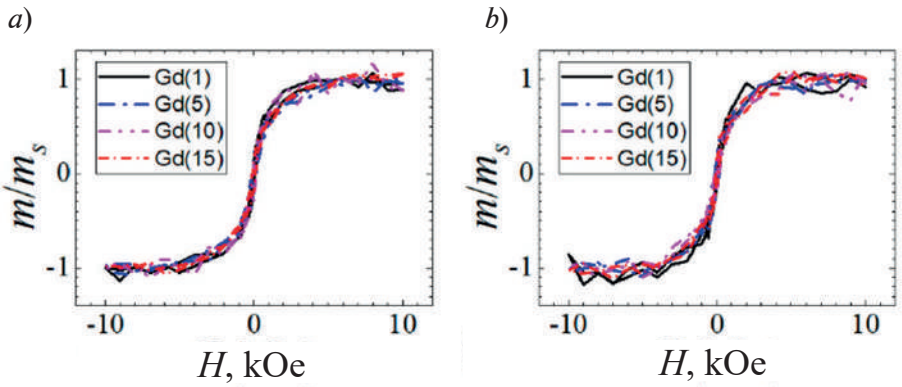

Fig. 2. Normalized magnetic hysteresis loops of the samples with the magnetic field oriented: in the film plane (IP) (*a*), perpendicular to the film plane (OOP) (*b*)

The hysteresis loops of all samples have a similar shape: they are isotropic and exhibit no hysteresis. Varying the Gd layer thickness from 1 to 15 nm does not affect the shape of the loops. Thus, it can be concluded that changes in the crystalline structure of Gd with increasing thickness do not significantly influence the magnetic properties of the system. The behavior of the samples resembles superparamagnetic systems composed of non-interacting magnetic nanoparticles or isolated magnetic crystalline grains with randomly oriented magnetic moments due to thermal fluctuations [10, 11, 12].

It is worth noting that hysteresis-free loops can be observed in Gd films at temperatures close to their Curie temperature [13]. The magnetic hysteresis loops of the samples measured by VSM were recorded at $T = 293$ K, which coincides with the Curie temperature of bulk Gd. However, in Gd films thinner than 5 nm, a reduction in the Curie temperature compared to bulk Gd is expected due to size effects [14, 15, 16]. In such a case, the hysteresis loop shape of the Gd(1) sample would significantly differ from those of samples with Gd thicknesses of 5 nm and above, which is not observed experimentally.

Fig. 3 shows the dependence of the saturation magnetic moment normalized to unit area on the Gd layer thickness. It is evident that the magnetic moment increases only slightly with increasing Gd thickness, indicating its interfacial origin. The dependence of the saturation magnetic moment, ms, on the thickness of the Gd magnetic layer, dGd, is described by the equation:

$$\frac{m_s}{S} = M_{s,\mathrm{V}} d_{\mathrm{Gd}} + \frac{m_{s,\mathrm{int.}}}{S}, \tag{1}$$

where $M_{s,\mathrm{V}}$ is the volumetric saturation magnetization of Gd, $m_{s,\mathrm{int.}}$ is the interfacial saturation magnetic moment of Gd, and S is the area of the magnetic film. Extrapolating the experimentally obtained graph to its intersection with the magnetic moment axis according to equation (1) yields the value of the interfacial magnetic moment normalized to unit area, $m_{s,\mathrm{int}}/S = 14.5$ μergG^{-1}cm^{-2}. Since approximately the same interfacial magnetic moment is observed in the Gd(1) sample with the smallest Gd thickness of 1 nm, it can be assumed that in all samples the interfacial saturation magnetic moment originates from Gd layers with a total thickness of about 1 nm. Then, the volumetric magnetization of these interfacial layers can be estimated as: $M_{s,\mathrm{int}} = m_{s,\mathrm{int}}/S/(1\ \mathrm{nm}) = 145$ ergG^{-1}cm^{-3}. The volumetric magnetization of the inner Gd layers in samples with Gd thickness greater than 1 nm, calculated according to equation (1) from the slope of the straight line shown in Fig. 3, is $M_{s,\mathrm{V}} = 3$ ergG^{-1}cm^{-3}.

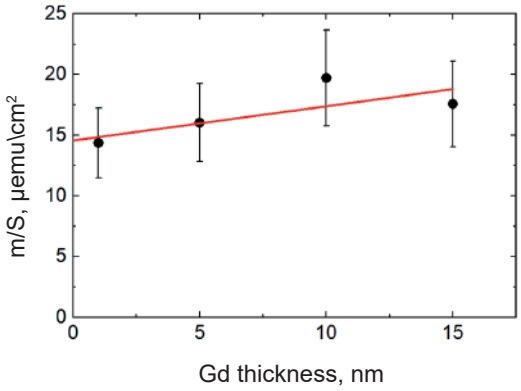

Fig. 3. Dependence of the saturation magnetic moment normalized to unit area on the thickness of the Gd layer; the solid line represents the linear approximation of the experimental data according to equation (1)

Temperature-dependent measurements of the saturation magnetic moment were performed for the series of samples (Fig. 4). The results show that the magnetic moment increases by only 10–20% compared to the value measured at room temperature when cooled down to 110 K. These findings support the conclusion that the absence of hysteresis and isotropy of the loops are not caused by the samples being close to their Curie temperature. Cooling the samples by 200 K below the Curie temperature would be expected to result in a significant increase in the saturation magnetic moment.

Interfacial superparamagnetism may be observed in Pt/Gd/Pt samples. Deposition by magnetron sputtering can sometimes cause intermixing of materials at the layer interfaces [17]. Further detailed investigation of the interface structure in this system is necessary. Nevertheless, assuming that the nonlinear magnetic signal arises from Gd magnetic clusters embedded in the Pt matrix, blocking of these nanoclusters can be expected at sufficiently low temperatures [10].

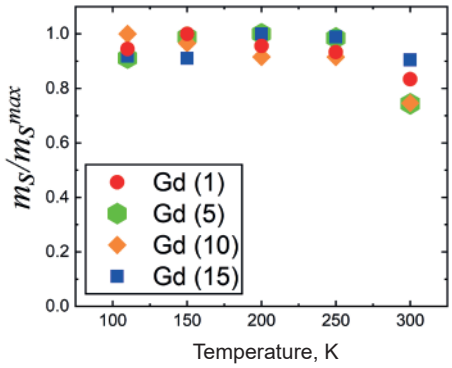

Fig. 4. Temperature dependence of the saturation magnetic moment (normalized to the maximum value in the temperature range) for samples with Gd layer thicknesses from 1 to 15 nm

Fig. 5 shows the magnetic hysteresis loops of the Gd(10) sample measured by SQUID magnetometry over the temperature range from 4 to 300 K. It can be seen that at 4 K the magnetization reversal occurs by a jump, while at other temperatures the reversal is gradual. Thus, the blocking temperature of this sample lies between 4 and 50 K. A more precise determination of the blocking temperature can be achieved by analyzing magnetization curves measured at different temperatures under different cooling conditions – with and without an applied magnetic field (FC – ZFC) [18].

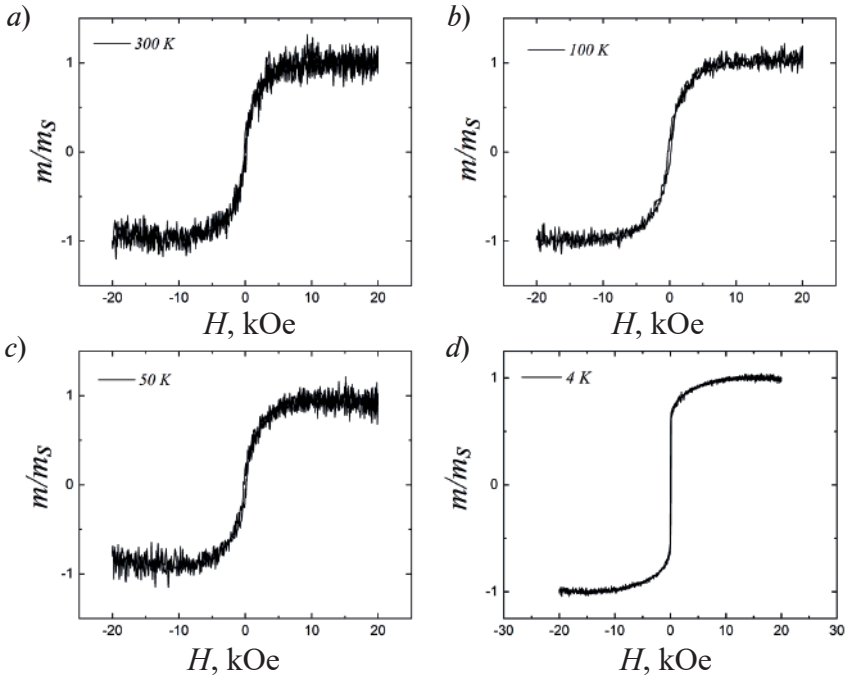

Fig. 5. Normalized magnetic hysteresis loops of the Gd(10) sample measured with the magnetic field oriented in the film plane at various temperatures: 300 K (*a*), 100 K (*b*), 50 K (*c*), 4 K (*d*)

In addition to the idea of interfacial superparamagnetism of Gd nanoclusters, the formation of a Pt-Gd alloy at the interfaces, exhibiting ferromagnetism at room temperature, can be considered to explain the observed results. However, no studies confirming this hypothesis have been found in the scientific literature. It is possible that the induced magnetization of Pt atoms due to the magnetic proximity effect plays some role in the observed ferromagnetism of the samples [19]. Notably, the magnetic proximity effect in Pt layers has been experimentally observed in systems where Pt layers form interfaces with alloys of transition and rare-earth metals. Moreover, the

direction of the induced magnetization in the Pt layers coincides with the magnetization direction in the transition metal layers, regardless of whether the magnetization of the sublattices of the transition or rare-earth metals predominates in the alloy [20]. Thus, the nature of the observed interfacial ferromagnetism in the Pt/Gd/Pt system remains unclear, and further studies are required to clarify it.

Conclusion

Isotropic superparamagnetic behavior independent of Gd layer thickness is observed in the symmetric trilayer Pt(3 nm)/Gd(1–15 nm)/Pt(3 nm) system. The saturation magnetization of the samples is predominantly due to interfacial effects, while the contribution from the bulk Gd layers is negligible. Films with Gd thicknesses below 10 nm remain amorphous, whereas a polycrystalline fcc phase forms at a Gd thickness of 15 nm. The interfacial magnetic moment value in the samples is 14.5 $\mu ergG^{-1}cm^{-2}$ at room temperature. The results demonstrate the possibility of realizing weak interfacial ferromagnetism of Gd adjacent to heavy metal Pt layers at room temperature.

Acknowledgments

The work of A.A. Turpak, N.N. Chernousov, and A.V. Davydenko was supported by the Russian Science Foundation, grant No. 25-42-00083, https://rscf.ru/project/25-42-00083/. A.S. Pashenko, E.V. Tarasov, A.V. Prikhodchenko, M.A. Kuznetsova acknowledge support within the framework of the state assignment of the Ministry of Science and Higher Education of the Russian Federation (project No. FZNS-2023-0012).

REFERENCES

1. **Scheunert G., Hendren W.R., Ward C., et al.,** Magnetization of 2.6 T in gadolinium thin films, Appl. Phys. Lett. 101 (2012) 142407.

2. **Bertelli P., Passamani C., Larica C., et al.,** Ferromagnetic properties of fcc Gd thin films, Appl. Phys. 117 (2015) 203904.

3. **Wang J., Li B., An Y., et al.,** Interplay between magnetization compensation temperature and thickness in ferrimagnetic CoGd alloy films, Appl. Phys. Lett. 126 (2025) 072401.

4. **Bläsing R., Ma T., Yang S.-H., et al.,** Exchange coupling torque in ferrimagnetic Co/Gd bilayer maximized near angular momentum compensation temperature, Nature Communications 9. (2018) 4984.

5. **Brandro J., Carvalho P., Miranda I., et al.,** Proximity-induced flipped spin state in synthetic ferrimagnetic Pt/Co/Gd heterolayers, Communications Physics. 8(22) (2025).

6. **Yu J., Qiu X., Wu Y., et al.,** Spin orbit torques and DzyaloshinskiiMoriya interaction in dual-interfaced Co-Ni multilayers, Scientific Reports. 6 (2016) 32629.

7. **Nembach H., Shaw J., Weiler M., et al.,** Linear relation between Heisenberg exchange and interfacial Dzyaloshinskii–Moriya interaction in metal films, Nat Phys. 11(10) (2015) 825–829.

8. **Fert A., Reyren N., Cros V.,** Magnetic skyrmions: advances in physics and potential applications, Nature Reviews Materials. 2 (2017) 17031.

9. **Nishimura T., Kim D.-Y., Kim D.-H., et al.,** Interfacial Dzyaloshinskii-Moriya interaction and dampinglike spin-orbit torque in [Co/Gd/Pt]n magnetic multilayers, Physical Review B. 103 (2021) 104409.

10. **Bean C., Livingston J.,** Superparamagnetism, J. Appl. Phys. 30 (1959) 120–129.

11. **Huang C-C., Liu T-Y., Su C-H., et all.,** Superparamagnetic Hollow and Paramagnetic Porous Gd_2O_3 Particles, Chem. Mater. 20 (2008) 3840–3848.

12. **Cao Y., Kumar P., Zhao Y., et al.,** High magnetization Co-GdOX superparamagnetic granular films as magnetic coating materials for high-sensitivity alternating magnetic force microscopy tip, Journal of Magnetism and Magnetic Materials. 462 (2018) 119–126.

13. **Binek C., Abbas Shah S.Q., Balasubramanian B.,** Thermodynamics and entropic inference of nanoscale magnetic structures in Gd, J. Phys.: Condens. Matter. 37 (2025) 065705.

14. **Svalov A., Vas'kovskiy V., Barandiarõn J., et al.,** Structure and Magnetic Properties of Gd/Ti Nanoscale Multilayers, Solid State Phenomena. (168-169) (2010) 281–284.

15. **Farle M., Baberschke K., Stetter U.,** Thickness-dependent Curie temperature of Gd(0001)/W(110) and its dependence on the growth conditions, Physical Review. B 47(17) (1993) 11571.

16. **Springell R., Zochowski S., Ward R., et al.,** A study of uranium-based multilayers: II. Magnetic properties, J. Phys.: Condens. Matter. 22 (2008) 215230.

17. **Pershyn Y., Gullikson E., Kondratenko V., et al.,** Effect of working gas pressure on interlayer mixing in magnetron-deposited Mo/Si multilayers, Optical Engineering. 52 (9) (2013) 095104.

18. **Ncube S., Coleman C., Flahaut E., et al.,** Observation of a superparamagnetic breakdown in gadolinium chloride filled double-walled carbon nanotubes, AIP Advances. 11 (2021) 035206.

19. **Lim W., Ebrahim-Zadeh N., Owens J., et al.,** Temperature-dependent proximity magnetism in Pt, Applied Physics Letters. 102 (16) (2013) 162404.

20. **Swindells C., Nicholson B., Inyang O., et al.,** Proximity-induced magnetism in Pt layered with rare-earth–transition-metal ferrimagnetic alloys, Phys. Rev. Res. 2 (2020) 033280.

THE AUTHORS

TURPAK Aleksandr A.
turpak.aa@dvfu.ru
ORCID: 0009-0002-3519-4418

CHERNOUSOV Nikolay N.
chernousov.nn@dvfu.ru
ORCID: 0000-0001-6214-9642

PASHENKO Aleksandr S.
pashenko.ase@dvfu.ru
ORCID: 0009-0009-4554-3053

KUZNETSOVA Maria A.
kuznetcova.mal@dvfu.ru
ORCID: 0000-0002-0070-2817

PRIKHODCHENKO Alena V.
prikhodchenko.av@dvfu.ru
ORCID: 0009-0006-2778-8143

DAVYDENKO Aleksandr V.
davydenko.av@dvfu.ru
ORCID: 0000-0002-2697-8563

TARASOV Egor V.
tarasov.ev@dvfu.ru
ORCID: 0000-0002-0372-4552

Received 20.09.2025. Approved after reviewing 19.11.2025. Accepted 19.11.2025.

Conference materials
UDC 538.975
DOI: https://doi.org/10.18721/JPM.184.110

MBE growth of GaAs nanowires with a silicon rich particle on the top

N.V. Sibirev [1], I.V. Ilkiv [2], E.V. Ubyivovk [1], I.P. Soshnikov [3],
I.V. Shtrom [1] ✉, R.R. Reznik [1], V.V. Brukhanova [1], G.E. Cirlin [2]

[1] St. Petersburg State University, St. Petersburg, Russia;
[2] Alferov University, St. Petersburg, Russia;
[3] Ioffe Institute, St. Petersburg, Russia
✉ igorstrohm@mail.ru

Abstract. The paper discusses the low-temperature growth of gallium arsenide (GaAs) nanowires on a silicon substrate initiated by a thin layer of lead. Typically, the growth of III-V semiconductor nanowires occurs via a vapor-liquid-solid mechanism with a droplet at the tip of the nanowire. The particles on the nanowire's tip act as physical catalysts, reducing the nucleation barrier. In case of GaAs nanowire, the droplet at the tip typically consists of Ga and a foreign catalyst. However, at a low growth temperature of 350 °C, a different situation was observed. The particle at the nanowire tip was found to contain a high concentration of arsenic. This suggests that the mechanism of nanowire formation is different from the classic vapor-liquid-solid process. The particle at the tip turned out to be a mixture of silicon and arsenic, rather than lead and gallium, indicating that the growth process followed a vapor-solid-solid mechanism.

Keywords: nanowires, lead initiated growth, silicon catalyzed growth, Vapor-Solid-Solid mechanism, molecular beam epitaxy

Funding: This work was performed with financial support from St. Petersburg State University under grant No. 129360164. Research on morphological properties using a scanning electron microscope was conducted with support from RSF grant No. 25-79-10101.

Citation: Sibirev N.V., Ilkiv I.V., Ubyivovk E.V., Soshnikov I.P., Shtrom I.V., Reznik R.R., Brukhanova V.V., Cirlin G.E., MBE growth of GaAs nanowires with a silicon rich particle on the top, St. Petersburg State Polytechnical University Journal. Physics and Mathematics. 18 (4.1) (2025) 62–66. DOI: https://doi.org/10.18721/JPM.184.110

Материалы конференции
УДК 538.975
DOI: https://doi.org/10.18721/JPM.184.110

Рост нитевидных нанокристаллов GaAs с частицей, богатой кремнием на вершине

Н.В. Сибирев [1], И.В. Илькив [2], Е.В. Убыйвовк [1], И.П. Сошников [3],
И.В. Штром [1] ✉, Р.Р. Резник [1], В.В. Брюханова [1], Г.Э. Цырлин [2]

[1] Санкт-Петербургский государственный университет, Санкт-Петербург, Россия;
[2] Академический университет им. Ж.И. Алфёрова РАН, Санкт-Петербург, Россия;
[3] Физико-технический институт им. А.Ф. Иоффе РАН, Санкт-Петербург, Россия
✉ igorstrohm@mail.ru

Аннотация. В работе обсуждается низкотемпературный рост нитевидных нанокристаллов арсенида галлия на кремнии с использованием свинца. Обычно формирование A3B5

нитевидных нанокристаллов происходит по механизму пар-жидкость-кристалл. Их рост проводят с использованием катализатора, хорошо растворяющего только элемент III группы. В данной работе в качестве инициатора роста использовался свинец, который так же хорошо растворяет элемент V группы – мышьяк. Оказалось, что при низкой температуре роста 350 °C, механизм формирования нитевидных нанокристаллов сильно отличается от классического. Частица-катализатор на вершине оказалась не свинцовым, а кремниевым арсенидом. Это позволяет утверждать, что рост нитевидных нанокристаллов проходил по механизму пар-кристалл-кристалл.

Ключевые слова: нитевидных нанокристаллы, инициируемый свинцом рост, рост с кремниевым катализатором, механизм пар-кристалл-кристалл, молекулярно-пучковая эпитаксия

Финансирование: Работа выполнена при финансовой поддержке Санкт-Петербургского государственного университета в рамках гранта № 129360164. Исследования морфологических свойств с использованием сканирующего электронного микроскопа проведены при поддержке гранта РНФ № 25-79-10101.

Ссылка при цитировании: Сибирев Н.В., Илькив И.В., Убыйвовк Е.В., Сошников И.П., Штром И.В., Резник Р.Р., Брюханова В.В., Цырлин Г.Э., Рост нитевидных нанокристаллов GaAs с частицей, богатой кремнием на вершине // Научно-технические ведомости СПбГПУ. Физико-математические науки. 2025. Т. 18. № 4.1. С. 62–66. DOI: https://doi.org/10.18721/JPM.184.110

Introduction

The growth of arsenides and phosphides nanowires (NWs) by the Vapor-Liquid-Solid (VLS) mechanism almost always occurs using a catalyst that dissolves group III element well [1], but poorly dissolves group V element. The most commonly growers use precious metals such as gold [1, 2], rarely silver [1] or copper [3], or group III elements (gallium, indium) [1, 2]. These materials dissolve the element of the third group well, but arsenic or phosphorus poorly, which complicates the possibility of obtaining *n*-type doping of NWs [2, 4]. Another disadvantage is the blurring of the heterojunction in InGaAs/GaAs or AlGaAs/AlAs [3–5].

These problems already have some technological solutions. However, it is proposed to consider an alternative solution for the growth of A3B5 NWs with a drop rich in element group V (nitrogen group), rather than metal. Only two such catalysts are mentioned in the literature: tin [6, 7] and lead [5]. NWs already grown with such catalyst, but tin is quite easily integrated into arsenides and phosphides. Even more in paper [6] shown that droplet composition is Sn-As.

In this paper, the growth of GaAs NWs with a lead (Pb) catalyst is discussed. Pb dissolves both Ga [8] and As [9] as well. Ga and Pb are immiscible liquids and easily separate into two distinct layers [8]. Pb with As forms an eutectic system [9].

Materials and Methods

Growth experiments were carried out in a Riber Compact 12 MBE system, equipped with effusion sources of gallium and arsenic. The growth of GaAs NWs proceeds on Si(111) substrates with a pre-deposited layer of lead. In more details growth method is described here [5].

In order to remove the defective oxide layer, the substrates were previously treated in a weak hydrofluoric acid solution. The deposition of a 10 nm thick lead film was carried out by electron beam evaporation on an Auto500 (Boc Edwards) system with oil-free pumping at a residual vacuum of at least 5×10^{-6} Torr and a sample table temperature of about 80 °C. The thickness of the deposited layer was controlled by an optical meter and fixed to 5 nm. The purity of lead was at least 99.99%.

After that, the substrates were transferred to a growth chamber. The substrate was heated to a rising temperature of 350 °C. Lead dissolves quite easily in silicon, so we avoided long annealing to prevent lead droplets from dissolving in the substrate. After stabilization of the substrate

temperature, the gallium and arsenic deposition started and NWs growth began. The gallium flux during NW synthesis corresponded to the growth rate of the GaAs planar layer is 0.7 ML/sec. The flow of arsenic was ten times greater than the flow of gallium. The growth time was 10 minutes.

The morphology of the surface of the samples was studied using a Supra 25 scanning electron microscope (SEM) (C.Zeiss) equipped with the Ultim microanalysis console (Oxford Instruments inc.). Studies of the structural properties and composition of synthesized the NWs were performed using transmission electron methods (TEM) on a Zeiss Libra 200FE microscope equipped with an X-Max energy dispersive X-ray detector.

Results and discussion

The results of morphology studies did not bring any surprises, most of the NWs were needle-shaped, and some still had droplets on them, see Figure 1.

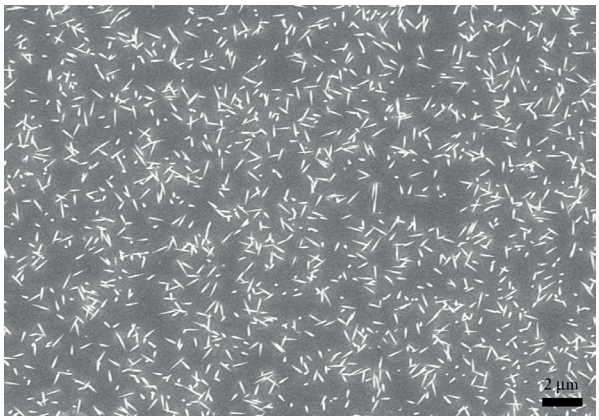

Fig.1. SEM image of GaAs NWs

It is natural to explain the NW shape by the gradual dissolution of lead in the NW body, as well as the superiority of arsenic flux over gallium. The length of the NW was approximately 1.5 microns, which corresponds well with usual idea of a 10-fold increase in the NW growth rate. The base radius is about 70 nm.

The study of the NW composition gives unexpected results. The lead level turned out to be extremely low and practically did not differ from the error of the energy dispersion detector (EDX). Only near the NW tips signal was greater than 2%. At the same time, the silicon content was significantly higher than that of lead. These data for five different NWs are shown in Figure 2.

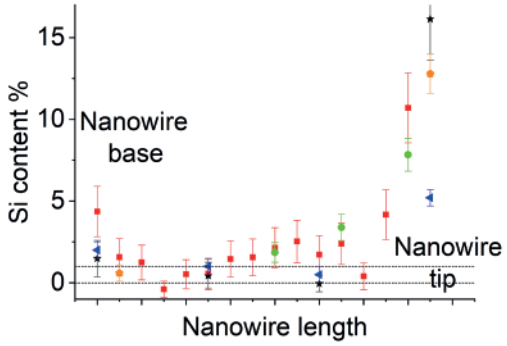

Fig. 2. The results of measuring the Si content along NW length. Different symbols (squares, stars, circles, triangles and pentagons) correspond to different NWs

The TEM image of the NW tip showed an elementary contrast. Several layers at the NW tips clearly differed in composition, see Figure 3. EDX clearly indicated that the particle on the nanowire tip contains a lot of silicon.

The solubility of silicon in lead at this growth temperature does not exceed 1%, that is, it cannot be silicon that got into the droplet at the initial stage. Autocatalytic growth of GaAs NWs at such a temperature is usually not observed, and the solubility of silicon in gallium is also not high, less than 1% [4, 10]. This means that during the growth of the NW, silicon was constantly coming from the substrate. Silicon was etched with lead from the wafer. The mechanism of Si etching is similar to the formation of black silicon (*b*-Si) via metal-assisted chemical etching [11]. Pb acted as a catalyst to etch the Si substrate surface. However, there is a difference between our process and the formation of *b*-Si. In our method, active Si atoms diffuse to the NW, whereas in the formation of *b*-Si, atoms are removed through gas or liquid flow.

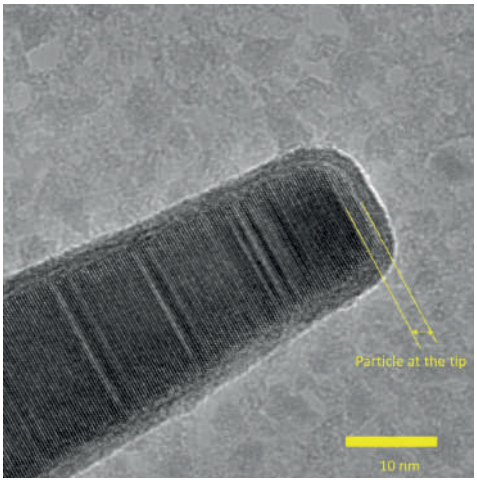

Fig. 3. TEM image of NW tip

No Pb was found at the top, but Si and As clearly observed. Most probably it means that particle on the tip is one of the polytypes of SiAs. The crystal structure of SiAs has really similar to GaAs(111)B facets [12]. Arsenic atoms form an elongated octahedron around a pair of silicon atoms. The distance between neighboring atoms varies in range 3.7–4.7Å. In the most stable configuration, the direction of the elongated axis alternates through three layers, in our case it's not necessary. The As octahedra can be rotated so that the lattice mismatch between the GaAs(111)B and SiAs facet is less than 2%.

Conclusion

The paper discusses the unusual growth of GaAs gallium arsenide NWs initiated by lead. The growth was carried out by the MBE method in a highly nonequilibrium regime on a Si substrate. High supersaturation was achieved by a low substrate temperature of 350 °C. At this temperature, the solubility of Si in Ga-Pb mixtures, or Pb-As solution is less than 1%. An unexpected formation of SiAs solid particle on the NW tip was observed. The NW growth rate with solid particle on the tip was of the same order as for convenient Vapor-Liquid-Solid method.

Acknowledgments

The work was carried out with the financial support of St. Petersburg State University grant No. 129360164. The study of morphological properties using scanning electron microscopy was carried out with the financial support of RSCF grant No. 25-79-10101. Studies of the elemental composition were carried out at the MRC in the direction of "Nanotechnology" at the St. Petersburg State University Science Park.

REFERENCES

1. **Nebol'sin V.A., Swaikat N.,** About Some Fundamental Aspects of the Growth Mechanism Vapor-Liquid-Solid Nanowires, Journal of Nanotechnology. 2023 (2023) 7906045.

2. **Dubrovskii V.G., Hijazi H., Goktas N.I., LaPierre R.R.,** Be Te, and Si Doping of GaAs Nanowires: Theory and Experiment, Journal of Physical Chemistry C. 124 (2020) 17299–17307.

3. **Leshchenko E.D., Sibirev N.V.,** Recent Advances in the Growth and Compositional Modelling of III–V Nanowire Heterostructures, Nanomaterials. 14 (2024)1816.

4. **Kim W., Güniat L., Fontcuberta I Morral A., Piazza V.,** Doping challenges and pathways to industrial scalability of III-V nanowire arrays, Appl Phys Rev. 8 (2021) 011304.

5. **Shtrom I.V., Sibirev N.V., Soshnikov I.P., Ilkiv I.V., Ubyivovk E.V., Reznik R.R., Cirlin G.E.,** Lead Catalyzed GaAs Nanowires Grown by Molecular Beam Epitaxy, Nanomaterials. 14 (2024) 1860.

6. **Sun R., Vainorius N., Jacobsson D., Pistol M.E., Lehmann S., Dick K.A.,** Sn-seeded GaAs nanowires grown by MOVPE, Nanotechnology. 27 (2016) 215603.

7. **Karlina L.B., Vlasov A.S. Smirnova I. P., Soshnikov I.P.,** Sn-Assisted Growth of Ga(In)AsP Nanowires from Vapor Phase in a Quasi-Closed Volume, Journal of Physics: Conference Series 1697 (1) (2020) 012109.

8. **Plevachuk Y., Filippov V., Kononenko V., Popel P., Rjabina A., Sidorov V., Sklyarchuk V.,** Investigation of the miscibility gap region in liquid Ga-Pb alloys, Zeitschrift fuer Met Res Adv Tech. 94 (2003) 1034–1039.

9. **Shishin D., Chen J., Hidayat T., Jak E.,** Thermodynamic Modeling of the Pb-As and Cu-Pb-As Systems Supported by Experimental Study, Journal of Phase Equilibria Diffus. 40 (2019) 758–767.

10. **Seema R., Shekhar C.,** Thermodynamic modelling of Ga-Si nano phase diagram including shape effect, Journal of Nanoparticle Research. 27 (47) (2025).

11. **Arafat M.Y., Islam M.A., Mahmood A.W. Bin, Abdullah F., Nur-E-Alam M., Kiong T.S., Amin N.,** Fabrication of black silicon via metal-assisted chemical Etching – a review, Sustain. 13 (2021) 1–18.

12. **Wadsten T.,** The Crystal Structure of SiAs, Acta Chemica Scandinavica 19 (1965) 1232.

THE AUTHORS

SIBIREV Nickolay V.
n.sibirev@mail.spbu.ru
ORCID: 0000-0002-7566-2522

ILKIV Igor V.
fiskerr@ymail.com
ORCID: 0000-0001-8968-3626

UBYIVOVK Evgenii V.
e.ubyivovk@mail.spbu.ru

SOSHNIKOV Iliya P.
ipsosh@beam.ioffe.ru

SHTROM Igor V.
igorstrohm@mail.ru

REZNIK Rodion R.
moment92@mail.ru
ORCID: 0000-0003-1420-7515

BRUKHANOVA Vera V.
brukhanova@mail.spbu.ru

CIRLIN George E.
george.cirlin@mail.ru

Received 20.09.2025. Approved after reviewing 05.12.2025. Accepted 05.12.2025.

Conference materials
UDC 537.9
DOI: https://doi.org/10.18721/JPM.184.111

Magnetic structure of bilayer systems of thin films Pt/Co/(CoO)

M.A. Kuznetsova [1] ✉, A.A. Turpak [1], A.G. Kozlov [1], A.V. Prikhodchenko [1]

[1] Far Eastern Federal University, Vladivostok, Russia

✉ kuznetcova.mal@dvfu.ru

Abstract. Effect of oxidation ferromagnet Co layer on magnetic parameters of thin polycrystalline bilayers Pt/Co/(CoO)/Pt films have been studied. Films was obtained by magnetron sputtering. It is established that the oxidation of the cobalt layer leads to an increase in perpendicular magnetic anisotropy (PMA) in comparison with non-oxidized system also the order of oxidation layer is important. Heat treatment causes a decrease in PMA and an increase in magnetization, which is explained by interlayer diffusion and the formation of a Pt-Co alloy. Structural XRR-analysis showed that oxidation increases the thickness of the Co/CoO layer and reduces the roughness of the adjacent layers. The dependence of the coercive force and anisotropy on the oxidation sequence of the layers is found, which indicates the importance of the structural organization for controlling magnetic properties. The results demonstrate the promise of controlled oxidation in PMA tuning and exchange interaction in Pt/Co systems, which can be used in spintronic devices, including skyrmion memory and elements controlled by spin orbital momentum.

Keywords: perpendicular magnetic anisotropy, Pt/Co multilayer structures, cobalt oxidation, spin-orbit interaction, X-ray reflectometry, domain structure

Funding: Kuznetsova M.A., Prikhodchenko A.V., Turpak A.A. thank the Ministry of Science and Higher Education of the Russian Federation within the project No. FZNS-2023-0012, Kozlov A.G. thanks the Russian Science Foundation for support within the research Project No. 24-72-00162.

Citation: Kuznetsova M.A., Turpak A.A., Kozlov A.G., Prikhodchenko A.V., Magnetic structure of bilayer systems of thin films Pt/Co/(CoO). St. Petersburg State Polytechnical University Journal. Physics and Mathematics. 18 (4.1) (2025) 67–72. DOI: https://doi.org/10.18721/JPM.184.111

Материалы конференции
УДК 537.9
DOI: https://doi.org/10.18721/JPM.184.111

Магнитная структура двуслойных систем тонких пленок Pt/Co/(CoO)

М.А. Кузнецова [1] ✉, А.А. Турпак [1], А.Г. Козлов [1], А.В. Приходченко [1]

[1] Дальневосточный федеральный университет, г. Владивосток, Россия

✉ kuznetcova.mal@dvfu.ru

Аннотация. Исследовано влияние окисления слоя ферромагнетика Co на магнитные параметры тонких поликристаллических двуслойных пленок Pt/Co/(CoO)/Pt. Образцы были получены методом магнетронного распыления. Установлено, что окисление слоя кобальта приводит к увеличению перпендикулярной магнитной анизотропии (ПМА) по сравнению с неокисленной системой, а также что порядок окисленного слоя существенно влияет на магнитные характеристики. Нагрев такой системы приводит к уменьшению

ПМА и увеличению намагниченности, что объясняется интерфейсной диффузией и образованием сплава Pt-Co. Рентгенографический анализ показал, что окисление увеличивает толщину слоя Co/CoO и уменьшает шероховатость соседних слоев. Обнаружена зависимость коэрцитивной силы и анизотропии от последовательности окисления слоев, что указывает на важность структурной организации для управления магнитными свойствами. Результаты демонстрируют перспективность контролируемого окисления при настройке ПМА и обменного взаимодействия в системах Pt/Co, которые могут быть использованы в устройствах спинтроники, включая скирмионную память и элементы, управляемые спин-орбитальным моментом.

Ключевые слова: перпендикулярная магнитная анизотропия, многослойные пленки, оксидирование кобальта, спин-орбитальное взаимодействие, рентгеновская рефлектометрия, доменная структура

Финансирование: Государственное задание №FZNS-2023-0012, РНФ №24-72-00162.

Ссылка при цитировании: Кузнецова М.А., Турпак А.А., Козлов А.Г., Приходченко А.В. Магнитная структура двуслойных систем тонких пленок Pt/Co/(CoO) // Научно-технические ведомости СПбГПУ. Физико-математические науки. 2025. Т. 18. № 4.1. С. 67–72. DOI: https://doi.org/10.18721/JPM.184.111

Introduction

Pt/Co and Pt/Co/MOx thin films (where M is an oxidizable metal such as Gd [1], Al [2], or Ni [3], etc.) have attracted considerable attention in spintronics research due to their unique interfacial magnetic properties. These systems exhibit perpendicular magnetic anisotropy (PMA) [4], efficient spin-orbit torque (SOT) generation via the spin Hall effect [5], and a pronounced Dzyaloshinskii-Moriya interaction (DMI) [6], all of which are crucial for next-generation magnetic devices.

The origin of PMA in Pt/Co interfaces stems from the hybridization of Pt's 5d electrons (which possess strong spin-orbit coupling) with the 3d electrons of the ferromagnetic Co layer [7]. This interaction leads to preferential out-of-plane magnetization, a key requirement for high-density spintronic applications. Further enhancement of PMA and DMI can be achieved through controlled oxidation of the ferromagnetic layer, as evidenced by studies on Pd/Co/CoO systems [8–9]. Additionally, oxidation can introduce exchange bias effects at low temperatures [10], which may be exploited for stabilizing magnetic configurations in device architectures.

While the Pt/Co/CoO presents a promising platform for investigating interfacial magnetic phenomena. The potential to tune PMA, DMI, and exchange coupling in this system makes it a candidate for advanced spintronic applications, including skyrmion-based racetrack memory [11], ultra-sensitive magnetic sensors [12] and other emerging spintronic devices that rely on precise control of magnetic interactions at metal/oxide interfaces.

Materials and Methods

The samples were prepared using magnetron sputtering under high vacuum conditions, with the SiO_2 substrate rotating at a speed of 40 rpm. The layer structure consisted of an initial 5 nm Pt layer, followed by a 1 nm Co layer, a 2 nm intermediate Pt layer, and a 3 nm Pt capping layer. The Co layer was oxidized in the magnetron load chamber under a constant pressure of $P = 1\times10^{-3}$ Torr for two minutes. As a result, 6 samples were obtained (two single-layer and four bilayer films, thicknesses are given in brackets in nanometers, molar volume ratio CoO/Co $k \approx 1.74$):

1. SiO_2/Pt(5)/Co(1)/Pt(3)
2. SiO_2/Pt(5)/Co(1–x)/CoO($k\times x$)/Pt(3)
3. SiO_2/Pt(5)/Co(1)/Pt(2)/Co(1)/Pt(3)
4. SiO_2/Pt(5)/Co(1–x)/CoO($k\times x$)/Pt(2)/Co(1)/Pt(3)

5. SiO_2/Pt(5)/Co(1)/Pt(2)/Co(1–x)/CoO(k×x)/Pt(3)
6. SiO_2/Pt(5)/Co(1–x)/CoO(k×x)/Pt(2)/ Co(1–x)/CoO(k×x)/Pt(3)

The films were heated in a vacuum oven under working pressure $P = 2\times10^{-3}$ Torr for 10 minutes at $T = 300$ °C.

The magnetic properties (magnetic moment, anisotropy field, coercive force) were determined by analyzing hysteresis loops measured using a vibrating sample magnetometer (VSM by LakeShore). Additionally, domain wall motion dynamics were studied using Kerr microscopy (EvicoMagnetics), and layer roughness was evaluated based on X-ray reflectometry (XRR) spectra.

Results and Discussion

All samples exhibited perpendicular magnetic anisotropy (PMA), as confirmed by the hysteresis loops in Fig. 1, *a*. The strength of the anisotropy was found to scale with the number of oxidized layers, suggesting that interfacial oxidation plays a crucial role in enhancing PMA, likely due to increased interfacial spin-orbit coupling and structural modifications at the Co/CoO interface.

After heating (Fig. 1, *b*, red dots), a noticeable reduction in PMA was observed, accompanied by a significant increase in magnetization. This behavior can be attributed to interfacial diffusion and structural relaxation. Heating likely promotes intermixing at the Pt/Co interface, leading to the formation of a Pt-Co alloy, which alters magnetic interactions. The displacement of the CoO layer and possible reduction of oxygen vacancies may weaken the anisotropy while enhancing magnetization due to improved ferromagnetic ordering.

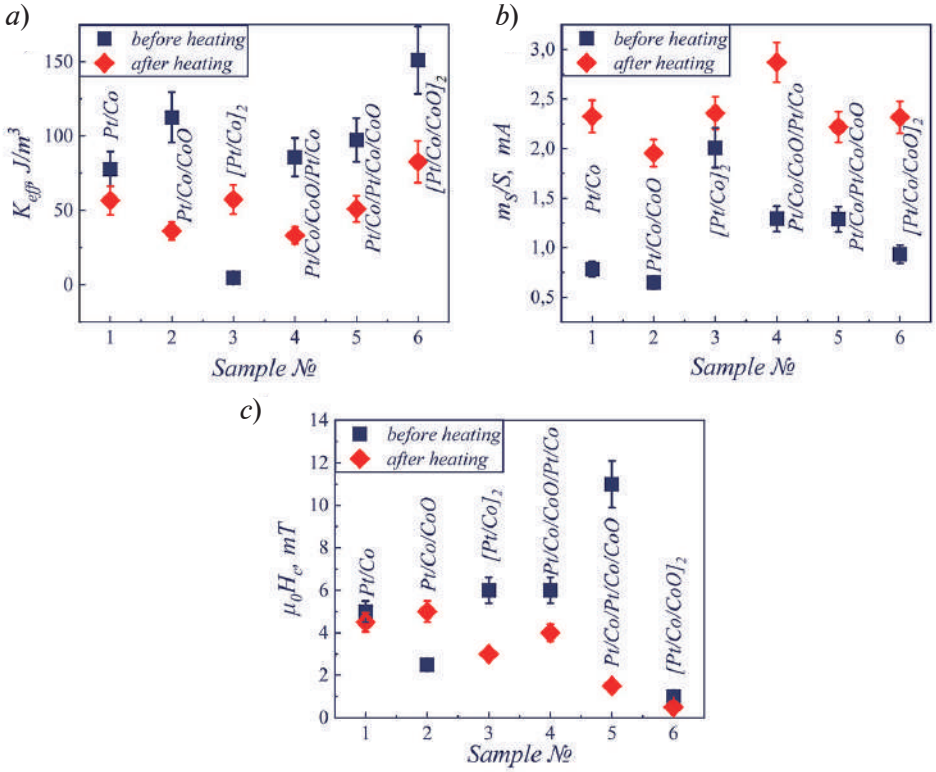

Fig. 1. Magnetic parameters of samples after and before heating (*a*) anisotropy field, (*b*) saturation magnetization per area, (*c*) coercive force

The magnetic properties of the samples varied not only with the number of oxidized layers but also with the sequence of oxidation (whether the first or second Co layer was oxidized). This dependence implies that the stacking order of oxidized and non-oxidized layers influences interfacial spin interactions and strain distribution. Such variations may arise from differences in:

· Crystal structure distortion: oxidation modifies the local coordination of Co atoms, affecting magnetocrystalline anisotropy.

· Interfacial roughness and strain as seen in Fig. 2, *a*, the order of oxidation impacts the structural morphology, which in turn alters magnetic coupling.

The coercivity of the samples was also sensitive to oxidation conditions (Fig. 1, *c*), likely due to the redistribution of defects that act as pinning sites for domain walls. An increase in defect density typically leads to higher coercivity, whereas annealing may reduce it by promoting defect annihilation or recrystallization.

Structural characterization (Fig. 2, *b*) revealed that oxidation leads to an expansion of the Co/(CoO) layer beyond its initial nominal thickness (1 nm), consistent with the incorporation of oxygen and the formation of a graded interface. Additionally, Fig. 2, *c* demonstrates that the presence of the oxide layer reduces the roughness of the adjacent Pt layer, suggesting that oxidation induces interfacial smoothing, possibly due to stress relaxation or atomic rearrangement.

The magnetic domain structure, imaged by Kerr microscopy (Fig. 3), displayed small, irregular domains with jagged walls, indicative of strong pinning effects.

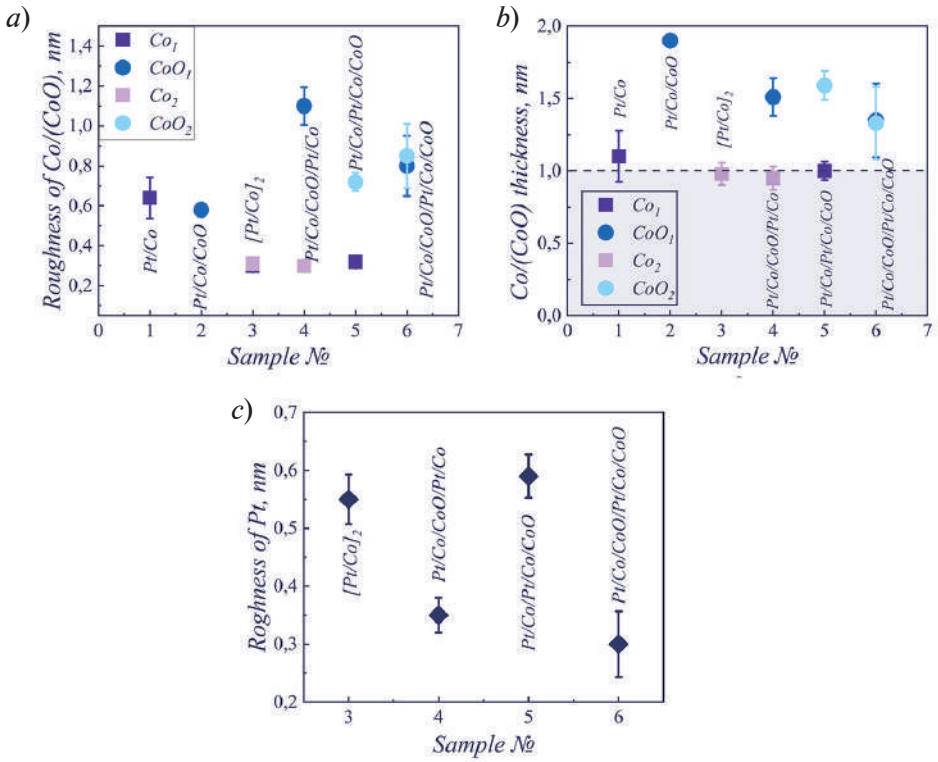

Fig. 2. XRR-measurements (*a*) roughness of Co/(CoO) layers, (*b*) thickness of Co/(CoO) layers, (*c*) roughness of Pt-interlayer in bilayers systems

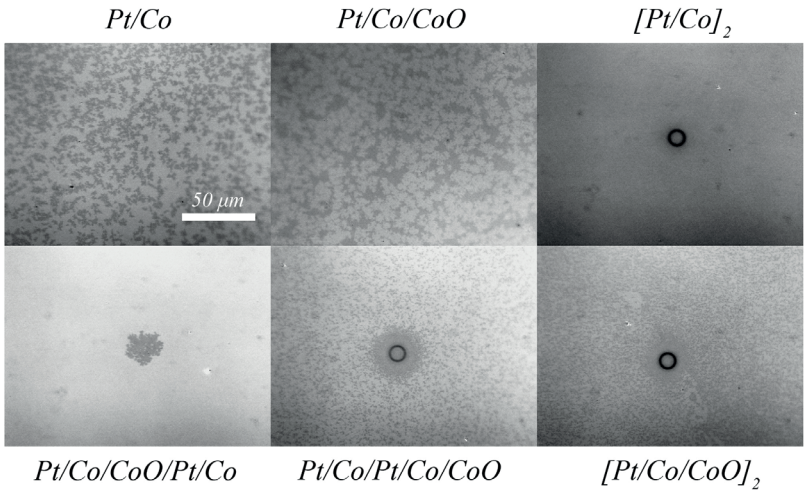

Fig. 3. Kerr-images of domain structure after the 0.2 ms pulse of perpendicular field $Hz = 10.8$ mT

Conclusion

The study of polycrystalline Pt/Co/(CoO)/Pt films, fabricated by magnetron sputtering, reveals a strong dependence of their magnetic properties on the structural organization of the layers. A critical finding is that the presence and order of oxidation in the CoO layer play a decisive role in modulating the interfacial magnetic interactions. These films exhibit pronounced perpendicular magnetic anisotropy (PMA), with the anisotropy field (Ha) increasing systematically as the number of oxidized layers grows, suggesting that controlled oxidation enhances spin-orbit coupling effects at the Pt/CoO interface.

Interestingly, while oxidation strengthens PMA, it also introduces competing effects: a reduction in magnetic anisotropy is observed alongside an increase in the film's net magnetic moment. This behavior is attributed to two interrelated factors – the displacement of the oxide layer, which alters interfacial hybridization, and the release of bulk metallic Co, which contributes to a stronger ferromagnetic response but reduces anisotropy contributions from the interface. Structural characterization via X-ray reflectometry (XRR) further supports these observations, confirming that the CoO layer thickness exceeds that of the metallic Co, indicating deep oxidation penetration and possible interfacial diffusion.

These findings highlight the delicate balance between oxidation depth, interfacial structure, and magnetic performance in Pt/Co-based multilayers. The ability to tailor PMA through controlled oxidation makes this system promising for advanced spintronic applications, including skyrmion-based memory and spin-orbit torque devices.

Acknowledgments

Kuznetsova M.A., Prikhodchenko A.V., Turpak A.A. thank the Ministry of Science and Higher Education of the Russian Federation within the project No. FZNS-2023-0012, Kozlov A.G. thanks the Russian Science Foundation for support within the research Project No. 24-72-00162.

REFERENCES

1. **Li M., et al.,** Magnetic properties and microstructural analyses of Pt/Co/Gd_2O_3 films, Vacuum. 205 (2022) 111410.

2. **Schott M., et al.,** Electric field control of interfacial Dzyaloshinskii-Moriya interaction in Pt/Co/AlO_x thin films, Journal of Magnetism and Magnetic Materials. 520 (2021) 167122.

3. **Lin K.W., et al.,** In-plane and perpendicular exchange bias in [Pt/Co]/NiO multilayers, physica status solidi (a). 204 (12) (2007) 3970–3974.

4. **Kisielewski M., et al.,** Magnetic anisotropy and magnetization reversal processes in Pt/Co/Pt films, Journal of magnetism and magnetic materials. 260 (1–2) (2003) 231–243.

5. **Chen S., et al.,** Temperature dependence of spin–orbit torques in Pt/Co/Pt multilayers, Journal of Physics D: Applied Physics. 51 (9) (2018) 095001.

6. **Wells A.W.J., et al.,** Effect of interfacial intermixing on the Dzyaloshinskii-Moriya interaction in Pt/Co/Pt, Physical review B. 95 (5) (2017) 054428.

7. **Yang H., et al.,** Anatomy of Dzyaloshinskii-Moriya Interaction at Co/Pt Interfaces, Physical review letters. 115 (26) (2015) 267210.

8. **Kozlov A.G., et al.,** Effects of Interfacial Nanoengineering through an Artificial Oxidation of Epitaxial Pd/Co Ultrathin Films on Perpendicular Magnetic Anisotropy and the Dzyaloshinskii–Moriya Interaction, ACS Applied Electronic Materials. 6 (7) (2024) 4928–4938.

9. **Kozlov A.G., et al.,** Magnetic Properties of Epitaxial $[Pd/Co/CoO]_n$ Superlattices, Journal of Magnetics. 29 (1) (2024) 143–148.

10. **Anyfantis D.I., et al.,** Magnetic anisotropies and exchange bias of Co/CoO multilayers with intermediate ultrathin Pt layers, Materials. 16 (4) (2023) 1378.

11. **Parkin S., Yang S.H.,** Memory on the racetrack, Nature nanotechnology. 10 (3) (2015) 195–198.

12. **Lenz J., Edelstein S.,** Magnetic sensors and their applications, IEEE Sensors journal. 6 (3) (2006) 631–649.

THE AUTHORS

KUZNETSOVA Maria A.
kuznetcova.mal@dvfu.ru
ORCID: 0000-0002-0070-2817

KOZLOV Aleksei G.
kozlov.ag@dvfu.ru
ORCID: 0000-0001-8774-0631

TURPAK Aleksandr A.
turpak.aa@dvfu.ru
ORCID: 0009-0002-3519-4418

PRIKHODCHENKO Alena V.
prikhodchenko.av@dvfu.ru
ORCID: 0009-0006-2778-8143

Received 23.09.2025. Approved after reviewing 01.10.2025. Accepted 27.10.2025.

Conference materials
UDC 539.23+539.26+535.39
DOI: https://doi.org/10.18721/JPM.184.112

Ca_5Si_3 film MBE growth on Si(111) substrate: structure and optical properties

N.G. Galkin [1], K.N. Galkin [1] ✉, O.V. Kropachev [1], S.A. Dotsenko [1]

[1] Institute of Automation and Control Processes FEB RAS, Vladivostok, Russia

✉ galkinkn@iacp.dvo.ru

Abstract. In this work calcium silicide films grown by MBE method on a Si(111) substrate at a temperature of 500 °C with deposition flux ratios NCa : NSi = 3.49, 3.98, the formation of a epitaxial Ca_5Si_3 film with a thickness of up to 40 nm was detected, which was proven by XRD method. Reflection peaks in the region of interband transitions at 2.2, 2.75, 3.57 and 4.4 eV, a semi-metallic character of reflection at energies less than 0.5 eV, partial transmittance at 0.4–1.25 eV and a unique phonon structure with Raman shifts at 102, 110, 124, 160, 190, 220, 241, 344 and 379 cm^{-1} were detected for the first time in the reflection and Raman spectra of the Ca_5Si_3 film.

Keywords: silicon, Ca_5Si_3, MBE growth, film, crystal structure, optical functions, IR transparency, free carrier absorption

Funding: The work was carried out with the support of the state assignment of the IACP FEB RAS (Theme FWFW-2026-0007).

Citation: Galkin N.G., Galkin K.N., Kropachev O.V., Dotsenko S.A., Ca_5Si_3 film MBE growth on Si(111) substrate: structure and optical properties, St. Petersburg State Polytechnical University Journal. Physics and Mathematics. 18 (4.1) (2025) 73–78. DOI: https://doi.org/10.18721/JPM.184.112

Материалы конференции
УДК 539.23+535.39+537.32
DOI: https://doi.org/10.18721/JPM.184.112

Рост пленок Ca_5Si_3 методом МЛЭ на подложке Si(111): структура и оптические свойства

Н.Г. Галкин [1], К.Н. Галкин [1] ✉, О.В. Кропачев [1], С.А. Доценко [1]

[1] Институт автоматики и процессов управления ДВО РАН, г. Владивосток, Россия

✉ galkinkn@iacp.dvo.ru

Аннотация. В данной работе на пленках силицида кальция, выращенных методом молекулярно-лучевой эпитаксии на подложке Si(111) при температуре 500 °C с соотношениями потоков осаждения NCa : NSi = 3,49, 3,98, обнаружено образование эпитаксиальной пленки Ca_5Si_3 толщиной до 40 нм, что подтверждено методом рентгеновской дифракции. Впервые в спектрах отражения и комбинационного рассеяния пленки Ca_5Si_3 обнаружены пики отражения в области межзонных переходов при 2,2, 2,75, 3,57 и 4,4 эВ, полуметаллический характер отражения при энергиях менее 0,5 эВ, частичное пропускание при 0,4–1,25 эВ и уникальная фононная структура с КРС сдвигами при 102, 110, 124, 160, 190, 220, 241, 344 и 379 $см^{-1}$.

Ключевые слова: кремний, Ca_5Si_3, МЛЭ рост, пленка, кристаллическая структура, оптические функции, ИК прозрачность, поглощение на свободных носителях

Финансирование: Работа выполнена при поддержке государственного задания ИАПУ ДВО РАН (Тема FWFW-2026-0007).

Ссылка при цитировании: Галкин Н.Г., Галкин К.Н., Кропачев О.В., Доценко С.А. Рост пленок Ca_5Si_3 методом МЛЭ на подложке Si(111): структура и оптические свойства // Научно-технические ведомости СПбГПУ. Физико-математические науки. 2025. Т. 18. № 4.1. С. 73–78. DOI: https://doi.org/10.18721/JPM.184.112

Introduction

Among calcium silicides $CaSi_2$, Ca_2Si and CaSi are most common displaying interesting optical and electrical properties and they have been grown as single-phase films on silicon [1–4]. However, the other calcium silicide Ca_5Si_3 has not been easily grown as films and powders [5–7], because of the peritectic reactions during its formation in addition to close energies of formation of silicides in the Ca-Si system [8]. In paper [4] it was decided to follow the two-step method previously used for the formation of magnesium silicide. At the first stage, a CaSi layer was formed on the atomically clean silicon surface with the (001) orientation by the MBE (molecular beam epitaxy) method with an average Ca supersaturation (NCa : NSi = 3.2) at a temperature of 400 °C, and then, with additional step-by-step reactive deposition of calcium at temperatures of 490 °C, 600 °C and 700 °C, the transformation of the CaSi lattice into the Ca_5Si_3 lattice was ensured. However, according to the XRD (X-ray diffraction) data [4], the resulting film consisted of the contribution of Ca_5Si_3 grains (small narrow peaks) and a bigger contribution of CaSi grains (broadened peaks). The presence of two phases in the film did not allow analyzing the structure and determining their optical functions as well as the nature of optical conductivity.

In this work, we study the growth of the film by the MBE method with an increased ratio of Ca to Si deposition rates at a temperature of 500 °C with the following identification of the structure of the Ca_5Si_3 film by the XRD method and investigation the its optical and phonon properties, including the calculations of the optical functions.

Materials and Methods

Experiments on the formation of Ca_5Si_3 films on Si(111) substrate were carried out in an OMICRON Compact ultrahigh vacuum setup with a base vacuum of 1×10^{-10} Torr, as well as a block of Si and Ca molecular beam sources and a quartz thickness gauge. A rectangular strip of *n*-type silicon (4×17 mm^2) with a resistivity of 1000 Ohm × cm (Si(111)-FZ1000) served as a sublimation silicon source and a silicon substrate. The Knudsen cell made of pyrolytic boron nitride heated with direct current was used as a Ca source. For the grown samples, the deposition rates of Ca and Si were (7.3–8.4) nm min^{-1} and (0.9–0.95) nm min^{-1}, respectively, in different experiments. The morphology of the films was examined using a SPM Solver P47 in the tapping mode. The transmission and reflectance spectra were recorded at room temperature using Hitachi U-3010 spectrophotometers and a Bruker Vertex 80v Fourier transform spectrometer in the photon energy range of 0.05–6.50 eV. Calculations of optical functions were done in the frame of a two-layer optical model of the film-substrate system [9]. Raman spectra excited by light with wavelengths of 473 and 633 nm were recorded at room temperature using an NTEGRA SPECTRA II setup. The crystal structure of the grown films was examined by X-ray diffraction on a RIGAKU SmartLab diffractometer (ICH FEB RAS) in the 2θ angle range from 5° to 80° with a step of 2θ = 0.01°.

Results and Discussion

Two samples (A and B) were respectively grown at different calcium to silicon flux ratios ($N_{Ca} : N_{Si} = 3.49$ and 3.98) and the same deposition time. After reloading of samples the morphology of grown films were studied. At the minimal ratio of Ca to Si atom flows in samples A (Fig. 1, *a*), the small number of islands on the film surfaces and the film root mean square roughness

(σ_{rms}) 3.7 nm is observed. At the maximum ratio of Ca/Si atomic flow (sample B, Fig. 1, *b*), a certain density of rectangular elongated nanocrystals (NC) on the film surface with σ_{rms} = 4.23 nm is observed.

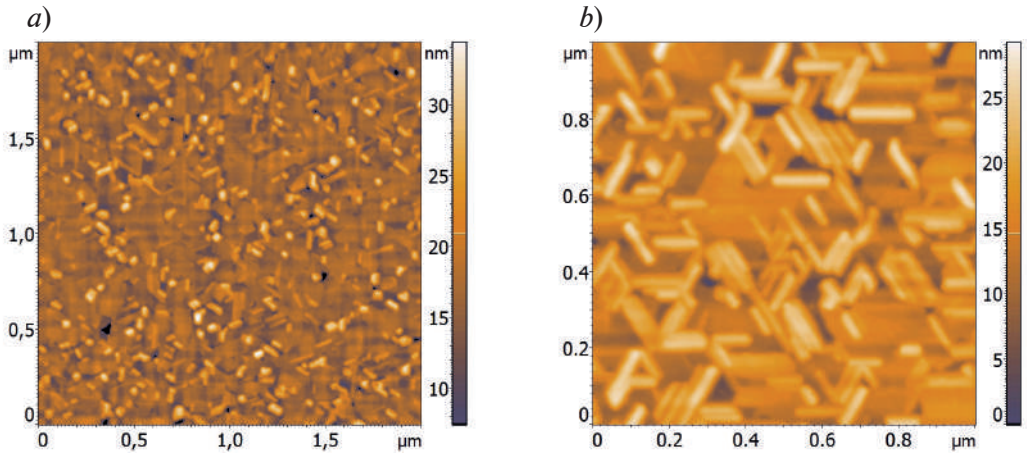

Fig. 1. AFM images of the surface of the Ca silicide films in samples A (*a*) and B (*b*)

The XRD spectrum was recorded immediately after unloading from the chamber for sample B. The XRD spectrum (Fig. 2) shows contributions from the Si substrate on which the film was grown at 28.45° and 58.86°, corresponding to diffraction from the Si(111) and Si(222) planes. In addition, it shows peaks from the film at several angles 2Θ: 16.1°, 32.5°, 40.16°, 44.5°, 49.6° and 75.6°. The first peak corresponds to trigonal-rhombohedral $CaSi_2$ polymorphs (space group $R\bar{3}m$) of the $CaSi_2$-3R(003) [10] plane. The second peak can be attributed to two silicides: $CaSi_2$-3R(006) and tetragonal Ca_5Si_3(220) (space group I4/mcm) [11]. According to databases, the intensities of these peaks are approximately the same, so it is difficult to unambiguously interpret which silicide a given peak belongs to. The third peak is in good agreement with the Ca_5Si_3(125). The other three peaks are characterized by an intensity less than 1% of the intensity of the peak 2Θ = 32.5° and correspond to Ca_5Si_3 with planes (134), (141) and (12 11), respectively.

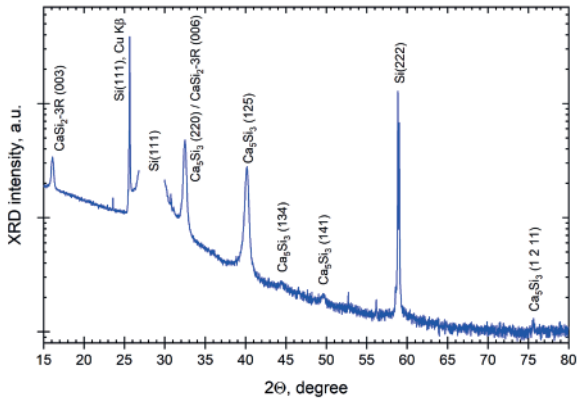

Fig. 2. XRD spectrum of the film Ca_5Si_3 film in the sample B

Studies of the optical transmission and reflection spectra of Ca_5Si_3 showed (Fig. 3) that the highest velocity ratio (3.95, sample B) provides a larger reflectivity amplitude in the 0.1–1.2 eV range and narrower peaks, indicating better crystalline film quality. In addition, in the reflection spectra for samples A and B in the region of photon energies greater than 2 eV, peaks with energies of 2.20, 2.75, 3.57 and 4.4 eV are observed, which almost do not coincide with the peaks CaSi (1.95, 2.6, 3.5 and 4.4 eV) and $CaSi_2$ (1.9, 3.2, 3.9 and 5.0) [4]. According to the XRD data (Fig. 2) in the sample B there is an admixture of the $CaSi_2$ phase on the film surface. Calculations of the true reflectance spectrum of the calcium silicide film for sample B from the two-layer model [9] in the energy range of 0.1–1.2 eV showed (Fig. 3, curve R_{0}_B) that at energies below

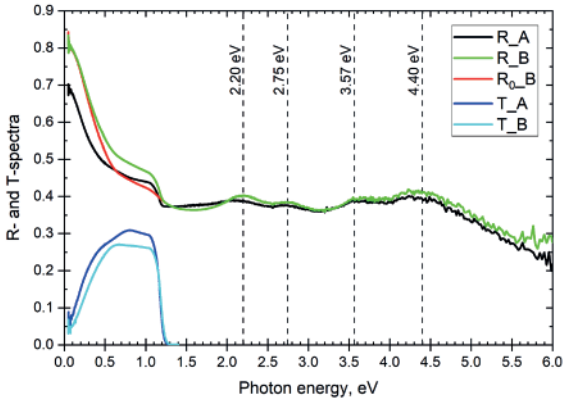

Fig. 3. Reflectance (R) and transmittance (T) spectra for samples A and B

1 eV a weak minimum with an energy of about 0.6 eV is observed [4]. Reflectance in all films below 0.5 eV increases to 0.6–0.8 indicating a metallic character in the films. Registration of transmission spectra in the far IR region (50–700 cm^{-1}) showed that Ca_5Si_3 films are characterized by the absence of IR-active phonon modes.

From the reflection and transmission spectra, within the framework of the two-layer model [9], calculations of the optical functions for the Ca_5Si_3 film were performed. The spectra of the refractive index (n) and extinction (k) are shown in Fig. 4, *a*. Sample B is characterized by higher values of the refractive index and extinction coefficient than sample A, which is due to less scattering at grain boundaries, i.e. better crystalline quality in comparison. Calculations of the absorption coefficient in films (Fig. 4, *b*) showed the relative transparency of the films in the photon energy range of 0.4–1.25 eV and a smooth increase at lower energies, which is determined by the absorption on free carriers in them [12].

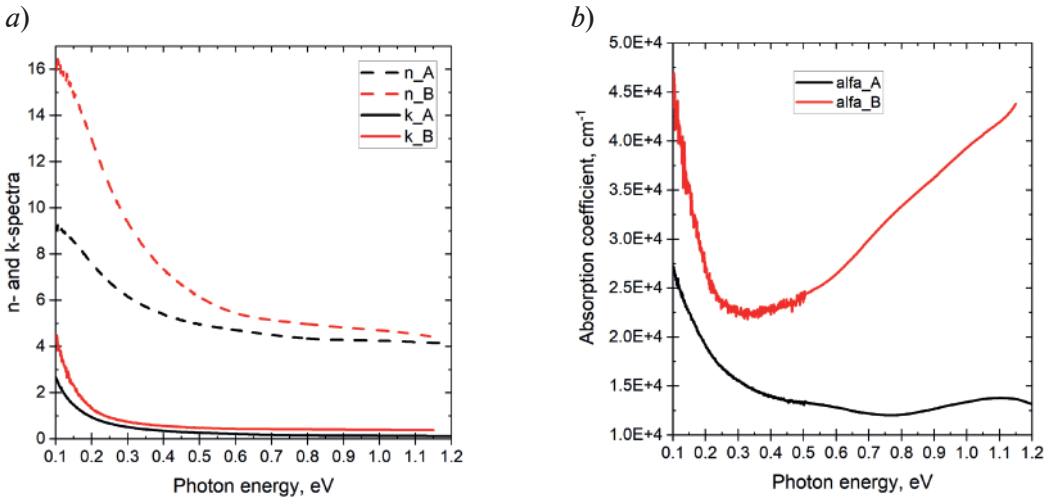

Fig. 4. Spectra of refraction index (n) and extinction coefficient (k) (*a*) and spectra of absorption coefficient for films in the samples A and B (*b*)

The studies of the Raman spectrum of the film in sample B upon excitation by a laser with a wavelength of 633 nm showed the appearance of a pronounced structure of 14 peaks with Raman shifts (102, 110, 124, 160, 190, 220, 241, 304, 344, 379, 387, 416, 449 and 521 cm^{-1}). When the laser wavelength is reduced to 473 nm, some of the peaks below 190 cm^{-1} and the peak at 304 cm^{-1} disappear from the spectrum, but the rest repeat the peaks with large Raman shifts. The peaks at 304 and 521 cm^{-1} are attributed to the silicon substrate phonons (2TA and TO s, respectively). It is known [4, 10] that a peaks at 387, 416 and 449 cm^{-1} is observed in the $CaSi_2$ film, which confirms the presence of the $CaSi_2$ phase detected according to the XRD data in the grown film. The remaining 9 peaks 102, 110, 124, 160, 190, 220, 241, 344 and 379 cm^{-1}correspond to the

Ca_5Si_3 phase, for which there are currently no data on active Raman phonons in the literature. These calculations are planned to be carried out together with first-principles calculations of the electronic structure and presented in the next article.

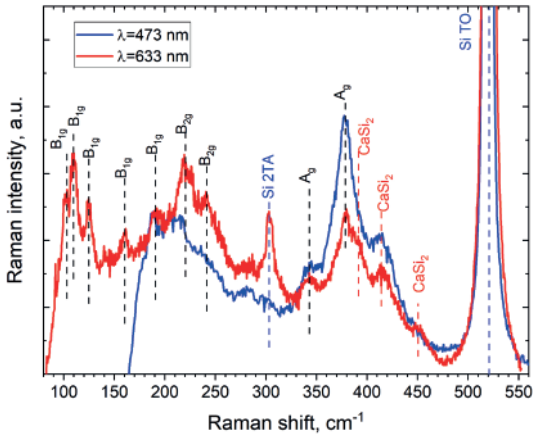

Fig. 5. Raman spectra of the Ca_5Si_3 film in the sample *C* on the Si substrate

Conclusion

A technique for growing Ca_5Si_3 films by molecular beam epitaxy with a variable calcium-to-silicon flux ratio at a substrate temperature of $T = 500$ °C has been developed. According to X-ray diffraction and morphology studies, it has been established that the maximum single-phase state of the Ca_5Si_3 film is achieved with a calcium-to-silicon flux ratio of 3.98. A study of the optical reflection and transmission spectra, as well as the Raman spectra of calcium silicide films, has shown that the polycrystalline Ca_5Si_3 film is characterized by a reflection spectrum with unique peaks at 2.20, 2.75, 3.57, and 4.4 eV and a reflection coefficient of 0.38–0.43 with an increase in the reflection coefficient to $R = 0.8$ in the far IR range. It was found that the Ca_5Si_3 film has a unique phonon structure with 9 peaks in the Raman shift range from 102 to 379 cm^{-1}. Calculations of the optical functions of the Ca_5Si_3 films showed that it exhibits semi-metallic properties with transparency in the photon energy range of 0.4–1.1 eV and absorption on free carriers at phonon energies of 0.1–0.4 eV.

Acknowledgments

The study was carried out within the framework of the state assignment of the Institute of IACP FEB RAS (state budget topic FWFW-2026-0007). X-ray measurements were performed using the equipment at the Institute of Chemistry, Far Eastern Branch of the Russian Academy of Sciences.

REFERENCES

1. **Affronte M., Laborde O., Olsece G.L., and Palenzona A.,** Low temperature properties of calcium mono-and disilicides, J. Alloys Compd. 274 (1998) 68–73.

2. **Wu H., Zhou W., Udovic T.J., Rush J.J.,** Structure and hydrogenation properties of the ternary alloys $Ca_{2-x}Mg_xSi$ ($0 \le x \le 1$), J. Alloys Compd. 446–447 (2007) 101–105.

3. **Galkin N.G., Galkin K.N., Tupkalo A.V., Fogarassy Z., Pécz B.,** A low temperature growth of Ca silicides on Si (100) and Si (111) substrates: Formation, structure, optical properties and energy band structure parameters, J. Alloys Compd. 813 (2020) 152101.

4. **Galkin N.G., Galkin K.N., Goroshko D.L., Dotsenko S.A., Serhiienko I.A., Khovaylo V.V., Gutakovskii A.K.,** Ca silicide films–promising materials for silicon optoelectronics, Jpn. J. Appl. Phys. 62 (2023) SD0803.

5. **Uehara M., Akiyama K., Shimizu, T. Matsushima, M. Uchida, H. Kimura, Y., & Funakubo H.,** Synthesis and characterization of $CaSi_2$ films for hydrogenated 2D Si nanosheets, Journal of Electronic Materials. 45 (6) (2016) 3121.

6. **Inaba T., Kato A., Miura K., Akasaka M., Iida T., Momose Y., Tatsuoka H.,** Preparation and electrical properties of Ca_5Si_3 and Sr_5Si_3 powders, Thin Solid Films. 515 (2007) 8226–8229.

7. **Brutti S., Nguyen-Manh D., Pettifor D.G., Manfrinetti P., Napoletano M., Canepa F.,** Electronic, electrical and thermodynamic properties of Ca_5Si_3 by first principles calculations and low temperature experimental techniques, CALPHAD. 33 (2009) 260–264.

8. **Manfrietti P., Fornasini M.L., and Palenzona A.,** The phase diagram of the Ca–Si system, Intermetallics. 8 (2000) 223–228.

9. **Galkin N.G., Maslov A.M., Konchenko A.V.,** Optical and photospectral properties of $CrSi_2$ A-type epitaxial films on Si (111), Thin Solid Films. 311 (1997) 230–238.

10. **Castillo S.M., Tang Zh., Litvinchuk A.P., Guloy A.M.,** Lattice dynamics of the rhombohedral polymorphs of $CaSi_2$, Inorganic Chemistry, V.55, Iss. 20 (2016) 10203–10207.

11. **Eisenmann B., Schäfer H.,** The crystal structures of Ca_5Si_3 and Ca_5Ge_3, Zeitschrift für Naturforschung (Z. Naturforsch.). (29b) (1974) 460–463.

12. **Smith R.A.,** Semiconductors (Cambridge University Press edition) 2nd ed. (1978).

THE AUTHORS

GALKIN Nikolay G.
galkin@iacp.dvo.ru
ORCID: 0000-0003-4127-2988

KROPACHEV Oleg V.
chernobez@gmail.com
ORCID: 0000-0003-4300-0070

GALKIN Konstantin N.
galkinkn@iacp.dvo.ru
ORCID: 0000-0001-5386-1013

DOTSENKO Sergey A.
docenko@iacp.dvo.ru
ORCID: 0000-0002-0052-7465

Received 02.10.2025. Approved after reviewing 04.12.2025. Accepted 08.12.2025.

Conference materials
UDC 538.975 + 681.782.473 + 535-15 + 535.375.54
DOI: https://doi.org/10.18721/JPM.184.113

Optical, phononic and semiconductor properties of magnesium silicide films formed on silicon by layer-by-layer (Mg+Si) reactive epitaxy

D.V. Fomin [1], A.V. Polyakov [1] ✉, I.O. Sholygin [1], N.G. Galkin [2], K.N. Galkin [2]

[1] Amur State University, Blagoveshchensk, Russia;

[2] Institute of Automation and Control Processes FEB RAS, Vladivostok, Russia

✉ polyakov_a_1999@mail.ru

Abstract. Magnesium silicide films were formed on *n*-type Si (111) substrates with resistivities ranging from 2 to 15 Ohm·cm (samples 1 and 2) and from 0.1 to 0.5 Ohm·cm (samples 3 and 4) using reactive epitaxy with layer-by-layer deposition of magnesium and silicon layers at a temperature of 250 °C. The article presents the results of a study of the morphology, optical and phononic properties, and the band gap of samples containing magnesium silicide films with thicknesses of 496, 682, 1143, and 414 nm, according to SEM data on a cross section. Atomic force microscopy showed that the films of all samples were formed by the Volmer-Weber mechanism, with the islands coalescing into clusters and grains. The island area of the film of the first sample ranges from 0.12 to 0.48 μm^2, the second − from 0.02 to 0.06 μm^2, the third − from 0.01 to 0.04 μm^2, and the fourth − from 0.04 to 0.09 μm^2. The islands coalesce into clusters and grains. In all grown films, Raman scattering (RS) peaks were detected at 258, 348, and 693 cm^{-1}, which correspond to the formation of Mg_2Si. In the IR spectra, the minimum transmittance at a wavenumber of 270 cm^{-1} varies from 0.04 to 0.01, which corresponds to an increase in the absorption of IR photons with an increase in the thickness of the Mg_2Si films in the grown samples. The reflection and transmission spectra of the grown films revealed both interference peaks (below 1.5 eV) and a peak with an energy of 2.2−2.3 eV, corresponding to the interband transition in Mg_2Si. Based on the infrared absorption spectra, the indirect band gap width was calculated for each film: 0.80 and 0.86 eV for samples 1 and 2; 0.77 and 0.79 eV for samples 3 and 4.

Keywords: magnesium silicide, nanofilms, optical spectra, band gap, surface morphology

Funding: The growth of Mg_2Si films and the calculation of their optical constants were carried out as part of the AmSU state assignment (internal AmSU grant for 2025-2026). The research on the optical and phononic properties of the samples was supported by the state assignment of the IACP of the FEB RAS (Topic FWFW-2026-0008).

Citation: Fomin D.V., Polyakov A.V., Sholygin I.O., Galkin N.G., Galkin K.N., Optical, phononic and semiconductor properties of magnesium silicide films formed on silicon by layer-by-layer (Mg+Si) reactive epitaxy, St. Petersburg State Polytechnical University Journal. Physics and Mathematics. 18 (4.1) (2025) 79−86. DOI: https://doi.org/10.18721/JPM.184.113

Материалы конференции
УДК 538.975 + 681.782.473 + 535-15 + 535.375.54
DOI: https://doi.org/10.18721/JPM.184.113

Оптические, фононные и полупроводниковые свойства пленок силицида магния, сформированных на кремнии методом послойной (Mg+Si) реактивной эпитаксии

Д.В. Фомин [1], А.В. Поляков [1] ✉, И.О. Шолыгин [1], Н.Г. Галкин [2], К.Н. Галкин [2]

[1] Амурский государственный университет, г. Благовещенск, Россия;
[2] Институт автоматики и процессов управления ДВО РАН, г. Владивосток, Россия
✉ polyakov_a_1999@mail.ru

Аннотация. Формирование пленок силицида магния осуществлялось на подложках *n*-типа Si (111) с удельным сопротивлением от 2 до 15 Ом·см (образцы 1, 2) и от 0,1 до 0,5 Ом·см (образцы 3 и 4) способом реактивной эпитаксии при послойном осаждении слоев магния и кремния при температуре 250 °C. В статье представлены результаты исследования морфологии, оптических, фононных свойств и ширины запрещенной зоны образцов, содержащих пленки силицида магния с толщинами 496, 682, 1143 и 414 нм по данным СЭМ на поперечном срезе. Методом атомно-силовой микроскопии показано, что пленки всех образцов формировались по механизму Вольмера-Вебера, при этом островки коалесцируют в кластеры и зерна. Во всех выращенных пленках обнаружены пики комбинационного рассеяния света (КРС) 258, 348, 693 см$^{-1}$, которые соответствуют формированию Mg_2Si. В ИК-спектрах минимальное пропускание при волновом числе 270 см$^{-1}$ изменяется от 0,04 до 0,01, что соответствует увеличению поглощения ИК-фотонов с ростом толщины пленок Mg_2Si в выращенных образцах. В спектрах отражения и пропускания выращенных пленок обнаружены как интерференционные пики (ниже 1,5 эВ), так и пик с энергией 2,2–2,3 эВ, соответствующий межзонному переходу в Mg_2Si. По данным инфракрасных спектров поглощения, рассчитана непрямая ширина запрещенной зоны для каждой пленки: 0,80 и 0,86 эВ – образцы 1 и 2; 0,77 и 0,79 эВ – образцы 3 и 4.

Ключевые слова: силицид магния, нанопленки, оптические спектры, запрещенная зона, морфология поверхности

Финансирование: Рост пленок Mg_2Si и расчеты их оптических констант проводили в рамках госзадания АмГУ (внутренний грант АмГУ на 2025-2026 гг.). Исследования оптических и фононных свойств образцов выполнены при поддержке государственного задания ИАПУ ДВО РАН (Тема FWFW-2026-0008).

Ссылка при цитировании: Фомин Д.В., Поляков А.В., Шолыгин И.О., Галкин Н.Г., Галкин К.Н. Оптические, фононные и полупроводниковые свойства пленок силицида магния, сформированных на кремнии методом послойной (Mg+Si) реактивной эпитаксии // Научно-технические ведомости СПбГПУ. Физико-математические науки. 2025. Т. 18. № 4.1. С. 79–86. DOI: https://doi.org/10.18721/JPM.184.113

Introduction

Currently, areas related to nano- and microelectronics are being widely developed in science and technology. Many modern researchers in the field of photovoltaics are searching for promising materials with new properties in order to increase the conversion rate of light energy into electrical energy. One of these materials is Mg_2Si nanofilms [1–3]. This material is a narrow-band semiconductor with an indirect band gap (from 0.6 to 0.8 eV) [1, 2]. Mg_2Si films have a wide spectral photostability range (200–1800 nm) and a high maximum absorption coefficient (95%) in this wavelength range [3]. The epitaxial growth of magnesium silicide in the film form is complicated by the high degree of Mg atom desorption from the silicon substrate at temperatures

above 300 °C [5]. Therefore, one of the main tasks of modern researchers is also to find an effective method for their formation. This paper discusses the optical, electronic properties, and surface morphology of Mg_2Si films formed on silicon.

Materials and Methods

The formation of Mg_2Si films was carried out in the surface physics laboratory of AmSU in a Varian vacuum chamber, a PHI-590 device, with a base pressure of 10^{-7} Pa. Two experiments were conducted to grow Mg_2Si films on *n*-type Si (111) substrates. The first experiment used substrates with a resistivity of 2 to 15 Ohm·cm, while the second experiment used substrates with a resistivity of 0.1 to 0.5 Ohm·cm. In both cases, the deposition of silicon and magnesium on the substrates was performed using the following thermal sources: *n*-type Si (111) with a resistivity of 50 to 85 Ohm·cm and Mg with a purity of 99.999%. Before the films were grown, the substrates and sources were chemically and thermally cleaned.

All samples with films were formed by the reactive epitaxy method at the substrate heating temperature of 250 °C. A Si (60 nm) buffer layer was formed on the substrates beforehand, the successive deposition of portions of Mg and Si was carried out.

In the first experiment, Mg and Si layers were deposited three times in a thickness ratio of 2.75:1 (sample 1) and 3:1 (sample 2). The deposition rates of magnesium and silicon were 9.4 and 1.1 nm/min, respectively. In the second experiment, Mg and Si layers were deposited in a thickness ratio of 3:1, three times (sample 3) and four times (sample 4). The deposition rates of magnesium and silicon were 10.7 and 1.7 nm/min, respectively.

The thickness of the formed films was determined using scanning electron microscopy (SEM), their optical properties were researched using Raman, infrared, and visible spectroscopy, and their surface morphology was researched using atomic force microscopy.

Results and Discussion

The AFM images of the samples (Fig. 1 and 2) were obtained using the Solver P47 microscope in semi-contact mode.

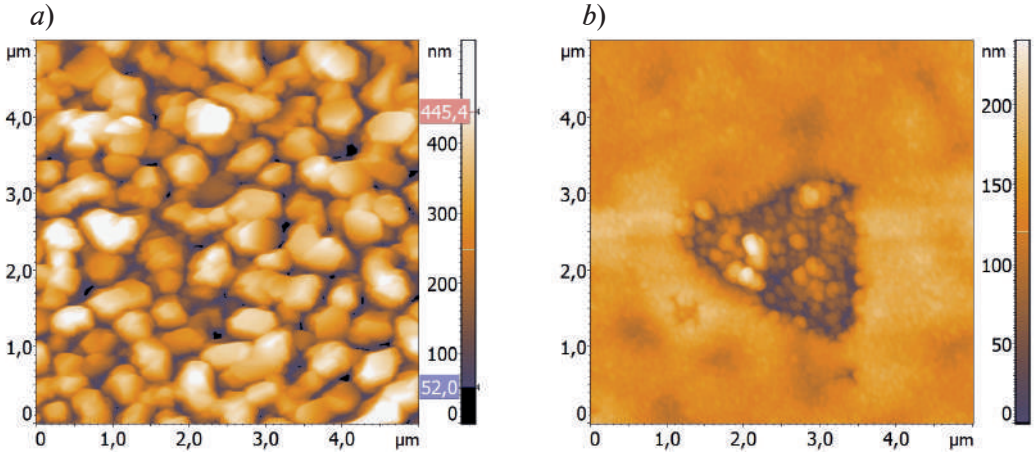

Fig. 1. AFM images of the surface of the first (*a*) and second (*b*) samples

Analysis of the AFM images of the film surface (Fig. 1) showed that both the first and the second sample have a Volmer-Weber island growth mechanism [6, 7]. The lateral dimensions of the particles are in the following ranges: length from 0.4 to 0.8 μm (sample 1) and from 0.2 to 0.3 μm (sample 2), and width from 0.3 to 0.6 μm (sample 1) and from 0.1 to 0.2 μm (sample 2). Based on the geometric measurements, the area of the islands for the first sample ranges from 0.12 to 0.48 μm^2, and for the second sample, it ranges from 0.02 to 0.06 μm^2. Visualization of the AFM images showed that the islands did not completely fuse in sample 1, but in sample 2, they coalesced and formed clusters. The cluster sizes of the second sample in the XY plane are as follows: length from 1.4 to 1.8 μm, and width from 0.7 to 1.4 μm. Their area ranged from 0.98 to 2.52 μm^2. In addition to the islands, a triangular step with a depth of 30 nm is clearly visible in the surface relief. Based on the above, the first sample has a more developed surface relief than the second.

By analyzing the AFM images of samples 3 and 4 (Fig. 2), it was found that the growth of the films also followed the Volmer-Weber mechanism [6, 7]. In the third sample, the size of the islands ranges from 0.1 to 0.2 μm, and in the fourth sample, it ranges from 0.2 to 0.3 μm. The area of the islands ranges from 0.01 to 0.04 μm^2 (sample 3) and from 0.04 to 0.09 μm^2 (sample 4). The islands coalesce into larger grains of about 0.5 μm, with an area of 0.25 μm^2, in sample 3. In sample 4, the coalescence of the islands is less pronounced. There is heterogeneity due to the presence of punctures with a depth of about 20 nm in the surface relief of the third sample. The fourth sample has almost no punctures. Based on the above, it can be concluded that sample 4, compared to sample 3, contains a film with a less developed surface relief.

The thickness of the grown films was determined from the analysis of the SEM images of the cross-sections of the samples obtained using a Hitachi S-3400N electron microscope (Fig. 3). Based on the image analysis results, the film thickness of sample 1 is 496 nm, sample 2 is 682 nm, sample 3 is 1143 nm, and sample 4 is 414 nm.

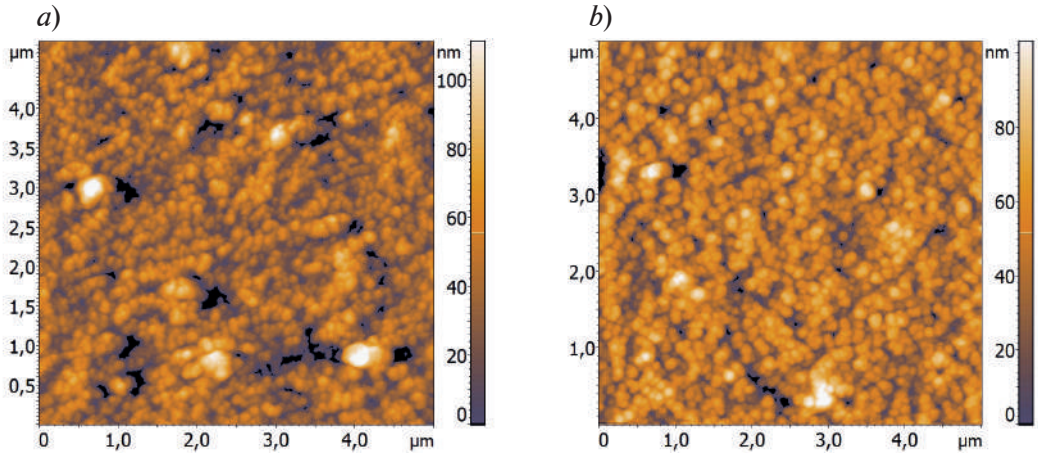

Fig. 2. AFM images of the surface of the third (*a*) and fourth (*b*) samples

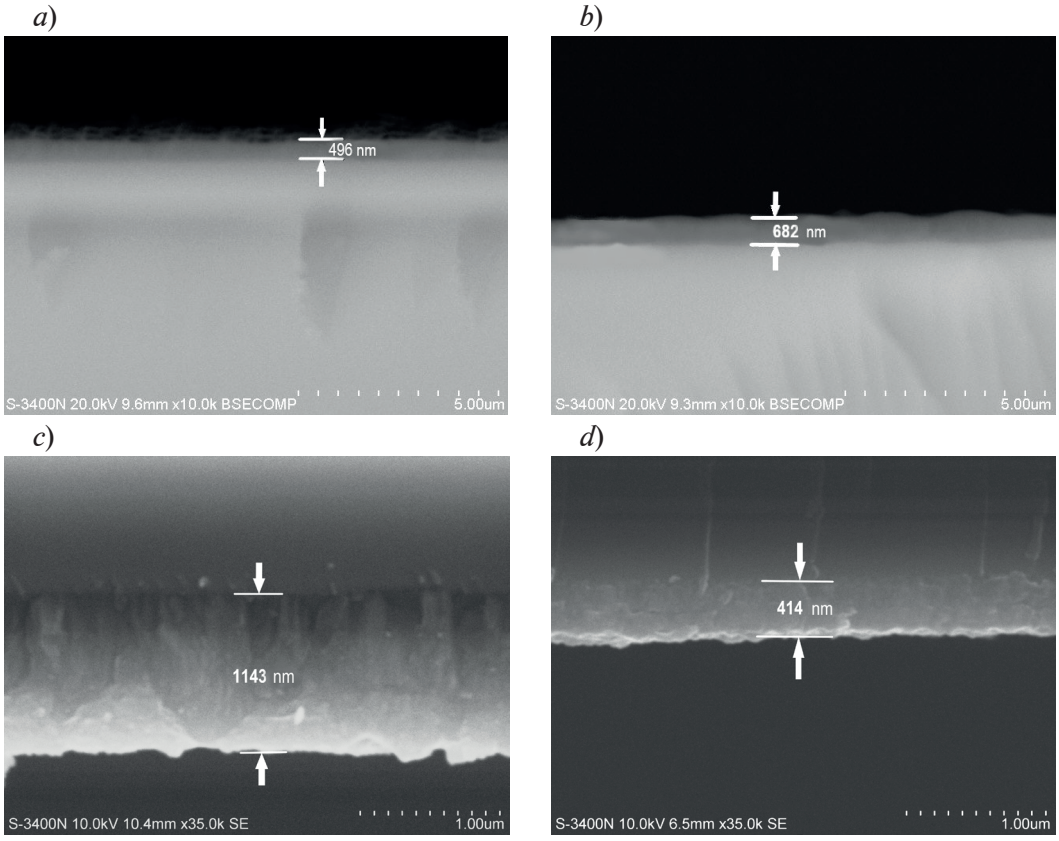

Fig. 3. SEM images of samples 1 (*a*), 2 (*b*), 3 (*c*), and 4 (*d*)

The samples were examined by Raman spectroscopy using an NTEGRA Spectra II (NT-MDT) spectrophotometer at a laser wavelength of 473 nm. Raman spectra are shown in Figure 4.

The spectra have all the peaks characteristic of Mg_2Si at raman shifts of 259, 349, and 693 cm^{-1} [4, 8, 9]. These maxima indicate the excitation of longitudinal optical phonons (F_{2g}, LO, 2LO, respectively) in this film material. The graphs (Fig. 4) show a low-amplitude peak at 480 cm^{-1}, which is consistent with amorphous silicon according to [4, 8].

The far-infrared transmission vibrational spectra (Fig. 5) were obtained using a Bruker VERTEX 80v Fourier spectrophotometer.

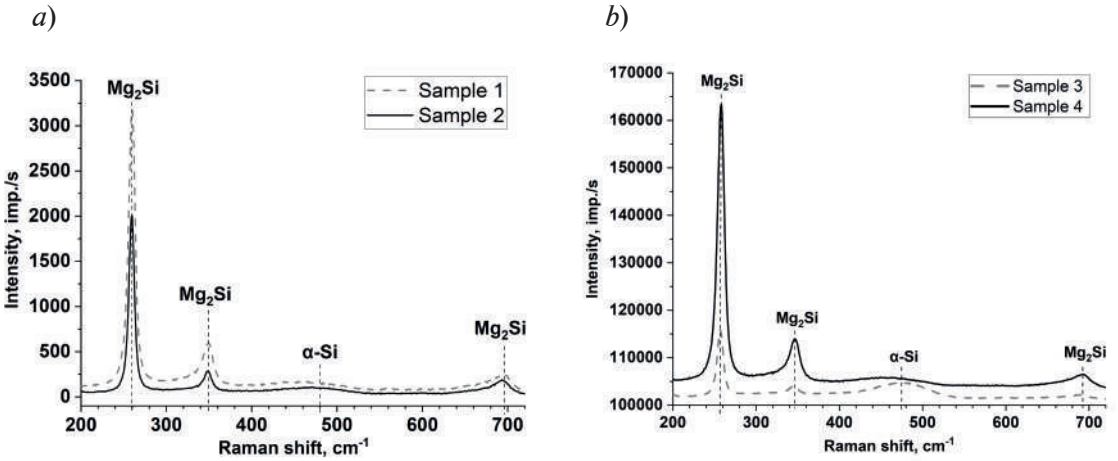

Fig. 4. Raman scattering spectra for samples 1 and 2 (*a*), 3 and 4 (*b*)

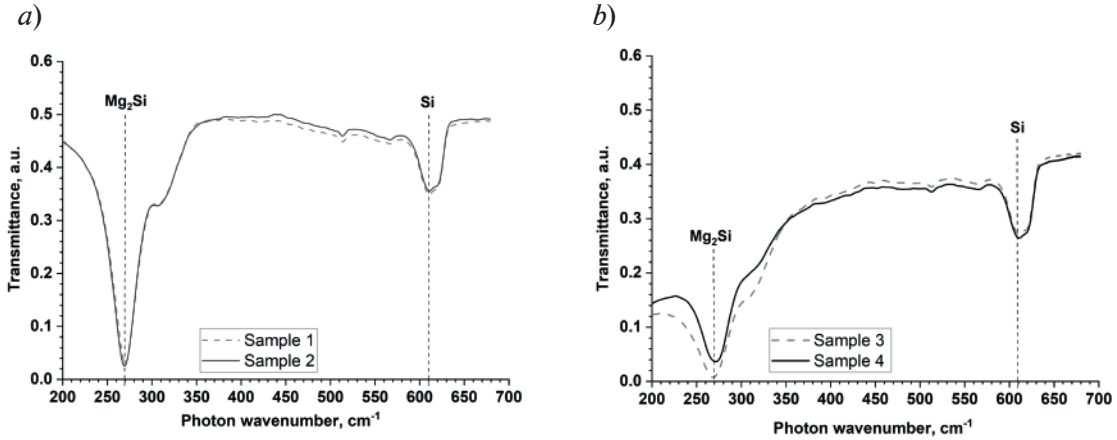

Fig. 5. Infrared transmission spectra for samples 1 and 2 (*a*), 3 and 4 (*b*)

The light transmission spectra through the samples (Fig. 5) show a minimum at a photon wave number of 610 cm^{-1}. According to sources [8, 10], this peak corresponds to the excitation of a phonon in Si. At the same time, the graphs show a minimum in the transmission coefficient at 270 cm^{-1}, which, according to [8, 10, 11], corresponds to the fact that the formed films contain Mg_2Si. The presence of a peak at 270 cm^{-1} is due to the excitation of the transverse optical phonon TO, which is responsible for the absorption in the silicide films of all samples. The minimum transmission value corresponding to Mg_2Si for the formed films is 0.03 (sample 1), 0.02 (sample 2), 0.01 (sample 3), and 0.04 (sample 4). This is due to the fact that thicker films transmit less of the incident light. The above results are consistent with the SEM data presented in Figure 3.

The IR-UV transmission spectra (Fig. 6) and reflection spectra (Fig. 7) were obtained using the following spectrometers: Bruker VERTEX 80v and Spectrophotometer U-3010.

From the graphs of the transmission coefficient as a function of photon energy (Fig. 6), it can be seen that there is an alternation of minima and maxima in the range from 0.2 to 1.1 eV.

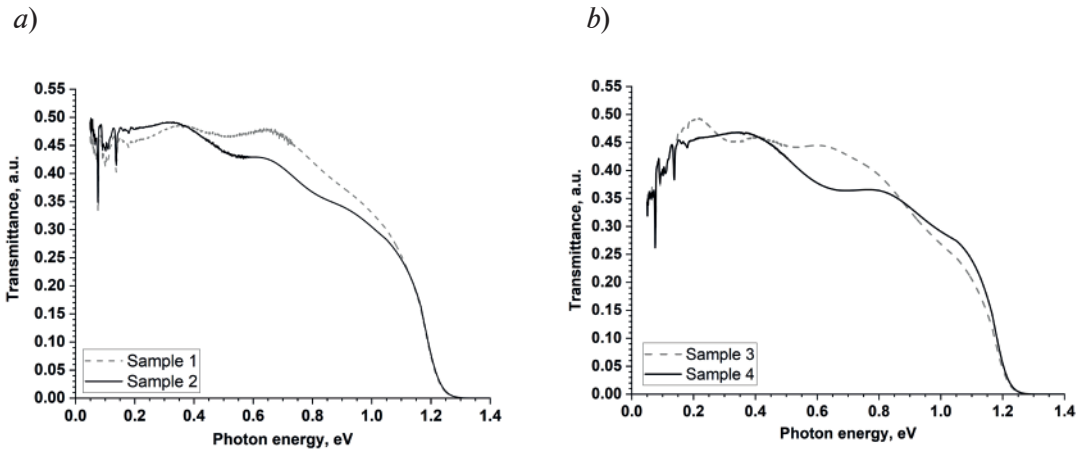

Fig. 6. Near- and mid-infrared transmission spectra for samples 1 and 2 (*a*), 3 and 4 (*b*)

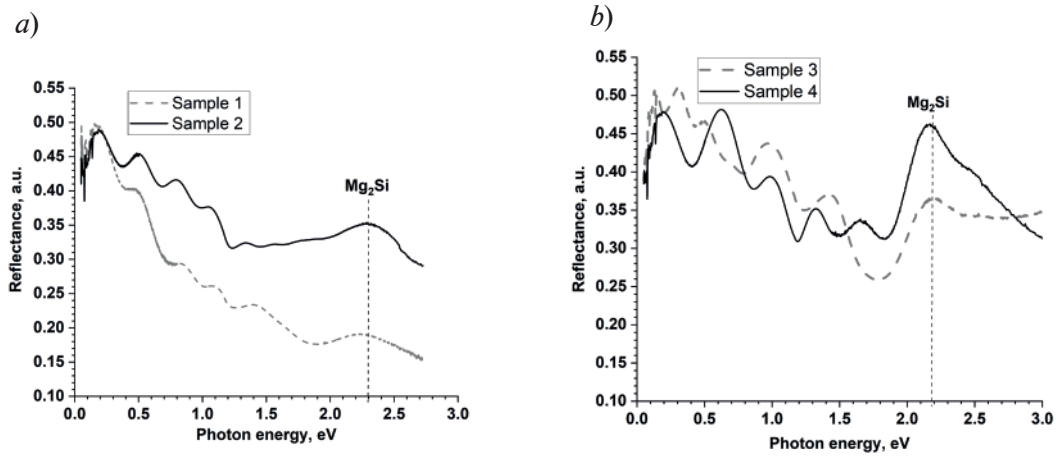

Fig. 7. Reflection spectra for samples 1 and 2 (*a*), 3 and 4 (*b*)

This, according to [1, 2], indicates the interference features of the films. In the energy range of 1.1 to 1.3 eV, there is a significant decrease in the transmission value. This is due to absorption, both in silicon [12] and partially in magnesium silicide [3], which is related to the specific electronic structure of magnesium silicide films in the samples. At energies above 1.3 eV, the absorption coefficient of silicon increases significantly, and the transmission of the film-substrate system approaches zero. The absorption coefficient in magnesium silicide also increases due to interband transitions, which is characteristic of the semiconductor Mg_2Si [10].

The reflection spectra in the IR region of the spectrum in the energy ranges from 0.2 to 1.8 eV (Fig. 7) show alternating maxima and minima of interference, as well as peaks in the visible region at 2.3 (samples 1, 2) and 2.2 eV (samples 3, 4), which are attributed to indirect band Mg_2Si according to [6, 8, 10]. Due to the relatively small thickness, the transmission of Mg_2Si films is still noticeable at photon energies in the range of 1.2–1.5 eV [3]. This leads to the appearance of the first interference maximum in the reflection spectrum at a photon energy of about 1.5 eV (Fig. 7) when light is reflected from the film-opaque silicon substrate system at these energies. The intensity of the maxima increases smoothly with decreasing photon energy, which is due to a decrease in the absorption coefficient in the transparency region, but not to zero. The latter is determined by the absorption on defects [12] in the grown films. The increase in the intensity of the peaks at 2.3 and 2.2 eV is associated with a decrease in grain scattering in the films in samples 3 and 4, as well as with an improvement in their crystalline quality. The latter is confirmed not only by an increase in intensity, but also by a decrease in the half-width of the reflection peaks. In samples 1 and 2, an increase in light scattering on the film grains reduces the reflection coefficient due to multiple reflections on the grains and partial loss of light during absorption in the grains.

To calculate the indirect band gap of the formed Mg_2Si semiconductor films, we plotted the dependence of the square root of the absorption coefficient on the photon energy (Fig. 8).

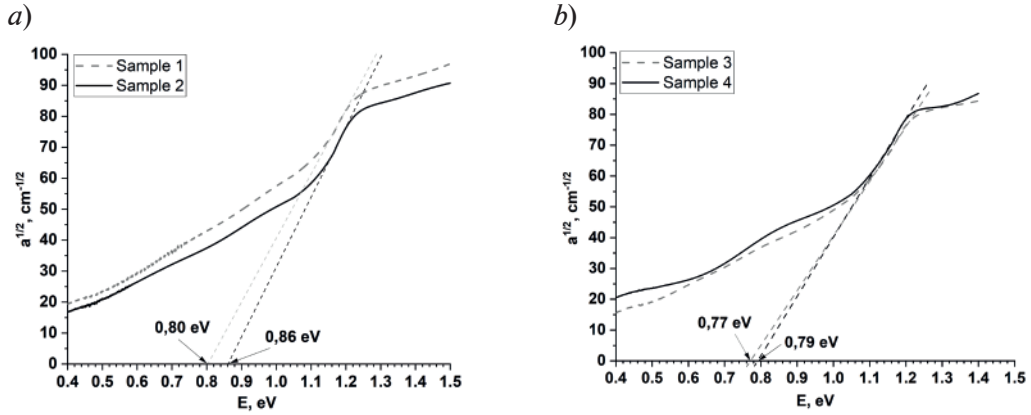

Fig. 8. Absorption coefficient spectra for samples 1 and 2 (*a*), 3 and 4 (*b*)

According to the results of geometric calculation of the indirect band gap from absorption spectra, according to the method described in [6, 7], the following values of this parameter were obtained: 0.80 and 0.86 eV for the first and second samples; 0.77 and 0.79 eV for the third and fourth samples. These values are close to the reference values (0.6–0.8 eV) [1, 2]. Higher values of the indirect band gap in Mg_2Si films in samples 1 and 2 compared to samples 3 and 4 may be due to increased uncontrolled scattering of light on numerous grains and increased errors in extrapolating experimental data.

Conclusion

Thus, this work presents the results of Mg_2Si film formation on Si (111) by reactive epitaxy with layer-by-layer deposition of magnesium and silicon at a substrate heating temperature of 250 °C. The film thicknesses in the samples were 496, 682, 1143, and 414 nm for the first, second, third, and fourth samples, respectively. The island growth mechanism of films was revealed using atomic force microscopy. The area of the film islands varies in the following ranges: from 0.12 to 0.48 μm^2 (sample 1), from 0.02 to 0.06 μm^2 (sample 2), from 0.01 to 0.04 μm^2 (sample 3), and from 0.04 to 0.09 μm^2 (sample 4). The surface morphology of the films is also characterized by the presence of grains and clusters caused by the coalescence of islands. Using the Raman spectroscopy method, silicide formation was detected in all samples based on the peaks corresponding to Mg_2Si phonons: F_{2g} (259 cm^{-1}), LO (349 cm^{-1}), and 2LO (693 cm^{-1}). The formation of Mg_2Si in the films of all samples was confirmed by IR vibrational spectroscopy, based on the presence of a strong absorption peak for the 270 cm^{-1} phonon in the transmission spectrum, whose amplitude correlates with the thickness of the grown films. The reflection spectra of the grown films show a peak at an energy of 2.2–2.3 eV, which also confirms the formation of Mg_2Si in all the films. However, the best crystal quality of the films and the maximum amplitudes of the reflection peak at 2.3 eV are observed for samples grown with an increased ratio of magnesium deposition rates to silicon, which provides a more uniform surface with minimal roughness. Based on the results of geometric calculations of the band gap width of Mg_2Si films, it was found that the band gap width for the first sample is 0.80 eV, for the second sample it is 0.86 eV, for the third sample it is 0.77 eV, and for the fourth sample it is 0.79 eV. Based on the above, it can be concluded that the reactive epitaxy method, with the sequential deposition of magnesium and silicon portions, allows for the formation of magnesium silicide films with specified properties by changing the deposition rate ratio towards magnesium enrichment.

REFERENCES

1. **Hong Yu, Shentong Ji, Xiangyan Luo, Quan Xie,** Technology CAD (TCAD) Simulations of Mg_2Si/Si Heterojunction Photodetector Based on the Thickness Effect, Sensors. 26 (16) (2021) 5559.

2. **Hong Yu, Rui Deng, Zhangjie Mo, Shentong Ji, Quan Xie,** Fabrication and Characterization of Visible to Near-Infrared Photodetector Based on Multilayer Graphene/Mg_2Si/Si Heterojunction, Nanomaterials. 12 (18) (2022) 3230.

3. **Shevlyagin A., Il'yaschenko V., Kuchmizhak A., Mitsai E., Sergeev A., Gerasimenko A., Gutakovskii A.,** Mg_2Si is the new black: introducing a black silicide with 95 % average absorption at 200–1800 nm wavelengths, Applied Surface Science. 602 (2022) 154321.

4. **Shevlyagin A.V., Il'yaschenko V.M., Kuchmizhak A.A., Mitsai E.V., Amosov A.V., Balagan S.A., Kulinich S.A.,** Textured Stainless Steel as a Platform for Black Mg_2Si/Si Heterojunction Solar Cells with Advanced Photovoltaic Performance, Materials. 15 (19) (2022) 6637.

5. **Chernev I.M., Subbotin E.Yu., Argunov E.V., Kozlov A.G., Gerasimenko A.V., Galkin N.G., Poliakov M.V., Volkova L.S., Dudin A.A., Gouralnik A.S.,** Mg_2Si film on Si (111) prepared by Ultra-Fast Mg reactive deposition: crystal structure and thermoelectric properties, St. Petersburg State Polytechnical University Journal. Physics and Mathematics. 16 (3.1) (2023) 106–111.

6. **Galkin N.G., Vavanova S.V., Galkin K.N., Batalov R.I., Bayazitov R.M., Nuzhdin V.I.,** Pulsed nanosecond annealing of magnesium-implanted silicon, Technical Physics. 58 (1) (2013) 94–99.

7. **Oura K., Lifshits V.G., Saranin A.A., Zotov A.V., Katayama M.,** Surface Science: an introduction (in Russian), Nauka, Moscow. 2006.

8. **Terai Y., Hoshida H., Kinoshita R., Shevlyagin A., Chernev I., Gouralnik A.,** Photoreflectance spectra of highly-oriented Mg_2Si (111)/ Si (111) films, JJAP Conference Proceedings. 8 (2020) 011004-1–011004-4.

9. **Onari S., Cardona M.,** Resonant Raman scattering in the II-IV semiconductors Mg_2Si, Mg_2Ge, and Mg_2Sn, Phys. Rev. B. 14 (1976) 3520–3531.

10. **Sholygin I.O., Fomin D.V.., Galkin N.G., Galkin K.N., Chernev I.M., Polyakov A.V.,** Formirovanie i svoystva photodiodnykh struktur Al/Mg_2Si/Si/Au–Sb [Formirovaniye i svoystva fotodiodnykh struktur Al/Mg_2Si/Si/Au–Sb], Izvestiya Vysshikh Uchebnykh Zavedeniy. 68 (3) (2025) 22–31 (in Russian).

11. **Baleva M., Marinova M., Atanassov A.,** Infrared spectra of semiconducting silicides nanolayers, Journal of Physics: Conference Series. 113 (1) (2008) 012043.

12. **Shalimova K.V.,** Physics of Semiconductors, Energoatomizdat, Moscow. (1985) (in Russian).

THE AUTHORS

FOMIN Dmitriy V.
e-office@yandex.ru
ORCID: 0000-0002-5474-5281

GALKIN Nikolay G.
galkin@iacp.dvo.ru
ORCID: 0000-0003-4127-2988

POLYAKOV Aleksey V.
polyakov_a_1999@mail.ru
ORCID: 0009-0009-5104-5966

GALKIN Konstantin N.
galkinkn@iacp.dvo.ru
ORCID: 0000-0001-5386-1013

SHOLYGIN Ilya O.
ilia.sholygin235@bk.ru
ORCID: 0009-0004-6651-1468

Received 07.10.2025. Approved after reviewing 25.11.2025. Accepted 21.12.2025.

SIMULATION OF PHYSICAL PROCESSES

Conference materials
UDC 539.1.072+615.849.5
DOI: https://doi.org/10.18721/JPM.184.114

Nanoparticle size and quantity impact on X-ray induced secondary emission for magnetite-gold systems

N.S. Markin [1, 2] ✉, I.S. Gordeev [3, 4], S.I. Ivannikov [2],
A.Yu. Samardak [1], A.S. Samardak [1], A.V. Ognev [1]

[1] Far Eastern Federal University, Vladivostok, Russia;
[2] Institute of Chemistry FEB RAS, Vladivostok, Russia;
[3] Joint Institute for Nuclear Research, Dubna, Russia;
[4] Dubna State University, Dubna, Russia
✉ markkin.ns@gmail.com

Abstract. The work presents the results of Monte Carlo modeling (PHITS) of irradiation of Fe_3O_4-SiO_2-Au nanoparticles – promising agents for enhancing the effectiveness of radiation therapy with X-ray radiation. Within the model of a single nanoparticle in a water phantom, it was shown that, assuming a uniform distribution of gold nanoparticles over the surface of the adhesion layer, the particle density and their size do not have a significant impact on the efficiency of therapeutic X-ray beam conversion. The main factors determining the configuration of dose fields are the chemical composition of the nanoparticles and the energy of the primary photon beam.

Keywords: gold nanoparticles, Monte Carlo simulation, radiosensitizer, radiation therapy

Funding: The study of Markin N.S., Samardak A.Yu., Ognev A.V. was supported by the Russian Ministry of Science and Higher Education (State Task No. FZNS-2023-0012).

Citation: Markin N.S., Gordeev I.S., Ivannikov S.I., Samardak A.Yu., Samardak A.S., Ognev A.V., Nanoparticle size and quantity impact on X-ray induced secondary emission for magnetite-gold systems, St. Petersburg State Polytechnical University Journal. Physics and Mathematics. 18 (4.1) (2025) 87–92. DOI: https://doi.org/10.18721/JPM.184.114

Материалы конференции
УДК 539.1.072+615.849.5
DOI: https://doi.org/10.18721/JPM.184.114

Влияние размера и числа золотых наночастиц в системе магнетит-золото на эмиссию рентген-индуцированного вторичного излучения

Н.С. Маркин [1, 2] ✉, И.С. Гордеев [3, 4], С.И. Иванников [2],
А.Ю. Самардак [1], А.С. Самардак [1], А.В. Огнев [1]

[1] Дальневосточный федеральный университет, г. Владивосток, Россия;
[2] Институт химии ДВО РАН, г. Владивосток, Россия;
[3] Объединенный институт ядерных исследований, г. Дубна, Россия
[4] Государственный университет «Дубна», г. Дубна, Россия
✉ markkin.ns@gmail.com

Аннотация. В работе представлены результаты Монте-Карло моделирования (PHITS) облучения наночастицы состава Fe_3O_4-SiO_2-Au – перспективного агента для повышения

эффективности лучевой терапии – рентгеновским излучением. В рамках одночастичной модели наночастицы в водном фантоме показано, что при условии равномерного распределения наночастиц золота по поверхности адгезионного слоя плотность нанесения частиц и их размер не оказывают значимого воздействия на эффективность конверсии рентгеновского излучения. Основными факторами, определяющими конфигурацию дозовых полей, являются химический состав наночастиц и энергия первичного фотонного пучка.

Ключевые слова: золотые наночастицы, Монте-Карло моделирование, радиосенсибилизатор, лучевая терапия

Финансирование: Государственное задание Дальневосточного федерального университета No. FZNS-2023-0012.

Ссылка при цитировании: Маркин Н.С., Гордеев И.С., Иванников С.И., Самардак А.Ю., Самардак А.С., Огнев А.В. Влияние размера и числа золотых наночастиц в системе магнетит-золото на эмиссию рентген-индуцированного вторичного излучения // Научно-технические ведомости СПбГПУ. Физико-математические науки. 2025. Т. 18. № 4.1. С. 87–92. DOI: https://doi.org/10.18721/JPM.184.114

Introduction

One of the main limitations of X-ray radiotherapy is the lack of selectivity of ionizing radiation action on the tumor, which leads to increased risks of unwanted irradiation of healthy tissues and, consequently, the occurrence of side effects such as inflammation, scarring, and functional impairments in the irradiated area. An equally important aspect of this problem is the impracticability to deliver radiation doses sufficient for radical treatment, which, in turn, necessitates additional fractionation of radiotherapy sessions [1, 2], thereby increasing the burden on medical personnel and equipment as well as on patients.

Therefore, a relevant task is to develop new methods to enhance the efficiency of converting the energy of therapeutic X-ray beams within a targeted region of the body. One promising approach to increase tumor contrast involves introducing high atomic number nanoparticles into the specified volume [3, 4]. The increased probability of interactions between metals and photons, relative to biological tissue, results in a higher number of interaction events between nanoparticles and radiation. In its turn, induced secondary radiation creates an additional dose component in the vicinity of the nanoparticle, thereby amplifying its destructive effect on the tumor. The short mean free path characteristic of X-ray-induced secondary radiation ensures that these effects are localized, reducing the risks of overexposure to non-targeted organs and tissues.

This work aims to investigate the features of irradiation of composite Fe_3O_4-SiO_2-Au nanoparticles, specifically focusing on determining how the size and number of gold nanoparticles on the surface of Fe_3O_4-SiO_2 influence the yield of secondary radiation emitted from nanoparticle surfaces.

Materials and Methods

The nanoparticle model was based on data from real systems with a “core-shell-satellite” structure: a magnetite core coated with a thin film of amino silica, onto which gold nanoparticles are attached [5]. The systems are presented in two configurations which differ in the nanoparticle coverage density on the surface of the SiO_2 adhesion layer. The average number of GNP per Fe_3O_4-SiO_2 nanoparticle was 16 ± 4 for the first system and 40 ± 12 for the second. The average size of the iron-containing core was 62 ± 10 nm for both systems. The size of the gold nanoparticles (GNP) on the adhesive layer surface was 13.7 ± 1.9 nm and 9.5 ± 1.8 nm for the first and second systems, respectively [5].

A series of numerical experiments was performed to identify the features of X-ray irradiation of the described nanoparticles. A more detailed description of the simulation model, creation method, and calculation methodology is presented in our previous work [5]. Here are the key parameters.

The simulation of radiation transfer processes was performed using the general-purpose radiation transport Monte Carlo code PHITS version 3.33 [6–9]. In this work, the track-structure mode was utilized in all geometric areas for particles with energies ranging from 100 eV to 10 keV. For interactions involving particles with energies higher than 10 keV, the EGS5 (Electron-Gamma Shower) code was used as part of PHITS.

Table 1

Geometric parameters of targets and model comparison

	This work				A system equivalent in chemical composition [5]			
	$d[Fe_3O_4]$, nm	$\tau[SiO_2]$, nm	d[Au], nm	n[Au]	$d[Fe_3O_4]$, nm	$\tau[SiO_2]$, nm	d[Au], nm	n[Au]
Set1	87	2	10	31	87	2	5	331
Set2	87	2	10	62	87	2	5	661
Set3	87	2	10	208	87	2	5**	–

Notations: $d[Fe_3O_4]$, d[Au] – diameter of Fe_3O_4 core and Au nanoparticles; $\tau[SiO_2]$ – thickness of SiO_2 adhesive layer; n[Au] – the number of Au nanoparticles on SiO_2 adhesive layer.
**The adhesive layer was coated with a continuous layer (shell) of Au with a thickness of 5 nm.

An approach based on a spherical Fibonacci lattice was used to implement a physical model of the experimentally obtained core-shell nanoparticles [10]. Such approach allows to achieve uniform distribution of gold nanoparticles on the surface of adhesion layer of SiO_2. The coordinates of the AuNPs on the SiO_2 shell surface were defined in the geometry for PHITS simulations using the FitsGeo code [11]. This study considered four configurations of core-shell-satellite geometry. The targets parameters are demonstrated in Table 1.

The target was irradiated with a parallel monoenergetic X-ray beam. The photon energy was 50, 100, and 150 keV. At each independent simulation, 108 primaries were transported to provide good statistics. The flat circular radiation source was positioned so that its axis coincided with the centre of the nanoparticle. The diameter of the source coincided with that of the nanoparticle. The source was placed close to the nanoparticle.

We considered the physical processes responsible for electron generation and the spectra of secondary electrons crossing the sphere that encloses the target. To account for changes in the geometric parameters of the radiation source and detectors (their area) relative to similar parameters used in previous work [5], data on the particle flux crossing the sphere was renormalized.

Results and Discussion

At the first stage, the spectra of secondary electrons emitted from the target surface were analyzed. The overall shape of the spectra for a system with large gold nanoparticles (10 nm) is similar to that recorded from the surface of previously analyzed systems with smaller nanoparticles (5 nm) [5]. To assess the effect of nanoparticle size, the obtained spectra were conventionally divided into several regions: the Auger electron region (6–10 keV), and the photoelectron regions at 30–40 keV, 70–95 keV, and 80–120 keV for primary beam energies of 50, 100, and 150 keV, respectively, corresponding to emissions from iron and gold. The electron fluences within each of these energy ranges were summed. The intensity of electron emission for systems with different nanoparticle sizes but identical gold content is comparable across all energy ranges, regardless of the primary photon energy. The data indicates the absence of self-shielding effects as particle size increases for high-energy (>1 keV) electrons.

A significant reduction in secondary electron emission with an increase in the GNPs size in the system was recorded in the low energy region (< 1 keV) of the spectrum (Table 2). A dependence of this effect on the density of the GNPs coverage was also identified. Let Φ_5 and Φ_{11} be the flux of secondary electrons with kinetic energy <1 keV for systems with a GNPs diameter of 5 and 11 nm, respectively. The ratio Φ_{11}/Φ_5 increases with an increase in the surface concentration of GNP on the SiO_2 shell.

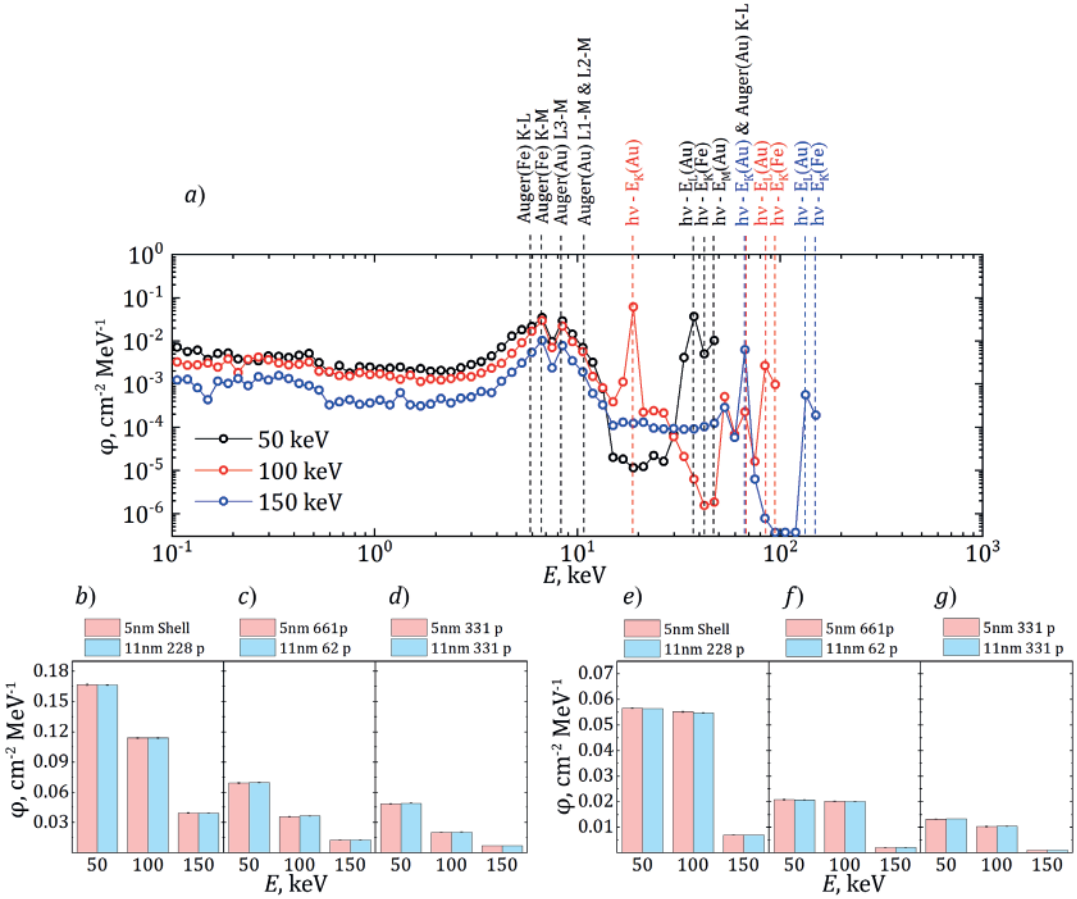

Fig. 1 Simulated spectra of secondary electrons emitted from the target (for example, 11nm 228p system) surface during its irradiation by photons with different energy (where K-L, K-M, L3-M, L2-M, and L1-M indicate the energy differences between the corresponding electron shells of atoms) (*a*); comparison of the emission intensity of Auger electrons (*b*, *c*, *d*) and photoelectrons (*e*, *f*, *g*) from the target surface for 50, 100, and 150 keV photons respectively

Table 2

Geometric parameters of targets and model comparison

	Φ_5, $cm^{-2}\,MeV^{-1}$	$\Phi_{11}\cdot10^{-3}$, $cm^{-2}\,MeV^{-1}$	Φ_{11}/Φ_5	$V_{Water\_5}\cdot10^{-3}$, nm^3	$V_{Water\_11}\cdot10^{-3}$, nm^3	Φ_{11}/Φ_5
*Set1	4.61 (5.5)	2.99 (4.2)	0.648 (4.3)	123.2	339.2	0.363
*Set2	5.19 (6.7)	3.57 (3.8)	0.688 (3.8)	101.5	318.3	0.319
*Set3	8.25 (4.2)	8.12 (2.5)	0.985 (2.5)	0	215.9	0

Notations: *Set1-3 corresponds to the numbering in Table 1.
The relative error in determining the parameters is given in parentheses.

The increase in electron emission with increasing of GNP lattice density can be attributed to a decrease in electron path length into the aqueous medium. In rarefied systems, the mean path length of secondary electrons passes through the water-filled volume between the GNPs and the detector increases. This leads to lower measurement results. This hypothesis is confirmed by the value of the Pearson coefficient $R = 1$ for the dependence $\Phi_{11}/\Phi_5 = f(V_{Water\_11} / V_{Water\_5})$, where V_{Water_11} and V_{Water_5} – is the volume of water filling the space between the GNP and the bounding sphere (electron detector) for systems with a GNP size of 5 and 11 nm, respectively.

Conclusion

PHITS calculations revealed that the emission intensity of secondary electrons with energies above 1 keV from Fe_3O_4–SiO_2–Au nanoparticles is independent of the size of the gold nanoparticles, given their uniform distribution on the adhesive layer. The stability of the secondary electron emission intensity with energy >1 keV is because the average thickness of the gold layer that an electron must pass does not exceed its mean free path in gold [12]. A decrease in emission intensity was observed in the low energy region of the spectrum ($E < 1$ keV). This effect is attributed to the model parameters, specifically the absorption of electrons in the water filling the volume between the GNPs. The presence of this effect precludes a definitive conclusion regarding the presence or absence of effects associated with the self-shielding of electron of this energy group. In the future, it is planned to replace the interparticle medium with a vacuum.

The main factors controlling the configuration of dose fields are the chemical composition of the nanoparticles and the energy of the primary photon beam.

REFERENCES

1. **Kaanders J.H., Ang K.K.,** Early reactions as dose-limiting factors in radiotherapy, Seminars in radiation oncology. 4 (2) (1994) 55–67.

2. **Gaya A.M., Ashford R.F.U.,** Cardiac complications of radiation therapy, Clinical oncology. 17(3) (2005) 153–159.

3. **Siddique S., Chow J.C.L.,** Application of nanomaterials in biomedical imaging and cancer therapy, Nanomaterials. 10 (9) (2020) 1700.

4. **Song G., Cheng L., Chao Y., Yang K., Liu Z.,** Emerging nanotechnology and advanced materials for cancer radiation therapy, Advanced materials 29 (32) (2017) 1700996.

5. **Markin N.S., Gordeev I.S., Fu H.E., Ivannikov S.I., Kim Y.B., Samardak A.Y., Samardak A.S., Kim Y.K., Ognev A.V.,** Secondary electron dynamics in core–shell–satellite nanoparticles: a computational strategy for targeted cancer treatment, Nanoscale. 17 (18) (2025) 11691–11702.

6. **Sato T., Iwamoto Y., Hashimoto S., Ogawa T., Furuta T., Abe S.-I., Kai T., Matsuya Y., Matsuda N., Hirata Y., Sekikawa T., Yao L., Tsai P.-E., Ratliff H.N., Iwase H., Sakaki Y., Sugihara K., Shigyo N., Sihver L., Niita K.,** Recent improvements of the particle and heavy ion transport code system–PHITS version 3.33, Journal of Nuclear Science and Technology. 61 (1) (2024) 127–135.

7. **Sato T., Iwamoto Y., Hashimoto S., Ogawa T., Furuta T., Abe S.-I., Kai T., Tsai P.-E., Matsuda N., Iwase H., Shigyo N., Sihver L., Niita K.,** Features of particle and heavy ion transport code system (PHITS) version 3.02, Journal of Nuclear Science and Technology. 55 (6) (2018) 684–690.

8. **Hirayama H., Namito Y., Nelson W.R., Bielajew A.F., Wilderman S.J.,** The EGS5 Code System, Department of Energy Stanford University: Stanford, CA, USA. (SLAC-R-730). (2005).

9. **Kai T., Yokoya A., Ukai M., Fujii K., Watanabe R.,** Thermal equilibrium and prehydration processes of electrons injected into liquid water calculated by dynamic Monte Carlo method, Radiation Physics and Chemistry. 115 (2015) 1–5.

10. **González Á.,** Measurement of areas on a sphere using Fibonacci and latitude–longitude lattices, Mathematical geosciences. 42 (2010) 49–64.

11. **Gordeev I.,** FitsGeo – Python package for PHITS geometry development and visualization, arXiv preprint arXiv:2008. 03298 (2020).

12. **Chaynikov A.P., Kochur A.G., Dudenko A.I.,** Simulation of energy absorption processes in water near the surface of gold nanoparticle under X-ray photon irradiation, Journal of Experimental and Theoretical Physics. 166 (2) (2024) 194–208.

THE AUTHORS

MARKIN Nikita S.
markkin.ns@gmail.com
ORCID: 0000-0001-8974-2235

GORDEEV Ivan S.
gordeev@jinr.ru
ORCID: 0000-0003-3120-3401

IVANNIKOV Sergey I.
fyajkfqn@mail.ru
ORCID: 0000-0002-5889-3409

SAMARDAK Aleksei Yu.
samardak.aiu@dvfu.ru
ORCID: 0000-0002-0795-374X

SAMARDAK Alexander S.
samardak.as@dvfu.ru
ORCID: 0000-0001-5917-4361

OGNEV Alexey V.
ognev.av@dvfu.ru
ORCID: 0000-0002-1619-3666

Received 11.09.2025. Approved after reviewing 25.09.2025. Accepted 29.09.2025.

ATOM PHYSICS AND PHYSICS OF CLUSTERS AND NANOSTRUCTURES

Conference materials
UDC 538.911+546.82+544.6+544.478
DOI: https://doi.org/10.18721/JPM.184.115

Fabrication of TiO_2 nanopillar arrays and their structural evolution

L.S. Volkova [1, 2] ✉, T.S. Grishin [1], 2, A.A. Dudin [1], Yu.V. Nazarkina [2],
S.V. Dubkov [2], D.G. Gromov [2], S.A. Gavrilov [2]

[1] Institute of Nanotechnology of Microelectronics RAS, Moscow, Russia;
[2] National Research University of Electronic Technology, Zelenograd, Moscow, Russia
✉ lidiya.volkova.96@mail.ru

Abstract. We report the fabrication and structural study of TiO_2 nanopillar arrays produced by two-step anodization of Al/TiN bilayer (1000 nm/250 nm). The as-prepared nanopillars are amorphous; their structural evolution was investigated upon air annealing in the 300–800 °C range. Annealing at 300 °C initiates crystallization, at 500 °C predominantly nanocrystalline anatase is formed, while at 800 °C grain growth and coexistence of anatase and rutile are observed. The array morphology (diameter ~20 nm, pitch ~50 nm, height ~150 nm) remains intact even after high-temperature treatment. These results indicate that ~500 °C is an optimal annealing condition to obtain pure anatase while preserving the nanostructured geometry, which is important for photocatalytic applications and for using TiO_2 nanopillar arrays as platforms for hybrid SERS-substrates.

Keywords: TiO_2 nanopillars, anodization, photocatalysis, anatase, rutile

Funding: This research was funded by the Russian Science Foundation (Project No. 24-19-00610), https://rscf.ru/project/24-19-00610. The samples were obtained in the laboratory "Photonic Sensorics and Plasmonic Materials" of the National Research University MIET under State Assignment FSMR-2024–0012.

Citation: Volkova L.S., Grishin T.S., Dudin A.A., Nazarkina Yu.V., Dubkov S.V., Gromov D.G., Gavrilov S.A., Fabrication of TiO_2 nanopillar arrays and their structural evolution, St. Petersburg State Polytechnical University Journal. Physics and Mathematics. 18 (4.1) (2025) 93–98. DOI: https://doi.org/10.18721/JPM.184.115

Материалы конференции
УДК 538.911+546.82+544.6+544.478
DOI: https://doi.org/10.18721/JPM.184.115

Формирование массивов наностолбиков TiO_2 и их структурная эволюция

Л.С. Волкова [1, 2] ✉, Т.С. Гришин [1, 2,] А.А. Дудин [1], Ю.В. Назаркина [2],
С.В. Дубков [2], Д.Г. Громов [2], С.А. Гаврилов [2]

[1] Институт нанотехнологий микроэлектроники РАН, Москва, Россия;
[2] Национальный исследовательский университет «МИЭТ», г. Зеленоград, Москва, Россия
✉ lidiya.volkova.96@mail.ru

Аннотация. Представлены изготовление и структурное исследование массивов наностолбиков TiO_2, полученных методом двухстадийного анодирования двухслойной

структуры Al/TiN (1000 нм/250 нм). В исходном состоянии наностолбики аморфны. Отжиг при 300 °C инициирует кристаллизацию; при 500 °C формируется преимущественно нанокристаллический анатаз; при 800 °C наблюдаются рост зерен и сосуществование анатаза и рутила. Морфология массива (диаметр ~20 нм, шаг ~50 нм, высота ~150 нм) сохраняется даже после высокотемпературной обработки без спекания столбиков. Показано, что ~500 °C является оптимальным режимом получения анатаза при сохранении наноструктурированной геометрии, что важно для фотокаталитических приложений и использования массивов наностолбиков TiO_2 как платформ для гибридных SERS-подложек.

Ключевые слова: наностолбики TiO_2, анодирование, фотокатализ, анатаз, рутил

Финансирование: Исследование выполнено при финансовой поддержке Российского научного фонда (проект № 24-19-00610), https://rscf.ru/project/24-19-00610. Образцы получены в НИЛ ФСПМ НИУ «МИЭТ» по государственному заданию FSMR-2024–0012.

Ссылка при цитировании: Волкова Л.С., Гришин Т.С., Дудин А.А., Назаркина Ю.В., Дубков С.В., Громов Д.Г., Гаврилов С.А. Формирование массивов наностолбиков TiO_2 и их структурная эволюция // Научно-технические ведомости СПбГПУ. Физико-математические науки. 2025. Т. 18. № 4.1. С. 93–98. DOI: https://doi.org/10.18721/JPM.184.115

Introduction

Titanium dioxide (TiO_2) is a popular functional material in nanotechnology due to its excellent photocatalytic properties [1–3], chemical stability, and bioinertness [4, 5]. It is widely used for photocatalytic decomposition of organic pollutants, water and air purification [6], as well as in solar energy devices [7] and sensors [8]. The photocatalytic activity of TiO_2 essentially depends on its phase state and surface morphology. Amorphous TiO_2 is known to have much lower photocatalytic activity compared to crystalline forms due to rapid recombination of charge carriers [9]. Anatase (metastable tetragonal phase of TiO_2 with a bandgap width of ~3.2 eV) usually exhibits higher photocatalytic efficiency than rutile (stable tetragonal phase with a bandgap width of ~3.0 eV) due to slower recombination of photogenerated electron-hole pairs [10]. Rutile, in turn, possessing a narrower band gap, has an absorption spectrum extended into the visible region, but the high rate of charge recombination reduces the efficiency of rutile-only photocatalysts [11]. On the other hand, a combination of phases (e.g., anatase-rutile mixed structure) can improve the total photocatalytic activity by broadening the spectral response [12]. Therefore, the control of the phase composition of TiO_2 is a key factor in the development of high-performance photocatalytic systems.

To date, many approaches to obtain nanostructured TiO_2 [13] have been proposed, ranging from sol-gel technologies [14] and hydrothermal synthesis [15] to anodic oxidation [16–18]. Among them, the anodization of massive titanium is particularly prominent, which allows the formation of highly ordered arrays of TiO_2 nanotubes directly on the metal surface [19]. Classical anodization of Ti leads to the formation of an array of densely packed hollow nanotubes. In recent years, the approach of anodizing thin films of Ti or TiN through a sacrificial Al layer has been developed, which allows to obtain arrays of vertically oriented TiO_2 nanopillars [20] separated by a certain distance. By varying the anodization modes and heat treatment conditions, it is possible to vary the geometry of such an array as well as the phase composition of TiO_2. Thus, the combined anodization of Al/TiN layers opens possibilities for the synthesis of ordered 3D nanostructured TiO_2 substrates with controlled morphology and phase state. In this work, two step anodic synthesis of TiO nanopillar arrays on Al/TiN substrate was realized and their morphology and structural evolution during thermal annealing in the range of 300–800 °C were investigated.

Materials and Methods

TiO_2 nanopillar arrays were fabricated by two-step anodization of a silicon substrate with Al/TiN/SiO_2 layers (1000 nm/250 nm/300 nm). The anodization procedure followed the scheme described in [21]. In the first step, the Al layer was anodized in a 5% H_2SO_4 electrolyte at a constant current of $I_1 = 0.07$ mA and voltage $U_1 = 30$ V for $t_1 = 2.5$ min. During this stage, a layer of nanoporous anodic aluminum oxide (AAO) was formed and subsequently removed by chemical etching in a $CrO_3 + H_2SO_4$ solution. As a result, a quasi-ordered hexagonal array of dimples was formed on the surface of the remaining Al.

In the second step, the anodization of the Al layer was carried out in the same electrolyte, starting from $U_1 = 30$ V with a voltage ramp of 1 V every 5 s up to $U_2 = 115$ V, followed by a constant-voltage anodization for $t_2 = 5$ min. At this stage, the anodic oxidation front reached the TiN layer through the thin AAO barrier layer, initiating localized oxidation of TiN at the pore bottoms and leading to the formation of vertically oriented TiO_2 nanopillars confined by the pore geometry. The remaining porous AAO was removed by a second etching in $CrO_3 + H_2SO_4$ solution for 10 min, after which the samples were rinsed with deionized water and air-dried.

To investigate the phase evolution of the fabricated TiO_2 nanopillars, the samples were annealed in air for 60 min at 300 °C, 500 °C, and 800 °C. Annealing was performed in a muffle furnace with a heating rate of ~5 °C/min. After annealing, the samples were allowed to cool naturally to room temperature together with the furnace.

The morphology of the obtained nanostructures was examined using a dual-beam scanning electron microscope (SEM) Helios G4 CX (TFS, USA). The internal structure and phase composition of the nanopillars were studied with a transmission electron microscope (TEM) JEM-2100 Plus (JEOL, Japan). For TEM analysis, thin cross-sectional lamellae of the arrays were prepared using a focused ion beam (FIB). To protect the region of interest from unwanted ion-beam damage, the samples were pre-coated with a thin amorphous carbon layer.

Results and Discussion

Fig. 1 shows typical SEM images of the fabricated TiO_2 nanopillar arrays. The top-view image (Fig. 1, *a*) confirms the regularity of the structure: the nanopillars form an ordered hexagonal array with a pitch of ~50 nm. SEM images with 52° tilt (Fig. 1, *b*) demonstrate that the nanopillars are approximately 150 nm in height. The pillars have slightly conical shape; some of them are bended at the base, but their tips are predominantly oriented perpendicular to the substrate. The nanopillar diameter at the base is ~20 nm, tapering to ~10 nm toward the top.

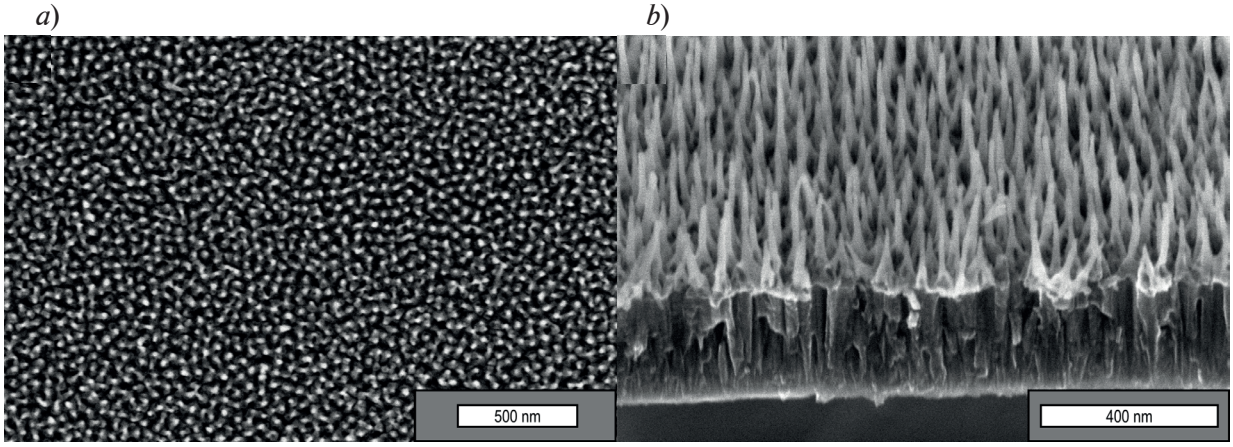

Fig. 1. SEM images of the formed array of TiO_2 nanopillars: top view (*a*), 52° view (*b*)

The nanopillars are firmly anchored to a thin continuous underlayer formed as a result of TiN anodization. This layer provides mechanical stability of the array and prevents delamination from the substrate. Thus, the two-step anodization method enabled the formation of vertically oriented TiO_2 nanopillar arrays with reproducible geometric parameters (diameter, height, and pitch), robustly fixed to the substrate. No residual Al or porous AAO fragments are observed on the surface, which confirms the completeness of the anodization and subsequent etching process.

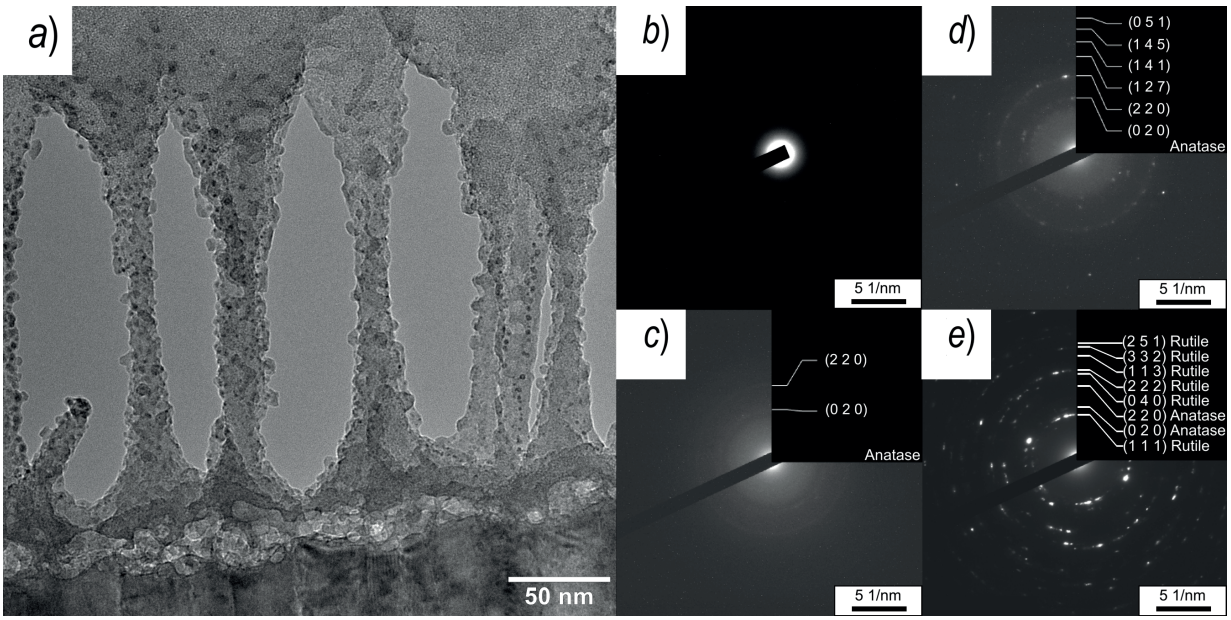

Fig. 2. TEM image of a cross-sectional view of TiO_2 nanopillars array before annealing. The nanopillars are coated with amorphous carbon, which was sputtered to protect the array from undesirable effects of the ion beam (*a*). Electron diffraction patterns obtained from unannealed (*b*), annealed at 300 °C (*c*), 500 °C (*d*), 800 °C (*e*) nanopillars

Despite their well-defined morphology, the nanopillars are amorphous immediately after anodization, as confirmed by TEM observations (Fig. 2, *a*): HRTEM images do not reveal ordered atomic planes typical of crystalline structures, and the selected area electron diffraction (SAED) pattern shows only an amorphous halo and a bright central spot corresponding to the direct beam (Fig. 2, *b*). The absence of distinct diffraction rings indicates the lack of crystalline grains of appreciable size. The high intensity of the central spot with a very weak amorphous background is explained by the fact that the electron beam passes mainly through empty space between the pillars (due to the low material filling of the selected area), so the fraction of electrons scattered by the structure is small.

Low-temperature annealing at 300 °C initiates the onset of TiO_2 crystallization, although the overall degree of crystallinity remains low. After annealing at 300 °C, the nanopillars are still predominantly amorphous; however, the SAED pattern exhibits the first signs of ordering: weak diffraction rings are observed (Fig. 2, *c*), most likely corresponding to anatase reflections. Due to the small number of reflections and low intensity of the rings, definite phase identification is not possible. It is likely that at 300 °C nanocrystallites with a size of only a few nanometers begin to form within the nanopillars.

Significant structural changes occur after annealing the nanopillars at 500 °C (Fig. 2, *d*). Direct observation of nanocrystallites in HRTEM images is complicated by the carbon coating; nevertheless, the SAED patterns clearly indicate the presence of anatase. Compared to the 300 °C sample, the amorphous halo in the 500 °C diffraction pattern is substantially weakened, and the diffraction rings have “spotty” appearance. Such “spotty” ring appearance may indicate crystallite growth and a modest orientation spread; however, this interpretation could not be confirmed by HRTEM because direct lattice imaging was limited by the carbon coating on the FIB-prepared lamella.

During annealing at 800 °C, the most pronounced changes in the phase composition of TiO_2 occur. The SAED pattern of the sample annealed at 800 °C (Fig. 2, *e*) is characterized by the appearance of well-defined diffraction rings of significantly higher intensity, with distinct spot reflections, indicating an increased degree of crystallinity. The measured interplanar spacings suggest the coexistence of both anatase and rutile phases. Thus, at 800 °C the onset of the anatase-to-rutile phase transition is observed, which is consistent with literature data on the stability ranges of TiO_2 polymorphs [22]. It should be emphasized that the nanopillar morphology is preserved after crystallization.

Conclusion

Two-step anodization of the Al/TiN structure (1000 nm/250 nm) enables the formation of quasi-ordered arrays of vertically aligned TiO_2 nanopillars with a diameter of about 20 nm and a height of ~150 nm. In the as-prepared state, the nanopillars are amorphous. Annealing at 300 °C initiates their crystallization, while annealing at 500 °C results in crystallization into the anatase phase, with preservation of the nanostructured morphology. High-temperature treatment at 800 °C leads to grain growth and the coexistence of anatase and rutile phases, while the original nanopillar morphology is retained.

Crystallization of TiO_2 into the anatase phase at ~500 °C is important for achieving high photocatalytic activity under UV irradiation. This annealing temperature can be considered optimal for realizing UV-induced photocatalytic self-cleaning of the surface. In addition, TiO_2 nanopillars can serve as a 3D-scaffold for plasmonic nanoparticles [23], opening the possibility of creating hybrid SERS substrates that combine Raman signal enhancement with photocatalytic surface self-cleaning [24].

REFERENCES

1. **Armaković S.J., Savanović M.M., Armaković S.,** Titanium Dioxide as the Most Used Photocatalyst for Water Purification: An Overview, Catalysts. MDPI AG. 13 (1) (2022) 26.

2. **Jain A., Vaya D.,** Photocatalytic activity of TiO_2 nanomaterial, J. Chil. Chem. Soc. SciELO Agencia Nacional de Investigacion y Desarrollo (ANID).62 (4) (2017) 3683–3690.

3. **Ali I., et al.,** Recent advances in syntheses, properties and applications of TiO_2 nanostructures, RSC Adv. Royal Society of Chemistry (RSC). 8 (53) (2018) 30125–30147.

4. **Racovita A.D.,** Titanium Dioxide: Structure, Impact, and Toxicity, IJERPH. MDPI AG. 19 (9) (2022) 5681.

5. **Rempel A.A., et al.,** Titanium dioxide nanotubes: synthesis, structure, properties and applications, Russ. Chem. Rev. 90 (11) (2021). 1397–1414.

6. **Muscetta M., Russo D.,** Photocatalytic Applications in Wastewater and Air Treatment: A Patent Review (2010–2020), Catalysts. MDPI AG. 11 (7) (2021) 834.

7. **Gnida P., et al.,** Impact of TiO_2 Nanostructures on Dye-Sensitized Solar Cells Performance, Materials. MDPI AG. 14 (7) (2021). 1633.

8. **Ramanavicius S., Jagminas A., Ramanavicius A.,** Gas Sensors Based on Titanium Oxides (Review), Coatings. MDPI AG. 12 (5) (2022). 699.

9. **Kéri O., et al.,** Photocatalytic Crystalline and Amorphous TiO_2 Nanotubes Prepared by Electrospinning and Atomic Layer Deposition, Molecules. MDPI AG. 26 (19) (2021) 5917.

10. **Luttrell T., et al.,** Why is anatase a better photocatalyst than rutile - Model studies on epitaxial TiO_2 films, Sci Rep. Springer Science and Business Media LLC. 4 (1) (2014).

11. **Sachs M., et al.,** Evaluation of Surface State Mediated Charge Recombination in Anatase and Rutile TiO_2, J. Phys. Chem. Lett. American Chemical Society (ACS). 7 (19) (2016) 3742–3746.

12. **Ishigaki T., et al.,** Enhanced visible-light photocatalytic activity of anatase-rutile mixed-phase nano-size powder given by high-temperature heat treatment, R. Soc. open sci. The Royal Society. 7 (1) (2020) 191539.

13. **Zuo F., et al.,** Titanium Dioxide Nanomaterials: Progress in Synthesis and Application in Drug Delivery, Pharmaceutics. MDPI AG. 16 (9) (2024) 1214.

14. **Calabrese C., et al.,** Novel Sol-Gel Synthesis of TiO_2 Spherical Porous Nanoparticles Assemblies with Photocatalytic Activity, Nanomaterials. MDPI AG. 13 (13) (2023) 1928.

15. **Nassar M., et al.,** Efficient One-Pot Hydrothermal Synthesis of TiO_2 Nanostructures for Reactive Black 5 Dye Removal: Experimental and Theoretical Insights, Processes. MDPI AG. 12 (12) (2024) 2786.

16. **Savchuk T.P., et al.,** Synthesis and investigation of multifunctional TiO_2 photocatalysts modified by metal nanoparticles, Catalysis Communications. Elsevier BV. 187 (2024) 106907.

17. **Gavrilin I., et al.,** Differences in the local structure and composition of anodic TiO_2 nanotubes annealed in vacuum and air, Applied Surface Science. Elsevier BV. 516 (2020) 146120.

18. **Szaniawska-Białas E., et al.,** Recent Advances in Preparation, Modification, and Application of Free-Standing and Flow-Through Anodic TiO_2 Nanotube Membranes, Molecules. MDPI AG. 29 (23) (2024) 5638.

19. **Cao W., Chen K., Xue D.,** Highly Ordered TiO_2 Nanotube Arrays with Engineered Electrochemical Energy Storage Performances, Materials. MDPI AG. 14 (3) (2021) 510.

20. **Sjöström T., Fox N., Su B.,** Through-mask anodization of titania dot- and pillar-like nanostructures on bulk Ti substrates using a nanoporous anodic alumina mask, Nanotechnology. IOP Publishing. 20 (13) (2009) 135305.

21. **Chen P.-L., et al.,** Self-organized titanium oxide nanodot arrays by electrochemical anodization, Applied Physics Letters. AIP Publishing. 82 (17) (2003) 2796–2798.

22. **Hanaor D.A.H., Sorrell C.C.,** Review of the anatase to rutile phase transformation, J Mater Sci. Springer Science and Business Media LLC. 46 (4) (2010) 855–874.

23. **Grishin T.S., et al.,** Evolution of morphological parameters in self-assembled Ag nanoparticle arrays for high-performance SERS, Optical Materials. Elsevier BV. 167 (2025) 117260.

24. **Wu H.-Y., et al.,** Highly Sensitive, Robust, and Recyclable TiO_2/AgNP Substrate for SERS Detection, Molecules. MDPI AG. 27 (19) (2022) 6755.

THE AUTHORS

VOLKOVA Lidiya S.
lidiya.volkova.96@mail.ru
ORCID: 0000-0003-4860-0585

DUBKOV Sergey V.
sv.dubkov@gmail.com
ORCID: 0000-0003-1507-8807

GRISHIN Timofey S.
grishin.t@outlook.com
ORCID: 0000-0001-6261-5316

GROMOV Dmitry G.
gromadima@gmail.com
ORCID: 0000-0002-4563-9831

DUDIN Alexander A.
dudin.aa@outlook.com
ORCID: 0000-0001-7617-8815

GAVRILOV Sergey A.
rector@miet.ru
ORCID: 0000-0002-2967-272X

NAZARKINA Yulia V.
engvel@mail.ru
ORCID: 0000-0002-5200-9299

Received 15.09.2025. Approved after reviewing 17.11.2025. Accepted 17.11.2025.

Conference materials
UDC 538.91+539.89+544.22
DOI: https://doi.org/10.18721/JPM.184.116

Magnesium based Si-Ge alloys under pressure: DFT evolutionary search results

Yu.V. Luniakov [1] ✉

[1] Institute of Automation and Control Processes FEB RAS, Vladivostok, Russia
✉ luniakov@iacp.dvo.ru

Abstract. The search of minimal enthalpy structures of ternary magnesium alloys of different stoichiometry $Mg_xSi_yGe_z$ under pressure $P \leq 6$ GPa has been performed using the software suite USPEX implementing the evolution algorithm combined with the density functional theory (DFT) approach. The evolutionary search has yielded new possible ternary compounds of the stoichiometries $Mg_{12}Ge_3Si$, $Mg_6Ge_4Si_3$, $Mg_6Ge_3Si_4$, Mg_6GeSi_3, $Mg_4Ge_3Si_2$, $Mg_4Ge_3Si_2$, Mg_4SiGe, and Mg_2GeSi, which have negative enthalpy of formation at pressures in the range of 0 to 10 GPa and which are not substitution solutions of Ge on Mg_2Si matrix (or Si on Mg_2Ge matrix). These compounds have metallic properties and formation enthalpies comparable to those of binary silicides Mg_2Si. Phonon spectra investigations indicate that only first five of them are stable showing no imaginary frequencies.

Keywords: $Mg_xSi_yGe_z$, crystal structure, hydrostatic pressure, evolutionary search, density functional theory

Funding: This study was carried out within the State assignment "Physics of low-dimensional structures and semiconductor nanomaterials" (Theme FWFW-2021-0002).

Citation: Luniakov Yu.V., Magnesium based Si-Ge alloys under pressure: DFT evolutionary search results, St. Petersburg State Polytechnical University Journal. Physics and Mathematics. 18 (4.1) (2025) 99–104. DOI: https://doi.org/10.18721/JPM.184.116

Материалы конференции
УДК 538.91+539.89+544.22
DOI: https://doi.org/10.18721/JPM.184.116

Кремниево-германиевые сплавы на основе магния: результаты эволюционного поиска из первых принципов

Ю.В. Луняков [1] ✉

[1] Институт автоматики и процессов управления ДВО РАН, г. Владивосток, Россия
✉ luniakov@iacp.dvo.ru

Аннотация. С помощью пакета программ USPEX, реализующих эволюционные алгоритмы на базе теории функционала плотности, был проведен поиск оптимальных структур твердых растворов магния, олова и магния разной стехиометрии $Mg_xSi_yGe_z$ под давлением $P \leq 6$ ГПа. В результате эволюционного поиска обнаружены новые возможные трехкомпонентные структуры состава $Mg_{12}Ge_3Si$, $Mg_6Ge_4Si_3$, $Mg_6Ge_3Si_4$, Mg_6GeSi_3, $Mg_4Ge_3Si_2$, $Mg_4Ge_3Si_2$, Mg_4SiGe, и Mg_2GeSi, которые имеют отрицательную энтальпию формирования в диапазоне давлений $0 < P \leq 10$ ГПа и не являются твердыми растворами замещения атомов Si атомами Ge в Mg_2Si-матрице или атомов Ge атомами Si в Mg_2Ge-матрице. Эти соединения имеют металлические свойства и их энтальпия образования соизмерима с энтальпией образования бинарных силицидов Mg_2Si. Стабильность пяти из полученных структур подтверждается расчетами их фононных спектрах, в которых не наблюдается мнимых фононных мод.

Ключевые слова: $Mg_xSi_yGe_z$, кристаллическая структура, гидростатическое давление, эволюционный поиск, методы функционала плотности

Финансирование: Исследование выполнено в рамках Государственного задания «Физика низкоразмерных структур и полупроводниковых наноматериалов» (код темы № FWFW-2021-0002).

Ссылка при цитировании: Луняков Ю.В. Кремниево-германиевые сплавы на основе магния: результаты эволюционного поиска из первых принципов // Научно-технические ведомости СПбГПУ. Физико-математические науки. 2025. Т. 18. № 4.1. С. 99–104. DOI: https://doi.org/10.18721/JPM.184.116

Introduction

Since the 1960s, Mg_2X (X = Si, Ge, Sn) compounds and their solid solutions have shown promise for thermoelectric energy conversion due to high efficiencies, high melting points, narrow band gaps, and environmental safety. These materials are used in thermal elements, infrared detectors, solar cells, and hydrogen energy storage. Despite waning interest in the early 2000s, compositional flexibility and similar crystal structures have revived interest. Mg_2Ge is soluble in Mg_2Si and *vice versa* [1–8], enhancing thermoelectric performance through improved conductivity [9]. Varying germanium concentration tailors properties for energy conversion. For example, $Mg_2Si_{1-x}Sn_x$ with low thermal conductivity is favorable for thermoelectric energy conversion [10]. However, challenges exist in forming solid solutions and optimizing microstructure. Successful synthesis requires uniform structures [11, 12], highlighting the need for thorough investigation. Further research is needed to improve properties by exploring dopants and optimizing synthesis techniques [13].

Computational methods are crucial in material discovery, being more efficient than experiments. These computational searches allow researchers to rapidly explore a wide range of systems, uncovering novel phenomena and facilitating the discovery of new promising materials. Recent successes with two-component magnesium-based compounds suggest potential for three-component $Mg_xSi_yGe_z$ alloys. Anti-fluorite structure is the only one considered in the analysis of magnesium stannides, as both magnesium silicide and magnesium germanide share this structural form. Evolutionary optimization has reproduced known phases and predicted new structures under high pressures. The aim of this study is to identify optimal structures in the three-component $Mg_xSi_yGe_z$ system using modern evolutionary optimization techniques [14], and to investigate the stability of these structures both at ambient pressure conditions as well as at pressures ranging from 0 to 10 GPa.

Calculation procedure

For evolutionary modeling of the three-component Mg-Si-Ge system, Universal Structure Predictor: Evolutionary Xtallography (USPEX) algorithms were applied in the variable composition mode [15–17]. During the evolutionary search, from 40 to 60 generations of structures were produced depending on the convergence, which was considered to be achieved when the most energetically favorable structure remained unchanged for 20 consecutive generations. Each generation contained 20 structures and the first generation contained more than 120 structures, with 4 to 32 atoms per every structure. The structures of the first generation were randomly selected from the list of 230 space groups. In the following generations, 50% of the lowest-energy structures were inherited from the previous generation, 10% of the structures were produced by lattice mutation, 10% of the structures were obtained by atom transmutation, and the remaining 30% of the structures were generated randomly. All USPEX generated structures were then relaxed using the conjugate gradient method implemented in the VASP software [18], the one-electron wave functions were expanded in a plane-wave basis with a kinetic energy cutoff of E_{cut} = 500 eV. The exchange-correlation potential chosen based on the Purdue-Burke-Ernzerhof parameterization in the generalized gradient approximation [19]. Brillouin zone sampling was

performed using a Monkhorst-Pack mesh with a *k*-point resolution of $\pi\times0.1$ Å^{-1}. The enthalpy at a zero temperature was determined using relationship $F = E + PV$, where E is the total energy, P is the external pressure, and V is the primitive cell volume.

Results and Discussion

For calculations of three-component structures at ambient pressure conditions it is useful to carry out their studies at several pressures [20–22]. Then there are quite a lot of them compared to the calculations at ambient pressure conditions, which allows to study their $E(P)$ dependences in more detail and to select the most stable compounds. Three pressure values of 1 GPa, 4 GPa and 6 GPa were used to calculate germanium-silicon alloys and more than five and a half thousand structures were obtained by evolutionary search. Thus, if at 6 GPa we more than a hundred structures with negative enthalpy of formation, at 4 GPa there are only two, and at 1 GPa there are only three with energy close to zero. Since too few three-component systems are stable at low pressures, the structures obtained at non-zero pressures were used for their calculation, as will be shown below.

Table shows the lattice parameters and enthalpies of formation of the most stable convex hull compounds of magnesium, silicon and germanium obtained by evolutionary methods at external hydrostatic pressures of 1, 4 and 6 GPa. At a pressure of $P = 1$ GPa, the convex hull is formed by five vertices, one of which corresponds to the ternary compound Mg_6GeSi_3 of space group 146 and two of which correspond to the binary silicides Mg_2Si and Mg_3Si_2 of space groups 129 and 167, respectively.

Table

Structures, corresponding to the vertices of the convex shell at pressures of 1, 4 and 6 GPa

Pressure/ Composition	Lattice parameters	Symmetry
1 GPA/ Mg_6Si_3Ge	$a = b = c = 7.46$ Å, $\alpha = \beta = 90°$, $\gamma = 120°$	*R*3 (146)
1 GPA/ Mg_3Si_2	$a = b = 7.44$ Å, $c = 12.22$ Å, $\alpha = \beta = \gamma = 90°$	*R*-3*C* (167)
1 GPA/ Mg_2Si	$a = b = 4.14$ Å, $c = 6.90$ Å, $\alpha = \beta = \gamma = 90°$	*P*4/*nmm* (129)
4 GPA/ $Mg_6Si_4Ge_3$	$a = 8.4$ Å, $b = 5.31$ Å, $c = 5.25$ Å, $\alpha = 93.9°$, $\beta = 90.2°$, $\gamma = 95.3°$	*P*1(1)
4 GPA/ $Mg_6Si_3Ge_4$	$a = 8.46$ Å, $b = 5.34$ Å, $c = 5.26$ Å, $\alpha = 93.8°$, $\beta = 90.4°$, $\gamma = 95.6°$	*P*1(*1*)
4 GPA/ Mg_2Si	$a = b = c = 6.23$ Å, $\alpha = \beta = 90°$, $\gamma = 120°$	$Fm\bar{3}m$ (225)
6 GPA/ Mg_2SiGe	$a = 4.17$ Å, $b = 3.66$ Å, $c = 5.00$ Å, $\alpha = 90°$, $\beta = 70.6°$, $\gamma = 90°$	*Pm* (6)
6 GPA/ $Mg_4Si_2Ge_3$	$a = 5.06$ Å, $b = 8.46$ Å, $c = 8.04$ Å, $\alpha = 78.0°$, $\beta = 90.5°$, $\gamma = 73.3°$	*P*1(1)
6 GPA/ Mg_6Si_3Ge	$a = 4.95$ Å, $b = 5.68$ Å, $c = 6.59$ Å, $\alpha = 76.3°$, $\beta = 103.9°$, $\gamma = 98.1°$	*P*1(1)
6 GPA/ Mg_2Si	$a = b = 4.52$ Å, $c = 5.82$ Å, $\alpha = \beta = 90°$, $\gamma = 120°$	$P6_3/mmc$ (194)
6 GPA/ MgSi	$a = 5.38$ Å, $b = 5.25$ Å, $c = 5.19$ Å, $\alpha = 89.4°$, $\beta = 79.7°$, $\gamma = 111.4°$	*P*-*1*(2)
6 GPA/ $MgSi_3$	$a = b = 7.62$ Å, $c = 15.05$ Å, $\alpha = \beta = 90°$, $\gamma = 120°$	*R*-3*m* (166)

The remaining two structures, corresponding to the bulk structures of germanium and silicon, are not shown in Table and described below. At a pressure $P = 4$ GPa, the convex hull includes bulk Ge and Si structures, two asymmetric ternary compounds $Mg_6Ge_4Si_3$ and $Mg_6Ge_3Si_4$, and a binary silicide Mg_2Si of correctly defined space symmetry group 225. At a pressure $P = 6$ GPa, the convex hull is formed by three ternary alloys $Mg_4Si_2Ge_3$, Mg_6Si_3Ge, Mg_2SiGe and three binary silicides of different stoichiometries from 2/3 of Mg and 1/3 of Si (Mg_2Si) to 1/4 of Mg and 3/4 of Si ($MgSi_3$), in addition to the bulk Ge and Si structures. The ternary alloys at this pressure have symmetries down to 1 (P1) for $Mg_4Si_2Ge_3$ and Mg_6Si_3Ge and 6 (Pm) for Mg_2GeSi. The binary silicides have symmetries as low as 2 for MgSi and as high as 166 for $MgSi_3$ and 194 for Mg_2Si.

For a detailed study of the stability of energetically favorable structures under various pressures, Table results were recalculated for pressures from 0 to 10 GPa with geometry re-optimization. Fig. shows the most stable structures with negative formation enthalpy obtained by optimizing evolutionary search results. It also includes calculations for ternary compounds formed by Sn→Ge substitution or rearrangement in Mg-Si-Sn structures [23], as well as optimized convex hull structures from Si↔Ge atom exchange. Surprisingly, these structures are more stable than those obtained from evolutionary search. For example, Mg_6SiGe_3, derived from Mg_6Si_3Ge by Si↔Ge atoms exchange and relaxation, is the most stable structure in the 1.15–10 GPa range. At ambient

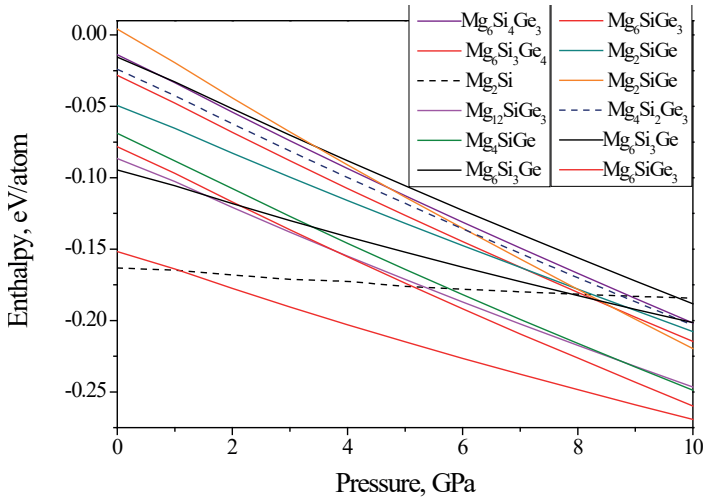

Fig. Enthalpy-pressure $E(P)$ dependence for the most energetically favorable crystal structures obtained by optimizing the results of the evolutionary search and their corresponding derivatives from the Mg-Si-Sn structures (see text for details)

pressure, only the cubic anti-fluorite Mg_2Si structure ($Fm\bar{3}m$ symmetry) is more stable than them. Linear extrapolation from Fig. suggests Mg_6Si_3Ge will become less stable at around 11.5 GPa, with Mg_4SiGe being the most stable above 15 GPa. $Mg_{12}SiGe3$ structure (I4/mmm symmetry) was created from $Mg_{12}SiSn_3$ by replacing Sn atoms with Ge ones. Another structure, Mg_4SiGe (P-1 symmetry), was derived similarly from Mg_4SiSn, At pressures $P > 44$ GPa, Mg_4SiGe becomes more stable than both Mg_6SiGe_3 structures. Mg_6Si_3Ge structures from evolutionary search, shown on Fig., are lower in enthalpy than Mg_2Si one at pressures $P > 8$ GPa, but higher than $Mg_6Si_3Ge_4$ and Mg_2SiGe ones at $P = 4$ GPa and $P = 6$ GPa, respectively. The latter structures may become more stable at higher pressures based on linear extrapolation of $E(P)$ dependencies. Therefore, their electronic structures should also be examined.

In order to investigate the conductive properties of three-component systems at ambient pressure conditions, the band structures and total density of states of the most energetically favorable compounds $Mg_xSi_yGe_z$ have been calculated. All of the alloys considered have states at the Fermi level, indicating that they all exhibit metallic properties to some extent, unlike the binary compounds Mg_2Si and Mg_2Ge, which are semiconductors under normal conditions.

To verify the dynamical stability of three-component alloys, phonon dispersion curves at ambient pressure conditions have been calculated for most of the lowest energy structures – see additive materials in [24]). This analysis was conducted by deriving force constants from atomic

forces and displacements, as implemented in the PHONOPY code [25, 26]. The results indicate that the phonon dispersion curves do not exhibit any imaginary frequencies for $Mg_{12}Ge_3Si$, $Mg_6Ge_4Si_3$, $Mg_6Ge_3Si_4$, triclinic Mg_6SiGe_3, $Mg_4Ge_3Si_2$, thereby confirming the stability of the respective compounds. In contrast, the spectra of hexagonal Mg_6SiGe_3, orthorhombic Mg_2SiGe and monoclinic Mg_4SiGe structures displays a pronounced negative dip near special k-points (see additive materials in [24]), providing evidence for their instability relative to the other ones. Nevertheless, structures energetically favorable at high pressures non-symmetric Mg_6SiGe_3 and cubic $Mg_{12}SiGe_3$ are still stable, which makes it possible for them to exist along with the known Mg_2Si and Mg_2Ge structures.

Conclusion

The results of the evolutionary search of three-component systems allowed to obtain new possible structures of the stoichiometries Mg_6SiGe_3, Mg_6GeSi_3, $Mg_{12}Ge_3Si$, Mg_4SiGe, $Mg_4Ge_3Si_2$, Mg_2SiGe, $Mg_6Si_4Ge_3$ and $Mg_6Si_3Ge_4$ with the ternary compound $Mg_{12}Ge_3Si$ being the most stable one. All of them have a negative enthalpy of formation, comparable to the enthalpy of formation of binary structures Mg_2Si and Mg_2Ge in the studied pressure range $0 < P \leq 10$ GPa. Phonon dispersion and density of states calculations confirmed the dynamical stability and metallic properties of the newly identified ternary alloys besides the Mg_2SiGe, Mg_4SiGe and Mg_6SiGe_3 ones. Density of states calculations indicate the ternary alloys exhibit metallic properties, unlike the binary silicides and germanides.

Acknowledgments

All calculations were carried out using IACP FEB RAS Shared Resource Center “Far Eastern Computing Resource” equipment (https://cc.dvo.ru).

REFERENCES

1. **Akasaka M., Iida T., Nishino K., Takanashi Y.,** Composition dependent thermoelectric properties of sintered $Mg_2Si_{1-x}Ge_x$ (x = 0 to 1) initiated from a melt-grown polycrystalline source, Thin Solid Films. 515(22) (2007) 8237–8241.

2. **Hayakawa Y., et al.,** Growth of homogeneous polycrystalline $Si_{1-x}Ge_x$ and $Mg_2Si_{1-x}Ge_x$ for thermoelectric application, Thin Solid Films. 519(24) (2011) 8532–8537.

3. **Viennois R., Colinet C., Jund P., Tedenac J.C.,** Phase stability of ternary antifluorite type compounds in the quasi-binary systems Mg_2X–Mg_2Y (X, Y= Si, Ge, Sn) via ab-initio calculations, Intermetallics. 31 (2012) 145–151.

4. **You S.W., Kim I.H.,** Thermoelectric properties of $Mg_2Si_{1-x}Ge_x$ prepared by using a solid-state reaction, Journal of the Korean Physical Society. 64 (5) (2014) 690–694.

5. **Bhattacharya S., Madsen G.K.H.,** High-throughput exploration of alloying as design strategy for thermoelectrics, Physical Review. B. 92 (8) (2015) 085205.

6. **Zhang L.M., Leng Y.G., Jiang H.Y., Chen L.D., Hirai T.,** Synthesis of $Mg_2Si_{1-x}Ge_x$ thermoelectric compound by solid phase reaction, Materials Science and Engineering B. 86 (3) (2001) 195–199.

7. **Aizawa T., Song R., Yamamoto A.,** Solid-state synthesis of thermoelectric materials in Mg-Si-Ge system, Materials transactions. 46 (7) (2005) 1490–1496.

8. **Mizuyoshi Y., Yamada R., Ohishi T., Saito Y., Koyama T., Hayakawa Y., Matsuyama T., Tatsuoka H.,** Growth of $Mg_2Si_{1-x}Ge_x$ layers on silicon–germanium substrates, Thin Solid Films. 508(1-2) (2006) 70–73.

9. The International Energy Agency (IEA), URL: https://www.iea.org.

10. **Beretta D., Neophytou N., Hodges J.M., Kanatzidis M.G., Narducci D., Martin-Gonzalez M., Beekman M., Balke B., Cerretti G., Tremel W., Zevalkink A.,** Thermoelectrics: From history, a window to the future, Materials Science and Engineering: R: Reports. 138 (2019) 100501.

11. **Clark C.R., Wright C., Suryanarayana C., Baburaj E.G. and Froes F.H.,** Synthesis of Mg_2X (X = Si, Ge, or Sn) intermetallics by mechanical alloying, Materials Letters. 33 (1997) 71–75.

12. **Busch G., Winkler U.,** Elektrische Leitfahigkeit Und Hall-Effekt Intermetallischer Verbindungen, Helvetica Physica Acta. 26 (3-4) (1953) 395–398.

13. **Laboz R.J., Mason D.R., Okane D.F.,** The thermoelectric properties of mixed crystals of $Mg_2Ge_xSi_{1-x}$, Journal of the Electrochemical Society. 110 (1963) 127–134.
14. **Oganov A.R., Pickard C.J., Zhu Q., Needs R.J.,** Structure prediction drives materials discovery, Nature Reviews Materials. 4 (5) (2019) 331–348.
15. **Lyakhov A.O., Oganov A.R., Stokes H.T., Zhu Q.,** New developments in evolutionary structure prediction algorithm USPEX, Computer Physics Communications. 184 (4) (2013) 1172–1182.
16. **Oganov A.R., Lyakhov A.O., Valle M.,** How Evolutionary Crystal Structure Prediction Works – and Why, Accounts of chemical research. 44 (3) (2011) 227–237.
17. **Oganov A.R., Glass C.W.,** Crystal structure prediction using ab initio evolutionary techniques: Principles and applications, The Journal of chemical physics. 124 (24) (2006) 244704.
18. **Kresse G., Furthmuller J.E.,** Efficient iterative schemes for ab initio total-energy calculations using a plane-wave basis set, Physical Review B. 54 (16) (1996) 11169–11186.
19. **Perdew J.P., Burke K., Ernzerhof M.,** Generalized Gradient Approximation Made Simple, Physical Review Letters. 77 (18) (1996) 3865–3868.
20. **Lunyakov Yu.V.,** Mg_2Si silicide under pressure: first-principles evolution search results, Physics of the Solid State. 62 (5) (2020) 880–884.
21. **Lunyakov Yu.V.,** Mg_2Sn stannide under pressure: first-principles evolutionary search results. Physics of the Solid State. 63 (4) (2021) 590–594.
22. **Lunyakov Yu.V.,** Mg_2Ge germanide under pressure: first principle evolutionary search results, Physics of the Solid State. 64 (10) (2022) 1414–1419.
23. **Lunyakov Yu.V.,** Magnesium based tin-silicon alloys under pressure: first-principles evolution search results, Nanosystems: physics, chemistry, mathematics. 15 (2024) 621–631.
24. **Lunyakov Yu.V.,** Phonon dispersion curves of Mg-Si-Ge compounds, see files in https://doi.org/10.17605/OSF.IO/KE2J8.
25. **Togo A., Chaput L., Tadano T., Tanaka I.,** Implementation strategies in phonopy and phono3py, Journal of Physics: Condensed Matter. 35 (35) (2023) 353001.
26. **Togo A.,** First-principles phonon calculations with Phonopy and Phono3py. Journal of the Physical Society of Japan. 92 (1) (2023) 012001.

THE AUTHORS

LUNIAKOV Yuriy V.
luniakov@iacp.dvo.ru
ORCID: 0000-0002-6254-0972

Received 16.09.2025. Approved after reviewing 17.11.2025. Accepted 19.11.2025.

Conference materials
UDC 539.24
DOI: https://doi.org/10.18721/JPM.184.117

Methodology for quantitative analysis of interparticle spacings in arrays of nanoparticles on solid-state substrates

T.S. Grishin [1, 2] ✉, L.S. Volkova [1, 2], A.A. Dudin [1],
S.V. Dubkov [2], D.G. Gromov [2], S.A. Gavrilov [2]

[1] Institute of Nanotechnology of Microelectronics, Moscow, Russia;
[2] National Research University of Electronic Technology, Zelenograd, Moscow, Russia
✉ grishin.t@outlook.com

Abstract. A methodological approach is presented for quantitative analysis of geometric parameters of nanoparticle arrays, in particular the measurement of interparticle spacings, using a Delaunay triangulation algorithm. The development is motivated by the critical role of interparticle spacings in the formation of "hot spots" in surface-enhanced Raman scattering (SERS). The algorithm for automatic identification of nanoparticle centers in microscopy images and calculation of distances between nearest neighboring particles via Delaunay triangulation is described, along with data filtering criteria and the accounting of boundary effects to improve statistical reliability. The methodology is demonstrated on self-assembled arrays of nanoparticles obtained by thermal annealing of thin Ag films. The advantages of the proposed method and its limitations are discussed. The originality of the approach and its applicability to nanometrology and morphological analysis of nanostructured surfaces are emphasized.

Keywords: nanoparticles, interparticle spacings, Delaunay triangulation, SERS, hot spots, nanometrology, surface morphology

Funding: This research was funded by the Russian Science Foundation (Project No. 24-19-00610), https://rscf.ru/project/24-19-00610. The samples were obtained in the laboratory "Photonic Sensorics and Plasmonic Materials" of the National Research University MIET under State Assignment FSMR-2024–0012.

Citation: Grishin T.S., Volkova L.S., Dudin A.A., Dubkov S.V., Gromov D.G., Gavrilov S.A., Methodology for quantitative analysis of interparticle spacings in arrays of nanoparticles on solid-state substrates, St. Petersburg State Polytechnical University Journal. Physics and Mathematics. 18 (4.1) (2025) 105–110. DOI: https://doi.org/10.18721/JPM.184.117

Материалы конференции
УДК 538.911+546.82+544.6+544.478
DOI: https://doi.org/10.18721/JPM.184.117

Методика количественного анализа межчастичных расстояний в массивах наночастиц на твердотельных подложках

Т.С. Гришин [1, 2] ✉, Л.С. Волкова [1, 2], А.А. Дудин [1],
С.В. Дубков [2], Д.Г. Громов [2], С.А. Гаврилов [2]

[1] Институт нанотехнологий микроэлектроники РАН, Москва, Россия;
[2] Национальный исследовательский университет «МИЭТ», г. Зеленоград, Москва, Россия,
✉ grishin.t@outlook.com

Аннотация. В работе представлена методика количественного анализа геометрических параметров массивов наночастиц, в частности межчастичных расстояний,

с использованием алгоритма триангуляции Делоне. Актуальность такого подхода обусловлена ключевой ролью межчастичных зазоров в формировании «горячих точек» в спектроскопии гигантского комбинационного рассеяния (ГКР). В работе описан подход к автоматическому определению центров наночастиц на микроскопических изображениях и вычислению расстояний между ближайшими соседними наночастицами, включая фильтрацию данных и учет краевых эффектов для повышения статистической надежности. Методика продемонстрирована на примере самоорганизованных массивов наночастиц, сформированных при термическом отжиге тонких пленок Ag. Обсуждаются преимущества предложенного подхода и его ограничения, а также его применимость в нанометрологии и морфологическом анализе наноструктурированных поверхностей.

Ключевые слова: наночастицы, межчастичные расстояния, триангуляция Делоне, SERS, горячие точки, нанометрология, морфология поверхности

Финансирование: Исследование выполнено при финансовой поддержке Российского научного фонда (проект № 24-19-00610), https://rscf.ru/project/24-19-00610. Образцы получены в НИЛ ФСПМ НИУ «МИЭТ» по государственному заданию FSMR-2024–0012.

Ссылка при цитировании: Гришин Т.С., Волкова Л.С., Дудин А.А., Дубков С.В., Громов Д.Г., Гаврилов С.А., Методика количественного анализа межчастичных расстояний в массивах наночастиц на твердотельных подложках // Научно-технические ведомости СПбГПУ. Физико-математические науки. 2025. Т. 18. № 4.1. С. 105–110. DOI: https://doi.org/10.18721/JPM.184.117

Introduction

Formation of arrays of plasmonic nanoparticles on solid surfaces is actively used to create substrates exhibiting the surface-enhanced Raman scattering (SERS) effect [1]. One of the most technologically straightforward methods for forming such arrays is the self-assembly of nanoparticles by thermal annealing of thin metal films [2]. At the same time, they do not possess the strict regularity achieved by lithographic methods, but significantly surpass structures obtained in liquid-phase processes in terms of the uniformity of spatial distribution [3]. Nevertheless, the morphology of such arrays remains sensitive to the formation conditions, which requires its quantitative control [4].

The efficiency of SERS signal enhancement in such arrays is largely determined by their morphology: particle size, array density, and, in particular, interparticle spacing. Narrow gaps between nanoparticles lead to the formation of so-called “hot spots” [5], providing maximal enhancement. As we showed previously [6], for arrays of silver nanoparticles the optimal gap is on the order of 20 nm, whereas an increase beyond ~40 nm leads to a sharp decrease in the probability of hot-spot formation.

For optimal tuning, a quantitative morphological analysis is required, including the evaluation of the distribution of interparticle spacings. While existing approaches to evaluate the mean nanoparticle size [7], particle sphericity [8], and array density are satisfactory, traditional approaches to estimate the mean interparticle spacing (e.g. manual measurements or indirect, density-based estimates) are subjective or labor-intensive. In this work, we present a methodological approach for automated evaluation of interparticle spacings in arrays of plasmonic nanoparticles based on Delaunay triangulation. The approach is demonstrated on arrays of nanoparticles formed by annealing a thin Ag film.

Materials and Methods

Ag nanoparticle arrays were formed on Si (100) substrates with a thermally grown SiO_2 layer 300 nm thick. Thin Ag films with equivalent thicknesses of 2–12 nm were deposited by magnetron sputtering (Q300TD Plus, Quorum, UK) using a 99.995% Ag target. The base pressure was

~1 × 10^{-5} mbar and the argon working pressure was ~1 × 10^{-2} mbar. Thermal annealing was carried out at 80–300 °C in N_2 for 10 min. The sample morphology was examined by scanning electron microscopy (Helios G4 CX, Thermo Fisher Scientific, USA), and the images were used as input data for subsequent quantitative analysis of interparticle spacings.

Results and Discussion

To quantitatively evaluate interparticle spacings in arrays of plasmonic nanoparticles, we employed an algorithm based on Delaunay triangulation [9]. This approach objectively identifies pairs of nearest neighbors and computes the distribution of distances across the entire array. The main steps of the method are outlined below.

At the first step, images of nanoparticle arrays are processed using a watershed segmentation algorithm based on the classical Vincent algorithm [10]. This approach makes it possible to correctly identify individual nanoparticles, including segmentation of closely spaced objects. After segmentation, the coordinates of their centers of mass (x_i, y_j) are determined and used for subsequent calculations.

At the second step, a Delaunay triangulation is constructed over the set of nanoparticle centroid coordinates – the plane is partitioned into triangles such that no other point lies inside the circumcircle of any triangle. Owing to this property, the edges of the triangulation connect nearest-neighbor pairs, which enables identification of nanoparticle pairs for the subsequent calculation of interparticle spacings.

At the third step, for each pair of neighboring nanoparticles (i, j), defined by the edges of the triangulation, the Euclidean distance between their centers is calculated (1):

$$d_{ij}^{\text{center}} = \sqrt{\left(x_i - x_j\right)^2 + \left(y_i - y_j\right)^2}. \quad (1)$$

The resulting array d_{ij} describes the distribution of center-to-center distances across the entire nanoparticle array. From this dataset, statistical parameters can be calculated, such as the mean center-to-center distance.

In the fourth step, the center-to-center distances are, if necessary, converted into edge-to-edge (interparticle) distances (2):

$$d_{ij}^{\text{spacing}} = d_{ij}^{\text{center}} - \left(r_i + r_j\right), \quad (2)$$

where r_i и r_j are the radii of the corresponding nanoparticles.

Since real nanoparticles are not ideal spheres, the radius of an equivalent disk is used as a size metric (3):

$$r_{eq} = \sqrt{\frac{S}{\pi}}, \quad (3)$$

where S is the projected area of the particle in the image.

When analyzing the data, filtering criteria must be applied to exclude distorting factors and random artifacts. First, any incorrectly identified "particles" should be excluded – for example, small noise objects from segmentation or fused agglomerates that do not represent individual nanoparticles. To achieve this, constraints on the allowable range of object area/size are introduced at the segmentation stage (for instance, objects much smaller or larger than typical nanoparticles in the sample are excluded by default).

Secondly, after constructing the Delaunay triangulation, it may be necessary to filter out edges that do not correspond to true nearest neighbors. While the triangulation generally links actual nearest neighbors, in cases of non-uniform nanoparticle distribution some edges may be significantly longer than the average. Excessively large distances between points indicate that, although these particles are connected by a triangulation edge, they are in fact too far apart. In the context of plasmonic resonance interactions, such particles cannot be considered nearest neighbors. Therefore, an upper threshold $d_{\max}$ can be introduced for d_{ij}, with edges exceeding this value excluded from the statistics. The threshold is selected based on physical considerations; filtering by dmax allows one to focus specifically on local interparticle distances that are critical for the formation of "hot spots".

When analyzing nanoparticle arrays, particular care must be taken with those located at the image boundaries. A nanoparticle situated near the edge of the image may not have all of its nearest neighbors within the field of view; as a result, the Delaunay triangulation for such a limited dataset connects it only with neighbors inside the frame, often yielding overestimated distances. Moreover, for a nanoparticle positioned at the image boundary (whose projected area is only partially captured), the equivalent disk radius will be strongly underestimated. To eliminate systematic error, the influence of boundary nanoparticles must be minimized. Therefore, in the analysis, only nanoparticles fully contained within the image area should be considered. An alternative or complementary approach involves introducing an artificial boundary: beyond the image, mirror reflections of edge nanoparticles are drawn, creating the effect of a periodic continuation of the structure. When the triangulation is constructed, this artificial periphery makes it possible to obtain more accurate connections for boundary nanoparticles.

To obtain reliable estimates of interparticle distances, a sufficiently large sample size is required – an analysis of hundreds of nanoparticles and thousands of neighbor pairs usually provides the necessary statistics. The assessment of stability includes not only the mean value but also measures of dispersion: the standard deviation (σ), the coefficient of variation ($C_{var} = \sigma/d_{avg}$). As the number of analyzed nanoparticles increases, the error of the mean decreases as (4):

$$\Delta d = \frac{\sigma}{\sqrt{M}}, \tag{4}$$

where M is the number of neighbor pairs.

In addition, the shape of the distance distribution is also taken into account. In real arrays, it may deviate from a purely random form due to correlations in particle arrangement: regular structures lead to a narrowing of the distribution, whereas aggregation results in a “tail” of large distances. Constructing histograms and evaluating their characteristics makes it possible to identify and describe these features in the arrays.

Example of application

The proposed methodology was applied to analyze the evolution of morphological parameters in arrays of silver nanoparticles formed by thermal annealing of discontinuous Ag films with equivalent thicknesses of 2–12 nm on Si/SiO_2 substrates [6]. Figure 1 shows typical SEM images for a series of samples: with increasing annealing temperature, the nanoparticles grow larger and the structure becomes less dense as a result of fragmentation, surface diffusion, Ostwald ripening, and coalescence.

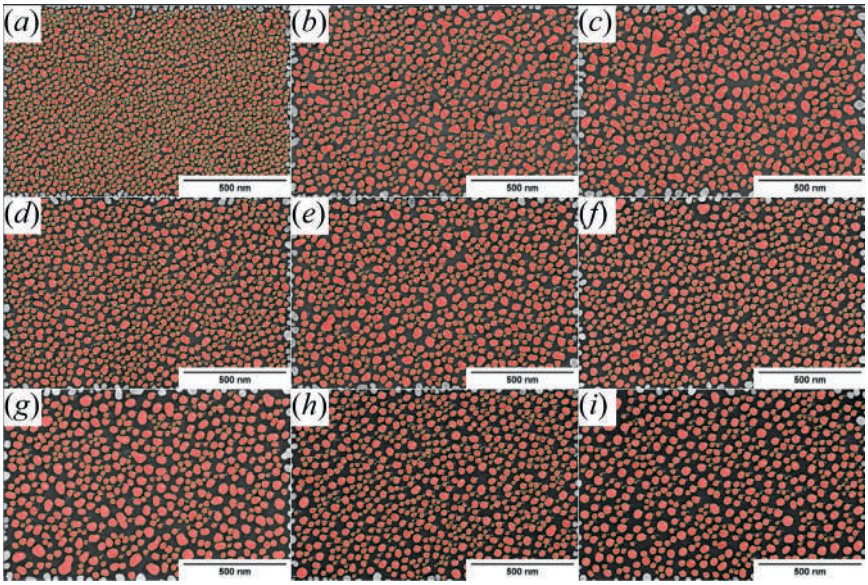

Fig. 1. Morphology of Ag nanoparticle arrays obtained by annealing a 6 nm thick film at different temperatures: (*a*) without annealing; (*b*) 80 °C; (*c*) 90 °C; (*d*) 100 °C, (*e*) 110 °C, (*f*) 120 °C, (*g*) 140 °C, (*h*) 160 °C, (*i*) 200 °C

Each image was analyzed using the Delaunay triangulation method, which made it possible to automatically determine the distribution of interparticle distances. Figure 2 shows the dependence of the mean distance on the annealing temperature for films of different initial thicknesses. For thinner initial films (≤ 6 nm), a monotonic increase in interparticle distance is observed, whereas for thicker films (≥ 8 nm), non-monotonic trends appear, associated with the competition between particle coalescence and growth.

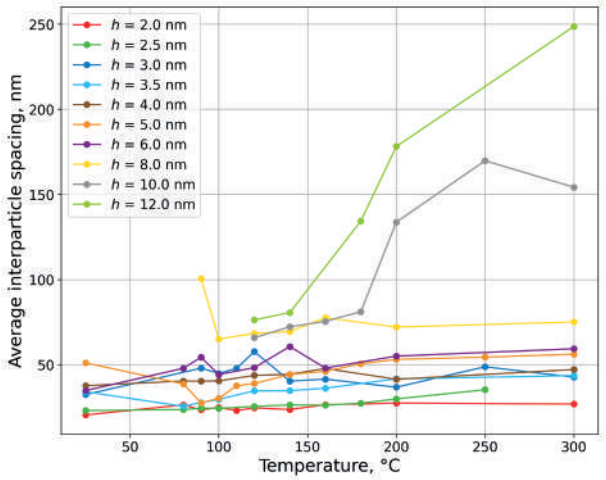

Fig. 2. Dependence of the mean interparticle spacing between Ag nanoparticles on annealing temperature for different initial film thicknesses [6]

Conclusion

A methodological approach has been proposed for the quantitative evaluation of interparticle distances in arrays of plasmonic nanoparticles based on Delaunay triangulation. The method makes it possible to automate the processing of microscopic images, objectively identify pairs of neighboring nanoparticles, and calculate distance distributions while accounting for filtering criteria and the exclusion of boundary particles. The methodology described in this work was implemented in a software developed in Python 3 [11].

The application of the methodology to arrays of silver nanoparticles formed by thermal annealing of thin films demonstrated its effectiveness for analyzing morphological evolution. The obtained dependencies of the mean interparticle distance on annealing temperature and initial film thickness reflect the competition between fragmentation, diffusion, and coalescence processes.

The described approach represents a convenient and reproducible tool for nanometrology, enabling the correlation of morphological characteristics with the functional properties of nanostructured substrates.

REFERENCES

1. **Schlücker S.,** Surface-Enhanced Raman Spectroscopy: Concepts and Chemical Applications, Angew Chem Int Ed. Wiley. 53 (19) (2014). 4756–4795.

2. **Gromov D.G., et al.,** Optimization of nanostructures based on Au, Ag, Au Ag nanoparticles formed by thermal evaporation in vacuum for SERS applications, Applied Surface Science. Elsevier BV. 489 (2019) 701–707.

3. **Barad H.-N., et al.,** Large Area Patterning of Nanoparticles and Nanostructures: Current Status and Future Prospects, ACS Nano. American Chemical Society (ACS). 15 (4) (2021) 5861–5875.

4. **Seney C.S., Gutzman B.M., Goddard R.H.,** Correlation of Size and Surface-Enhanced Raman Scattering Activity of Optical and Spectroscopic Properties for Silver Nanoparticles, J. Phys. Chem. C. American Chemical Society (ACS). 113 (1) (2008) 74–80.

5. **Chen A., et al.,** Self-Assembled Large Au Nanoparticle Arrays with Regular Hot Spots for SERS, Small. Wiley. 7 (16) (2011) 2365–2371.

6. **Grishin T.S., et al.,** Evolution of morphological parameters in self-assembled Ag nanoparticle arrays for high-performance SERS, Optical Materials. Elsevier BV. 167 (2025) 117260.

7. **Teulon J.-M., et al.,** On the Operational Aspects of Measuring Nanoparticle Sizes, Nanomaterials. MDPI AG. 9 (18) (2018) 18.

8. **Szerakowska S., et al.,** Comparison of Methods Determining Particle Sphericity, AMM. Trans Tech Publications, Ltd. 797 (2015) 231–237.

9. **Lee D.T., Schachter B.J.,** Two algorithms for constructing a Delaunay triangulation, International Journal of Computer and Information Sciences. Springer Science and Business Media LLC. 9 (3) (1980) 219–242.

10. **Vincent L., Soille P.,** Watersheds in digital spaces: an efficient algorithm based on immersion simulations, IEEE Trans. Pattern Anal. Machine Intell. Institute of Electrical and Electronics Engineers (IEEE). 13 (6) (1991) 583–598.

11. **Grishin T.S., et al.,** Software Nanoparticle Array Analyzer for automated analysis of mask images of nanoparticle arrays on substrates, Certificate of State Registration of Computer Program No. 2024691686, Federal Service for Intellectual Property (Rospatent), Russia, Registered on December 23, 2024. Application No. 2024689298, filed on December 4, 2024.

THE AUTHORS

GRISHIN Timofey S.
grishin.t@outlook.com
ORCID: 0000-0001-6261-5316

DUBKOV Sergey V.
sv.dubkov@gmail.com
ORCID: 0000-0003-1507-8807

VOLKOVA Lidiya S.
lidiya.volkova.96@mail.ru
ORCID: 0000-0003-4860-0585

GROMOV Dmitry G.
gromadima@gmail.com
ORCID: 0000-0002-4563-9831

DUDIN Alexander A.
dudin.aa@outlook.com
ORCID: 0000-0001-7617-8815

GAVRILOV Sergey A.
rector@miet.ru
ORCID: 0000-0002-2967-272X

Received 18.09.2025. Approved after reviewing 01.11.2025. Accepted 03.11.2025.

PHYSICAL OPTICS

Conference materials
UDC 535.8
DOI: https://doi.org/10.18721/JPM.184.118

Formation of 2D laser-induced periodic surface structures on metal and phase change materials

V.E. Fedyaj [1, 2] ✉, K.A. Bronnikov [3], A.E. Simanchuk [1], P.I. Lazarenko [4], A.O. Yakubov [4], A.Yu. Zhizhchenko [5], A.A. Kuchmizhak [5, 6], A.V. Dostovalov [1, 2]

[1] Institute of Automation and Electrometry of the Siberian Branch of the RAS, Novosibirsk, Russia;
[2] Novosibirsk State University, Novosibirsk, Russia;
[3] ITMO University, St. Petersburg, Russia;
[4] National Research University of Electronic Technology, Zelenograd, Moscow, Russia;
[5] Institute of Automation and Control Processes FEB RAS, Vladivostok, Russia;
[6] Far Eastern Federal University, Vladivostok, Russia
✉ fedyajve@iae.nsk.su

Abstract. The laser-induced periodic surface structures (LIPSS) represent an effective technique to modify optical, mechanical, and chemical surface characteristics. While most studies focus on one-dimensional (1D) LIPSS formation on bulk and thin-film materials with orientation direction depending on laser polarization state, more complex morphologies are highly demanded for advanced applications. Here, we demonstrate the formation of two-dimensional (2D) square and hexagonal LIPSS on metal (Cr, Hf) and phase-change material ($Ge_2Sb_2Te_5$) thin films, driven by thermochemical and plasmonic mechanisms, respectively. These findings expand the potential for applications in tunable photonic devices, diffractive optical elements, and structurally colored metals with 2D anisotropic optical properties.

Keywords: LIPSS, GST, femtosecond laser pulses, self-organized structures, surface structuring

Funding: This study was funded by the grant from the Russian Science Foundation (RSF) No. 21-72-20162-P, https://rscf.ru/project/21-72-20162-P.

Citation: Fedyaj V.E., Bronnikov K.A., Simanchuk A.E., Lazarenko P.I., Yakubov A.O., Zhizhchenko A.Yu., Kuchmizhak A.A., Dostovalov A.V., Formation of 2D laser-induced periodic surface structures on metal and phase change materials, St. Petersburg State Polytechnical University Journal. Physics and Mathematics. 18 (4.1) (2025) 111–116. DOI: https://doi.org/10.18721/JPM.184.118

Материалы конференции
УДК 535.8
DOI: https://doi.org/10.18721/JPM.184.118

Формирование двумерных лазерно-индуцированных периодических поверхностных структур на металлах и фазопеременных материалах

В.Е. Федяй [1, 2] ✉, К.А. Бронников [3], А.Э. Симанчук [1], П.И. Лазаренко [4], А.О. Якубов [4], А.Ю. Жижченко [5], А.А. Кучмижак [5, 6], А.В. Достовалов [1, 2]

[1] Институт автоматики и электрометрии Сибирского отделения РАН, г. Новосибирск, Россия;

[2] Новосибирский государственный университет, г. Новосибирск, Россия;
[3] Университет ИТМО, Санкт-Петербург, Россия;
[4] Национальный исследовательский университет «МИЭТ», г. Зеленоград, Москва, Россия;
[5] Институт автоматики и процессов управления ДВО РАН, г. Владивосток, Россия;
[6] Дальневосточный федеральный университет, г. Владивосток, Россия
✉ fedyajve@iae.nsk.su

Аннотация. Лазерно-индуцированные периодические поверхностные структуры (ЛИППС) представляют собой эффективный метод изменения оптических, механических и химических свойств поверхности. В то время как большинство исследований посвящено формированию одномерных ЛИППС на объемных и тонкопленочных материалах с направлением ориентации, зависящим от состояния поляризации лазера, более сложные морфологии очень востребованы для перспективных применений. Здесь мы демонстрируем формирование двумерных квадратных и гексагональных ЛИППС на тонких пленках металлов (Cr, Hf) и фазопеременных материалов ($Ge_2Sb_2Te_5$), обусловленное, соответственно, термохимическими и плазмонными механизмами. Эти результаты расширяют возможности их применения в перестраиваемых фотонных устройствах, дифракционных оптических элементах и структурно окрашенных металлах с двумерными анизотропными оптическими свойствами.

Ключевые слова: ЛИППС, GST, фемтосекундные лазерные импульсы, самоорганизующиеся структуры, поверхностное структурирование

Финансирование: Исследование выполнено за счет гранта Российского научного фонда (РНФ) № 21-72-20162-П, https://rscf.ru/project/21-72-20162-P.

Ссылка при цитировании: Федяй В.Е., Бронников К.А., Симанчук А.Э., Лазаренко П.И., Якубов А.О., Жижченко А.Ю., Кучмижак А.А., Достовалов А.В. Формирование двумерных лазерно-индуцированных периодических поверхностных структур на металлах и фазопеременных материалах // Научно-технические ведомости СПбГПУ. Физико-математические науки. 2025. Т. 18. № 4.1. С. 111–116. DOI: https://doi.org/10.18721/JPM.184.118

Introduction

Laser-Induced Periodic Surface Structures (LIPSS) represent micro- and nano-scale surface relief patterns formed on material surfaces under impact of laser irradiation [1]. The LIPSS morphology (period and orientation direction) determined by both laser parameters (wavelength, polarization, pulse energy) and the material properties enables to tailor optical, mechanical, and chemical properties of surfaces through a direct and cost-effective fabrication process. As a result, LIPSS have used in diverse fields of applications such as photonics [2], sensing [3], and biomedicine [4].

Traditionally sub-wavelength one-dimensional (1D) LIPSS formed with linear polarized laser irradiation were studied on surfaces of metals, semiconductors, and dielectrics under the impact of continuous wave or pulsed lasers radiation ranging from ns to femtosecond pulse time duration. Moreover, two-dimensional (2D) LIPSS exhibiting multi-directional periodicity have recently attracted significant research interest. Various techniques were proposed to induce 2D LIPSS, including the impact of laser irradiation with polarization state differ from linear one and more sophisticated approaches such as double-pulse irradiation with orthogonal polarization directions. In particular, using circular or elliptical laser polarization, 2D LIPSS pattern in form of hexagonal lattices were demonstrated in case of Si thin film processing [5]. In addition, impact of cross-polarized laser pulses enables a diversity of 2D morphology from squared to, triangular and rhombic lattice on surface of cobalt [6]. There are also studies demonstrating 2D LIPSS formation using linear polarization and double-pass approach [7].

The formation of 2D LIPSS on the surface of chalcogenide phase-change materials (PCMs) has attracted significant interest due to its potential for applications in tunable photonic devices

and metasurface manufacturing. For instance, the formation of 2D LIPSS was demonstrated on the surface of bulk As_2S_3 chalcogenide glasses irradiated by a focused beam from a femtosecond Ti:sapphire laser [8]. These structures represent a superposition of LIPSS with the period of 760 nm oriented simultaneously in the direction parallel and perpendicular to the polarization of incident light. In another study, a hierarchical structure is observed in the form of a highly ordered two-dimensional grating induced by femtosecond laser irradiation on a surface of chalcogenide vitreous semiconductors thin films (As_2Se_3) [9]. The periodicity along one axis is provided by the presence of low spatial frequency LIPSS (LSFL) with a period of 490 ± 5 nm, and in the orthogonal direction—by high spatial frequency LIPSS (HSFL) with the period of 190 ± 10 nm resulting from the interference of various plasmon polariton modes generated under intense photoexcitation of nonequilibrium carriers within the film.

Here, we present the results on the formation of hexagonal thermochemical 2D LIPSS on thin metal films (Cr and Hf) based on the impact of linear polarized laser radiation and double-pass approaches. Moreover, the formation of two-dimensional structures of different morphology on thin film of phase change material $Ge_2Sb_2Te_5$ (GST) was demonstrated despite a different mechanism of LIPSS formation in this case.

Materials and Methods

Amorphous GST (200 nm), Cr (20 nm) and Hf (15 and 50 nm) films were deposited by using a DC magnetron sputtering system onto glass substrates. Experiments on formation LIPSS on thin films were performed under the impact of linearly polarized laser radiation with a wavelength of $\lambda = 1026$ nm, a pulse duration of 232 fs and the pulse repetition rate $f = 200$ kHz. The round shape Gaussian laser beam was transformed to the astigmatic beam with the size of 15×150 microns using cylindrical lens with focal length of −1000 mm. The pulse energy E and scanning speed V was optimized to obtain structures with the best regularity.

The formation of LIPSS was carried out using double-pass approach with orthogonal polarization direction (Fig. 1, *a*, *b*). It has been demonstrated that the polarization direction of the first pass significantly influences on the regularity and morphology of LIPSS. In particular, when the laser polarization direction is aligned parallel to the scanning direction (Fig. 1, *c*), the resulting LIPSS exhibit improved regularity compared to the case where the first-pass polarization is orthogonal to the scanning direction (Fig. 1, *d*).

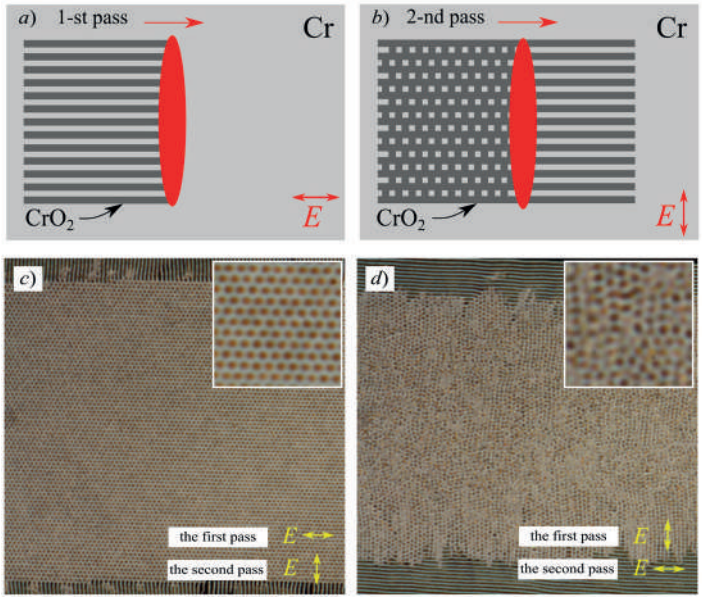

Fig. 1. Schematic of LIPSS fabrication using a two-pass writing technique with crossed polarizations and an astigmatic Gaussian beam: the first pass (*a*) and the second pass (*b*). Optical images of TLIPSS with hexagonal periodicity formed on a 20 nm-thick Cr film at writing parameters $E = 2.12$ μJ, $V = 100$ μm/s. In the first pass, the polarization is aligned parallel to the beam scanning direction, while in the second pass, it is orthogonal (*c*). In the first pass, the polarization is oriented perpendicular to the beam scanning direction, while in the second scan, it is parallel (*d*)

This effect can be explained by the increased influence of positive feedback on the LIPSS formation in case of astigmatic Gaussian beam impact, oriented perpendicular to the scanning direction and with polarization aligned along the scanning direction. In this case, a large number of structure periods (more than 100 periods) are simultaneously formed within the elliptic focal spot, and the light scattering from these periods facilitates the coherent formation of LIPSS during beam scanning. In contrast, in the second case, only a small number (about 10 periods) of structure periods are formed simultaneously in the focal spot, reducing scattering and hence to weaken the effect of positive feedback on LIPSS formation. For this reason, all experiments on metal films were carried out in a configuration where the polarization in the first pass and the second was aligned along and perpendicular to the scanning direction, respectively. As in case of $Ge_2Sb_2Te_5$ films the mechanism of LIPSS formation is based on interference of surface plasmon polariton waves and incident radiation, the polarization in the first pass was oriented perpendicular to the scanning direction to ensure parallel structures orientation to the scanning direction, as in the case of metals. Whereas, in the second pass, the polarization was aligned parallel to the scanning direction.

LIPSS surface morphology was investigated by AFM Park NX20, SEM Hitachi TM 3000 and optical microscope ZEISS Axio Imager 2.

Results and Discussion

Fig. 2, *a* shows SEM image of highly-ordered hexagonal LIPSS with the period of 690 nm formed on a 20 nm-thick metal Cr film under fs-laser irradiation with a pulse energy of 1.6 μJ and a scanning speed of 100 μm/s. The ordered structure exhibits high regularity across the entire track width of ~100 μm confirmed by the insets of magnified SEM images of the structures and optical images.

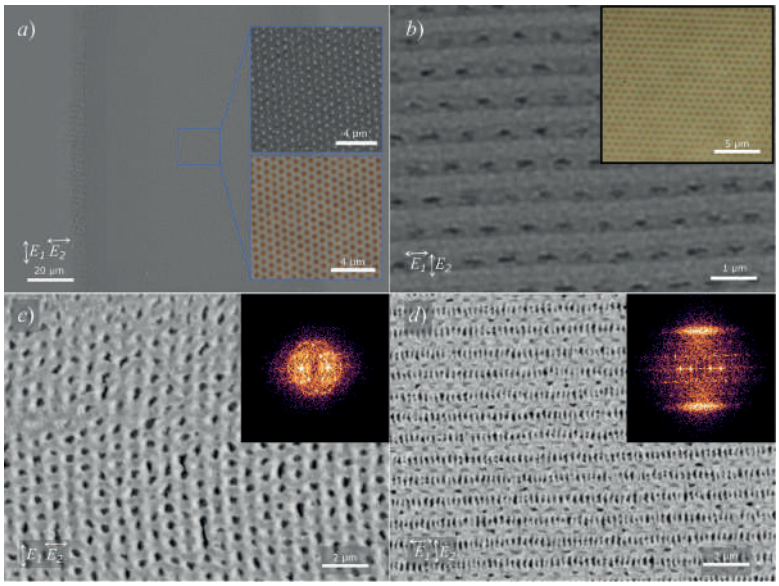

Fig. 2. SEM images of hexagonal TLIPSS formed on a 20 nm-thick Cr film with a pulse energy of 1.6 μJ and scanning speed of 100 μm/s (*a*), on a 15 nm-thick Hf film at 1.5 μJ, 100 μm/s (*b*), on a 50 nm-thick Hf film at 1.25 μJ, 50 μm/s (*c*) and 2 μJ, 2000 μm/s (*d*)

The same LIPSS morphology of hexagonal periodic structure with a period of ~800 nm was observed in the case of a 15 nm-thick Hf thin metal film at pulse energies of 0.875–1.5 μJ and scanning speeds of 10–2000 μm/s (Fig. 2, *b*). For a 50 nm-thick Hf film, ordered hexagonal structures with a period of ~900 nm are also observed. However, the morphology depends on experimental parameters. At low scanning speed (50 μm/s) and pulse energy (1.25 μJ), isolated modifications are formed (Fig. 2, *c*), while at higher pulse energy (2 μJ) and scanning speed (2000 μm/s), the oxide area of hexagonal structure exhibits a 250-nm periods modulation (Fig. 2, *d*).

The two-dimensional LIPSS on the 200-nm-thick GST film was obtained by the impact of fs laser radiation at pulse energy $E = 105$ nJ and scanning speed of 400 μm/s in a double-pass approach.

Specifically, after the first pass with the polarization direction perpendicular to the scanning direction, highly regular 1D LIPSS aligned parallel to the scanning direction and with the period of 1 μm was observed as a result of interference of surface plasmon polariton waves and incident radiation with subsequent crystallization of the initial amorphous film in the intensity maxima. After that, the second pass with orthogonal polarization direction leads to the two-dimensional LIPSS formation, as in the case of thermochemical LIPSS on metallic thin films. However, the initial overlap area of the tracks is characterized by square-shaped structures (Fig. 3, *a*). After this area, the morphology evolution proceeds through a non-periodic crystalline regime into a hexagonal lattice formation in the central part of the track. At a certain distance from the overlap area, the hexagonal structures are formed completely on the entire scan area (Fig. 3, *b*). The relief profiles of both hexagonal (Fig. 3, *c*, *d*) and square-shaped structures (Fig. 3, *e*, *f*) were measured in orthogonal directions. The 1D LIPSS formed during the first pass has a deep of about 4 nm due to local crystallization process of initial amorphous film, while the second pass provides approximately 2 nm in depth.

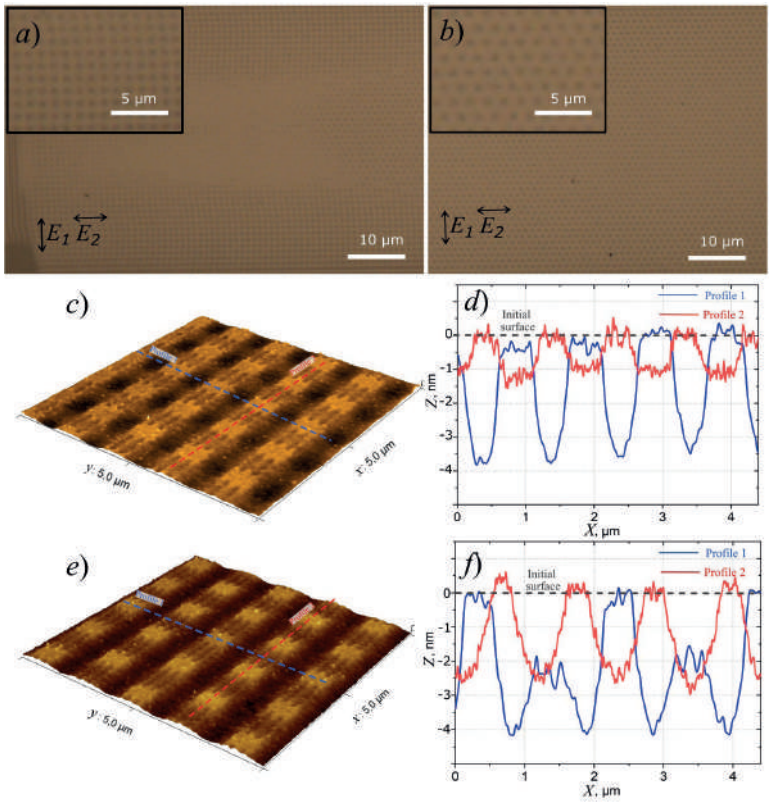

Fig. 3. Optical images of two-dimensional LIPSS formed on 200-nm-thick GST films: squared (*a*) and hexagonal (*b*) morphology. AFM images of corresponding structures of squared (*c*, *d*) and hexagonal (*e*, *f*) at pulse energy $E = 105$ nJ and scanning speed of 400 μm/s

Conclusion

In conclusion, the formation of two-dimensional LIPSS on thin metal films (Cr and Hf) was demonstrated using a double-pass technique with femtosecond laser pulses of orthogonal polarization. Highly regular hexagonal LIPSS with periods of 690 nm and 800 nm were observed at optimal processing parameters for 20-nm thick Cr and 15-nm thick Hf films, respectively. Moreover, this approach was used to induce two-dimensional LIPSS on the advanced functional phase-change material GST. Both square and hexagonal LIPSS morphologies were obtained on a 200-nm thick GST film, with a surface relief modulation depth of up to 4 nm. These findings expand the range of LIPSS-based surface morphologies and open new possibilities for practical applications, including tunable photonic devices, diffractive optical elements and structural coloration of metals.

REFERENCES

1. **Bonse J., Höhm S., Kirner S.V., Rosenfeld A., Krüger J.,** Laser-induced periodic surface structures — a scientific evergreen, IEEE Journal of Selected Topics in Quantum Electronics. 23 (2017) 109–123.

2. **Borodaenko Y., Cherepakhin A., Gurbatov S.O., Modin E., Shevlyagin A.V., Kuchmizhak A.A.,** Polarized *p–n* junction Si photodetector enabled by direct laser-induced periodic surface structuring, Surfaces and Interfaces. 56 (2025) 105568.

3. **Dostovalov A., Bronnikov K., Korolkov V., Babin S., Mitsai E., Mironenko A., Tutov M., Zhang D., Sugioka K., Maksimovic J., Katkus T., Juodkazis S., Zhizhchenko A., Kuchmizhak A.,** Hierarchical anti-reflective laser-induced periodic surface structures (LIPSSs) on amorphous Si films for sensing applications, Nanoscale. 12 (2020) 13431–13441.

4. **Fosodeder P., Baumgartner W., Steinwender C., Hassel A.W., Florian C., Bonse J., Heitz J.,** Repellent rings at titanium cylinders against overgrowth by fibroblasts, Advanced Optical Technologies. 9 (2020) 113–120.

5. **Durbach S., Hampp N.,** Generation of 2D-arrays of anisotropically shaped nanoparticles by nanosecond laser-induced periodic surface patterning, Applied Surface Science. 556 (2021) 149803.

6. **Jalil S.A., Yang J., ElKabbash M., Cong C., Guo C.,** Formation of controllable 1D and 2D periodic surface structures on cobalt by femtosecond double pulse laser irradiation, Applied Physics Letters. 115 (2019) 031601.

7. **Ibrahim Q., Andreeva Y., Suvorov A., Khmelenin D., Grigoryev E., Shcherbakov A., Sinev D.,** Laser fabrication of 1D and 2D periodic subwavelength gratings on titanium films, Optics & Laser Technology. 174 (2024) 110642.

8. **Messaddeq S.H., Dumont A., Douaud A., El-Amraoui M., Messaddeq Y.,** Formation of cross-superposed LIPSSs on bulk chalcogenide glasses using fs-laser, Advanced Optical Technologies. 7 (2018) 311–319.

9. **Shuleiko D., Zabotnov S., Sokolovskaya O., Poliakov M., Volkova L., Kunkel T., Kuzmin E., Danilov P., Kudryashov S., Pepelayev D., Kozyukhin S., Golovan L., Kashkarov P.,** Hierarchical Surface Structures and Large-Area Nanoscale Gratings in As_2S_3 and As_2Se_3 Films Irradiated with Femtosecond Laser Pulses, Materials. 16 (2023) 4524.

THE AUTHORS

FEDYAJ Vladislav E.
fedyajve@iae.nsk.su
ORCID: 0009-0007-9013-2988

BRONNIKOV Kirill A.
bronnikovkirill@gmail.com
ORCID: 0000-0001-5107-0111

SIMANCHUK Andrei E.
simmk@yandex.ru

LAZARENKO Petr I.
aka.jum@gmail.com
ORCID: 0000-0003-4309-3481

YAKUBOV Alexey O.
alexsey007@mail.ru

ZHIZHCHENKO Alexey Yu.
g89leksig@mail.ru
ORCID: 0000-0001-6878-679X

KUCHMIZHAK Aleksandr A.
alex.iacp.dvo@mail.ru
ORCID: 0000-0002-5376-5555

DOSTOVALOV Alexander V.
alexdost@gmail.com
ORCID: 0000-0002-9043-3197

Received 10.09.2025. Approved after reviewing 27.10.2025. Accepted 04.11.2025.

Conference materials
UDC 535.21
DOI: https://doi.org/10.18721/JPM.184.119

Femtosecond laser modification of amorphous silicon films for photovoltaic and polarization optics applications

D.V. Shuleiko [1], O.I. Sokolovskaya [1] ✉, M.N. Martyshov [1], A.A. Serdobintsev [2], L.D. Volkovoynova [2], S.B. Venig [2], P.P. Pakholchuk [1, 3], E.V. Kuzmin [1, 3], S.V. Zabotnov [1], P.K. Kashkarov [1, 4]

[1] Lomonosov Moscow State University, Faculty of Physics, Moscow, Russia;
[2] Saratov State University, Saratov, Russia;
[3] P.N.Lebedev Physical Institute of the RAS, Moscow, Russia;
[4] National Research Centre "Kurchatov Institute", Moscow, Russia
✉ sokolovskayaoi@my.msu.ru

Abstract. Femtosecond laser structuring is a promising method for obtaining amorphous-crystalline silicon (*a*-Si/*c*-Si) heterojunction in *a*-Si thin films, as well as surface structures with optical anisotropy. Depth-resolved Raman spectroscopy of an *a*-Si film irradiated at laser fluence of 0.1 J/cm^2, which is below *a*-Si ablation threshold, revealed its surface crystallization with the crystallized layer characteristic depth of 45 ± 5 nm. As a result of such laser irradiation, the electric current rectification coefficient in the film, determined from electrophysical measurements, increased from 2.7 to 13.6 indicating possible formation of an *a*-Si/*c*-Si heterojunction. The presence of 10-nm-thick Al coating decreases the number of pulses per unit area required for *a*-Si crystallization by 2.5 times. Optical anisotropy of the laser-crystallized *a*-Si films is manifested in their optical retardance of 280 ± 40 nm, caused by the formation of one-dimensional surface relief with the period of 1100 ± 50 nm.

Keywords: femtosecond laser pulses, amorphous silicon, heterojunction, laser-induced periodic surface structures, optical retardance

Funding: This study was funded by the Russian Science Foundation, grant number 22-19-00035-П, https://rscf.ru/en/project/22-19-00035/.

Citation: Shuleiko D.V., Sokolovskaya O.I., Martyshov M.N., Serdobintsev A.A., Volkovoynova L.D., Venig S.B., Pakholchuk P.P., Kuzmin E.V., Zabotnov S.V., Kashkarov P.K., Femtosecond laser modification of amorphous silicon films for photovoltaic and polarization optics applications, St. Petersburg State Polytechnical University Journal. Physics and Mathematics. 18 (4.1) (2025) 117–122. DOI: https://doi.org/10.18721/JPM.184.119

Материалы конференции
УДК 535.21
DOI: https://doi.org/10.18721/JPM.184.119

Фемтосекундная лазерная модификация пленок аморфного кремния для приложений фотовольтаики и поляризационной оптики

Д.В. Шулейко [1], О.И. Соколовская [1] ✉, М.Н. Мартышов [1], А.А. Сердобинцев [2], Л.Д. Волковойнова [2], С.Б. Вениг [2], П.П. Пахольчук [1, 3], Е.В. Кузьмин [1, 3], С.В. Заботнов [1], П.К. Кашкаров [1, 4]

[1] Московский государственный университет им. М.В. Ломоносова, физический факультет, Москва, Россия;
[2] Саратовский национальный исследовательский государственный университет им. Н.Г. Чернышевского, г. Саратов, Россия;
[3] Физический институт имени П.Н. Лебедева РАН, Москва, Россия;
[4] Национальный исследовательский центр «Курчатовский институт», Москва, Россия
✉ sokolovskayaoi@my.msu.ru

Аннотация. Фемтосекундное лазерное структурирование является перспективным методом получения гетероперехода «аморфный-кристаллический кремний» (*a*-Si/*c*-Si) в тонких пленках *a*-Si, а также поверхностных структур с оптической анизотропией. Методом спектроскопии комбинационного рассеяния света с разрешением по глубине в пленке *a*-Si, облученной лазерными импульсами с плотностью энергии ниже порога абляции (0.1 Дж/см^2), обнаружено формирование поверхностного кристаллизованного слоя с характерной толщиной 45 ± 5 нм. Электрофизические измерения показали, что в результате подобного облучения пленки коэффициент выпрямления электрического тока в ней увеличился с 2.7 до 13.6, что указывает на возможное образование гетероперехода *a*-Si/*c*-Si. Наличие алюминиевого покрытия толщиной 10 нм уменьшает количество импульсов на единицу площади, необходимое для кристаллизации *a*-Si, в 2.5 раза. Оптическая анизотропия лазерно-кристаллизованных пленок *a*-Si проявляется в виде оптического запаздывания до 280 ± 40 нм за счет формирования одномерного поверхностного рельефа с периодом 1100 ± 50 нм.

Ключевые слова: фемтосекундные лазерные импульсы, аморфный кремний, гетеропереход, лазерно-индуцированные поверхностные периодические структуры, оптическое запаздывание

Финансирование: Работа выполнена в рамках гранта Российского научного фонда (РНФ) № 22-19-00035-П, https://rscf.ru/en/project/22-19-00035/.

Ссылка при цитировании: Шулейко Д.В., Соколовская О.И., Мартышов М.Н., Сердобинцев А.А., Волковойнова Л.Д., Вениг С.Б., Пахольчук П.П., Кузьмин Е.В., Заботнов С.В., Кашкаров П.К. Фемтосекундная лазерная модификация пленок аморфного кремния для приложений фотовольтаики и поляризационной оптики // Научно-технические ведомости СПбГПУ. Физико-математические науки. 2025. Т. 18. № 4.1. С. 117–122. DOI: https://doi.org/10.18721/JPM.184.119

Introduction

Advances in the ultrafast laser-assisted fabrication technologies open up prospects for improvement of photovoltaic devices based on thin amorphous silicon (*a*-Si) layers with heterojunctions "*a*-Si – crystalline silicon (*c*-Si)", as well as polarization-sensitive optical elements for the near and middle infrared (IR) ranges, based on thin *a*-Si layers with submicron surface relief that possess optical and electrophysical anisotropy [1, 2]. Employing ultrafast laser

pulses leads to well-known phenomenon of laser-induced periodic surface structures (LIPSS) formation. The presence of optical anisotropy in the LIPSS allows fabricating optical elements that are sensitive to polarization, by direct femtosecond laser irradiation of thin films without photoresists and lithography. Such integrated optical elements may be of interest for polarization optical measurements, forming structured light beams, and for telecommunications, as selectors of polarized light signals in fiber-optic communication lines [3, 4].

Another femtosecond laser pulses application is laser-induced crystallization, being of interest for thin *a*-Si layers due to possibility of *a*-Si/*c*-Si heterojunction formation, which can increase Si-based solar cells efficiency. Primarily, this approach seems beneficial for HIT structures (Heterojunction with Intrinsic Thin-layer solar cells), where layers of amorphous silicon are deposited on a *c*-Si wafer by the PECVD method. The maximum efficiency for HIT solar cells is 26.7% [5], and the maximum thermodynamic efficiency limit for fully silicon solar cells is estimated at about 33% [6]. Thus, it is relevant to search for techniques of Si-based solar cells efficiency increasing. Employing laser pulses of femtosecond duration, compared to longer ones, for *a*-Si crystallization [7, 8], especially in context of heterojunction formation in thin *a*-Si layers seems beneficial due to more effective localization of laser action at sub-thermal timescale. Also, the additional *a*-Si/*c*-Si heterojunctions resulted from film laser-induced crystallization as well as higher charge mobility in *c*-Si compared to *a*-Si could contribute to efficiency increase of solar cells based on HIT structures.

Materials and Methods

To fabricate a *a*-Si/*c*-Si heterojunction by laser-induced *a*-Si crystallization, at the first stage, 1 μm-thick undoped *a*-Si film was magnetron-sputtered (Robvac VSM 300, 500W) at direct current on a glass substrate, covered by pre-deposited 500 nm-thick ITO layer, acting as a bottom contact for electrical measurements. On the second stage, laser radiation parameters required for *a*-Si thin surface layer crystallization to form a heterojunction, were determined. For that purpose, single scan lines were formed via irradiating the film by Satsuma femtosecond laser ($\lambda = 515$ nm, $\tau = 300$ fs, $\upsilon = 1$ kHz) with constant scanning speed $V = 300$ μm/s and laser spot diameter $D = 50$ μm, while the fluence E varied from 0.01 to 0.1 J/cm^2 from line to line.

To investigate the distribution of *c*-Si phase over the irradiated *a*-Si film depth, a uniformly deepening profile was etched (Perkin-Elmer PHI 4300, argon ions, 4 keV, 100 nA) with depth increasing by 10 ± 1 nm for each 100 ± 10 μm along the scan line, and the Raman spectra (Renishaw Raman spectrometer, excitation 532 nm) were measured in the mapping mode with 10 μm step along the etched profile. Then, *c*-Si phase volume fraction f_c for each point of Raman map was calculated using the integral intensities of Raman lines corresponding to TO phonon modes in *a*-Si (I_A, 480 cm^{-1}) and *c*-Si (I_C, 521 cm^{-1}) as $f_c = I_C/(\sigma I_A + I_C)$, where $\sigma = 0.1$ is an empirical ratio for the integral Raman scattering cross sections in *c*-Si and *a*-Si phases.

To investigate the effect of additional thin aluminum (Al) coating on *a*-Si laser crystallization, 1 μm-thick *a*-Si films with or without Al coating were deposited on glass substrates and irradiated in scanning mode. The irradiation was performed by ytterbium solid-state femtosecond laser Avesta TEMA-DUO (1050 nm, 150 fs, 130 nJ, 78 MHz, laser spot diameter 25 μm) which was purchased within the framework of the Lomonosov Moscow State University Program of Development and the National Project "Science and Universities" No. DS/45-pr on 28.12.2023 under contract No. 0784-44-2024 on 12.07.2024. The scanning was realized by moving the sample using an Aerotech motorized translator system in a horizontal plane orthogonally to laser beam with constant speed, varying from 2 to 2000 mm/s from line to line, resulting in the variation of the acting laser pulses number N_p per unit area from 10^6 to 10^3.

On the third stage, a large area (5×10 mm^2) was irradiated on the surface of *a*-Si film in raster mode with a 40 μm step ($< D$) between the scan lines, using selected laser radiation parameters (see Results section). To conduct electrophysical measurements in the direction orthogonal to the sample surface plane, aluminum square-shaped 300×300 μm contacts were deposited by thermal evaporation in vacuum (VUP-5) on top of both initial and irradiated areas. The current-voltage characteristics of both initial and irradiated *a*-Si samples were measured in the range from -2 to 2 V in air at room temperature using a Keithley 6487 picoammeter with integrated power supply. The measurements were carried out in the dark and under illumination (white light, $I = 100$ mW/cm^2) from the downside through a transparent conductive ITO layer.

To analyze polarizing properties of LIPSS, the prototypes of 0.5×0.5 cm² *a*-Si films-based waveplates were fabricated. For this purpose, a 1 μm-thick *a*-Si film without pre-deposited contacts or Al coating was irradiated by femtosecond laser (Avesta, 1250 nm, 150 fs, 10 Hz) at fluence $E = 0.15$ J/cm², higher than ablation threshold. The irradiated surface was analyzed by scanning electron microscopy (SEM, Vega 3, Tescan). Optical delay measurements were performed in the near and middle IR ranges using a Bruker IFS 66v/S IR Fourier spectrometer in transmission geometry with varied polarization of the transmitted radiation.

Results and Discussion

Depth-resolved Raman spectroscopy of etched meanders demonstrated that the intensity of the narrow peak corresponding to *c*-Si TO mode (521 cm⁻¹) decreases rapidly along the etched meander, which indicates the presence of crystalline Si phase only in the thin surface layer (Fig 1, *a*). The dependence of f_c on the irradiated *a*-Si film depth determined from the Raman spectra has a sharp character (Fig. 1, *b*): at the film surface f_c is 86 ± 4%, remaining the same up to the depth of 20 ± 5 nm, and then decreases rapidly, reaching zero at a depth of 45 ± 5 nm.

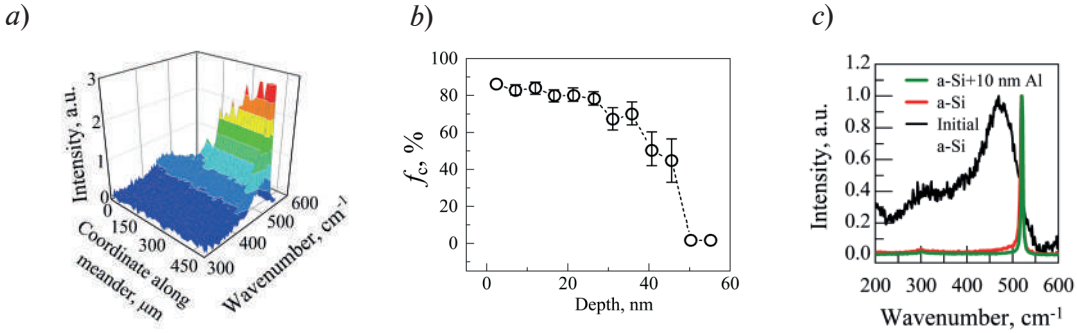

Fig. 1. Depth dependent Raman spectra of meander area (zero coordinate along meander corresponds to the center of ion etched crater) (*a*); crystalline silicon volume fraction dependence on *a*-Si film depth (*b*); Raman spectra for the *a*-Si with 10 nm Al layer irradiated with 80 000 laser pulses; *a*-Si without Al, irradiated with 200 000 laser pulses; and initial *a*-Si film (*c*)

Comparison of the Raman spectra for the irradiated *a*-Si films with and without Al coating (Fig.1, *c*) revealed that for the film without Al layer no crystallization is observed below laser pulses number $N_p = 200\,000$, while above this value almost complete crystallization of the film is achieved, with f_c up to 96 ± 1%. On the other hand, for the *a*-Si film with a 10 nm-thick Al coating, Raman spectroscopy data has shown that laser-induced crystallization begins to occur at $N_p = 80000$, which is 2.5 times less than that required for crystallization of *a*-Si without Al coating. Such results can be attributed to the higher absorption of Al compared to Si, and, consequently, more efficient laser-induced heating of the *a*-Si film with an Al coating. At $N_p = 80000$ and above the film is also almost completely crystallized with $f_c = 99 \pm 1\%$, while at lower N_p however, only Al layer melting is observed without Si film crystallization.

The obtained f_c distribution data allowed to set up the following optimal laser irradiation parameters for *a*-Si/*c*-Si heterojunction fabrication in the *a*-Si film: fluence 0.1 J/cm², repetition rate 1 kHz, scanning speed 300 μm/s.

The current-voltage characteristics both for the initial *a*-Si film and for *a*-Si/*c*-Si heterojunction, fabricated using the mentioned above laser irradiation parameters, demonstrate a pronounced diode character (Fig. 2, *a*, *b*), indicating the presence of a potential barrier in both structures. However, the resistance of the laser-irradiated *a*-Si film decreased about 500 times compared to the initial one, being the result of upper layer partial crystallization with crystalline Si (nanocrystalline, *nc*-Si) phase formation, which is known to have a lower resistivity compared to *a*-Si. Both samples' current-voltage characteristics demonstrate "rectifying" character with the rectification coefficient *k* calculated as the ratio of the current strength in the forward and reverse voltage bias increasing from 2.7 to 13.6 at a voltage of $U = 2$ V after laser irradiation. Increased rectification coefficient can be attributed to the laser-induced formation of an additional potential barrier for free charge carriers in the form of a *a*-Si/*nc*-Si heterojunction.

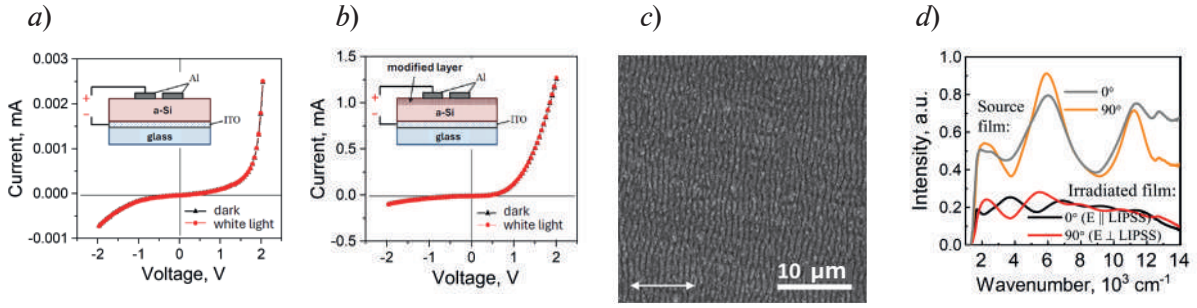

Fig. 2. The current-voltage characteristics of (*a*) initial and (*b*) laser-processed *a*-Si film with ITO contact, insets show its connection to the picoammeter; (*c*) SEM image of the irradiated region with LIPSS on *a*-Si surface, (*d*) IR transmission spectra for the initial *a*-Si film and the film irradiated in LIPSS formation mode

For the 1 μm-thick *a*-Si film on a glass substrate fabricated as waveplate prototype, low spatial frequency LIPSS (LSFL) presence with a period of 1100 ± 50 nm was confirmed by SEM (Fig. 2, *c*). Formed as a result of femtosecond laser irradiation with fluence above the ablation threshold, these structures possess high regularity. The IR transmission spectra (Fig. 2, *d*) demonstrate alternating maxima and minima in the spectra of both the initial and irradiated films, emerging as interference in the layered structure of the samples. The decreased transmittance and lower interference amplitude for the laser-irradiated sample is associated with the formation of a crystalline phase in it, as well as diffuse scattering on the formed surface relief. More importantly, the interference maxima at 0° polarization of the transmitted light in the laser-irradiated film are shifted significantly, compared to the initial film. Based on this shift in the interference maxima positions, a difference in refractive indices of ordinary and extraordinary waves was determined as 0.47 ± 0.07. The anisotropy axis orientation was also determined to be parallel to the ridges of the formed LSFL. Thus, the fabricated waveplate prototype based on *a*-Si demonstrates an optical retardance value of 280 ± 40 nm, which can be attributed to the anisotropic surface relief of LSFL in the form of alternating *nc*-Si/air micron-scale ridges.

Conclusion

In this study, for a thin surface layer (45 ± 5 nm) of *a*-Si film exposed to femtosecond laser pulses the crystallization with a high crystalline Si volume fraction of $86 \pm 4\%$ was achieved Moreover, employing Al coating on *a*-Si film not only decreases the number of pulses required for its effective crystallization due to more effective light absorption, but also leads to almost complete crystallization of the film thin surface layer, with volume fraction reaching up to $99 \pm 1\%$. The formed structures are showing increased rectification coefficient due to formation of *a*-Si/*c*-Si heterojunction, which is promising for photovoltaic cells improvement. Irradiation of *a*-Si films by femtosecond laser pulses with the fluence higher than *a*-Si ablation threshold leads to LIPSS formation. This surface relief, in a form of LSFL, possesses the optical retardance of up to 300 nm. Such optically anisotropic structures could be used as a basis for creating polarization-sensitive optic elements, for example, quarter-wave plates for the near-infrared range.

REFERENCES

1. **Shi W., Qi D., Wang W., Li Z., Zhang J., Zheng H., Yang B., Sun T., Wei J. and Chen S.,** Study of femtosecond laser induced periodic structure on amorphous silicon films and crystallization characteristics, Optics and Laser Technology 181B. (1–8) (2025) 111764.

2. **Xu L., Yan W., Cui W. and Qiu M.,** Repetition frequency-dependent formation of oxidized LIPSSs on amorphous silicon films, Photonics. 12 (1–15) (2025) 667.

3. **Kikuchi K.,** Fundamentals of coherent optical fiber communications, Journal of Lightwave Technology. 34 (2015) 157–179.

4. **Skoulas E., Tasolamprou A.C., Kenanakis G., Stratakis E.,** Laser induced periodic surface structures as polarizing optical elements, Applied Surface Science. 541 (1-7) (2021) 148470.

5. **Yoshikawa K., Kawasaki H., Yoshida W., Irie T., Konishi K., Nakano K., Uto T., Adachi D., Kanematsu M., Uzu H., Yamamoto K.,** Silicon heterojunction solar cell with interdigitated back contacts for a photoconversion efficiency over 26%, Nature Energy. 2 (1–8) (2017) 17032.

6. **Tiedje T., Yablonovitch E., Cody G.D., Brooks B.G.,** Limiting efficiency of silicon solar cells, IEEE Transactions on Electron Devices. 31 (5) (1984) 711–716.

7. **Neizvestniy I.G., Volodin V.A., Gismatulin A.A., Kamaev G.N., Antonenko A.H., Cherkov A.G., Litovchenko V.G., Lisovsky I.P., Maidanchuk I.Yu.,** Formation of Si nanocrystals in SiO_x, SiO_x:C:H films and Si/SiO_2 multilayer nano-heterostructures by pulse laser treatments, Proceedings of SPIE. 9440 (1–11) (2014) 94400F.

8. **Dostovalov A., Bronnikov K., Korolkov V., Babin S., Mitsai E., Mironenko A., Tutov M., Zhang D., Sugioka K., Maksimovic J., Katkus T., Juodkazis S., Zhizhchenko A., Kuchmizhak A.,** Hierarchical anti-reflective laser-induced periodic surface structures (LIPSSs) on amorphous Si films for sensing applications, Nanoscale. 12 (25) (2020) 13431–13441.

THE AUTHORS

SHULEIKO Dmitrii V.
shuleyko.dmitriy@physics.msu.ru
ORCID: 0000-0003-3555-6693

VENIG Sergey B.
Sergey.Venig@gmail.com
ORCID: 0000-0002-4759-5828

SOKOLOVSKAYA Olga I.
sokolovskayaoi@my.msu.ru
ORCID: 0000-0001-8017-9984

PAKHOLCHUK Petr P.
petr.pakholchuk@mail.ru
ORCID: 0000-0002-2608-7621

MARTYSHOV Mikhail N.
martyshov@physics.msu.ru
ORCID: 0000-0002-6363-4970

KUZMIN Evgeny V.
kuzmine@lebedev.ru
ORCID: 0000-0002-6322-6838

SERDOBINTSEV Alexey A.
alexas80@bk.ru
ORCID: 0000-0003-3281-8352

ZABOTNOV Stanislav V.
zabotnov@physics.msu.ru
ORCID: 0000-0002-2528-4869

VOLKOVOYNOVA Larisa D.
loris.volkoff@gmail.com
ORCID: 0000-0001-6780-9865

KASHKAROV Pavel K.
p.kashkarov@mail.ru
ORCID: 0000-0001-6889-001X

Received 16.09.2025. Approved after reviewing 08.12.2025. Accepted 08.12.2025.

Conference materials
UDC 535.512
DOI: https://doi.org/10.18721/JPM.184.120

Model of orthogonal two-wave mixing in photorefractive crystal of cubic symmetry with optical activity

M.N. Bezruk [1] ✉, R.V. Romashko [1], T.A. Efimov [1], D.V. Storozhenko [1]

[1] Institute of Automation and Control Processes FEB RAS, Vladivostok, Russia

✉ bezmisha@list.ru

Abstract. We developed a physical model describing the process of two-wave vectorial mixing in optically active photorefractive crystal of cubic symmetry for an orthogonal scheme of interaction. Using the model, we calculated the two-wave interaction in a photorefractive crystal of bismuth silicate $Bi_{12}SiO_{20}$ having optical activity. We have determined conditions at that polarization changes don't influence two-wave mixing. It was found that it is possible to define the parameters of the crystal and interacting waves for the quasi-polarization independence mode, when changes of interferometer output signal caused by polarization instability of the signal wave is reduced to a minimum (no more than 3%). We developed a physical model describing vectorial two-wave mixing in optically active, cubic-symmetry photorefractive crystals for an orthogonal interaction geometry. We apply the model to bismuth silicate ($Bi_{12}SiO_{20}$), an optically active photorefractive crystal. We further show that by appropriately selecting crystal and wave parameters, a quasi-polarization-independent regime can be achieved, in which interferometer output fluctuations caused by signal-wave polarization instability are minimized to no more than 3%.

Keywords: photorefractive crystal, adaptive interferometer, dynamic hologram, polarization, optical activity

Funding: The study was supported by the Russian Science Foundation (project No. 24-22-00413).

Citation: Bezruk M.N., Romashko R.V., Efimov T.A., Storozhenko D.V., Model of orthogonal two-wave mixing in photorefractive crystal of cubic symmetry with optical activity, St. Petersburg State Polytechnical University Journal. Physics and Mathematics. 18 (4.1) (2025) 123–127. DOI: https://doi.org/10.18721/JPM.184.120

Материалы конференции
УДК 535.512
DOI: https://doi.org/10.18721/JPM.184.120

Модель ортогонального двухволнового взаимодействия в фоторефрактивном кристалле кубической симметрии с оптической активностью

М.Н. Безрук [1] ✉, Р.В. Ромашко [1], Т.А. Ефимов [1], Д.В. Стороженко [1]

[1] Институт автоматики и процессов управления ДВО РАН, г. Владивосток, Россия

✉ bezmisha@list.ru

Аннотация. Разработана физико-математическая модель, описывающая процесс двухволнового векторного взаимодействия в оптически активном фоторефрактивном кристалле кубической симметрии для ортогональной геометрии взаимодействия волн. С использованием модели выполнен расчет двухволнового взаимодействия

в фоторефрактивном кристалле силиката висмута $Bi_{12}SiO_{20}$, обладающем оптической активностью. Определены параметры фоторефрактивного кристалла и взаимодействующих волн для режима квази-поляризационной независимости, при котором изменения выходного сигнала интерферометра, вызванные поляризационной нестабильностью сигнальной волны, минимальны (не более 3%).

Ключевые слова: фоторефрактивный кристалл, адаптивный интерферометр, динамическая голограмма, поляризация, оптическая активность

Финансирование: Российский научный фонд, грант № 24-22-00413.

Ссылка при цитировании: Безрук М.Н., Ромашко Р.В., Ефимов Т.А., Стороженко Д.В. Модель ортогонального двухволнового взаимодействия в фоторефрактивном кристалле кубической симметрии с оптической активностью // Научно-технические ведомости СПбГПУ. Физико-математические науки. 2025. Т. 18. № 4.1. С. 123–127. DOI: https://doi.org/10.18721/JPM.184.120

Introduction

Adaptive holographic interferometers based on dynamic holographic gratings recorded in photorefractive crystals (PRCs) are effective tools for phase demodulation [1–10]. Continuous re-recording of the hologram in the PRC stabilizes the interferometer's operating point, while preserving high sensitivity and providing strong immunity to external noise [2, 4, 6]. However, as in traditional interferometers, the sensitivity of adaptive interferometers depends on the polarization of the light beams. Polarization fluctuations can significantly reduce, or even eliminate the signal, underscoring the need for an interferometer design whose output is insensitive to polarization.

This problem can be addressed by dependencies in combination with an orthogonal wave-mixing geometry. The authors previously developed a physical and mathematical model of vectorial two-wave mixing in photorefractive crystals with optical gyrotropy [11]. The model captures polarization evolution arising not only from the PRC's gyrotropy but also from the two-wave mixing process within the crystal. It enables more precise selection of the interacting waves' polarization parameters and the PRC dimensions, accounting for the crystal's material properties and the light's wavelength, which can yield polarization-independent operation of the adaptive interferometer. This paper presents calculations of two-wave vector interaction in the optically active PRC bismuth silicate $Bi_{12}SiO_{20}$ and identifies parameter regimes in which polarization fluctuations of the interacting waves do not degrade the stability of the adaptive holographic interferometer's output signal.

Model Overview

The developed physical and mathematical model builds on the theory of vectorial wave mixing in cubic photorefractive crystals for transmission geometry described by Sturman et al. [12]. A more detailed description of the model is provided in [11]. Its key elements are summarized here. Unlike collinear wave interaction, the orthogonal geometry has signal and reference waves propagating at right angles, producing spatially varying polarization states throughout the PRC. To address this, the model divides the intersection region of the signal wave *As* and the reference wave *Ar* within the PRC into an $M \times N$ grid of cells. The grid size was selected to ensure grid independence; 100×100 cells were sufficient. Further refinement did not change the results within numerical tolerance but significantly increased computation time. The signal and reference waves entering the cells of the first layer are defined as follows:

$$As_{m1}^{in} = As / N,\ Ar_{1n}^{in} = As / M. \quad (1)$$

Consider a cell (m, n), where m ranges from 0 to M and n from 0 to N (see Fig. 1). The amplitudes of the interacting waves entering this cell are equal to the amplitudes of the waves exiting the preceding cell:

$$As_{mn}^{in} = As_{m-1n}^{out},\ Ar_{mn}^{in} = Ar_{mn-1}^{out}. \tag{2}$$

Within each cell, vector two-wave mixing is computed. The polarization states of the waves *As* and *Ar* change due to both the crystal's optical gyrotropy and the mixing interaction. The waves then propagate to the next cells, (m+1, n) and (m, n+1), respectively, where the procedure is repeated. Because the measured information is encoded in the phase modulation φ of the signal wave *As*, its complex amplitude is written as $As \cdot e^{i\varphi}$. The amplitude of the signal wave at the output of cell (m, n) is then obtained from the two-wave mixing relations given by [11, 12]:

$$As_{mn}^{out}(\varphi) = (\hat{T}_{+}(y) As_{m-1n}^{out} e^{i\varphi} + e^{\pm i\varphi_0}\, \hat{T}_{-}(y) Ar_{mn-1}^{out}) e^{-\alpha \Delta L/2}, \tag{3}$$

where y denotes the propagation direction of the signal wave *As*, ΔL is the cell size, and α denotes the optical absorption coefficient of the PRC. The terms $\hat{T}_{+}$ and $\hat{T}_{-}$ are transformation matrices that account for the diffraction of wave *As* in the direction of *M* (zero-order diffraction) and the diffraction of reference wave *Ar* in the direction of *M*, respectively. The interferometer's output signal *S* is defined as the change in the intensity of the signal wave *As* at the exit of the "final cell layer" (where $m = M$), summed along the *N* direction:

$$S = \Sigma_{n-1}^{N} \left(As_{mn}^{out}(\varphi) \right)^2 - \left(As_{mn}^{out} \right)^2. \tag{4}$$

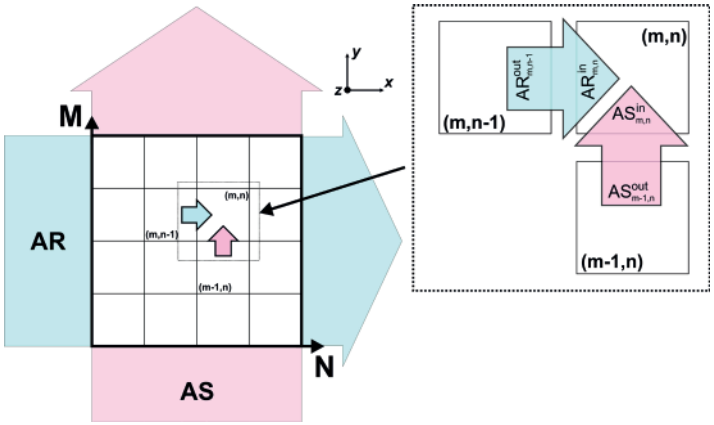

Fig. 1. Scheme of propagation of signal and reference waves in a photorefractive crystal

Results and Discussion

A physical and mathematical model was investigated using a gyrotropic photorefractive crystal of bismuth silicate $Bi_{12}SiO_{20}$ (BSO) of cubic symmetry. Numerical simulations were performed to study vectorial two-wave mixing in the PRC at wavelengths of 532 and 633 nm, for which the optical activity of BSO is 350 and 220 deg/cm, respectively. A linearly polarized signal wave *As* and a circularly polarized reference wave *Ar* were launched into the PRC. The developed model allowed for the investigation of the polarization independence of the BSO crystal.

Fig. 2 shows the dependence of the interferometer output signal on the azimuthal angle γ of the signal wave *As* for BSO crystal of varying lengths (1−30 mm), computed using the developed model Results are given for wavelengths of 532 and 633 nm. The simulations indicate that at certain crystal lengths L_p, the influence of polarization changes of *As* on the output signal is minimized. Thus, for wavelength 532 nm (Fig. 2, *a*), L_p occurs at 5.4, 10.7, 16.1 mm, etc. (i.e., multiples of 5.4 mm). For wavelength 633 nm (Fig. 2, *b*), L_p occurs at 8.7, 17.4, 26.0 mm, etc. (i.e., multiples of 8.7 mm). At these lengths, the variation of the output signal with γ is, on average, about 3% of its maximum possible modulation. Thus, a regime close to polarization independence (PI-mode) is achieved at a crystal length of L_p. However, complete polarization independence − where the

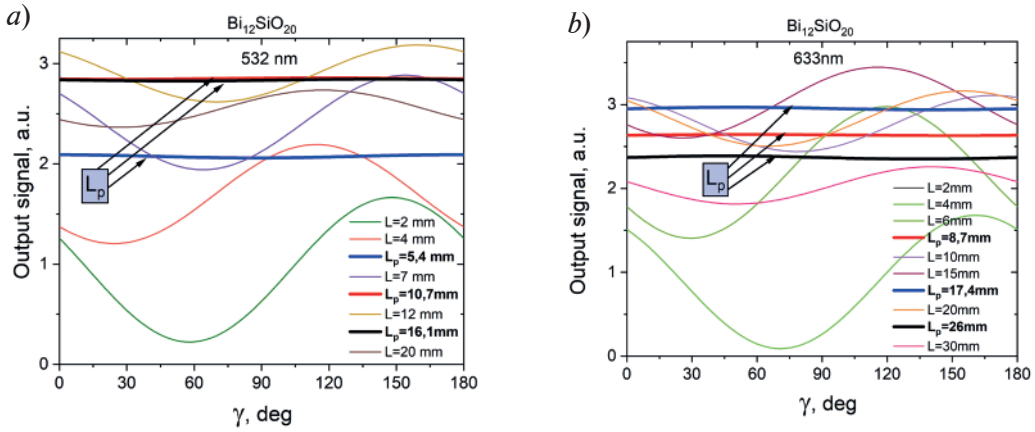

Fig. 2. Dependences of the output signal on the azimuthal angle of the signal wave, obtained for the BSO crystal at wavelength λ = 532 nm (*a*) and λ = 633 nm (*b*)

output signal is fully independent of the wave and crystal parameters – is not attainable, likely due to the nonlinear nature of light interaction within the PRC.

Fig. 3 shows the dependence of the interferometer output signal on the length of PRC BSO, at various azimuthal angles γ of the signal wave *As*, at wavelengths of 532 and 633 nm. The maximum and minimum achievable signal levels are indicated by red and blue lines, respectively. The plot shows that increasing the crystal length raises both the minimum and maximum signal levels. Thus, the output signal peaks when the crystal length is L_{opt} = 13.2 mm for wavelength 532 nm (Fig. 3, *a*) and L_{opt} = 13 mm for wavelength 633 nm (Fig. 3, *b*), achieved with a linearly polarized signal wave *As* oriented at γ = 140°. At crystal lengths of L_p = 5.4 mm and 10.7 mm for 532 nm, and L_p = 8.7 mm and 17.4 mm for 633 nm, the difference ΔS between the maximum and minimum achievable output signals is minimized to about 3% of the maximum possible signal. This implies that, regardless of the input polarization state of *As*, the output signal varies only within this narrow range.

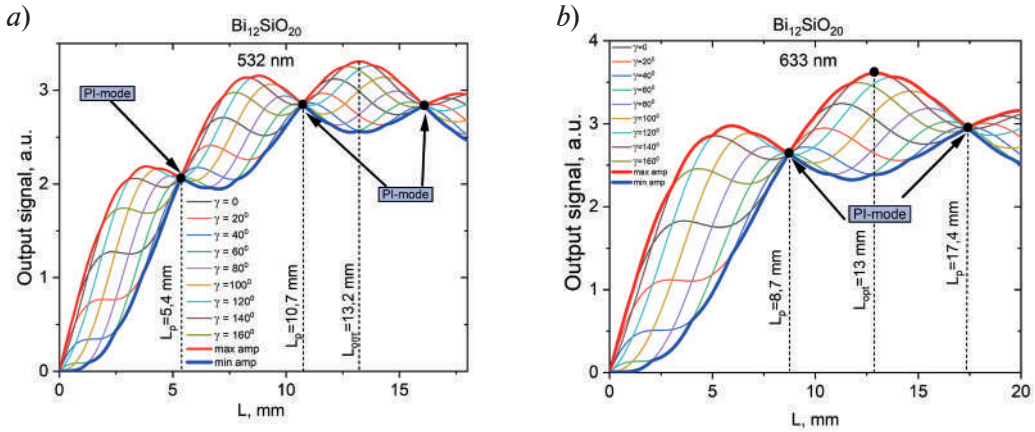

Fig. 3. Dependences of the interferometer output signal on the crystal length, obtained at different azimuthal angles of the signal wave λ = 532 nm (*a*), λ = 633 nm (*b*)

Conclusion

This paper presents a physical model for vectorial two-wave mixing in optically active photorefractive crystals with cubic symmetry, applied to an orthogonal interferometer configuration. Using this model, we analyzed two-wave mixing in a gyrotropic bismuth silicate ($Bi_{12}SiO_{20}$, BSO) photorefractive crystal at wavelengths of 532 nm and 633 nm. The results show that complete polarization independence is not achievable; however, by appropriate choice of crystal and wave parameters, signal variations due to polarization instability of the signal wave can be reduced to below 3%. We identify a quasi-polarization-independent operating regime at crystal lengths of 5.4 mm for 532 nm and 8.7 mm for 633 nm. In addition, the optimal crystal length was found to be approximately 13 mm, which maximizes the two-wave mixing efficiency.

REFERENCES

1. **Stepanov S.I.,** Adaptive interferometry: a new area of applications of photorefractive crystals, International trends in optics. (1991) 125–140.

2. **Kamshilin A.A., Romashko R.V., Kulchin Y.N.,** Adaptive interferometry with photorefractive crystals, Journal of Applied Physics. 3 (105) (2009) 031101.

3. **Murray T.W., Tuovinen H., Krishnaswamy S.,** Adaptive optical array receivers for detection of surface acoustic waves, Applied optics. 19 (39) (2000) 3276–3284.

4. **Anisimov R.I., Temereva A.S., Kolmakov A.A., Shandarov S.M.,** Volume Transmission Holograms in Lithium Niobate Crystals with Surface Copper Doping for Photovoltaic Tweezers, Optics and Spectroscopy. 2 (132) (2024) 86–94.

5. **Solymar L., Webb D.J., Grunnet-Jepsen A.,** The physics and applications of photorefractive materials. (11) (1996).

6. **Di Girolamo S., Romashko R.V., Kulchin Y.N., Kamshilin A.A.,** Orthogonal geometry of wave interaction in a photorefractive crystal for linear phase demodulation, Optics Communications. 1 (283) (2010) 128–131.

7. **Shandarov S.M., Zlobin A.O., Shmidt A.A., Burimov N.I., Mel'nik K.P., Shmakov S.S., Sokolov I.A.,** Determination of material parameters of photorefractive crystals using adaptive holographic interferometry, Optics and Spectroscopy. 129 (5) (2021) 576–580.

8. **Naunyka V.N.,** Diffraction and Mixing of Light Waves on a Reflection Holographic Grating in a Cubic Photorefractive Crystal, Journal of Applied Spectroscopy. 6 (91) (2025) 1301–1308.

9. **Shandarov S.M., Zlobin A.O., Shmidt A.A., Burimov N.I., Melnik K.P., Shmakov, S.S., Sokolov I.A.,** Adaptive holographic interferometry applied to determine the material parameters of photosensitive crystals, Optics and Spectroscopy. 4 (129) (2021) 413–417.

10. **Dai C.Q., Wang Y.Y.,** Coupled spatial periodic waves and solitons in the photovoltaic photorefractive crystals, Nonlinear dynamics. 3 (102) (2020) 1733–1741.

11. **Bezruk M.N., Efimov T.A., Storozhenko D.V., Romashko R.V.,** Model of Orthogonal Two-Wave Mixing in Optically Active Photorefractive Crystal of Cubic Symmetry, Bulletin of the Russian Academy of Sciences: Physics. 4 (88) (2024) S664–S669.

12. **Sturman B.I., Podivilov E.V., Ringhofer K.H., Shamonina E., Kamenov V.P., Nippolainen E., Prokofiev V., Kamshilin A.A.,** Theory of photorefractive vectorial wave coupling in cubic crystals, Physical Review E. 3 (60) (1999) 3332.

THE AUTHORS

BEZRUK Mikhail N.
bezmisha@list.ru
ORCID: 0000-0003-2127-2462

EFIMOV Timofey A.
efimov@dvo.ru
ORCID: 0000-0001-5398-9703

ROMASHKO Roman V.
romashko@dvo.ru
ORCID: 0000-0003-0869-0993

STOROZHENKO Dmitry V.
dbrados@dvo.ru
ORCID: 0000-0002-3521-5269

Received 07.10.2025. Approved after reviewing 17.11.2025. Accepted 18.11.2025.

PHYSICAL MATERIALS TECHNOLOGY

Conference materials
UDC 539.23+548.5
DOI: https://doi.org/10.18721/JPM.184.121

Physical deposition of atomic layers and growth of extremely thin films: four-decade series of the refractory metal-silicon system studies

N.I. Plusnin [1] ✉

[1] Institute of Nanotechnologies and Microelectronics of the RAS, Moscow, Russia
✉ plusnin.n@inme-ras.ru

Abstract. The article is devoted to the author's four-decade series of studies on growing extremely thin films (ETF) in the refractory metal-silicon system. To obtain ETF, it was necessary to develop a new growth method – physical atomic-layer deposition (PALD), which uses the technique of pulsed evaporation of adsorbate from a flat source located parallel to the substrate. Compared to the traditional molecular beam deposition (MBE) method, PALD reduces the vapor temperature, produces thinner layers, and expands the range of materials produced. The study showed that, with PALD using reduced substrate and vapor temperatures, not only two-dimensional surface phases (2D-SP) can form, but also two-dimensional (2D-SWL) and, subsequently, nanophase (ν-SWL) wetting layers (SWL). The series investigated the growth of ETFs Cr, Co, Fe, Cu and their silicides on Si(111) and Si(001), as well as the growth of Si on Si(111)7×7 and $CrSi_2$(0001). Single-layer and multilayer (Co-Cu-Fe-Cu) nanofilms were obtained. The main causes of phase transitions in SWL have been identified, and the role of vapor pressure and substrate temperatures in the structure and composition of SWL and the boundary layer of the substrate has been shown. The study showed that the films obtained by the PALD method have unique electrical, optical and magnetic properties and are promising for use in micro- and nanoelectronics nanodevices.

Keywords: atomic-layer deposition, surface phases, wetting layers, phase transitions, extremely ultrathin films, multilayer nanolayers, Cr, Co, Fe, Cu, silicides, Si(111) and Si(001), electrical, optical and magnetic properties

Citation: Plusnin N.I., Physical deposition of atomic layers and growth of extremely thin films: four-decade series of the refractory metal-silicon system studies, St. Petersburg State Polytechnical University Journal. Physics and Mathematics. 18 (4.1) (2025) 128–132. DOI: https://doi.org/10.18721/JPM.184.121

Материалы конференции
УДК 539.23+548.5
DOI: https://doi.org/10.18721/JPM.184.121

Физическое осаждение атомных слоев и рост предельно-тонких пленок: сорокалетняя серия исследований системы тугоплавкий металл-кремний

Н.И. Плюснин [1] ✉

[1] Институт нанотехнологий микроэлектроники РАН, Москва, Россия
✉ plusnin.n@inme-ras.ru

Аннотация. Статья посвящена сорокалетней серии исследований автора по выращиванию экстремально-тонких пленок (ETF) в системе тугоплавкий металл-кремний. Для получения ETF необходимо было разработать новый метод роста – физическое атомно-слоевое осаждение (PALD), использующее технику импульсного

испарения адсорбата из плоского источника, расположенного параллельно подложке. По сравнению с традиционным методом молекулярно-лучевого осаждения (MBE), PALD позволяет снизить температуру пара, получить более тонкие слои и расширить ассортимент получаемых материалов. Исследование показало, что, при PALD, использующем пониженные температуры подложки и пара, могут образовываться не только двумерные поверхностные фазы (2D-SP), но и двумерные (2D-SWL) и, затем, нанофазные (ν-SWL) смачивающие слои (SWL). В серии был исследован рост ETF Cr, Co, Fe, Cu и их силицидов на Si(111) и Si(001), а также рост Si на Si(111)7×7 и $CrSi_2$(0001). Были получены однослойные и многослойные (Co-Cu-Fe-Cu) нанопленки. Были выявлены основные причины фазовых переходов в SWL, а также показана роль давления, температур пара и подложки в структуре и составе SWL и пограничного слоя подложки. Исследование показало, что полученные методом PALD пленки, обладают уникальными электрическими, оптическими и магнитными свойствами и перспективны для использования в наноустройствах микро- и наноэлектроники.

Ключевые слова: атомно-слоевое осаждение, поверхностные фазы, смачивающие слои, фазовые переходы, предельно-тонкие пленки, многослойные нанослои, Cr, Co, Fe, Cu, силициды, Si(111) и Si(001), электрические, оптические и магнитные свойства

Ссылка при цитировании: Плюснин Н.И. Физическое осаждение атомных слоев и рост предельно-тонких пленок: сорокалетняя серия исследований системы тугоплавкий металл-кремний // Научно-технические ведомости СПбГПУ. Физико-математические науки. 2025. Т. 18. № 4.1. С. 128–132. DOI: https://doi.org/10.18721/JPM.184.121

Introduction

The fundamental basis for growing nanostructures of micro- and nanoelectronics is knowledge about the initial stage of thin film growth and the formation of its interface. This stage, in fact, is the formation of the elemental and phase composition, structure and morphology of 2D-SP, SWL, ETF and their interface with the substrate. However, it was only 30 years after the publication of our first papers [1, 2] that it became obvious (see below) that the thin-film phase (TP), which forms after 2D-SPS and before the growth of the first ETF layer, is an SWL in the form of first two-dimensional (2D-SWL) and then nanophase (ν-SWL) layer.

Historically, up to a certain stage, two approaches to ETF growth existed independently and moved towards each other: "approach I" – from three-dimensional massive phases (3D-BP) to ETF and "approach II" – from 2D-SP to ETF. In these approaches, the understanding of the nature of 2D-SP and SWL was influenced by differences in research methods, in particular, the degree of microscopicity of these methods. For example, the use of optical methodologies such as ellipsometry has led to the conceptualization of SWL as a metastable 3D-BP [3]. Conversely, the use of surface-sensitive techniques [4] led to the identification of exclusively interphase boundary phase [5] or 2D-SP [6, 7] with their own composition, thickness, density, and lattice [4]. A more complete understanding of the nature of SWL was obtained later (see below).

Based on a review of forty years of research on the cultivation of ETFs metals (Me) and their silicides (MSix) on silicon or silicon on Si or $MeSi_x$ substrates, this article presents a new perspective on ETFs formation. The results of these studies are systematized in chronological order in accordance with the developed theory of ETF growth within the framework of approach II developed by the author.

Chronological overview

In the very first works [1, 2], TP spectra were obtained by electron energy loss spectroscopy (EELS), which demonstrated a reduced electron density in TP compared to that in 3D-BP. In this study, TP was identified as a low-dimensional phase, called "atomically similar" because of its low density. However, this TP had a thickness of several monolayers (> 3 ML), which

is not typical for 2D-SP. Therefore, the authors of [1, 2] attributed it to a kind of "increased thickness" SP, implying that this "thick" SP, like the "submonolayer" 2D-SP, is stabilized by the substrate.

Subsequent studies focused on the mixing of Me-Si at low temperatures and its role in the formation of TP and ETF. Studies in the Si(111)-Cr system have shown that mixing and formation of mixed TP plays a significant role in the formation of both ordered and disordered ETF of silicides [1, 2, 8–10]. The data obtained was systematized in the form of a diagram describing the conditions for the formation of Cr-Si TP and $CrSi_2$ ETF [10]. These results showed thickness and temperature that determines the transition from 2D-TP to 3D-TP with increased thickness and two types of "patterns" of the $CrSi_2$ ETF, A- or B-type, with an azimuthal angle relative to Si(111) of 0° and 30°. The use of the appropriate TP and template made it possible for the first time to produce a epitaxial $CrSi_2$ A-type film with a thickness of 1000 Å and an increased carrier mobility.

It should be noted that these early studies were conducted at elevated steam temperature and reduced steam pressure (excluding the experiment [1, 2]). However, a number of studies of Cr-Si(111), Co-Si(111), and Si-$CrSi_2$(0001) systems have demonstrated that increasing vapor pressure (deposition rate) reduces mixing. To explain this phenomenon, a computer simulation cycle of growth kinetics was initiated. This modeling culminated in a probabilistic geometric analytical model of growth kinetics, which clarified the role of increasing vapor pressure in the aforementioned transition from mixing to growth [11]. Subsequent studies focused on the growth of amorphous Si on Si(111), the role of mixing in the formation of Co ETFs on Si(111), and the growth of amorphous TP and epitaxial Si ETF on $CrSi_2$(0001) [12].

However, to avoid mixing and reduce the thickness of the ETF, increased pressure or a lower vapor temperature was required. It was necessary to develop a technique for producing steam that would ensure either its high pressure or its low temperature. For this purpose, a deposition technique was developed [12] based on the previously known "hot wall" technique. This technique (double deposition) provided first pulsed deposition of adsorbate on a cold wall (secondary source), and then from this heated wall onto a cold substrate [13].

This innovative approach has led to the successful cultivation of TP and ETF containing almost pure Me (Si solid solution in Me) [12, 14]. It is noteworthy that "pseudo-three-dimensional" ν-TP have been identified, exhibiting nanoscale heterogeneity similar to that of known bulk nanophases (ν-phases) [15, 16]. The research cycle was completed by summarizing the results of [17] and investigating the role of steam temperature [18]. Subsequent studies focused on the growth of Cu-Si TP and Cu_3Si ETF, as well as layered ETF containing Co, Fe and Cu. The first generalization of these and previous results with the interpretation of TP as solid-phase wetting layers (SWL) was made in reviews [19–21]. The final period in the research series was associated with the formation of the SWL (or WL) concept [20]. In the review papers [21], the unique properties of the obtained nanostructures and potential applications in nano- and microelectronics were described. These include: nanocontacts or interconnects, electrodes and channels of field-effect (FET) and spin transistors, translucent contacts for infrared (IR) and ultraviolet (UV) sensors, cores for electromagnetic sensors, layers of spin filters and many other applications.

After that, experiments on SWL growth have been conducted and a phenomenological theory of its origin and growth has been developed (see references in [22–25]). Then SWL modeling has been performed for a number of Me-Si systems [26–29]. Recent first-principle modeling has shown that the main mechanism of the transition from SWL to ETF is a change in the coordination of atoms and electronic structure in SWL with increasing thickness, which leads to stress accumulation and atomic rearrangement in the film and the boundary layer of the substrate, and then to the destabilization of the film-substrate system and the transition of SWL to 3D-BP (ETF), accompanied by the release of latent energy in the form of heat.

Conclusion

This paper presents a series of studies devoted to the growth of extremely thin films from the vapor phase in a metal-silicon system. The role of a solid wetting layer in this process is demonstrated, and the fundamental causes of this phenomenon are discussed. A new growth method, physical atomic-layer deposition (PALD), has been developed through pulsed evaporation

of an adsorbate from a flat source positioned parallel to the substrate. This significantly reduced the vapor temperature in atomic streams and allowed for control of film thickness and composition. PALD has been used to produce extremely thin and nanofilms of refractory metals (Cr, Co, Fe) on silicon. These films possess a unique structure, electrical, optical, and magnetic properties, and hold promise for the development of micro- and nanotechnologies.

REFERENCES

1. **Lifshits V.G., Plyusnin N.I.,** Electronic interaction and s silicidization in the Cr-Si(111) system at the initial stage of growth, Phys., Chem. and Mech. of Surf. 9 (1984) 78.

2. **Lifshits V.G., Plyusnin N.I.,** Electronic structure and silicidization in thin films of transition metals on silicon, Preprint of Institute of Automation and Control Processes of Far Eastern Center of USSR Acad. Sci. (Vladivostok) No. 18 (127) (1984) 35 P.

3. **Kukushkin S.A., Osipov A.V.,** Determining polytype composition of silicon carbide films by UV ellipsometry, Technical Physics Letters. 42 (2016) 175.

4. **Lifshits V.G.,** Electron spectroscopy and atomic processes on the silicon surface, Ed. S.M. Repinsky. Moscow: Nauka. (1985) 200 P.

5. **Rossi G.,** *D* and *f* metal interface formation on silicon, Surface Sci. Rep. 7 (1-2) (1987) 1.

6. **Linford R.G.,** Surface energy of solids, Chemical Society Reviews. 1 (4) (1972) 445.

7. **Runnels L.K.,** Surface statistics, Crit. Rev. in Solid St. and Mat. Sci. 4 (1-4) (1973) 151.

8. **Galkin N.G., Plyusnin N.I., Lifshits V.G.,** Ordered surface phases in the Si(111)-Cr system, Physics, Chemistry and Mechanics of Surfaces. 12 (1987) 50.

9. **Plyusnin N.I., et al.,** Atomic mixing at the Si-Cr interface and the initial stages of $CrSi_2$ epitaxy, Physics, Chemistry and Mechanics of Surfaces. 9 (1989) 55.

10. **Plyusnin N.I., et al.,** Formation of Interfaces and Templates in the Si (111)-Cr System, Surface Review and Letters. (2) (1995) 439.

11. **Plyusnin N.I.,** Growth and mixing processes activated by the reaction at the interface in the transition metal-silicon systemю In: Heat and Mass Transfer Processes and Growth of Single Crystals and Thin Film Struct, Proc. 2-nd Rus. Symp. HT&CG'97 (Ed. V.P. Ginkin) Obninsk. (1998) 303.

12. **Plyusnin N.I.,** Substrate-stabilized phases and interface formation processes in 3d transition metal (Cr, Co) and silicon heterostructures, Thesis of Doctor of Phys. and Math. Sciences. Vladivostok. (2000).

13. **Lopez-Otero A.,** Hot wall epitaxy, Thin solid films. 49 (1) (1978) 3.

14. **Plusnin N.I., et al.,** Elevated Rate Growth of Nanolayers of Cr and $CrSi_2$ on Si(111), Phys. of Low-Dimens. Struct. 129 (2002) 9–10.

15. **Plusnin N., Il'iashchenko V., Krylov S.,** Metal thin-film nanophases and their interface with silicon, Journal of Physics: Conference Series. 100 (5) (2008) 052094.

16. **Plusnin N.I., et al.,** Formation, Electronic Structure, and Stability of Film Nanophases of Transition Metals on Silicon, Journal of Surface Investigation. 3 (2009) 734.

17. **Plyusnin N.I.,** Atomic-scale control of molecular beam growth of thin-film nanoheterostructures, Bulletin of the FEB of the Rus. Acad. of Sci. 5 (153) (2010) 26.

18. **Plyusnin, N.I., et al.,** Influence of the thermal power of a Fe atomic flux on the formation of Cu/Fe nanofilms on a Si (001) substrate, Technical Physics. 59 (7) (2014) 1017.

19. **Plusnin N.,** Atomic-scale control of molecular beam growth of nanolayers. In: Comprehensive Guide for Nanocoatings Technology, Characterization and Reliability. N.Y.: Nova Sci. Publ. Inc. 2 (2015) 87.

20. **Plusnin N.,** Atomic-Scale AES-EELS Analysis of Structure-Phase State and Growth Mechanism of Layered Nanostructures, Adv. in Materials Physics and Chemistry. 6 (7) (2016) 195.

21. **Plusnin N.,** Metallic nanofilms on single crystal silicon: growth, properties and applications, Modern Electronic Materials. 3 (2) (2017) 57.

22. **Plusnin N.,** The use of AES and EELS for complex analysis of two-dimensional coatings and their growth process, Modern Electronic Materials. 3 (4) (2017) 131.

23. **Plusnin N.,** Solid wetting layer, interphase formation, and thin-film nanomaterials. Brief review, Cond. Matter and Interphases. 25 (4) (2023) 594.

24. **Plusnin N.,** Solid phase wetting layer. In: Big Russian Encyclopedia. 3 (2024) 1.
25. **Plusnin N.,** Nanotechnology using solid-phase wetting layers and their prospects for silicon nanoelectronics, In: Abstracts of XV Conference "Silicon-2024". Irkutsk. (2024) 11.
26. **Zavodinsky V., Plusnin N., Gorkusha O.,** Quantum mechanical modeling of the Fe-Si(001) system at the stage of solid wetting layer growth, J. of Technical Physics. 94 (2) (2024) 231.
27. **Plusnin N., Zavodinsky V., Gorkusha O.,** Modeling of the atomic and electronic structure of a solid wetting layer of Fe on Si(001) obtained by layer-by-layer deposition, Solid State Physics. 66 (2) (2024) 275.
28. **Zavodinsky V., Gorkusha O., Plusnin N.,** Computer Simulation of Li and Be Wetting Layers on the Si (100) Surface, Computational nanotechnology. 11 (1) (2024) 121.
29. **Plyusnin N.I., Zavodinsky V.G., Gorkusha O.A.,** Formation of the atomic and electronic structure of two-dimensional Si layers on $CrSi_2$ (0001), Solid St. Phys. 67 (5) (2025) 889.

THE AUTHORS

PLYUSNIN Nikolay I.
plusnin.n@inme-ras.ru
ORCID: 0000-0001-9691-9721

Received 11.09.2025. Approved after reviewing 15.10.2025. Accepted 27.10.2025.

Научное издание

НАУЧНО-ТЕХНИЧЕСКИЕ ВЕДОМОСТИ САНКТ-ПЕТЕРБУРГСКОГО ГОСУДАРСТВЕННОГО ПОЛИТЕХНИЧЕСКОГО УНИВЕРСИТЕТА. ФИЗИКО-МАТЕМАТИЧЕСКИЕ НАУКИ

«ST. PETERSBURG STATE POLYTECHNICAL UNIVERSITY JOURNAL. PHYSICS AND MATHEMATICS»

ТОМ 18, № 4.1, 2025

Учредитель и издатель – Федеральное государственное автономное образовательное учреждение высшего образования «Санкт-Петербургский политехнический университет Петра Великого»

Журнал зарегистрирован Федеральной службой по надзору в сфере информационных технологий и массовых коммуникаций (Роскомнадзор).
Свидетельство о регистрации ПИ № ФС77-52144 от 11.12.2012 г.

Телефон редакции 8 (812) 552-62-16

Сайт https://physmath.spbstu.ru/

E-mail: physics@spbstu.ru

Компьютерная верстка *Н. А. Бушмановой*

Подписано в печать 29.12.2025 г. Дата выхода в свет 30.03.2026 г.
Формат 60x84/8. Печать цифровая.
Усл. печ. л. Тираж 1000. Заказ .
Цена: Бесплатно.

Отпечатано с готового оригинал-макета, предоставленного ИЦ "ИКИ",
в Издательско-полиграфическом центре
Санкт-Петербургского политехнического университета.
195251, Санкт-Петербург, Политехническая ул., 29.
Тел.: (812) 552-77-17; 550-40-14.

УСЛОВИЯ ПУБЛИКАЦИИ СТАТЕЙ

в журнале «Научно-технические ведомости
Санкт-Петербургского государственного политехнического университета.
Физико-математические науки»

1.ОБЩИЕ ПОЛОЖЕНИЯ

Журнал «Научно-технические ведомости Санкт-Петербургского государственного политехнического университета. Физико-математические науки» является периодическим печатным научным рецензируемым изданием. Зарегистрирован в Федеральной службе по надзору в сфере информационных технологий и массовых коммуникаций (Свидетельство ПИ №ФС77-52144 от 11 декабря 2012 г.) и распространяется по подписке агентства «Роспечать» (индекс издания 71823).

С 2008 года журнал издавался в составе сериального издания "Научно-технические ведомости СПбГПУ". **Сохраняя преемственность и продолжая научные и публикационные традиции сериального издания «Научно-технические ведомости СПбГПУ», журнал издавали под сдвоенными международными стандартными сериальными номерами ISSN 1994-2354 (сериальный) 2304-9782.** В 2012 году он зарегистрирован как самостоятельное периодическое издание **ISSN 2304-9782** (Свидетельство о регистрации ПИ № ФС77-52144 от 11 декабря 2012 г.). С 2012 г. начат выпуск журнала в двуязычном оформлении.

Издание входит в Перечень ведущих научных рецензируемых журналов и изданий (перечень ВАК) и принимает для печати материалы научных исследований, а также статьи для опубликования основных результатов диссертаций на соискание ученой степени доктора наук и кандидата наук по следующим основным научным направлениям: **Физика, Математика, Механика**, включая следующие шифры научных специальностей: 1.1.8., 1.1.9., 1.3.2., 1.3.3., 1.3.4., 1.3.5., 1.3.6., 1.3.7., 1.3.8., 1.3.11., 1.3.19.

Журнал представлен в Реферативном журнале ВИНИТИ РАН и включен в фонд научно-технической литературы (НТЛ) ВИНИТИ РАН, а также в международной системе по периодическим изданиям «Ulrich's Periodicals Directory». Индексирован в базах данных «Российский индекс научного цитирования» (РИНЦ), Web of Science (Emerging Sources Citation Index).

Периодичность выхода журнала – 4 номера в год.

Редакция журнала соблюдает права интеллектуальной собственности и со всеми авторами научных статей заключает издательский лицензионный договор.

2. ТРЕБОВАНИЯ К ПРЕДСТАВЛЯЕМЫМ МАТЕРИАЛАМ

2.1. Оформление материалов

1. Рекомендуемый объем статей – 12-20 страниц формата А-4 с учетом графических вложений. Количество графических вложений (диаграмм, графиков, рисунков, фотографий и т.п.) не должно превышать шести.

2. Число авторов статьи, как правило, не должно превышать пяти человек.

3. Авторы должны придерживаться следующей обобщенной структуры статьи: вводная часть (актуальность, существующие проблемы – объем 0,5 – 1 стр.); основная часть (постановка и описание задачи, методика исследования, изложение и обсуждение основных результатов); заключительная часть (предложения, выводы – объем 0,5 – 1 стр.); список литературы (оформление по ГОСТ 7.0.5-2008).

В списки литературы **рекомендуется** включать ссылки на научные статьи, монографии, сборники статей, сборники конференций, электронные ресурсы с указанием даты обращения, патенты.

Как правило, **нежелательны** ссылки на диссертации и авторефераты диссертаций (такие ссылки допускаются, если результаты исследований еще не опубликованы, или не представлены достаточно подробно).

В списки литературы **не рекомендуется** включать ссылки на учебники, учебно-методические пособия, конспекты лекций, ГОСТы и др. нормативные документы, на законы и постановления, а также на архивные документы (если все же необходимо указать такие источники, то они оформляются в виде сносок).

Рекомендуемый объем списка литературы для обзорных статей – не менее 50 источников, для остальных статей – не менее 10.

Доля источников давностью менее 5 лет должна составлять не менее половины. Допустимый процент самоцитирования – не выше 10 – 20. Объем ссылок на зарубежные источники должен быть не менее 20%.

4. УДК (UDC) оформляется и формируется в соответствии с ГОСТ 7.90-2007.

5. Набор **текста** осуществляется в редакторе **MS Word.**

6. **Формулы** набираются в редакторе MathType (не во встроенном редакторе Word) (мелкие формулы, символы и обозначения набираются без использования редактора формул). **Таблицы** набираются в том же формате, что и основной текст. В тексте буква «ё» заменяется на букву «е» и оставляется только в фамилиях.

7. **Рисунки** (в формате .tiff, .bmp, .jpeg) и **таблицы** оформляются в виде отдельных файлов. Шрифт – **Times New Roman**, размер шрифта основного текста – 14, интервал – 1,5. Таблицы большого размера могут быть набраны кеглем 12. Параметры страницы: поля слева – 3 см, сверху и снизу – 2 см, справа – 1,5 см. Текст размещается без знаков переноса. Абзацный отступ – 1 см.

2.2. Представление материалов

1. Представление всех материалов осуществляется в электронном виде через электронную редакцию (http://journals.spbstu.ru). После регистрации в системе электронной редакции автоматически формируется персональный профиль автора, позволяющий взаимодействовать как с редакцией, так и с рецензентом.

2. Вместе с материалами статьи должно быть представлено экспертное заключение о возможности опубликования материалов в открытой печати.

3. Файл статьи, подаваемый через электронную редакцию, должен содержать только сам текст без названия, списка литературы, аннотации и ключевых слов, фамилий и сведений об авторах. Все эти поля заполняются отдельно через электронную редакцию.

2.3. Рассмотрение материалов

Предоставленные материалы (п. 2.2) первоначально рассматриваются редакционной коллегией и передаются для рецензирования. После одобрения материалов, согласования различных вопросов с автором (при необходимости) редакционная коллегия сообщает автору решение об опубликовании статьи. В случае отказа в публикации статьи редакция направляет автору мотивированный отказ.

При отклонении материалов из-за нарушения сроков подачи, требований по оформлению или как не отвечающих тематике журнала материалы не публикуются и не возвращаются.

Редакционная коллегия не вступает в дискуссию с авторами отклоненных материалов.

При поступлении в редакцию значительного количества статей их прием в очередной номер может закончится **ДОСРОЧНО**.

E-mail: physics@spbstu.ru,
Тел. редакции 8 (812) 552-62-16.
Сайт журнала: https://physmath.spbstu.ru/